

12-2018

EVALUATION OF PRESAGE® AS A 3D DOSE VERIFICATION TOOL IN PROTON BEAMS

Mitchell Carroll

Follow this and additional works at: https://digitalcommons.library.tmc.edu/utgsbs_dissertations

 Part of the [Biological and Chemical Physics Commons](#), and the [Medicine and Health Sciences Commons](#)

Recommended Citation

Carroll, Mitchell, "EVALUATION OF PRESAGE® AS A 3D DOSE VERIFICATION TOOL IN PROTON BEAMS" (2018). *The University of Texas MD Anderson Cancer Center UTHealth Graduate School of Biomedical Sciences Dissertations and Theses (Open Access)*. 898.
https://digitalcommons.library.tmc.edu/utgsbs_dissertations/898

This Dissertation (PhD) is brought to you for free and open access by the The University of Texas MD Anderson Cancer Center UTHealth Graduate School of Biomedical Sciences at DigitalCommons@TMC. It has been accepted for inclusion in The University of Texas MD Anderson Cancer Center UTHealth Graduate School of Biomedical Sciences Dissertations and Theses (Open Access) by an authorized administrator of DigitalCommons@TMC. For more information, please contact digitalcommons@library.tmc.edu.

EVALUATION OF PRESAGE® AS A 3D DOSE VERIFICATION TOOL IN PROTON
BEAMS

by

Mitchell Scott Carroll

APPROVED:

Geoffrey Ibbott, Ph.D.
Advisory Professor

David Followill, Ph.D.

Michael Gillin, Ph.D.

Kenneth Hess, Ph.D.

Mark Oldham, Ph.D.

APPROVED:

Dean, The University of Texas
MD Anderson Cancer Center UTHHealth Graduate School of Biomedical Sciences

EVALUATION OF PRESAGE® AS A 3D DOSE VERIFICATION TOOL IN PROTON
BEAMS

A
DISSERTATION

Presented to the Faculty of
The University of Texas
MD Anderson Cancer Center UTHealth
Graduate School of Biomedical Sciences
in Partial Fulfillment
of the Requirements
for the Degree of
DOCTOR OF PHILOSOPHY

by
Mitchell Scott Carroll
Houston, Texas
December 2018

Acknowledgements

I would like to acknowledge the tireless efforts of my advisor, Dr. Geoffrey Ibbott, for his support and supervision over these many years. Somehow, between his running a large department and staying heavily involved with the field on the international stage, he was able to make time for his students consistently during our work. I'll never understand how he managed so many projects simultaneously and still could seemingly remember even the smallest detail of my work mentioned offhand months before.

I would also like to thank my additional committee members for their time and efforts. Dr. Followill and Dr. Gillin both offered a very clinically relevant analysis of my results at every committee meeting. Dr. Oldham did the same for PRESAGE® dosimeters. Dr. Hess offered a perspective outside of the Medical Physics field and helped to present the data in a statistically meaningful way.

Two specific departments deserve special mention. IROC-Houston was where I spent the first half of my graduate work and the physicists and staff there provided equipment and expertise in one of the most hospitable environments I could ever ask to work. In addition, I would like to thank the staff of the Proton Therapy Center because without their help I could not have conducted the research in this study. Specifically I would like to thank Dr. Sahoo and Matt Kerr for always making time on the machine for me and teaching me specific clinical procedures for proton therapy.

Finally, I would like to thank the other individuals who made this work possible. Dr. Mirkovic's support with MCNP made specific portions of this project possible and Dr. Alqathami who taught me the fundamentals of dosimeter manufacturing. Finally to my fellow students, although now all graduated, whose support and company helped me through everything. Thank you to Angela Steinmann, Hannah Lee, Yvonne Roed, Ryan Lafratta, "The Chris'," "The Kevin's," Jessie Huang, and those too many to name who came and went from the institution years ago.

EVALUATION OF PRESAGE® AS A 3D DOSE VERIFICATION TOOL IN PROTON BEAMS

Mitchell Scott Carroll

Advisory Professor: Geoffrey Ibbott, Ph.D.

Radiotherapy techniques have advanced and radiation dose plans have become much more complex over the last decade. This is especially true in proton therapy, which involves extremely steep dose gradients as a result of positioning the Bragg peak to cover the volumes to be treated. The Bragg peak can be shifted significantly in the patient as a result of nonuniformities in the tissue composition in its path, which can result in treatment complications. Some traditional dose verification tools used in proton beam commissioning and treatment plan verification are film, TLD, and ionization chambers. Such 0D and 2D dosimeters are incapable of fully registering a complete dose volume. This shortcoming has led to an interest in a robust 3D dosimeter with dosimetric accuracy matching that of traditional devices. PRESAGE®, a novel radiochromic dosimeter, has shown promise in dose verification of complex IMRT treatments. As such, there have been numerous studies of PRESAGE® as a 3D dosimetry tool in photon and electron radiotherapy, but little work towards adapting it to proton therapy. The primary limitation for using PRESAGE® in a proton beam has been the appearance of ‘quenching’, principally seen in the Bragg peak region of the delivered field, resulting in a pronounced dose under-response. Very little research has gone into investigating the cause of this quenching and no system is in place to account for it. Currently, PRESAGE® continues to find more of a place in photon radiation therapy research and clinical applications, and

while interest in proton therapy increases around the world, Presage has not been demonstrated to be an accurate dose verification system for proton therapy.

I hypothesized that the mechanisms causing signal quenching in PRESAGE® when irradiated by a proton beam can be evaluated and corrected for resulting in a system that yields relative dose measurements agreeing with ionization chamber measurements to $\pm 3\%$ in the Bragg peak and with calculated doses to 5%/5mm.

This hypothesis was tested using three aims. The first aim developed a PRESAGE® manufacturing protocol capable of producing dosimeters to meet the needs of a wide range of clinical applications. The second aim evaluated the effects of the concentrations of the active components in PRESAGE® formulation on specific dosimetric properties and optimized formulations minimizing signal quenching chemically. The final aim developed and applied a quenching correction factor to PRESAGE® as a way to reduce dose inaccuracies caused by quenching.

Table of Contents

Approval Page.....	i
Title Page	ii
Acknowledgements.....	iii
Abstract and dissertation outline.....	v
List of Illustrations.....	x
List of Tables	xix
Abbreviations.....	xxi
Chapter 1: Significance.....	1
Chapter 2: Introduction.....	4
2.1 Radiotherapy Practices.....	4
2.2 Proton radiotherapy.....	6
2.3 Mechanics of proton interactions.....	12
2.4 Proton Facility Design	21
2.5 Conventional dosimetry for proton therapy	32
2.6 Quality Assurance for passive scattering proton therapy	35
2.7 Three-dimensional dosimetry	40
2.8 PRESAGE® dosimeters	48
2.9 Signal quenching in a proton beam.....	50

2.10 Optical readout.....	52
2.11 Dissertation objectives	54
Chapter 3: PRESAGE® manufacture and characterization.....	56
3.1 Rationale	56
3.2 Materials and methods	56
3.3 Results and discussion	71
3.4 Conclusions.....	86
Chapter 4: Evaluation of PRESAGE® active components and development of a low-quenching formulation.....	87
4.1 Rationale	87
4.2 Evaluation of active components	87
4.3 Reduced quenching formula optimization	108
4.4 Conclusions.....	121
Chapter 5: Development of a semi-empirical correction model for dose quenching	122
5.1 Rationale	122
5.2 Materials and methods	123
5.3 Results and Discussion	130
5.4 Conclusions.....	145
Chapter 6: Conclusions and future works	147

6.1 Discussion and conclusions	147
6.2 Future works	151
Appendix.....	153
References.....	174
Vita.....	218

List of Illustrations

Figure 2.1: An illustration of the relative depth dose profile of 140 MeV protons. The dotted line represents the profile computed to result from a single proton and illustrates the sharp Bragg peak. The solid line represents the profile for a proton beam consisting of many particles and demonstrates the broadening of the Bragg peak as a result range straggling. (Based on data by Wilson (1946)) ³⁸	9
Figure 2.2: A comparison of depth dose curves in water for proton and 18MV photon (black) beams as well as an illustration of the formation of an SOBP. The pristine Bragg peaks (shown in red) are delivered with varying range and intensity which, when summed, result in the SOBP of uniform dose (shown in blue).	11
Figure 2.3: Illustration of the three primary interactions of a high energy proton. In (a), the proton (p+) undergoes an inelastic Coulombic interaction with the atomic electron shell and electrons (e-) are emitted. In (b), the proton is deflected by the atomic nucleus by elastic Coulombic scattering. Finally, in (c) the proton collides with the atomic nucleus leading to a nuclear interaction whereby the primary proton is absorbed and secondary particles are ejected. These secondary particles may include gammas (γ), neutrons, secondary protons (p+'), or nuclear fragments.	14
Figure 2.4: Comparison of range calculation methods (solid lines) for protons in water: the CSDA range (orange) and the projected range (blue). The detour factor (dashed grey) is the ratio of the projected range to CSDA range. The figure was generated using data available from NIST's PSTAR database ⁷⁴	19

Figure 2.5: A modular range modulator wheel (left) used by the Proton Therapy Center – Houston with a close up image of the range shifting steps (right).....	25
Figure 2.6: Photographs of an aperture (left) and range compensator (right) used for beam shaping at the Proton Therapy Center – Houston. Patient identifiers redacted.....	26
Figure 2.7: (Top) model of the PTC-H showing the center layout. Of the four treatment rooms, G1 and G2 treat with PSPT on rotating gantries, G3 treats with SSPT on a rotating gantry, and F1 and F2 treat using fixed beam PSPT. (Bottom) Photograph of G1 in the resting position.....	30
Figure 2.8: Schematic diagram of the devices intercepted by the beam line as it passes through a PSPT nozzle at the PTC-H. The beam profiler and reference dose ionization chamber measure positions of the beam center and width of the pristine beam. The first scatterer includes a scattering foil integrated with the RMW. The second scatterer flattens the beam which is then immediately attenuated through the range shifter which allows for improved range resolution. The Multilayer Faraday Cup (MLFC) measures the penetration of the beam after double scattering but only intercepts the beam during a pre-treatment beam check and is removed during treatment. Finally the beam passes into the snout which holds the aperture and range compensators used for field shaping before finally irradiating the target volume.	31
Figure 3.1: The molecular structure illustrating the transition of LMG into its oxidized product MG.....	58
Figure 3.2: Pressure tank and air compressor system used for polyurethane out-gassing.....	62

Figure 3.3: Photograph of the polystyrene slab used for cuvette irradiations (left) and the experimental setup including the Solid Water® beam attenuators (right).....	68
Figure 3.4: Diagram (top) and matching photograph (bottom) of the DMOS-IROC.....	70
Figure 3.5: Photograph of PRESAGE® cuvettes irradiated to varying doses to demonstrate the associated visual color change.....	72
Figure 3.6: Photographs of PRESAGE® dosimeters demonstrating the visible color change as a result of LMG oxidation in a large volume. Dosimeter (a) was unirradiated, dosimeter (b) was irradiated to 4 Gy, and dosimeter (c) was irradiated to over 50 Gy....	72
Figure 3.7: Images of many common fabrication artifacts. Schlieren bands (a and b), damage caused from dosimeter demolding (c and d), and undissolved particulates (e, f, and g).	75
Figure 3.8: X-ray CT axial cross sections taken at the top (a), center (b), and bottom (c) of a cylindrical dosimeter with a line profile of CT number values along the central axis.	77
Table 3.5: Area profile analysis of the CT values in axial planes taken from a cylindrical PRESAGE® dosimeter.	77
Figure 3.9: Polyurethane manufactured without pressurization (left) cures with trapped bubbles while the polyurethane pressurized to 60 psi (right) does not.....	78
Figure 3.10: ΔOD as a function of absorbed dose as measured by PRESAGE® cuvettes from three fabrications of the same formulation with linear trends represented by solid	

lines. Error bars represent the standard deviation of the response of three cuvettes from each batch irradiated to each dose point. 80

Figure 3.12: Change in dose response for PRESAGE® cuvettes irradiated to varying dose points over five days. Error bars represent the standard deviation between three cuvettes measured at each dose point. Lines were added between measurement points to aid the eye. 82

Figure 3.13: Cylindrical PRESAGE® irradiated from the top-down with a square field. The visual color change is shown in photographs of the top (a) and sides (b) of the dosimeter with lines drawn to give contrast. The dose image reconstruction in CERR is shown for the central transverse (c) and coronal (d) planes. 84

Figure 3.14: Isodose profiles of PRESAGE® top-down irradiation in a water phantom in the (a) sagittal plane with dashed lines representing axial cross section locations. Line profiles through these cross sections comparing the dose uniformity of PRESAGE® and TPS calculations are shown in (b) (c) and (d)..... 85

Figure 4.1: Solid Water® configuration used for irradiation of cuvettes with the F2 proton beamline. The polystyrene slab used to hold cuvettes is shown in the loading position (left) and in an irradiation position (right). 93

Figure 4.2: Zebra dosimetry system setup for depth dose profile measurements on the fixed beamline (F2) at the PTC-H. 95

Figure 4.3: Initial OD for each batch of PRESAGE® represented as a function of changes to specific active components. The data point for 1% DBTDL ($\Delta OD \approx 0.4$) is not shown

on this scale. Error bars represent the standard deviation among three batches for each formulation..... 98

Figure 4.4: ΔOD as a function of absorbed dose as measured by PRESAGE® batches with variable LMG concentrations. The linear trends are represented by solid lines and error bars represent the standard deviations of readings from all cuvettes at each dose point. 99

Figure 4.5: ΔOD as a function of absorbed dose measured by PRESAGE® batches with variable radical initiator type and concentration. The linear trends are represented by solid lines and error bars represent the standard deviations of readings from all cuvettes at each dose point..... 100

Figure 4.6: ΔOD as a function of absorbed dose as measured by PRESAGE® batches with variable DBTDL concentration. Batch 9 is covered by the x-axis. The linear trends are represented by solid lines and error bars represent the standard deviations of readings from all cuvettes at each dose point. 101

Figure 4.7: Change in dose signal over time for PRESAGE® cuvettes containing each formulation irradiated to 400 cGy. Lines between time points added to aid the eye. 103

Figure 4.8: Relative depth dose comparison in a 225-MeV proton beam with 10 cm SOBP as measured by Multi-layer Ion Chamber (blue), large volume proton PRESAGE® (red), and cuvettes of proton PRESAGE® (orange points). The agreement between large volume and cuvette measurements is shown (black line). 105

Figure 4.9: Dose responses for proton PRESAGE® when irradiated with photons and protons and calculated quenching. The linear trends are represented by solid lines. 106

Figure 4.10: The peak-to-plateau ratios for several depths at which low, medium, and high quenching was observed. Ratios are a function of formulation active components: (a) CHBr₃, (b) CHCl₃, (c) LMG, and (d) DBTDL..... 108

Figure 4.11: Photographs of two sample sets of cuvettes created for formulation optimization illustrating the visual dose response difference between formulations made using chloroform (left) and bromoform (right)..... 111

Figure 4.12: The percent of signal quenching measured at the distal-most point in the SOBP for each formulation using chloroform (top) and bromoform (bottom) as the radical initiator. Error bars represent the standard deviation between three intrabatch cuvette comparisons..... 113

Figure 4.13: Minimum percent of signal quenching for PRESAGE® formulations across all concentrations of radical initiator and for each concentration of LMG. Error bars represent the standard deviation among three intrabatch cuvette comparisons..... 114

Figure 4.14: Comparison of the ΔOD of unirradiated, low-quenching chloroform and bromoform formulations of PRESAGE® when stored in cold ($\leq 3^{\circ}\text{C}$) and warm ($\sim 21^{\circ}\text{C}$) conditions. Error bars represent the standard deviation among intrabatch cuvette comparisons and connecting lines added to aid the eye. 117

Figure 4.15: Temporal stability comparison between low-quenching chloroform and bromoform formulations of PRESAGE® when stored in cold ($\leq 3^{\circ}\text{C}$) and warm (room

temperature) conditions after being irradiated to 200 cGy. Dose signal was normalized to readings taken at 24 hours. Error bars represent the standard deviation among intrabatch cuvette comparisons and connecting lines added to aid the eye. 118

Figure 4.16: Dose responses for LQCl (left) and LQBr (right) PRESAGE® when irradiated by low-LET photons and high-LET protons and calculated quenching. Linear trends shown by solid lines. 119

Figure 4.17: RLSP values of the LQCl and LQBr PRESAGE® formulations plotted alongside the calibration curve used in the Eclipse® TPS. 120

Figure 5.1: A photograph of the irradiation setup used for the experimental measurements (left). Monte Carlo LET modeling (right) was generated by a cross-sectional plane based on the MCNP input deck using the visual editor Vised®. Material are labeled.. 127

Figure 5.2: Relative depth-dose curves as measured by the LQCl PRESAGE® and ionization chamber measurements for an unmodulated 140 MeV proton beam. PRESAGE® dose was normalized to a point approximately 0.5 cm deep in the dosimeter. 131

Figure 5.3: QCF(d) calculated from PRESAGE® and ionization chamber measurements along the beam central axis of the beam for an unmodulated 140 MeV PSPT proton irradiation along with LET_{ϕ} calculated using Monte Carlo. 132

Figure 5.4: The measured QCF as a function of LET for all dose depths as measured in the LQCl PRESAGE® dosimeter irradiated with unmodulated 140 MeV PSPT protons. A third order polynomial line has been fitted to the points. 133

Figure 5.5: Results of the calibration dosimeter used in the calculation of $QCF(LET_\phi)$ and its application to correct dose quenching for an unmodulated 140 MeV proton irradiation. Plot (a) compares the depth-dose curves of the uncorrected and quenching-corrected PRESAGE® with ionization chamber readings. The Monte Carlo calculated LET_ϕ and $QCF(LET_\phi)$ are shown in plot (b), and the agreement of PRESAGE® to ionization chamber is shown in plot (c). 135

Figure 5.6: Results of the quenching correction in Dosimeter A demonstrating reproducibility of the application of the $QCF(LET_\phi)$ function. Plot (a) compares the depth-dose curves of the uncorrected and quenching-corrected PRESAGE® with ionization chamber readings. The Monte Carlo calculated LET_ϕ and $QCF(LET_\phi)$ are shown in plot (b), and the agreement of PRESAGE® to ionization chamber is shown in plot (c). 137

Figure 5.7: Results of the quenching correction in Dosimeter B demonstrating the application of the $QCF(LET_\phi)$ function in a low dose irradiation. Plot (a) compares the depth-dose curves of the uncorrected and quenching-corrected PRESAGE® with ionization chamber readings. The Monte Carlo calculated LET_ϕ and $QCF(LET_\phi)$ are shown in plot (b), and the agreement of PRESAGE® to ionization chamber is shown in plot (c). 139

Figure 5.8: Results of the quenching correction in Dosimeter C demonstrating the application of the $QCF(LET_\phi)$ function when applied to a 180 MeV irradiation. Plot (a) compares the depth-dose curves of the uncorrected and quenching-corrected PRESAGE® with ionization chamber readings. The Monte Carlo calculated LET_ϕ and $QCF(LET_\phi)$ are

shown in plot (b), and the agreement of PRESAGE® to ionization chamber is shown in plot (c). 141

Figure 5.9: Results of the quenching correction in Dosimeter D demonstrating the application of the $QCF(LET_\phi)$ function when applied to a 140 MeV proton beam with a 4 cm SOBP. Plot (a) compares the depth-dose curves of the uncorrected and quenching-corrected PRESAGE® with ionization chamber readings. The Monte Carlo calculated LET_ϕ and $QCF(LET_\phi)$ are shown in plot (b), and the agreement of PRESAGE® to ionization chamber is shown in plot (c). 143

Figure 5.10: Representations of the gamma passing maps for the dose response of an LQCl PRESAGE® and an Eclipse® TPS prediction for a 4 cm SOBP, 140 MeV PSPT proton beam. Cross-sectional planes along the central axis of the transverse (a and d) and sagittal (b and e) planes. The coronal plane was taken at a depth approximately 1 cm proximal to the distal-90%. 145

List of Tables

Table 2.1: Clinical specifications of the PSPT beam lines at the PTC-H (Smith 2009 “proton therapy”).	28
Table 3.1: Elemental fractional components by weight of LMG	59
Table 3.2: Elemental percent of components by weight for halogenated hydrocarbons used as radical initiators.....	60
Table 3.3: Elemental fractional components by weight of polyurethane and the catalyst agent DBTDL relative to ICRP’s simplified four-component soft tissue composition....	61
Table 3.4: Comparison of the elemental fractional weights of the proton PRESAGE® (shown here as PRESAGE-1) investigated in literature ²⁶⁷ and PRESAGE® made in-house (shown here as PRESAGE-2).	64
Table 3.6: Results of PRESAGE® shrinkage when cured under different pressures. Temperatures at the time of pouring and when cured are included.....	79
Table 3.7: Dose uniformity measured by line profiles through three central axis cross sections.....	86
Table 4.1: Composition (percent by weight) of the active components used in each PRESAGE® batch.	89
Table 4.2: PRESAGE® batches used for comparing the concentration of LMG on dosimetric properties. Compositions are shown as percent by weight for each active component.....	96

Table 4.3 PRESAGE® batches used for comparing the type and concentration of the radical initiator on dosimetric properties. Compositions are shown as percent by weight for each active component.	97
Table 4.4: PRESAGE® batches used for comparing the concentration of the polyurethane catalyzing agent DBTDL on dosimetric properties. Compositions are shown as percent by weight for each active component.	97
Table 4.5: Changes to OD following irradiation for each formulation.....	102
Table 4.6: Chemical composition of low-quenching PRESAGE® formulations. Percentages are listed by weight.	115

Abbreviations

0D [Zero dimensional]	1
2D [Two dimensional]	1
3D [Three dimensional]	2
A [Atomic weight]	17
AAPM [American Association of Physicists in Medicine]	32
amu [Atomic mass unit]	12
CCD [Charge-coupled device]	53
CERR [A Computational Environmen for Radiotherapy Research]	70
CHBr ₃ [Bromoform]	59
CHCl ₃ [Chloroform]	46
CHI ₃ [Iodoform]	59
CSDA [Continuous slowing down approximation]	18
CT [Computed tomography]	35
DD [Dose difference]	37
DMOS-IROC [Duke Midsized Optical-CT Scanner for IROC-Houston]	69
DTA [Distance-to-agreement]	38
ERE [Electron return effect]	49
FBX [Fricke-benzoic-xlenol]	45
Gy [Gray (unit)]	5
HQ [High quenching]	106
I [Mean excitation potential]	17
IAEA [International Atomic Energy Agency]	32

ICRU [International Commission on Radiation Units and Measurements]	17
IROC-H [Imaging and Radiation Oncology Core in Houston]	39
LET [Linear Energy Transfer]	19
linac [Linear accelerator]	22
LMG [Leuco malachite green].....	57
LQ [Low quenching].....	106
LQBr [Low-quenching bromoform-based formulation].....	115
LQCl [Low-quenching chloroform-based formulation]	115
LS [Liquid scintillator]	46
MCNP [Monte Carlo N-Particle Transport Code].....	124
MeV [Megaelectronvolt]	15
MG [Malachite green].....	57
MLIC [Multilayer ionization chamber]	33
MQ [Mid quenching]	106
MRI [Magnetic resonance imaging]	42
MR-IGRTs [MR-image guided radiation therapies].....	49
MRT [microbeam radiotherapy]	10
MU [Monitor Unit]	37
NCI [National Cancer Institute].....	39
NIST [National Institute of Standards and Technology]	18
NTCP [Normal tissue complication probability]	5
OD [Optical density].....	48
PMMA [Polymethyl methacrylate].....	73

PPR [Peak-to-plateau ratio]	92
PSPT [Passive scattering proton therapy]	23
PTC-H [MD Anderson Proton Therapy Center in Houston]	27
Q% [Dose quenching percentage]	127
QA [Quality Assurance)	1
QCF [Quenching correction factor]	128
RBE [Relative biological effectiveness]	20
RLSP [Relative linear stopping power]	16
RMW [Range modulator wheel]	24
S [Stopping power]	15
SNR [Signal-to-noise ratio]	43
SOBP [Spread out Bragg peak]	8
SRS [Stereotactic radiosurgery]	10
SSPT [Spot scanning proton therapy]	23
Sv [Sievert (unit)]	5
TCP [Tumor control probability]	5
TG [Task Group report by the AAPM]	32
TLD [Thermoluminescent detector]	33
TPS [Treatment planning system]	2
TR [Therapeutic ratio]	1
VMAT [volumetric arc therapy]	10
Z [Atomic Number]	17
γ [Gamma value (dimensionless unit)]	38

ΔOD [Net optical density]	54
ρ [Mass density (unit)]	16

Chapter 1: Significance

Radiotherapy for the treatment of cancer has developed over the last century into many modalities, and alongside chemotherapy and surgery, it has become a primary curative tool. The principal goal of radiotherapy is tumor control which must be balanced with the need to limit normal tissue complications in a relationship known as the therapeutic ratio (TR). In the pursuit of improving this ratio, advances in modern technology have led to improvements in therapy machines and treatment planning systems enabling the delivery of greater and greater complexities of treatment. The most common modality used for radiotherapy has been external beam x-rays delivered by a linear accelerator, but over the last two decades the use of fast protons has seen a surge in availability in clinics around the world.

Quality Assurance (QA) programs have been developed for each modality to ensure accurate treatment delivery and patient safety. Typically performed by, or under the supervision of, a medical physics specialist, these programs traditionally have been performed by sampling measurements taken at points throughout an irradiated volume and detecting areas of abnormally high or low doses. Conventional detectors used for these measurements include point detectors (0D) and two dimensional (2D) detectors^{1,2}. A 2006 report demonstrated these limitations by showing more than 30% of institutions failed to meet standards set for credentialing to take part in NCI clinical trials related to complex photon plans³⁻⁵. Proton therapy typically delivers complex dose distributions with extreme dose gradients which cannot be comprehensively measured using these conventional tools. More recently, another report showed 20-30% of participating proton institutions failed credentialing criteria, indicating that beam commissioning might have

been inadequate⁶. These studies demonstrate that comprehensive measurements of the irradiated volume are necessary to ensure planning and delivery errors are detected during routine QA.

Three-dimensional (3D) dosimeters capable of comprehensive dosimetry have the potential to overcome many limitations specific to conventional dosimetry systems. Most commonly, these are chemical systems that undergo a physical change in response to irradiation allowing dose distributions to be measured using compatible imaging equipment. The potential applications of such devices would include radiotherapy device QA, patient plan verifications, and many facets of remote auditing. A wide variety of 3D devices have been investigated and in some instances incorporated into QA practices. The most commonly studied 3D dosimeters include polymer^{7,8} and Fricke⁹ gels, but over the last decade radiochromic plastics have seen a surge of development. Foremost among these, and the dosimeter in this study, is PRESAGE® (Heuris Inc., LLC, Skillman, NJ) which offers many specific advantages over gel 3D dosimeters. Highly conformal dosimetry measurements using PRESAGE® have previously been demonstrated including preliminary studies showing very close agreement between PRESAGE® and treatment planning systems (TPS) for external beam photon treatments^{10,11} as well as robustness for remote dosimetry¹².

Interest in clinical proton therapy continues to grow¹³, but the highly conformal dose distributions lead to challenges in performing QA measurements. A 3D dosimetry system could provide comprehensive volume measurements that are captured in a single irradiation and can potentially catch planning and delivery errors missed by conventional systems. Unfortunately, most 3D dosimetry systems show a reduced sensitivity towards

the end of the beam range. PRESAGE® is similarly affected making accurate proton dosimetry so far impossible¹⁴⁻¹⁶. No known studies have comprehensively investigated the mechanisms causing this quenching nor have chemically corrected for it. A PRESAGE® formulation with a predictable response to a proton irradiation could increase the accuracy of QA and reduce dose verification time which can lead to increased tumor control, improved patient safety, and reduced workload. In this study, the mechanisms leading to quenching were investigated as well as methods to improve PRESAGE® applications in clinical proton beams.

Chapter 2: Introduction

2.1 Radiotherapy Practices

2.1.1 History of radiation in cancer therapy

The use of radiation as a primary technique in palliative cancer treatment came about with the discovery of x-rays by Wilhelm Röntgen in 1885¹⁷. Physicians quickly recognized their therapeutic potential and within a year began using them to treat malignant diseases^{18–21}. Shortly after, Marie Curie's 1898 discovery of radium^{22,23} opened the door for a plethora of radiotherapy modalities specifically targeting surface lesions^{24–26}. As these gained traction over the following decades, physicians and researchers began to develop safer and more effective treatment protocols²⁷. Eventually nuclear reactors and cyclotron technologies lead to cheaper and more robust radioisotopes such as cobalt-60, while modern medical linear accelerators improved to generate higher energy x-rays and deliver more conformal radiotherapies. Today in the United States, cancer is the second leading cause of death with over 1.6 million new cases and an estimated 595,690 deaths in 2016²⁸. About half of these cases include radiation therapy as at least part of their primary treatment²⁹.

2.1.2 Brief overview of radiotherapy techniques

Radiation therapy delivers ionizing particles that damage the deoxyribonucleic acids (DNA) of cells leading to single-strand and double-strand breaks with the ultimate goal being cell death. Radiotherapy modalities include photons, electrons, and hadrons (such as protons) which offer unique dose conformity and radiobiological cell killing pathways which allow for tumor site specific treatment prescriptions. Often, these modalities are delivered using either an external beam or brachytherapy sources. Tumor

location, anatomical structure, stage, and radiosensitivity each contribute to the treatment selection. Radiotherapies are most often combined with chemotherapy, immunotherapy, and surgery.

Radiotherapy treatments deliver a prescribed dose of radiation measured in gray (Gy). This SI derived unit defines the physical quantity of energy absorbed per unit of mass as described below³⁰. The gray is independent of the target material and unlike the sievert (Sv), it ignores any biological context.

$$1 \text{ Gy} = 1 \frac{\text{J}}{\text{kg}} \quad \text{Eq. 2.1}$$

Ultimately, a radiotherapy treatment plan seeks to maximize tumor control probability (TCP) while minimizing normal tissue complication probability (NTCP) in a comparison referred to as the therapeutic ratio (TR). The radiation oncologist's goal is to prescribe sufficient dose to the target to kill all malignant cells while keeping doses to normal tissue volumes sufficiently low in order to minimize adverse secondary effects ranging from acute symptoms to late morbidity. Because of the penetrating nature of radiation, completely sparing normal tissue in the path of the beam is generally impossible. Instead, dose plans are generated to conform to the treatment volume while keeping vital tissue doses below specific dose thresholds. This is frequently performed using multiple fields converging onto a target (the tumor).

Dose prescriptions are generated to account for survival of both normal and tumor cells. Tumor cell repair pathways differ from those of healthy cells, usually resulting in

the tumor cells taking a greater amount of time to recover. Dose fractionation is a tool, first developed in 1922 by Henri Coutard, used in dose planning that accounts for these different pathways as a way to maintain a high tumor control while limiting normal tissue damage^{31,32}. The total doses prescribed depend on many characteristics of the tumor and patient but typically range from 40 to 70 Gy³³. Translational research has found optimal distributions of temporally spacing this dose so today a conventional fractionated treatment has daily doses of 1.5-2.5 Gy delivered in approximately 30 fractions^{34,35}. Modern treatment planning is optimized using specialized treatment planning software incorporating parameters specific to the radiotherapy equipment, beam quality, patient anatomy, and machine calibrations³⁶.

2.2 Proton radiotherapy

2.2.1 History of Proton Radiotherapy

In 1932, Ernest Lawrence invented the cyclotron which allowed for the acceleration of charged particles, including protons, to very high energies³⁷. Over the next decade, his laboratory at the University of California-Berkeley improved on a series of cyclotrons eventually earning him the Nobel Prize in physics in 1939. In 1946, a previous graduate student of Lawrence, Robert Wilson, recognized the therapeutic potential of accelerated protons and published a seminal paper proposing their use in treating deep-seated tumors³⁸. In this paper, Wilson discusses the physical mechanisms of proton dose deposition, the biological advantages over the conventional photon therapies, as well as the necessary engineering developments that would be required for clinical use.

In 1954, the Lawrence Berkeley Laboratory treated the first human patient with protons and over the next few years another 25 patients with metastatic breast cancer underwent pituitary irradiations³⁹. Outside of the United States, the cyclotron at Gustaf Werner Institute in Uppsala, Sweden also began treatment therapies. In the 1960s, Massachusetts General Hospital in Cambridge, MA began treating patients at the Harvard Cyclotron Laboratory and would go on to expand and improve technologies in proton beam delivery and safety⁴⁰. Finally, in 1990 the first high-energy, hospital-based proton therapy center was opened at the Loma Linda Medical Center in Loma Linda, CA and commercial systems became available in 2001. Since that time, the number of proton therapy facilities has rapidly increased. Today, there are 26 proton therapy centers in the United States and 49 more throughout the world in operation with approximately 60-70 more in various stages of development¹³. From the first patient treated in 1954 until 2015, 131,240 patients have been treated with protons¹³

2.2.2 Rationale for Proton Radiotherapy

The primary justification for proton therapy comes from its unique dose deposition which allows for spatial dose distributions not possible using photons. Due to the nature of their inherent charge, protons have a well-defined range of penetration as a result of continuous ionization of atoms along their paths. Energy deposition, or absorbed dose, along a proton particle's track length is inversely related to the particle's local energy, so as the protons slow down the energy deposited per unit track length increases. The terminal range of a proton beam is therefore a function of its initial energy and the composition of the medium. The depth-dose curve has two distinct regions. At shallow depths where a particle's energy is near its initial energy, dose deposition is

relatively small resulting in what is called the dose plateau. As the proton approaches the terminal range, the dose deposition quickly increases to a maximum when the particle comes to rest resulting in a very sharp dose peak. When many protons are delivered, this peak is slightly broadened as a result of statistical deviations in what is called range straggling^{38,41}, as shown in Figure 2.1. This dose peak, first observed in alpha particles by William Bragg in 1902, is therefore called the Bragg peak⁴². The depth of this peak in a patient can be controlled through careful beam energy selection and modulation, but often a target volume requires volume coverage greater than a single Bragg peak's longitudinal coverage. To account for this, multiple Bragg peaks with varying ranges and intensities are stacked to widen the dose peak and deliver a uniform dose across the whole target. This widened dose peak is called a spread out Bragg peak (SOBP) and is illustrated in Figure 2.2.

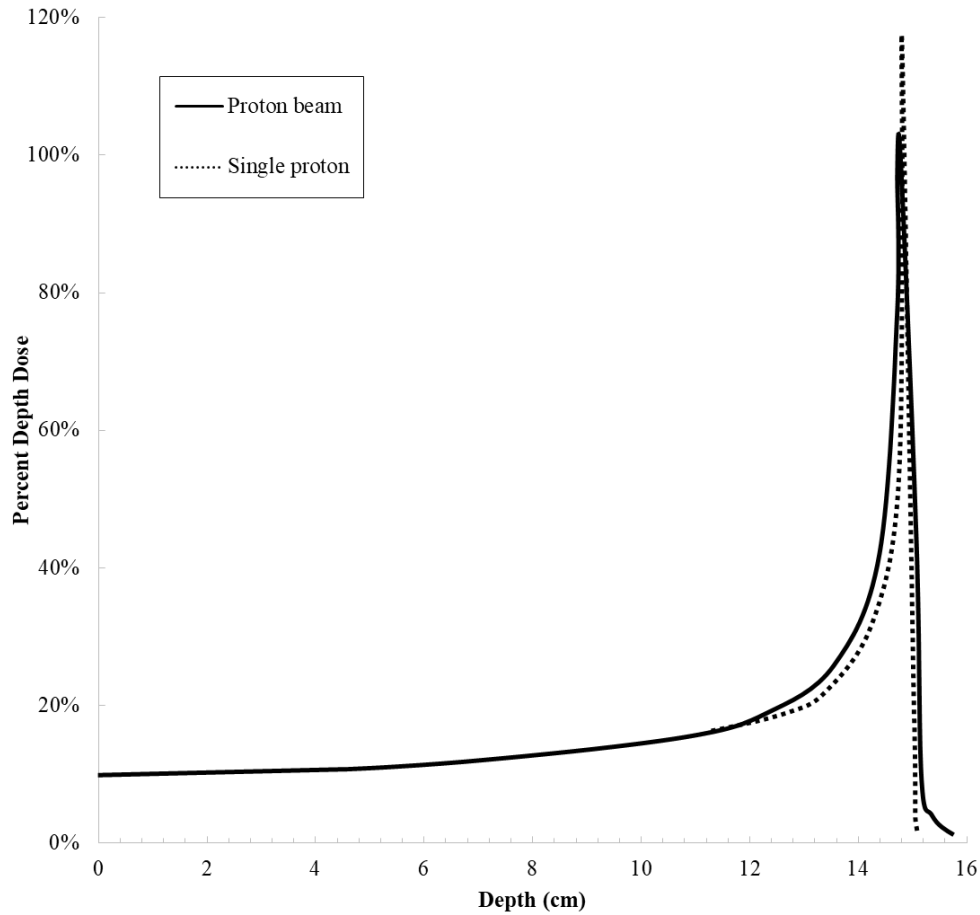


Figure 2.1: An illustration of the relative depth dose profile of 140 MeV protons. The dotted line represents the profile computed to result from a single proton and illustrates the sharp Bragg peak. The solid line represents the profile for a proton beam consisting of many particles and demonstrates the broadening of the Bragg peak as a result range straggling. (Based on data by Wilson (1946))³⁸.

A proton beam can deliver the maximum dose to a tumor located at the Bragg peak and much less to the healthy tissue in the plateau region and distal to the tumor,

leading to a highly conformal dose volume. The result is an increased TCP with a lower integral dose. By comparison, the depth dose profile of photons differs from that of protons as shown in Figure 2.2. The maximum dose from photons occurs within the first few centimeters of tissue when electron equilibrium is established. The dose to a deep-seated target is considerably less than that to the proximal attenuating tissue. Additionally, distal healthy tissue receives doses similar to that of the target. As a result, protons offer improved dose conformity for many deep-seated targets and greater healthy tissue sparing compared to traditional photon therapies⁴³. More recent advancements in photon beam technologies include IMRT, volumetric arc therapy (VMAT), stereotactic radiosurgery (SRS), and microbeam radiotherapy (MRT). These techniques utilize many beams to reduce the maximum dose to healthy tissues and provide highly conformal dose distributions which have allowed photon therapies to compete more favorably with proton therapy⁴⁴⁻⁴⁹.

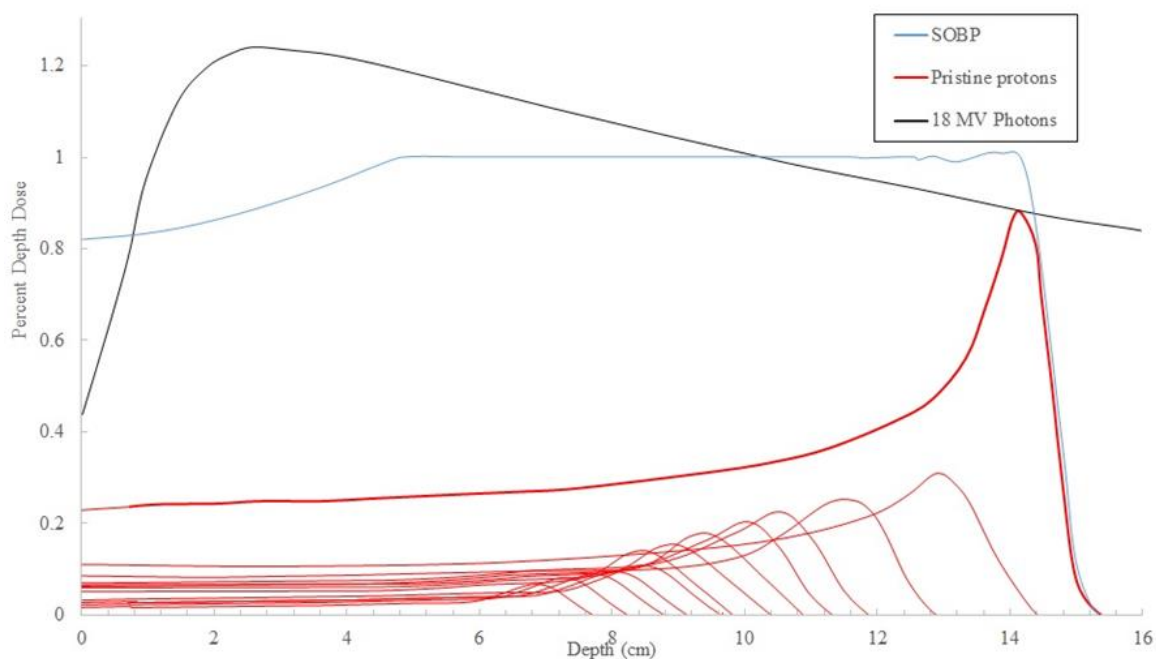


Figure 2.2: A comparison of depth dose curves in water for proton and 18MV photon (black) beams as well as an illustration of the formation of an SOBP. The pristine Bragg peaks (shown in red) are delivered with varying range and intensity which, when summed, result in the SOBP of uniform dose (shown in blue).

The financial investments of building a proton therapy center are much higher than that of any photon modality which contributes to a higher cost of proton treatment to the patient. The justification for continued research and development into protons requires evidence of their cost-effectiveness on TCP and NTCP calculations. Studies comparing proton and conventional photon therapies often have shown only small improvements in TCP and improvement in 5-year survival rates for many cancer types^{43,50–53}. In other cases, the use of protons over photons has resulted in reductions of secondary complications and improved tumor control. For lesions adjacent to critical

organs such as paraspinal or intracranial tumors, protons are often prescribed because of their advantages in reducing integral dose to the radiosensitive tissues^{45,54–59}. Proton therapy has been applied to successfully treat lung and prostate tumors^{60–62}. Perhaps the most beneficial application is in the treatment of pediatric patients. Studies showing substantial degradation in cognitive and physical development as a result of low doses to the brain and bone growth plates may result in many pediatric patients preferentially being prescribed protons^{63–66}. The immediate advantages of proton therapy for 5-year survival have been demonstrated for many tumor types, but the clinical relevance of low doses to large volumes and the generation of secondary cancers is an area of research that will continue to be investigated and may one day further validate the use of proton therapy.

2.3 Mechanics of proton interactions

Protons are subatomic particles with a charge (q^1) equal in magnitude but opposite in polarity to that of an electron. The rest mass of a proton, m_p^2 , is one atomic mass unit (1 amu) which is approximately the same as that of a neutron but 1832 times that of an electron. Along with neutrons, protons make up the nuclei of an atom and together are known as nucleons.

The interactions of protons in matter are very different from those of other particles as a result of the charged nature and mass of protons relative to both photons and electrons. Protons lose energy continuously along their path primarily through three distinct interactions (shown in Figure 2.3): collisions with atomic electrons

¹ $q = 1.6022 \times 10^{-19}$ Coulombs

² $m_p = 1.673 \times 10^{-27}$ kg or 938.27 MeV

(predominantly resulting in particle stopping), collisions with atomic nuclei (resulting in particle scatter), and nuclear reactions (in which the primary proton is absorbed). The final dose distribution is a manifestation of these three interactions.

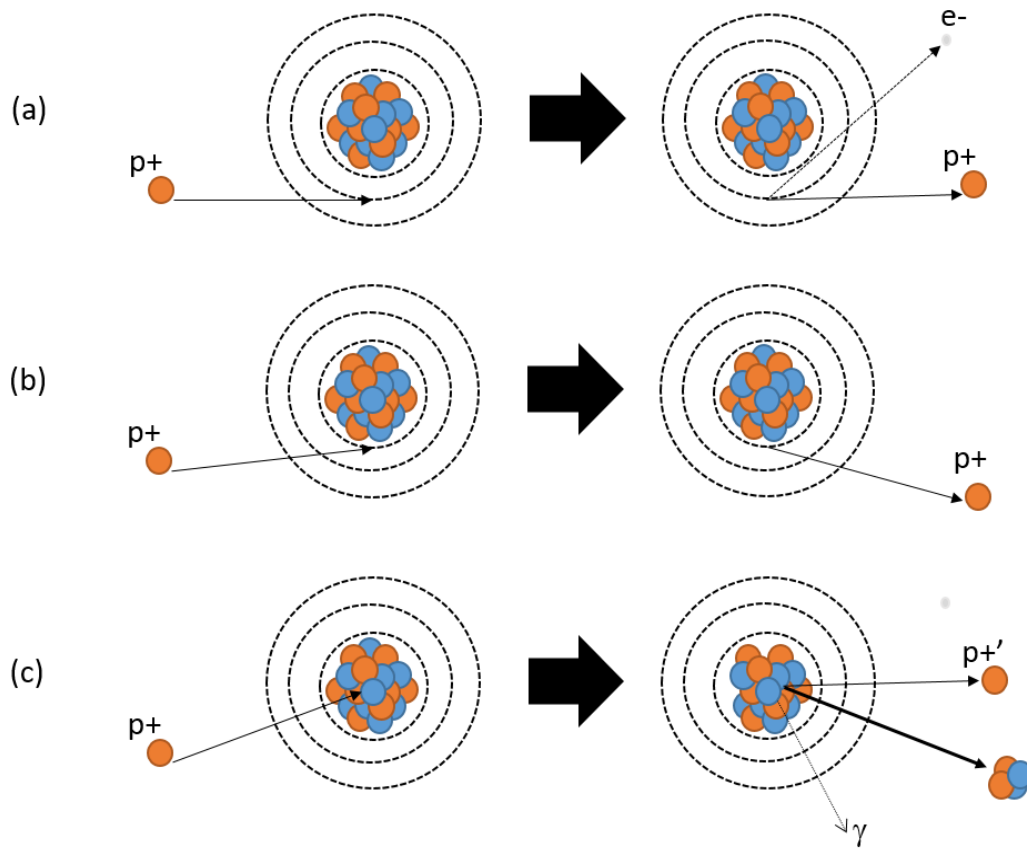


Figure 2.3: Illustration of the three primary interactions of a high energy proton. In (a), the proton (p^+) undergoes an inelastic Coulombic interaction with the atomic electron shell and electrons (e^-) are emitted. In (b), the proton is deflected by the atomic nucleus by elastic Coulombic scattering. Finally, in (c) the proton collides with the atomic nucleus leading to a nuclear interaction whereby the primary proton is absorbed and secondary particles are ejected. These secondary particles may include gammas (γ), neutrons, secondary protons ($p^{+'}$), or nuclear fragments.

2.3.1 Slowing down

Protons in the therapeutic energy range (1-350 MeV) deposit most of their energy through inelastic Coulombic interactions with atomic electrons. As a proton passes through matter, it is continuously losing energy through the ionization of nearby electrons. The more a proton is slowed, the greater the energy loss occurring in a set path length. As a result, the majority of the proton's energy is deposited near the end of the proton's range resulting in the particle's dose maximum in the distal end of the Bragg curve.

The rate of energy loss for a beam of charged particles, referred to as the linear stopping power (S), can be simply stated as such:

$$S = -\frac{dE}{dx} \left(\frac{\text{MeV}}{\text{cm}} \right) \quad \text{Eq. 2.2}$$

where dE is the mean energy lost and dx is the unit path length in a material. This energy loss is primarily a function of inelastic electron interactions (S_{el}) but also includes a contribution from elastic nuclear interactions (S_{nuc}). The final stopping power is therefore a sum of the two:

$$S = S_{\text{el}} + S_{\text{nuc}} \quad \text{Eq. 2.3}$$

An adaptation of the stopping power for conventional clinical use is the relative linear stopping power (RLSP) which relates the stopping power of a material to that of water.

To simplify calculations, stopping power generally is redefined to be independent of the mass density (ρ) of the material. This is referred to as the mass stopping power:

$$\frac{S}{\rho} = -\frac{dE}{\rho dx} \left(\text{MeV} \frac{\text{cm}^2}{\text{g}} \right) \quad \text{Eq. 2.4}$$

In order to be applied into practice, several mathematical models have been developed. One of the earliest models was developed by Bragg and Kleeman (BK model) for the calculation of alpha particles⁶⁷ which used empirical variables from experimental measurement and is still considered reasonably accurate⁶⁸. Most modern calculations are typically based on the model by Hans Bethe which include the quantum mechanical contributions of the particle interactions⁶⁹. The resulting model solves for Eq. 2.3 and is referred to as the Bethe formula:

$$\frac{S_{\text{el}}}{\rho} = 4\pi N_A r_e^2 m_e c^2 \frac{Z}{A} \frac{z^2}{\beta^2} \left(\ln \frac{2m_e c^2}{I(1 - \beta^2)} - \beta^2 \right) \quad \text{Eq. 2.5}$$

where the universal constants are: N_A is Avogadro's number, r_e is the classical electron radius ($r_e = \frac{e^2}{m_e c^2}$), m_e is the electron mass, and c is the speed of light. Parameters describing the incident particles are: z is the particle's charge and β is the relativistic

correction of velocity (v) relative to light ($\beta = v/c$). Properties of the irradiated materials are: Z is the atomic number, A is the atomic weight, and I is the mean excitation potential (roughly proportional to Z , but determined by experimental measured values and interpolation). It is important to note that Eq. 2.5 only calculates the mass stopping power from inelastic electron interactions. Energy loss from the elastic nuclear reactions described previously are omitted from the standard Bethe formula as their contribution is less than 0.1% for protons greater than 1 MeV^{70,71}.

Correction factors by Bloch, Barkas, and Fermi have also been added to the Bethe formula used in the International Commission on Radiation Units and Measurements (ICRU) Report 49⁷² to account for electron shell corrections necessary for high- Z targets and any electron density correction factor necessary for incident protons greater than 1 GeV⁷³. A comprehensive list of both electron and nuclear stopping powers of protons in various materials is included in ICRU Report 49⁷².

2.3.2 Range

The range of a single proton is difficult to calculate analytically because of the stochastic nature of its energy deposition. Variations in energy loss as a result of Coulombic interactions of the individual protons in a beam result in different terminal depths in an effect called ranging straggling (as shown previously in Figure 2.1). As a result, range is determined by the depth reached in a beam at which half of the particles have come to rest (called the projected range).

The path of the protons is generally considered to be in a straight line and deflections can in general be ignored. This is because the large mass of the protons

relative to atomic electrons results in energy being deposited continuously along their paths rather than their being deflected, except in rarer cases of atomic collisions. As a result, the range of protons (R) can simply be calculated by a one dimensional integration of the reciprocal of the linear stopping power equation, described in Eq. 2.2, with respect to the proton's initial kinetic energy (E_0):

$$R(E) = \int_0^{E_0} \frac{dx}{dE} dE \quad \text{Eq. 2.6}$$

This range model is called the continuous slowing down approximation (CSDA) and uses the assumption that proton lateral scattering is negligible. In actuality, the beam's projected range is slightly reduced as a result of the accumulation of many small deflections. The ratio of the projected range and R_{CSDA} is called the detour factor, a comprehensive database of which is available on the National Institute of Standards and Technology (NIST) PSTAR database. For clinical energies (greater than 1 MeV) and low-Z materials, this factor is greater than 0.99 (shown in Figure 2.4) therefore making the distinction minimal and the R_{CSDA} model appropriate for the studies described here.

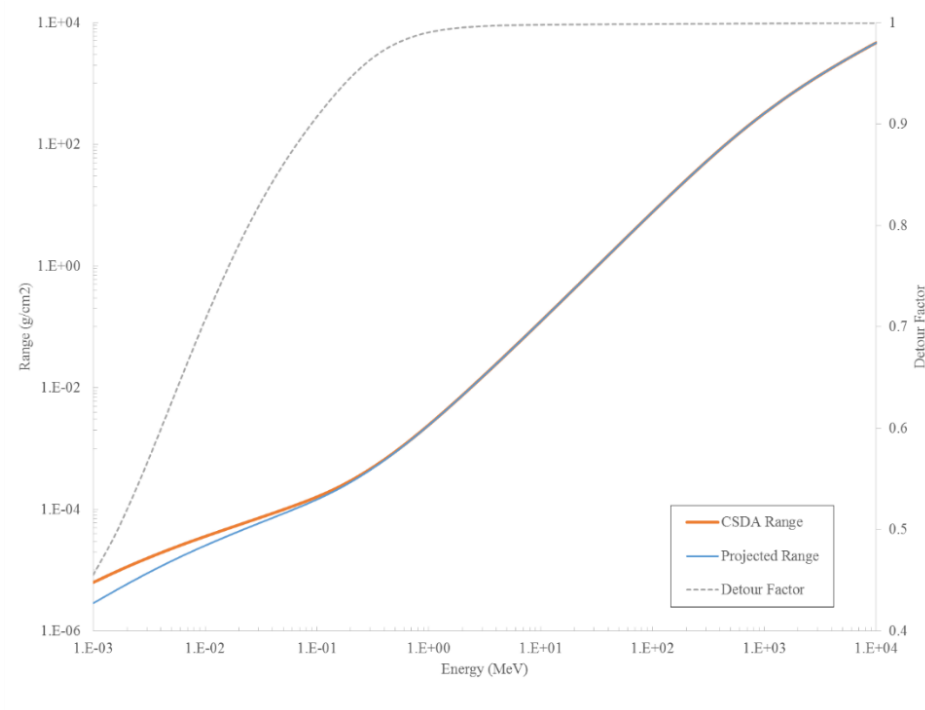


Figure 2.4: Comparison of range calculation methods (solid lines) for protons in water: the CSDA range (orange) and the projected range (blue). The detour factor (dashed grey) is the ratio of the projected range to CSDA range. The figure was generated using data available from NIST's PSTAR database⁷⁴.

2.3.3 Linear Energy Transfer

The mass stopping power represents the energy lost by the particle in a specific material and is of paramount importance for beam range characterization. For dosimetry purposes, only the energy absorbed by the local medium should be considered. Instead of using stopping power, the restricted linear electronic stopping power, or linear energy transfer (LET), is used. ICRU Report 85⁷⁵ clarifies the distinction of the two quantities as:

$$\text{LET} = \left| S_{\text{el}} - \frac{dE_{\text{ke},\Delta}}{dx} \right| \quad \text{Eq. 2.7}$$

where S_{el} is the linear electron collision stopping power and $dE_{\text{ke},\Delta}$ is the sum of kinetic energies greater than a specific energy threshold (Δ) that are carried out of the local medium through secondary charged particles. As a result, the energy absorbed locally is less than the energy lost by the proton beam. This is an especially important parameter for studies on the cellular scale. For example, in studies of relative biological effectiveness (RBE) where the range of high-energy electrons created by the incident particles is greater than the cellular scale, a restriction must be placed on secondary electron energies. When considering dosimetry on the millimeter scale though, the range of secondary electrons is sufficiently low and only the energy imparted to neutral secondary particles (neutrons and photons) can be ignored. Several studies have found the dose contribution of these secondary electrons to be negligible for clinical modeling and as a result, medical physicists generally consider LET with no such energy restrictions^{76–78}. This study intends to characterize dosimetry on the millimeter scale with no focus on radiobiological effects at this time. Therefore the unrestricted linear energy transfer, or equivalent to the magnitude of S_{el} , was used for dose calculations.

2.3.4 Scattering

In addition, protons slowing from Coulombic interactions with atomic nuclei leads to small deflections in their incident path. Individual deflections are usually insignificant, but across many interactions lateral spreading of the beam occurs. This is called multiple Coulomb scattering and the result is a nearly Gaussian distribution that

can be modeled multiple ways. Molière's theory, published shortly after Wilson's proposition³⁸, was the first to gain clinical prominence⁷⁹. Originally, this model was computationally complex leading to more generalized models adapted by Bethe⁸⁰ and Fano⁸¹. In 1975, Virgil Highland's Gaussian approximation simplified these calculations and is often used as a proxy for Molière's theory⁸². This was done by fitting a simplified Gaussian approximation to Molière's theory to solve for the angular distribution of the beam based on parameters of beam energy and scattering material:

$$\theta_0 = \frac{14.1 \text{ MeV}}{pv} \sqrt{\frac{L}{L_R} \left[1 + \frac{1}{9} \log_{10} \left(\frac{L}{L_R} \right) \right]} \text{ (rad)} \quad \text{Eq. 2.8}$$

where p is the momentum and v is the velocity of the proton, L is the thickness of the material, and L_R is the radiation length of the scattering material (the mean distance) in a material to reduce the energy of an electron by $\frac{1}{e}$. Although developed for thin material slabs, experimental measurements shows agreements within $\pm 5\%$, similar to the more rigorous calculations of Molière's theory⁸³.

2.4 Proton Facility Design

2.4.1 Facility Layout

A proton therapy facility requires a much larger building footprint than a typical x-ray therapy system as a consequence of the space needed for particle acceleration. It is best to consider a proton facility layout as two components: the particle transport system and the treatment delivery system.

The particle transport system includes the particle injector, accelerator, and beamline transport to the treatment room. Protons generated from ionization of plasmas (usually hydrogen gas) are fed into a linear accelerator (linac) which injects them into the primary accelerator. Early proton therapy centers used laboratory isochronous cyclotrons which accelerate protons on a spiraling path until they reach a threshold energy and then extract them, continuously, resulting in a uniform energy based on the strength of the magnetic field used. These cyclotrons were readily accessible at the time, but energy selection for specific treatments requires beam degraders, made of materials of varying composition and thickness, to intercept and slow the protons.

Synchrotrons were implemented in early hospital-based proton facilities. A synchrotron accelerates a proton bunch along a fixed circular ring using a magnetic field that increases in synchrony with the accelerating electric field to keep the protons along a fixed radius. The acceleration of quantized proton bunches, called spills, results in a pulsed beam with delays between pulses usually on the order of 0.5 to 5 seconds⁸⁴. Particles generated in this fashion can be extracted at any desired energy without the need of degraders which results in a beam with uniform intensity across all energies⁸⁵ as well as elimination of radioactivity produced by the degraders⁸⁶. The disadvantages of the synchrotron are primarily its larger size, cost, and complexity. The mechanisms of these accelerator systems are covered extensively in the ICRU Report 78⁸⁷. Whatever the acceleration system used, the extracted beam finally is delivered to a treatment room along a transport line which uses a series of bending magnets to focus and steer the beam to the treatment gantry. Typical proton facilities consist of multiple treatment rooms sharing a single proton accelerator.

The beamline feeds into the treatment delivery system which encompasses components of the treatment head. The simplest system uses a fixed beam to deliver a horizontal or vertical beam to the patient. This allows unaltered proton trajectories from the beamline to be used, but limits the number of treatment angles to be delivered to the patient. Patients must be moved to deliver subsequent treatment angles. As a result, fixed beams are typically used to deliver small, single-field ocular treatments or lateral field prostate treatments⁸⁸. Multiple fields are required to deliver conformal treatments. To facilitate this, the beam nozzle is affixed to a gantry system using magnetic fields to bend the beam allowing the nozzle to deliver isocentric beams from various angles. These gantries are usually very large and weighty relative to fixed beam gantries and require additional quality assurance protocols to ensure precise dose delivery, but allow for conformal dose distributions to a prone patient that would be impossible from a fixed beamline. All beam nozzles include beam monitoring ionization chambers to measure beam current, size, and uniformity.

2.4.2 Proton delivery systems

The beamline outputs a very narrow beam, usually about 1 cm in width, which must be shaped in the nozzle into a convenient delivery field. There are two types of delivery systems used clinically for beam shaping: passive scattering proton therapy (PSPT) and spot scanning proton therapy (SSPT).

In PSPT, the narrow beam is first broadened using one or more scattering foils. Single scatter systems using high-Z materials can be used for small fields, but when broadened to large fields, the wider scattering angles make creating fields with lateral dose uniformity difficult. For these larger fields, a double scattering system is used.

Here, the first scatterer broadens the beam into a fluence with a Gaussian energy distribution. The second scatterer then flattens this distribution. Typically this second scattering foil uses both high-Z, to promote scattering away from the center of the beamline, as well as low-Z materials to modulate beam range. The result is a flat field of uniform proton fluence and energy. Several double scattering system designs exist with specific advantages and disadvantages^{71,89-91}.

To properly cover large target volumes, PSPT uses range modulators to deliver a uniform dose distribution in depth. Typically, a rotating wheel with segments (or steps) of varying attenuating materials is used. This is known as a range modulator wheel (RMW) and is usually positioned prior to the beam broadening scatterers. The narrow beam is modulated discretely at each step and the result is a series of pristine Bragg peaks delivered to varying depths which sum to form the combined SOBP (shown previously in Figure 2.2). The SOBP width is created by proton beam gating at specific step positions, shown in Figure 2.5. Additionally, the RMW typically acts as part of the first scatterer in a double scattering system. Varying magnitudes of scattering occur at each step as the beam penetrates the material thickness. A single RMW will result in different scattering conditions for each beam energy. Therefore it is necessary for distinct RMWs be used in a single treatment head for each incident energy.

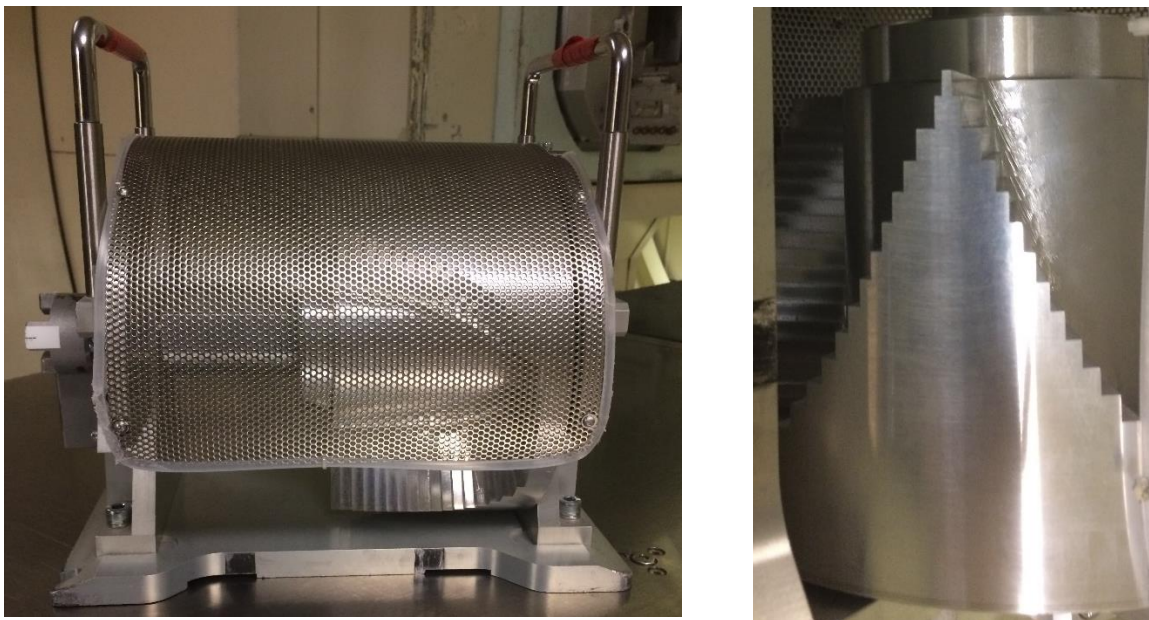


Figure 2.5: A modular range modulator wheel (left) used by the Proton Therapy Center – Houston with a close up image of the range shifting steps (right).

The final components of the PSPT nozzle are used for patient-specific target conformation. The treatment field is shaped laterally using milled apertures which are placed downstream of the secondary scatterer in the final portion of the treatment head known as the snout. Distinct apertures are necessary for each field delivered in a treatment plan and are shaped to the maximum area of the target volume as seen from the beam's reference. For higher beam energies, the apertures are sometimes stacked to ensure total out-of-field shielding, and as a result sometimes a dozen or more apertures are made for a single patient plan. Brass is commonly used as it offers ideal scattering conditions and the material is relatively easy to machine and recycle. The final nozzle

component situated downstream of the aperture is the range compensator which is made of a milled plastic. This shapes the distal part of the dose distribution and corrects for irregularities in target thickness and heterogeneities in the proximal tissue in the beam path. Similar to the RMW, the compensator consists of steps of varying attenuating thickness correlated to the necessary beam range correction in that vicinity, and similar to the aperture, a distinct compensator is used for each field. Both the aperture and range compensator (shown in Figure 2.6) are mounted on the snout and are manually exchanged by the therapist for each treatment field.

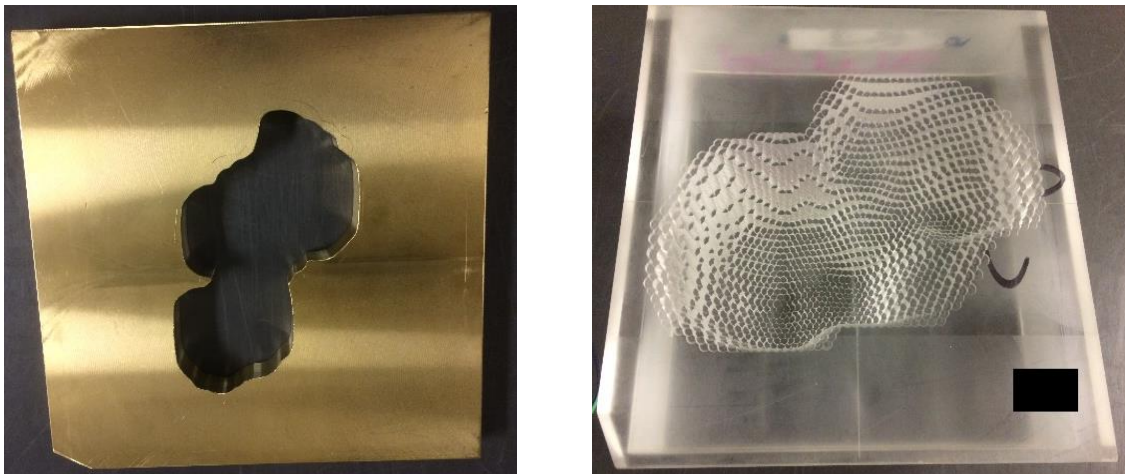


Figure 2.6: Photographs of an aperture (left) and range compensator (right) used for beam shaping at the Proton Therapy Center – Houston. Patient identifiers redacted.

In SSPT, rather than scattering and shaping the beamline as previously described, a narrow beam of protons, called a pencil beam, is magnetically steered across the target volume. The target is separated into smaller quantized target elements that can be

covered by a single pristine Bragg peak starting from the deepest volume. The beam is shifted laterally using two scanning magnets until all target elements at that range are irradiated, then the energy is reduced and the next deepest set of target volume elements is irradiated. Dose layers vary with beam energy as a result of tissue heterogeneities and proximal regions receive a cumulative dose from distal spots. As a result, varying optimization models have been developed to deliver SSPT^{92,93}. The flexibility of delivering highly conformal doses in a single field makes SSPT appealing to clinicians, although the computational and technical difficulties are much greater than those of PSPT. All irradiations performed in this study were done using PSPT and so a more thorough coverage of SSPT was left to other works^{85,92}.

2.4.3 Proton Therapy Center – Houston

So far, the discussion of proton facilities has been on a general case, but because all of the irradiations performed for this study took place at the University of Texas M. D. Anderson Proton Therapy Center in Houston (PTC-H), it is relevant to include a brief description of the facility's specifications. A more comprehensive description of the facility is available by Smith et al. (2009)⁸⁸, Arjomandy et al. (2009)⁹⁶, and Gillin et al. (2010)⁹⁴.

Opened to clinical operations in 2006, the PTC-H uses the ProBeat delivery synchrotron system designed by Hitachi, Ltd. (Tokyo, Japan) with support by Hitachi America, Ltd. (Tarrytown, NY). The proton source of the beam originates from an H^+ ion plasma injected into the synchrotron using a 7 MeV linac. The synchrotron is capable of further accelerating protons to 70-250 MeV which are extracted using an RF-driven slow extraction scheme. Proton spill lengths range between 0.5 and 5 seconds depending

on the energy selected. The technologies used in Hitachi's synchrotron are more thoroughly covered by Hiramoto et al. (2007)⁹⁷.

Table 2.1: Clinical specifications of the PSPT beam lines at the PTC-H (Smith 2009 “proton therapy”).

Available beam energies (MeV)	100	180
	120	200
	140	225
	160	250
Uncollimated field sizes (cm ²)	Large field:	25x25
	Medium field:	18x18
	Small field:	10x10
Maximum beam range (g/cm ²)	Large field:	25
	Medium field:	28.5
	Small field:	32.4
Minimum beam range (g/cm ²)	3.5	
Beam range resolution (g/cm ²)	0.1	
Maximum SOBP width (g/cm ²)	16	
SOBP increments (g/cm ²)	1	
Maximum dose rates (Gy/min at SOBP width)	Large field:	≥ 0.8
	Medium field:	≥ 1.3
	Small field:	≥ 2.5
Dose uniformity	±3%	
Dose reproducibility (day)	±0.5%	

The accelerated protons can be directed to one of the four treatment rooms (shown in Figure 2.7). Three of these rooms have isocentric gantries and the fourth supplies two horizontal fixed beams. The fixed beamlines include one large-field system, primarily used for prostate treatments, and one small-field system designed for treatment of ocular tumors. The fixed beamlines and two of the isocentric gantries use double-

scattering PSPT configured for eight treatment energies with clinical parameters show in Table 2.1. The three large-field PSPT nozzles are designed identically to allow patient plan deliveries to be duplicated in each room. As a result, the RMWs can be shared between treatment rooms. Besides the scatterers, the beam traverses several profile monitors before exiting the snout as illustrated in the nozzle schematic in Figure 2.8. Each nozzle allows for three uncollimated field sizes and accounting for the eight treatment energies, a total of twenty four RMWs and nine second scatterers are needed for comprehensive coverage of all scattering combinations.

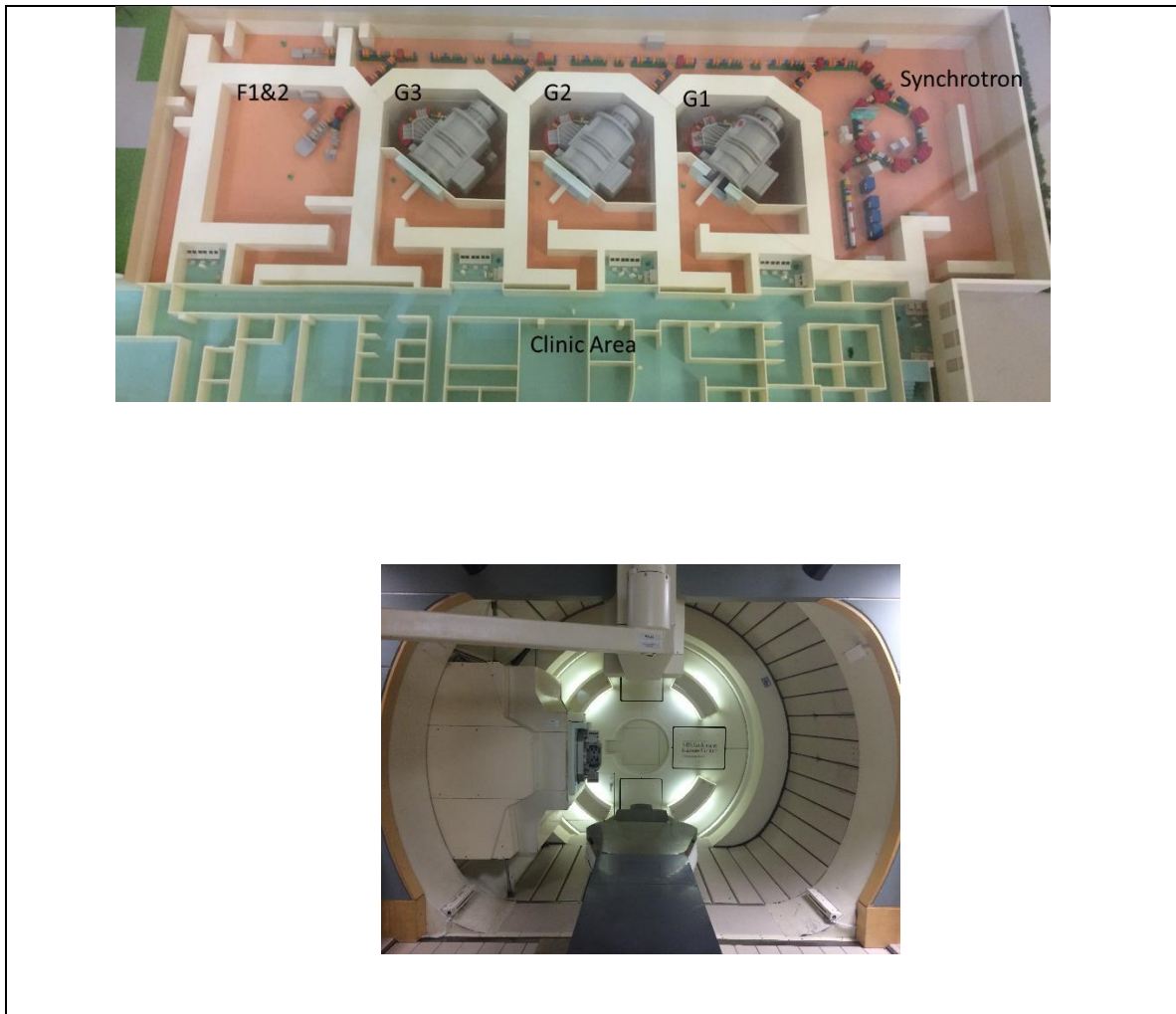


Figure 2.7: (Top) model of the PTC-H showing the center layout. Of the four treatment rooms, G1 and G2 treat with PSPT on rotating gantries, G3 treats with SSPT on a rotating gantry, and F1 and F2 treat using fixed beam PSPT. (Bottom) Photograph of G1 in the resting position.

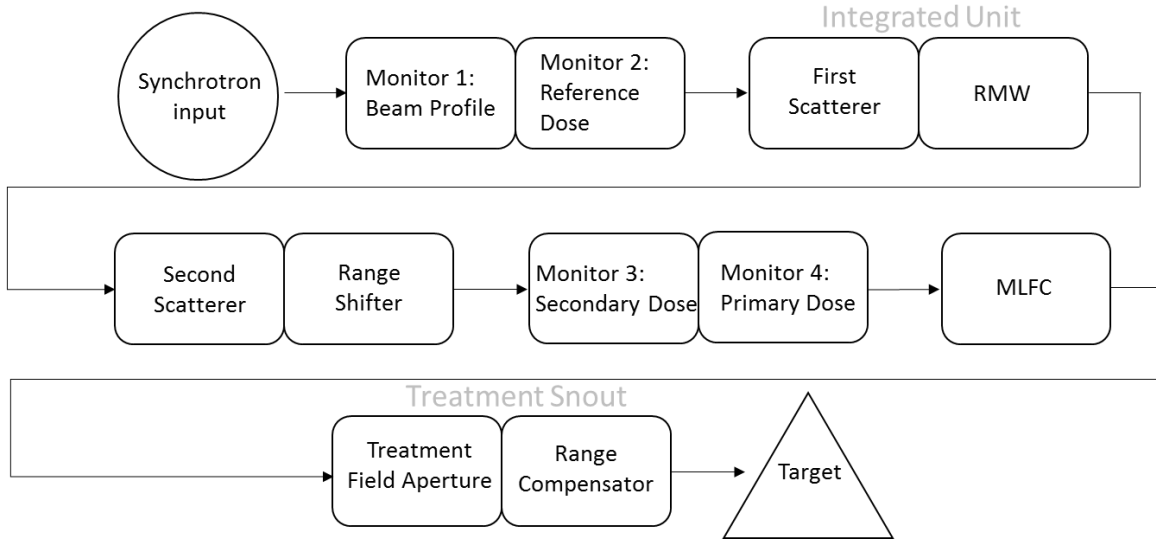


Figure 2.8: Schematic diagram of the devices intercepted by the beam line as it passes through a PSPT nozzle at the PTC-H. The beam profiler and reference dose ionization chamber measure positions of the beam center and width of the pristine beam. The first scatterer includes a scattering foil integrated with the RMW. The second scatterer flattens the beam which is then immediately attenuated through the range shifter which allows for improved range resolution. The Multilayer Faraday Cup (MLFC) measures the penetration of the beam after double scattering but only intercepts the beam during a pre-treatment beam check and is removed during treatment. Finally the beam passes into the snout which holds the aperture and range compensators used for field shaping before finally irradiating the target volume.

The remaining treatment room offers a SSPT nozzle on a rotating gantry. At the time of its commissioning, 64 distinct energies were available for treatment planning ranging from 72 to 221.8 MeV with distal ranges of 4 to 30 g/cm²⁸⁸. Configuration of

the nozzle differs from that of the PSPT systems as would be expected, but a similar arrangement of dose monitors are used along the beamline. A more thorough description of the SSPT system at the PTC-H is available from Gillin et al. (2010)⁹⁴.

2.5 Conventional dosimetry for proton therapy

Accurate and precise dosimetry systems have been a necessity in all modalities of radiation therapy. Literature investigations into clinical outcomes from poor treatment delivery have shown notable reduction in TCP as a result of even a 5% underdosage to the target volume^{98,99} and a similarly negative outcome can be expected from overdosage to surrounding normal tissue. The International Atomic Energy Agency's (IAEA) Technical Report Series no. 398 discusses dosimetry practices and standards for external beam radiotherapy and recommends keeping dosimetry uncertainty levels below 5%¹⁰⁰. In 1986, The American Association of Physicists in Medicine (AAPM) published Task Group Report 20 (TG20) discussing guidelines for dosimetry of proton and other heavy ions used therapeutically¹⁰¹. In it, dosimetry challenges for protons that go beyond those of photon and electron dosimetry include challenges from regions of high LET, chamber-dependence on stopping powers, energy depositions from nuclear reactions, and steep lateral and distal dose gradients. The report recommended dosimeter calibration in terms of exposure to air which was later changed to dose in water in ICRU Report 49 to better conform to practices for photon and electron dosimetry⁷². ICRU Report 59¹⁰² developed a dosimeter and calibration protocol, discussed later, using an air kerma calibration for ionization chambers which was later improved upon by TRS 398¹⁰⁰. In 2007, ICRU Report 78 incorporated the IAEA's changes to the dosimetry protocol and included

improved stopping power ratios for modern commercial dosimetry systems to account for contributions from secondary electrons and nonelastic nuclear collisions⁸⁷.

Many different types of dosimeters have been found to be appropriate for different procedures. Zero dimensional dosimeters are used to measure absorbed dose at a specific point in a volume where accuracy is not dependent upon spatial resolution^{87,102}. These are useful for beam output verification and absolute dosimetry and commonly include calorimeters, ionization chambers, and thermoluminescent detectors (TLDs). Calorimeters, which estimate the energy absorbed by a sensitive volume through a measurement of the increase in temperature, have provided a direct method to measure dose without being influenced by ionization mechanisms. TG20 discussed protocols for calibration techniques and recommended their use for absolute dosimetry¹⁰¹. Calorimeters have been used in electron and photon external beam dosimetry successfully¹⁰⁰, but are generally unwieldy and not commercially available. As a result, ICRU Report 59 made recommendations to use cylindrical ionization chambers, calibrated using Cobalt-60 and preferentially checked using a calorimeter, for absolute dose measurements¹⁰². The quality conversion factors which convert the calibrated chamber's reading to that for a proton beam of known quality have been provided in ICRU Reports 59 and 78^{87,102}. These have become the standard for point dosimetry for proton therapy in the clinical setting. For commissioning and routine QA, parallel plate detectors, such as a multilayer ionization chamber (MLIC), are frequently used to quickly measure depth-doses. Studies have shown reduced accuracy with MLICs in small fields¹⁰³. With TLDs, ionizing radiation excites electrons which are trapped in a crystal lattice and later released by heating resulting in the release of photons proportional to the

absorbed dose. These require a long stabilization time, but are reasonably robust and as a result are useful for remote dosimetry applications¹⁰⁴.

In a clinical setting, it is also convenient to measure 2D planar dose distributions to validate radiation beam qualities, such as field flatness and symmetry, as well as patient treatment plans. Film and detector arrays are the most common 2D dosimetry systems. Radiographic and radiochromic film dosimetry has been widely implemented for its high spatial resolution, dose dynamic range, and durability allowing it to be used in water tank and plastic water phantoms¹⁰⁵. Additionally, like TLDs, it is commonly used for remote dosimetry auditing¹⁰⁶. Investigations into many different films have found they have an LET dependence, especially manifested in the high-LET Bragg peak region, resulting in a substantial under-response reported as high as 20%^{107–113}.

Detector arrays provide accurate and fast planar dose distributions for routine QA and are usually constructed using ionization chambers or diode detectors. Commercial ionization chamber arrays, such as the MatriXX (IBA Dosimetry, Schwarzenbruck, Germany) have been investigated at proton facilities^{114,115} and found to be well suited for large field treatment plan verifications as well as beam flatness and symmetry, but suffered from 7% or higher discrepancies compared to film in the lateral penumbra and large dose gradients. This is a result of the large separation distance between individual chambers of the array (7.62 mm) leading to volume averaging artifacts and ultimately poor spatial resolution. Silicon diode arrays, on the other hand, use detectors having smaller active regions which results in the potential for better spatial resolution^{116–122}. Additionally, these detectors have demonstrated very little LET dependence making them ideal for end of range measurements¹¹⁷. However, the electronic components in the

irradiated volume have been shown to be especially sensitive to accumulated dose making them unreliable for absolute dosimetry¹²⁰.

2.6 Quality Assurance for passive scattering proton therapy

2.6.1 Uncertainty in the delivered dose

In all modalities of radiotherapy, there are uncertainties in the delivery of a precise dose distribution. These uncertainties manifest in terms of tumor control and preventable normal tissue damage and therefore are a leading concern for both medical physicists and physicians. The variable nature of radiation interaction mechanics makes some level of uncertainty inevitable, but understanding the sources of uncertainty allows one to reduce them where possible and account for their implications where impossible.

Proton therapy is particularly susceptible to uncertainties as a result of their finite range and high dose conformity^{123,124}. Variables contributing to uncertainty in beam range include not only characteristics of the beam output from the gantry but random and systemic uncertainties in patient setup and anatomy. Protons penetrating patient tissues lose energy and scatter by the mechanisms previously described by Eq. 2.5 and Eq. 2.8, respectively. Any inherent uncertainties in the beam characteristics or the material's linear stopping powers therefore contribute to uncertainty in the range which ultimately affects the accuracy of the delivered dose distribution.

In a clinical setting, patient treatment planning is performed on 3D computed tomography (CT) images taken prior to treatment. The CT numbers are derived from the Hounsfield scale which is a quantitative linear transformation of the measured linear attenuation coefficients to a dimensionless scale based on the definitions of air and water.

The CT number is then translated into the RLSP in a relationship known as CT-RLSP. Uncertainties in the RLSP result from tissue heterogeneities, imaging artifacts, and CT number conversion discrepancies and can vary by as much as 150⁷². Studies have shown range uncertainties from inaccurate conversions ranging from 5.0% to higher values in treated patients^{99,125} and higher values still in tissue-like materials used in anthropomorphic phantoms¹²⁶. Other sources of range uncertainty include patient alignment and setup errors, interfractional patient motion, intrafractional organ motion, changes to the patient's physiology including weight loss and shape of the target¹²⁷. As a result, the ICRU suggests methods to account for many systemic uncertainties such as target smearing^{71,87,128,129}.

2.6.2 Commissioning and routine quality assurance protocols

Recommendations for routine and commissioning QA procedures in conventional photon radiotherapies have been extensively modernized. The AAPM established protocols in TG Reports 40⁹⁶, 45¹³⁰, 142¹, 154², and 179¹³¹ which describe specific processes of QA tests and recommended tolerance values. As of yet, no similar guidelines for proton therapy have been published by the AAPM. This is subject to change soon as TG224, titled “Proton Machine QA,” is currently in development and may be released within the next year or two. Early clinical proton facilities were required to develop their own protocols^{89,132,133}. Specific recommendations on radiation and mechanical uncertainties laid out by TG40 and ICRU Report 50¹³⁴ can be used as a guideline, but the large number of distinct proton energies available as well as parameters unique to proton therapy (such as the Bragg peak) add additional challenges. The routine QA procedures developed at the Loma Linda Medical Center were included as an

example in the appendix of ICRU Report 59 published in 1998¹⁰². In 2007, the ICRU published Report 78 which included a chapter more comprehensively discussing the various components that must be monitored as well as listing some example periodic checks for both PSPT and SSPT systems⁸⁷. The first publication comprehensively reviewing a facility's QA procedures was released shortly after by Arjomandy et al. (2009)⁹⁶. Ultimately, these still only act as guidelines for institutions to adapt and develop their own protocols.

Commissioning protocols must ensure the proton therapy system meets safety and reliability thresholds in an end-to-end demonstration. Routine QA protocols verify the proton facility continues to meet those thresholds. These include mechanical and safety checks such as gantry collisions and radiation leakage¹³⁵. Additionally, characterization of the components of the TPS must be verified including CT-RLSP conversions, monitor unit (MU) calculation algorithms, and beam shaping accessories in the snout^{136,137}. The PTC-H published a thorough description of the commissioning process on their SSPT system⁹⁴ as well as their routine QA procedures⁹⁶ which can serve as a good detailed analysis of an individual institution.

2.6.3 Gamma Analysis

It is difficult to directly compare the accuracy of treatment delivery of multiple treatment plans. To quantitatively evaluate two dose distributions, typically one being measured and the other a TPS calculation, the dose matrices are first superimposed. From this, a dose-difference (DD) map can be generated as the point-by-point subtraction of one distribution from the other. This method has been shown to be susceptible to discrepancies within high dose gradient regions in which two fields may only be in error

spatially by a few millimeters but shown as large dose differences. An alternative approach is therefore to measure the distance-to-agreement (DTA) between pixels of both distributions that have the same dose. This measure can hide large errors in dose differences and instead inflate the dose value in regions of low dose conformation where points of matching dose might be very far apart¹³⁸. The concept of using both of these methods in a single analysis was first developed by Harms et al. (1998) who developed a pass-fail criterion for each point in the distribution¹³⁹. For this procedure, acceptance criteria are set for the tolerance to DD (%) and DTA (mm) then each point is evaluated using both criteria. This method results in a binary solution (pass or fail) at each point. Low et al. (1998) updated this with a numerical quality index to show the magnitude of minimum detected error to match those acceptance criteria¹⁴⁰. This results in the computation of the dimensionless gamma value (γ):

$$\gamma = \min \sqrt{\frac{|r_c - r_m|^2}{\Delta d_m} + \frac{(D_c(r_c) - D_m(r_m))^2}{\Delta D_m}} \quad \text{Eq. 2.9}$$

where $|r_c - r_m|$ is the DTA measurement and Δd_m is the DTA criterion. The DD measurement is defined by $(D_c(r_c) - D_m(r_m))$ and the matching criterion by ΔD_m .

The gamma value is usually calculated in 2D as conventional dosimeters measuring dose distributions are planar, but many studies have incorporated volumetric dosimeters and investigated the potential value of 3D gamma calculations^{10,141–144}.

2.6.4 Remote auditing QA

Finally, it is worth noting the dosimetry protocols of the Imaging and Radiation Oncology Core in Houston (IROC-H³). The mission of this institution is to develop quality assurance protocols for comparability and consistency between radiotherapy institutions, including end-to-end credentialing and QA audits, with the purpose of ensuring consistency among clinics participating in the National Cancer Institute's (NCI's) clinical trials. This organization has previously provided QA comparisons between institutions for other radiotherapy modalities which has helped to demonstrate statistical shortcomings and benefits from specific dosimetry protocols^{3,145,146}. In 2007, IROC-H implemented guidelines specifically for credentialing proton centers. These were updated in 2010 and then again in 2012 to monitor proton beam calibrations as a result of a number of proton institutions joining phase II clinical trials^{147–149}. Credentialing protocols include end-to-end evaluations for multiple anatomical disease sites using film and TLD dosimetry systems in anthropomorphic phantoms. These phantoms are made of materials simulating the CT-RLSP relationships of their corresponding anatomical tissues (adipose tissue, bone, lung, etc.) and measure how accurately a facility plans and delivers a treatment on a phantom mimicking human anatomy^{150,151}. Additionally, they have established an on-site protocol consisting of dose output measurements using ionization chambers and treatment verification using film and TLDs specifically for proton facilities delivering both PSPT and SSPT^{4,152}. The results of these investigations have demonstrated some specific failures in facility beam quality calculations and treatment^{6,150}. These highlight potential deficiencies in conventional QA systems currently being used in proton therapy institutions.

³ Formerly the Radiological Physics Center (or RPC)

2.7 Three-dimensional dosimetry

3D dosimetry systems are capable of measuring a comprehensive dose distribution within a volume. These can be broadly classified into categories of chemical dosimeters or detector arrays. The applications of 2D arrays for planar dosimetry have previously been discussed, but researchers have attempted measuring 3D dose distributions using arrays either layered or placed orthogonally^{153–155}. These array configurations attempt to reconstruct the full 3D dose distribution using software algorithms, but typically suffer from low resolution and perturbation factors resulting in these arrangements commonly being referred to as “quasi 3D dosimetry systems” and are not used for routine clinical QA.

Chemical dosimeters are typically homogenous devices that undergo some change to their physical properties as a result of ionizing radiation and are readout using one of several types of imaging systems. Many chemical dosimeters are nearly tissue equivalent and can be conformed to fit a specific volume. The three most common 3D chemical dosimetry systems include gels, volumetric scintillators, and radiochromic plastics.

2.7.1 Gel dosimeters

Gel-based dosimeters were among the earliest proposed 3D dosimeters^{156–158}, and have since been the most thoroughly studied of the 3D systems. Many different gel dosimeters have been developed. Polymer gels are perhaps the most prevalent variety, although several dosimeter types have been developed. The gelling agent itself does not provide a substantial signal from ionizing radiation, but instead acts as the 3D matrix holding radiosensitive structures and their dose-activated byproducts spatially fixed. These are typically aqueous solutions composed predominately of water, amino acids,

and proteins making them nearly radiologically tissue equivalent¹⁵⁹. Besides polymer gels, other common gel dosimeters include ferrous sulfate gels and radiochromic gels.

2.7.1.1 Polymer gels

Polymer gels were first proposed in 1954¹⁵⁷ and over the last few decades have seen numerous variations in chemical composition¹⁶⁰. The work of Gore et al. (1984), demonstrated their applications as a tool for modern radiation dosimetry and initiated a plethora of subsequent research leading up to this day¹⁶¹. Fundamentally all polymer gel formulations follow the same general radiation detection mechanisms. The dosimeters consist of monomers dissolved into an aqueous gelling solution. Ionizing radiation causes radiolysis in the dosimeter, resulting in the release of free radicals from the water molecules of the gel which convert those monomers into polymers. Clusters of these form large polymer chains which cause the dosimeters to become visibly opaque¹⁶². The magnitude of polymerization is a function of absorbed dose. Additionally, these polymer chains bond to the gel matrix minimizing the diffusion which allows ample time for dose readout¹⁶³.

Polymer gels vary primarily in composition and manufacturing processes. The most common monomers used include acrylamide, N,N'-methylenebis, acrylic acid, and methacrylic acid. Many publications discuss the differences these compositions have on the gel's radiological properties^{7,160,164–167}. Other recent developments have incorporated comonomers to further influence polymerization chains and reaction rates^{166,168,169}.

Polymer gels suffer from several complications in their manufacture and dosimetry applications. The primary obstacle in the manufacture of conventional

formulations is a sensitization to oxygen which binds to radicalized monomers and acts to prematurely terminate polymerization chains¹⁶⁰. Conventional manufacturing required mixing in an oxygen-free environment such as a nitrogen filled glove box to reduce atmospheric oxygen exposure and are generally referred to as hypoxic or anoxic polymer gel dosimeters^{166,170}. This cumbersome process led to new formulations that included oxygen scavengers that bound to oxygen molecules and allowed dosimeters to be manufactured openly on the bench-top. These are generally referred to as normoxic polymer gels and the first such formulation used ascorbic acid and copper sulfate in what are known as MAGIC gels⁷. Many alternative normoxic formulations have since been developed and although oxygen desensitization has been reduced it is not fully eliminated¹⁷¹. Additional obstacles of polymer gels include the use of external containers which act to reduce oxygen contamination after manufacturing and maintain the spatial stability. These containers reduce dosimeter homogeneity and introduce dose readout artifacts that must be accounted for. Also many components of polymer gels are considered toxic and require considerable safety protocols during manufacturing. Methacrylic-based polymer gels have also demonstrated dose rate dependence altering dose signal by as much as 24%¹⁷². Finally, temperature and pressure during manufacture and storage have also been shown to affect dose response and dosimeter reproducibility^{173,174}. Commercially available polymer gels have been made available such as the BANG® series¹⁷⁵ by MGS Research Inc. (Madison, Connecticut, USA) which has further stimulated interest in clinical applications.

There are several imaging modalities used to measure dose information from irradiated polymer gels. The most common include magnetic resonance imaging (MRI),

optical-CT, and x-ray CT. The response of polymerization chains created from ionizing radiation has been shown to be minimally sensitive to spin-lattice relaxation rate (R_1) MR scans¹⁷⁶, but susceptible to spin-spin relaxation rate (R_2) scans^{161,177}. Extensive investigations into methacrylic-based polymer gels have shown MRI dose mapping offers high sensitivity and little dependence on gel shape¹⁷⁸, but additional studies have shown they are highly susceptible to inhomogeneities and changes in imaging parameters as well as MRI being inaccessible to many laboratory settings¹⁷⁹. Optical-CT scans take advantage of the change in optical properties of the irradiated gels which become visibly opaque as a result of the polymer chains formed. Light scattering allows dose mapping through the measured changes in optical contrast between pre- and post- irradiation¹⁶². This offers a low cost alternative to MRI scanning, although it is susceptible to light-scattering artifacts especially at the transition between the gel and its container¹⁸⁰. X-ray CT is similar to optical-CT but measures the change in the linear attenuation coefficient as a result of the increased mass density from the polymerization chains¹⁸¹. X-ray CT is often more readily accessible but offers lower sensitivity than the previous readout methods and as a result has a lower signal-to-noise ratio (SNR)¹⁸². Additionally, exposure from ionizing x-rays will cause further polymerization in the dosimeter contributing to reduced dosimetric accuracy.

2.7.1.2 Ferrous Sulfate gels

The use of ferrous sulfate solutions as a means to measure dose was first proposed in 1927 by Hugo Fricke and dosimeters made from this solution therefore usually are referred to as Fricke gels¹⁵⁶. The underlying dosimetric basis of these gels differs from that of polymer gels in that the radiosensitive component is composed of ferrous ions

(Fe²⁺) dissolved by an acidic oxygenated solution into a gel matrix. Radiolysis of the water molecules from ionizing radiation creates hydroperoxy radicals that oxidize the ferrous ions into ferric ions (Fe³⁺)⁹. The concentration of these ferric ions is proportional to the absorbed dose. Fricke gels are constituted of generally non-toxic components and can be manufactured in normoxic conditions offering substantially simpler facility requirements.

The primary disadvantage of Fricke gels is the rapid diffusion of the ferric ions shortly after irradiation^{183–185}. Unlike polymer gels in which the polymerization chains bind to water molecules giving improved spatial integrity, the ferric ions are free in the gel matrix which results in blurring over time of the measured dose distribution and reducing accuracy of spatial dose information. The diffusion time varies with different gelling agents¹⁸⁶, but begins immediately after irradiation and can become severe within minutes^{187–189}. It is additionally dependent on temperature as well, making accurate reproducibility difficult⁹. This makes dosimetry of high dose gradients especially difficult, although chelators¹⁹⁰ as well as diffusion models have been incorporated to correct for this to some effect^{186,191}. Additionally, similar to polymer gels, Fricke gels require an external container to maintain spatial stability of the gel matrix.

Dose measurement in Fricke gel dosimeters is determined by the relative concentration of ferric ions. In 1984, Gore et al. proposed that MRI readout of the dose distribution was possible¹⁶¹. Unlike polymer gels which are primarily sensitive to R₂ protocols, Fricke gels show little sensitivity to R₂ and are typically measured using R₁ protocols which are sensitive to the paramagnetic characteristics of the ferric ions adjacent to water protons^{57,161,183,187,192,193}. Spectrophotometry can be used to measure

ferric ion density in small volumes. These have a photoabsorption peak at 224 nm which is heavily attenuated by the volume making 3D dosimetry in larger volumes difficult¹⁹⁴. Conventional Fricke gels offer no dose signal readout from x-ray CT readout systems.

2.7.1.3 Radiochromic gels

Radiochromic materials are those that undergo a change in color when exposed to ionizing radiation. Radiochromic films, discussed previously, are one such example, but more recently gels doped with various radiochromic materials have been developed. These gels are readout using specialized optical-CT systems (discussed in more detail later) that offer reduced stray-light artifacts compared to conventional optical-CT systems and potentially higher resolution, scan time, and cheaper equipment compared to MRI readout¹⁹⁵.

Various radiochromic gel systems have been developed, although the most commonly seen is an adaptation of Fricke gels called Fricke-benzoic-xlenol (FBX) gels. These FBX gels are made similar to Fricke gels but with the addition of the metal ion indicator xlenol orange which binds to the ferric ions resulting from ionization to produce a visible color change proportional to absorbed dose^{196–199}. In addition to offering an alternative readout method, FBX gels have demonstrated better sensitivity to low doses compared to conventional Fricke gels^{176,196,200}. These gels suffer from similar disadvantages to conventional Fricke gels including signal diffusion and temperature dependence⁹.

Radiochromic micelle gels are a more recent development in the field of gel dosimetry^{201–204}. These use a leuco dye dose reporter that changes color when exposed to

free radicals and is proportional to absorbed dose. These leuco dyes are insoluble in an aqueous gel and as a result surfactant molecules, called micelles, such as sodium dodecyl sulfate are incorporated to better homogenize the solution²⁰⁴. These micelles act by surrounding the leuco dye in a hydrogel matrix that insulates them from surrounding water molecules and allows them to readily disperse in the volume. To activate the dyes, free radicals are generated by radiolysis of the water molecules similarly to Fricke gels and polymer gels, but some researchers have included halogenated hydrocarbons such as chloroform (CHCl_3) to improve dose sensitivity. Compared to FBX gels, these gels report signal diffusion as low as one-twenty-fifth, allowing much greater signal stability in high dose gradient regions, but their biggest disadvantage is dose sensitivities much lower than that observed in conventional FBX gels²⁰⁵.

2.7.2 Volumetric Scintillators

Shortly after the discovery of x-rays by Wilhelm Röntgen, Sir William Crookes proposed the scintillator for dosimetry in 1903 which has since been further developed for many applications including general radiation detection and to a lesser extent for radiation dosimetry. Three dimensional scintillation, sometimes called volumetric scintillation, was proposed about a century later by Kirov et al. (2005) for dosimetry of brachytherapy for eye plaque applicators²⁰⁶. Over the last decade, further work has developed new applications for photons^{207–209} and protons^{210–212}. The scintillating materials can be divided into two categories: solid plastic scintillators and liquid scintillators (LS).

The basic mechanics of scintillation for plastics and LS are fundamentally similar. Ionizing radiation excites aromatic molecules in the scintillating materials which emit

fluorescent photons as they decay back to a stable state. The fluence of these photons is proportional to absorbed dose in the material for therapeutic photon beam energies²¹³. These photons are transmitted from the scintillating material and collected by a photodetector, or photodetectors in the case of volumetric dosimetry.

Volumetric scintillators have been shown to exhibit high spatial resolution and dose accuracy when properly configured^{207,214}. For accurate dosimetry, a number of material and incident beam corrections must be accounted for such as the self-attenuation of the fluorescent photons as well as Cerenkov light created in the material. Improper setup can also lead to spatial dose artifacts²¹³. There is currently very little commercial availability of volumetric scintillating systems making clinical dosimetry reliant on research devices²⁰⁸.

2.7.3 Radiochromic plastics

Radiochromic plastics incorporate dose responders similar to those described for radiochromic gels but replace the 3D gel matrix with a solid plastic resin. These resins are formed from precursors into rigid structures capable of being formed into any shape without the need of an external container. Additionally, signal diffusion is limited relative to gel dosimeters. The most prevalent radiochromic plastic is a polyurethane-based dosimeter commercially known as PRESAGE® and available through Heuris Inc. (Skillman, NJ, USA) which is discussed in greater detail in the next section²¹⁵. Another recent development is silicone-based radiochromic dosimeters whose elasticity can be controlled through formulation to produce a rigid-like-plastic or a deformable-like-gel matrix^{216–218}. One such dosimeter is known as Flexydos3D²¹⁹ which has been recently investigated for its improved tissue equivalence and ease of manufacturing relative to

PRESAGE®. The fundamental dose signaling mechanics of these dosimeters mirror those of PRESAGE®.

2.8 PRESAGE® dosimeters

First proposed in 2003, PRESAGE® is a volumetric radiochromic plastic dosimeter which has received thorough study over the last decade^{215,220}. When exposed to ionizing radiation, the dosimeter undergoes a change in optical density (OD) which can be readout by optical-CT. Changes in composition have been shown to alter the radiological and physical properties of the dosimeters allowing them to be tailored for specific applications^{221–225}. The 3D dosimeters used in this study were entirely comprised of various formulations of PRESAGE®.

2.8.1 Manufacture of PRESAGE® dosimeters

The precise formulation of commercialized PRESAGE® is proprietary and undisclosed. Regardless, the primary components have been described by Adamovics and Maryanski (2004) to consist of a transparent polyurethane matrix doped with a leuco dye dose reporter and a radical initiator²²⁶. Further studies have investigated the inclusion of additional components such as curing agents, ambient light desensitizers, and deoxygenating agents^{221,227}. The manufacturing process includes thoroughly homogenizing the solution and properly curing the compound resin into the desired shape under pressurized conditions.

2.8.2 Advantages and disadvantages of PRESAGE® dosimeters

Shortly after its introduction, the potential benefits of PRESAGE® were recognized^{228–230}. It was easy to handle and demonstrated a linear dose response over a

large dynamic range with very little dose rate dependence²³¹. Perhaps the primary advantage PRESAGE® dosimeters offer over most other conventional 3D dosimeters is the lack of an external container and the ability to be fabricated in any desired shape. These allow the dosimeter to be easily incorporated into any existing phantom or QA protocol. Additionally, the lack of container allows PRESAGE® to be used for low penetrating electron and brachytherapy dosimetries^{232–234}. This is especially vital for measurements of the electron return effect (ERE) currently being characterized in novel MR-image guided radiation therapies (MR-IGRTs)^{235,236}.

PRESAGE® has been shown as a stable dosimeter over long periods of time when properly stored making it ideal for remote dosimetry^{12,236,237}. The signal diffusion observed in gel dosimetry is minimized in the polyurethane matrix²³⁸.

A number of potential limitations to PRESAGE® have also been observed. Like many gel dosimeters, PRESAGE® is sensitive to UV exposure which activates the LMG dose responder²²¹. In addition, the dosimeters show a temperature and age sensitivity. Reduced dose signal was observed for dosimeters stored for prolonged periods of time and in extreme heat ($>60^{\circ}\text{C}$)²³⁹. Finally, unlike Fricke and polymer gels, the activated leuco dye does not result in a change in x-ray attenuation or in a transition of proton states and therefore cannot be readout by x-ray CT or MRI system.

2.8.3 Clinical applications of PRESAGE® dosimeters

Although available commercially, PRESAGE® (like other volumetric dosimeters) is being used for routine QA in only a very few clinics, and as such published clinical applications are preliminary works or verified alongside credentialed systems. Shortly

after being introduced researchers looked into its feasibility for routine radiotherapy procedures^{228–230}. Many early applications investigated PRESAGE® as an IMRT and VMAT verification system showing 3D gamma passing rates greater than 90% under strict 3%/3mm criteria^{11,141,240,241}. Similarly high passing rates were found in applications for SRS^{242,243,242,244} and IMRT^{245–247}. Surface and radial dose measurements of clinical brachytherapy systems have also been studied using dosimeters precisely molded to hold applicators^{232,248–250}.

One specifically attractive feature of PRESAGE® is its application for IROC-H auditing investigations. The reproducibility and dose accuracy of these dosimeters was investigated for remote dosimetry in which the dosimeters must be transported to a remote facility, stored for prolonged periods before irradiation, and then returned to the auditing institution for readout. A feasibility study by Juang et al. (2014) demonstrated that this was possible¹². Additionally, studies have demonstrated the success of replacing 0D and 2D systems in anthropomorphic QA phantoms used for end-to-end facility credentialing^{10,143,242,251,252}. Another novel field of PRESAGE® is that of constructing anthropomorphic shapes with heterogeneous structures within to mimic anatomical objects such as bony anatomy adjacent to soft tissue using combinations of multiple formulations²⁵³.

2.9 Signal quenching in a proton beam

Highly conformal dose distributions using proton therapy are commonly delivered adjacent to radiosensitive, normal tissues as described previously. In addition, recent investigations show that the dose deposition towards the distal end of the proton beam range may have a greater RBE weighting than previously believed²⁵⁴. As a result,

accurate dosimetry in this region of the beam profile is highly desirable. Unfortunately, chemical dosimeters have all shown a non-linear dose response in this region which has been attributed to the high LET in the Bragg peak²⁵⁵. Typically this phenomenon is manifested as an under-response of the dose signal and is often referred to as signal quenching, or just quenching, in the literature.

The quenching effect has been linked to high LET, but the mechanisms influencing the dose responders in the dosimeters are hotly debated. Following the basis of proton dosimetry using the track structure theory, in which a proton's energy deposition is localized around each particle's track through energy transfer to secondary electrons, high ionization density in the immediate vicinity of individual protons leads to saturation of the dose reporting components of the dosimeter. This was the conclusion by Jirasek and Duzenli (2002) for polymer gel investigations²⁵⁶. Alternatively, Gustavsson et al. (2004) proposed that the free radicals produced in this high ionization density will have a greater propensity of recombination, termed radical recombination, and as a result produce fewer activations of the dose responders²⁵⁷.

This quenching effect has been observed in nearly all chemical dosimeters to varying magnitudes. Radiographic and radiochromic films have both demonstrated this effect and require correction factors be applied for accurate dosimetry^{111,112,258}. Fricke gels²⁵⁹, polymer gels^{257,260,261}, and radiochromic micelle gels²⁶² demonstrated quenching sensitivity to different magnitudes. Similarly with LS^{263,264} and radiochromic silicone dosimeters²¹⁶, early formulations of PRESAGE® were found to under-respond by up to 20%^{265,266}. Shortly after, Heuris Inc. released a formulation intended for protons which investigations showed quenching was reduced to 12%^{267,268}.

Two correction methods have been proposed to correct for quenching in these dosimeters. The first is through chemical alteration, as shown with the altered formulation of PRESAGE®. This approach seeks to reduce the saturation point by elevating the concentration of dose responding agents^{216,267}. The alternative method is developing quenching models incorporating beam quality factors, such as LET, using Monte Carlo or analytical calculations to apply a correction to the dose readout^{263,269}.

2.10 Optical readout

The mechanisms of dose response in chemical dosimeters are varied as described previously, and as a result optical contrast can be measured in two unique ways: light scatter and absorption. Scatter based scanners, used for the optical readout of polymer gels, use a collimated light beam scanned across a translucent medium and measure optical density as a result of scatter attenuation¹⁶². These are commonly time consuming scans and characterized by a number of scattering artifacts. Light absorption based scans, used for the readout of radiochromic dosimeters such as PRESAGE® or FBX gels, use a variety of light configurations to measure optical density as a result of photoabsorption. These scans are typically faster as a result of the mechanisms used and less prone to scattering artifacts, although still suffer from specific challenges. As these are the primary tool for dose readout of PRESAGE®, they were the focus of this section.

2.10.1 Optical CT

The application of optical-CTs for dose readout is relatively novel, having been first introduced by Gore et al. (1996)¹⁶². A medium is imaged by a series of 2D images taken at multiple projection angles which are then passed through a radon transform to produce a sinogram for all angles. Afterwards an image filter is applied and then the

sinogram is deconvolved into a 3D map. Similar to x-ray systems, each image is taken by light projections using cone or parallel beams passing through a medium and registered by a photosensor, such as a charge-coupled device (CCD) camera, on the opposite side. The light attenuation coefficient, μ , is calculated at each pixel for each projection using the Beer-Lambert Law:

$$I = I_0 e^{-\int_0^l \mu(z) dz} \quad \text{Eq. 2.10}$$

where I_0 is the initial light intensity, I is the attenuated light intensity, l is the length across the medium, and z is the depth of the point. Further derivation provides the OD as a function of measured light intensities per unit path length:

$$\text{OD} = -\log_{10} \left(\frac{I}{I_0} \right) \text{ cm}^{-1} \quad \text{Eq. 2.11}$$

Additional corrections must be made to account for ambient attenuation, such as through refractive matching fluids, as well as for stray light.

2.10.2 Spectrophotometry

In addition to volumetric dosimetry, OD point measurements are useful for measuring dosimeter response for procedures such as depth-dose measurements and sometimes dosimeter calibrations. In these cases, small volume cuvette vials ($1 \times 1 \times 4 \text{ cm}^3$) are filled with the dosimeter material and irradiated. It is impractical to read these out using an optical-CT scanner. Spectrophotometry, in which the light of a specific

wavelength is transmitted through a sample volume of unit thickness, has been the conventional method of measuring OD for such experiments^{194,270,271}. The method of calculating OD is the same as that described in Eq. 2.11 and no 3D reconstructions are needed, making this a fast and simple method when applicable. Net OD (ΔOD) is calculated as such:

$$\Delta OD = OD_{\text{post irradiation}} - OD_{\text{preirradiation}} \quad \text{Eq. 2.12}$$

Spectrophotometer measurements for dose response calibration have been used for studies in the past^{223,253,272}, but more recent investigations have found them unreliable for precise translation to large volumes²⁴⁰. Regardless, the spectrophotometer measurements in this study were used only for relative dose response investigations between PRESAGE® formulations.

2.11 Dissertation objectives

The primary limitation for using PRESAGE® in a proton beam has been the appearance of ‘quenching’, principally seen in the Bragg peak region of the delivered field, resulting in a pronounced dose under-response. Very little research has gone into investigating the cause of this quenching and no system is in place to account for it. Currently, PRESAGE® continues to find more of a place in photon radiation therapy research and clinical applications, and while interest in proton therapy increases around the world, Presage has not been demonstrated to be an accurate dose verification system for proton therapy. The hypothesis of this dissertation is that the mechanisms causing signal quenching in PRESAGE® when irradiated by a proton beam can be evaluated and

corrected for resulting in a system that yields relative dose measurements agreeing with ionization chamber measurements to $\pm 3\%$ in the Bragg peak and with calculated doses to 5%/5mm.

The hypothesis was tested by three aims. The goal of the first aim was to develop a PRESAGE® manufacturing protocol capable of producing dosimeters to meet the needs of a wide range of clinical applications. The goal the second aim was to evaluate the effects of the concentrations of the active components in PRESAGE® formulation on signal quenching at high LET. Finally, the goal of the third aim was to develop and apply a quenching correction factor to PRESAGE® as a way to reduce dose inaccuracies caused by quenching.

Chapter 3: PRESAGE® manufacture and characterization

3.1 Rationale

The 3D dosimeters used for this study were manufactured within this laboratory. This allows dosimeters to be fabricated to meet specific criteria such as investigating the change in dosimetric response with modifications to chemical composition. Beyond proton applications, this allows further study of dosimeter sensitivities to dynamic dose range, dose rate, and temporal stability. Additionally, this will allow the lab to produce dosimeters adapted to meet specific requirements for all clinical applications as well as specific mechanical properties such as shape and size.

The goal of this specific aim was therefore to develop a PRESAGE® manufacturing protocol capable of producing dosimeters to meet the needs of a wide range of clinical applications. This method was used to manufacture a PRESAGE® formulation similar to one developed by Heuris Inc., and generally referred to as “proton PRESAGE®”²⁷². This dosimeter was used in subsequent portions of this study. Finally, the effectiveness of this protocol was examined.

3.2 Materials and methods

3.2.1 Developing a laboratory manufacturing protocol

The precise manufacturing process of commercially available PRESAGE® is a trade secret of Heuris Inc., but a general description of the process fabrication published by Adamovics and Maryanski (2004)²²⁶, along with works by Alqathami et. al (2016)²²⁷, which were used as the basis for developing the manufacturing protocol described here.

3.2.1.1 PRESAGE® materials and manufacturing equipment

PRESAGE® dosimeters are primarily composed of a polyurethane matrix, a catalyzing agent, a radical initiator, and a leuco dye dose responder. This section describes the components and procedures used to manufacture PRESAGE® to achieve specific dosimeter parameters, the processes used in storing and handling, as well as the procedures for dose readout.

3.2.1.1.1 Leuco dye

The dose responder in PRESAGE® is a leuco dye which, when oxidized, undergoes a measurable change in optical density. Early optimization studies for PRESAGE® investigated a number of potential dyes. Ultimately, leuco malachite green (LMG) was selected because of low relative photoreactivity and high activated dye optical absorption peak. LMG is initially in a colorless form, but when oxidized becomes the cation malachite green (MG) which takes on a visible green color. In its conventional state, this transition is stable and won't reduce back to its colorless form, allowing for delayed dose readout. The absorption peak of MG is approximately 633 nm which is ideal for many laboratory settings as it corresponded with many early optical-CT systems that used a helium-neon laser output (632.8 nm)²⁷³. The oxidation of LMG into MG is illustrated in Figure 3.1.

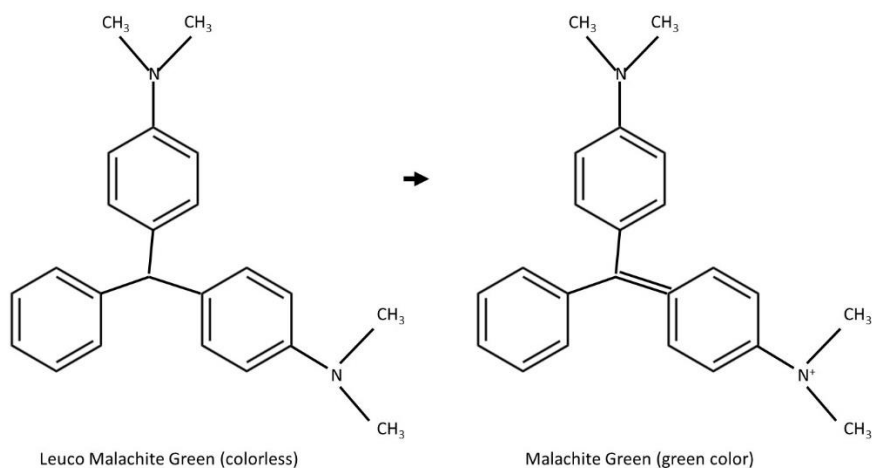


Figure 3.1: The molecular structure illustrating the transition of LMG into its oxidized product MG.

The molecular structure of LMG is a dimethylaniline (N,N-dimethylaniline) which is condensed with a benzaldehyde and is commercially available as 4,4'-Benzylidenebis(N,N-dimethylaniline). The atomic composition of LMG is shown in Table 3.1. Separate derivatives of LMG have been investigated for PRESAGE® which include substitutions to the benzaldehyde and have been shown to affect the radiological properties of the dosimeter including physical mass, Z_{eff} , and dose sensitivity^{222,232,274}. These derivations convert to MG by similar oxidation processes although by different binding pathways. The commercially available LMG purchased from Sigma Aldrich (St. Louis, MO, USA) was used for this experiment.

Table 3.1: Elemental fractional components by weight of LMG

Component	Empirical formula	W _H	W _N	W _C	M (g/mol)
LMG	C ₆ H ₅ CH[C ₆ H ₄ N(CH ₃) ₂] ₂	8.5	7.9	83.6	330.5

3.2.1.1.2 Radical initiators

Unlike gels which produce free radicals through hydrolysis, PRESAGE® dosimeters must be doped with radical initiators which are substances that, when ionized, produce oxidizing agents. These lead to the activation of the leuco dye (as described in Figure 3.1) resulting in the dose signal of the dosimeter. Early optimization studies of PRESAGE® investigated each of the most common types of radical initiators: carbonyl based, halocarbons, organic peroxides, and sulfur compounds. Based on stability and radiosensitivity, all but halocarbons were found to be unusable²⁷³. Halocarbons, also known as halogenated hydrocarbons, are compounds of halogen atoms covalently bonded to carbon atoms. The strength of these bonds varies with halocarbon resulting in a variety of activation energy thresholds²⁷⁵.

Previous studies investigating halocarbon substitutes have shown chloroform (CHCl₃), bromoform (CHBr₃), and iodoform ((CHI₃) to have the characteristics optimal for oxidizing the LMG dye. The differences in carbon-halogen bond dissociation energies of each halocarbon result in dosimeters having different dose sensitivities as demonstrated by Alqathami et al. (2012)²²¹. In addition to affecting dose sensitivity, the halogens have distinct physical properties that ultimately affect the radiological properties of the fabricated dosimeter (as shown in Table 3.2). Each of these was

investigated in this study. Each halocarbon substitute was supplied by Sigma Aldrich (St. Louis, MO, USA).

Table 3.2: Elemental percent of components by weight for halogenated hydrocarbons used as radical initiators.

Component	Empirical formula	W _H	W _C	W _{Cl}	W _{Br}	W _I	ρ (g/cm ³)	M (g/mol)
Chloroform	CHCL ₃	0.84	10.06	89.10			1.49	119.38
Bromoform	CHBr ₃	0.40	4.75		94.85		2.91	252.73
Iodoform	CHI ₃	0.26	3.05			96.69	4.11	393.72

3.2.1.1.3 Polyurethane matrix

Several transparent materials were considered for the PRESAGE® plastic matrix, such as acrylates, polyesters, polystyrenes, and polycarbonates, but these materials are generally only useable in very small volumes as a result of heat production during polymerization which causes degradation of the leuco dye²⁷³. Polyurethane cures at low temperature and is easily handled making it an ideal dosimeter matrix. This organic compound is composed of two liquid precursors which, when isolated in standard room conditions, remain in a stable state. The first precursor, referred to as Part A, is a pre-polymer comprised of a di- or poly-isocyanate. The second precursor, referred to as Part B, is a curative component comprised of a polyol and often a catalyzing agent. When the precursors are blended, a polymerization process occurs resulting in a polymer containing a urethane linkage.

The polyurethane used in this study was Crystal Clear 206 (Smooth-on, Easton, PA, USA) supplied by The Engineer Guy (Atlanta, GA, USA) as well as a catalyst agent, dibutyltin dilaurate (DBTDL) (Sigma Aldrich, St. Louis, MO, USA) used to improve structural stability. These components have been used in previous PRESAGE® formulation studies and were selected for near tissue equivalent properties along with a polymerization time sufficiently long to allow for proper dosimeter fabrication^{10,221,227,231}. The components have the elemental compositions, described by Adamovics and Maryanski (2006)²⁷⁶, shown in Table 3.3.

Table 3.3: Elemental fractional components by weight of polyurethane and the catalyst agent DBTDL relative to ICRP's simplified four-component soft tissue composition.

Component	Empirical formula	W _H	W _C	W _N	W _O	W _{Sn}	ρ (g/cm ³)
Polyurethane		9.00	61.00	10.00	20.00		1.04
DBTDL	C ₃₂ H ₆₄ O ₄ Sn	10.21	60.86		10.13	18.80	1.07
Soft Tissue		10.11	11.10	2.60	76.18		1

3.2.1.1.4 Pressure tank

A common issue of quickly mixing polyurethane resins is the trapped air bubbles in the cured formation. These bubbles are a result of air trapped during mixing as well as bubble nucleation resulting from the diisocyanate-polyol reactions. The trapped air is unable to migrate out of the solution before solidifying²⁷⁷. The solution to this is to store the combined polyurethane components in a pressurized container immediately following mixing to remove this trapped air, called out-gassing. The manufacturers of Crystal

Clear 206 recommend their casting be pressurized to 60 psi for a time variable to cast size.

To accommodate this, a 5 Gallon Pressure Chamber (Smooth-on, Easton, PA, USA) was paired with a 6310 Ultra Quiet Air Compressor (California Air Tools Inc., San Diego, CA, USA) which allowed pressure casting up to 80 psi for out-gassing of the fabricated dosimeters (shown in Figure 3.2).



Figure 3.2: Pressure tank and air compressor system used for polyurethane out-gassing.

3.2.1.2 Fabrication procedure

The fabrication process is an adaptation of the one described by Adamovics and Maryanski (2006)²⁷³. The components for Parts A (diisocyanate) to B (polyol) of the polyurethane should be kept in a ratio of 10:9 as per manufacturer recommendations to ensure the structural stability of the cured materials. All materials should be acclimated to room temperature prior to fabrication.

The fabrication process is as follows:

1. Measure and keep separated part A, part B, and LMG
2. Measure the radical initiator component and combine with LMG. Mix thoroughly to fully dissolve particulates. This may take anywhere from one to three minutes depending on volume, but should be expedited to account for evaporation of the radical initiator.
3. Solution from step (2) is then combined with the measured part B from step (1). Mix briefly.
4. The solution of step (3) is then blended with part A and mixed briefly.
5. The DBTDL catalyst is added to the blended solution of step (4) and mixed thoroughly.
6. The mixture is then poured into the mold, placed into the pressure tank, and stored at 60 psi for 12 hours (cuvettes) to 24 hours (large volume).
7. If dosimeters are removed prior to those times (such as in cases of rapid manufacturing), they should be stored at room temperature for the remainder of their curing times.

3.2.1.3 Storage and handling

Previous studies have shown PRESAGE® sensitivity to UV and thermal affects resulting in premature activation of the leuco dye^{12,239}. To reduce these factors, all dosimeters were stored in a cold environment (<3°C) in dark conditions. The effects of storing dosimeters below freezing temperatures were not studied here. Before readout and irradiating, these were allowed to re-acclimate to room temperature (~23°C). To

reduce exposure to light during handling, dosimeters were wrapped in the light-blocking, stretch film (Uline 80 gauge, Pleasant Prairie, WI, USA).

3.2.2 Production of proton PRESAGE®

The proton PRESAGE® previously described was replicated in part using the above method based on concentrations of radical initiator (bromoform in this case) and LMG obtained from Heuris Inc. The concentrations of only those two components were known so the concentrations of the other components were estimated from the existing literature and personal communication. The radiological properties of proton PRESAGE® was described by Gorjiara et al. (2012)²⁶⁷ and a comparison is shown in Table 3.4.

Dosimeters were cast into cylindrical molds with dimensions 6.5 x 6.5 cm³ (Diameter x Height) as well as in spectrophotometer cuvettes with dimensions 1 x 1 x 4.5 cm³ (Width x Length x Height).

Table 3.4: Comparison of the elemental fractional weights of the proton PRESAGE® (shown here as PRESAGE-1) investigated in literature²⁶⁷ and PRESAGE® made in-house (shown here as PRESAGE-2).

Component	W _H	W _C	W _N	W _O	W _{Sn}	W _{Br}
PRESAGE-1	9.03	64.10	4.92	20.00	0.56	1.4
PRESAGE-2	10.74	58.84	9.79	19.20	0.01	1.42

3.2.3 Procedures for characterizing dosimeter parameters

PRESAGE® produced in-house must be characterized to determine structural stability and dosimetric capacity. Similar studies have been performed on newly developed formulations of PRESAGE® dosimeters manufactured by Heuris, Inc.^{229,231,272}, and so a similar procedure was incorporated here. Dosimeters made in-house must demonstrate robustness and accuracy in a reproducible manner.

Commissioning of the manufacturing protocol tested five general components:

1. To verify proper mixing and diffusion of the individual components in the polyurethane matrix, cylindrical dosimeters were imaged with an x-ray CT scanner (Philips CT Big Bore) using 120 kV energy and 1 mm slice thickness. The variation of electron density was measured in slices taken through the center of the dosimeter (orthogonal to the height axis) and at cross-sections 1 cm from the top and bottom. Additionally, the dosimeters were visually inspected for Schlieren bands and undissolved particulates trapped in the polyurethane.
2. The importance of pressurization variables was also investigated to determine their effects on dosimeter shrinkage while curing. As previously stated, to eliminate outgassing the manufacturer of Crystal Clear recommends pressurization to 60 psi. This practice has been used in previous manufacturing studies^{227,276}, but has not been studied comprehensively. The protocol for curing commercial polyurethane often recommends fabrication in heated casts ($>90^{\circ}\text{C}$)²⁷⁸, but this is not recommended in the fabrication of PRESAGE® as it would lead to early activation of the leuco dye. It is important to account for volumetric changes of polyurethane when cast into shapes for applications such as

in an anthropomorphic phantom. To quantify volume changes, dosimeters were cast in a cylindrical mold with a diameter of 3 cm and a pour volume of 50 mL under varying magnitudes of pressurization. All dosimeters were fabricated in a temperature controlled laboratory (20-22°C). The dosimeter shrinkage was determined based on the pour volume (V_{pour}) and the cured volume (V_{cured}) as such:

$$\text{Shrinkage (\%)} = \frac{V_{\text{pour}} - V_{\text{cured}}}{V_{\text{pour}}} \times 100 \quad \text{Eq. 3.1}$$

3. The dose response curves of the dosimeters were investigated. Previous studies have demonstrated dose linearity in commercial PRESAGE® formulations up to at least 10 Gy (often much higher)^{143,222,229,238,241,272} which is vital for simple 3D dosimetry without the need for dose response correction factors. Cuvettes can be irradiated to known dose values and act as 0D detectors. The resulting dose response is then used for absolute calibration in some cases²⁴¹ but in this experiment was used to demonstrate dose response linearity. The interbatch reproducibility of the dosimeters was investigated using dosimeters made in three separate fabrications, or batches. For each batch, measurements were made in triplicate making a total of nine cuvettes at each dose point.

4. Volumetric dose response constancy is necessary to show robustness of homogenous dispersion of dose responding components in volumetric dosimeters. After dose response calibration, it is important to demonstrate all regions of a dosimeter receiving identical dose should undergo a similar dose response. To

demonstrate this, an adaptation of the B2 treatment plan benchmark test by Thomas et al. (2011)²⁴¹ was used to measure isodose distributions along axial cross-sections.

5. The temporal stability of the dosimeters demonstrates another form of robustness in the dosimeters. To investigate this, dosimeters were stored in refrigerated conditions ($<3^{\circ}\text{C}$) following initial readout. The optical density of the cuvettes was remeasured periodically and the change in dose signal was recorded.

3.2.3.1 Dosimeter irradiations

All irradiations were performed using a Versa HDTM linac (Elekta, AB, Stockholm, Sweden) delivering 6 MV photons. Cuvettes were placed in a high impact polystyrene slab and placed between slabs of Solid Water® to allow for measurement points at a depth of 10 cm (shown in Figure 3.3). An additional 5 cm of Solid Water® was placed below the cuvettes to maintain backscatter conditions. The field size was set to 20 cm x 20 cm and total doses delivered ranged from 0 to 12 Gy. For each dose point, three cuvettes (one from each batch) were irradiated at a time. Readout for the temporal study was done at 1, 4, 12, and 24 hours then once every 24 hours following for five days. Cuvette measurements were performed by spectrophotometry (described in section 3.2.3.2.3) with each reading recorded in triplicate.



Figure 3.3: Photograph of the polystyrene slab used for cuvette irradiations (left) and the experimental setup including the Solid Water® beam attenuators (right).

To investigate the isodose response uniformity in a fabricated PRESAGE® volume, a square field (4 cm x 4 cm), modeled using the Pinnacle 9.0 TPS (Philips Healthcare, Fitchburg, WI), was delivered to the cylindrical dosimeter along the central axis. The dosimeter was placed in a water phantom and irradiated from the top-down (AP) to 2 Gy prescribed dose to the center. The dose response was recorded and isodose cross-sections were taken orthogonal to the beam angle at varying dose levels.

3.2.3.2 Optical dose readout

3.2.3.2.1 Duke Midsized Optical-CT Scanner

The Duke Optical-CT Scanners are a series of optical-CT scanners manufactured by the Duke 3D Dosimetry and Optical Bio-Imaging Laboratory directed by Mark Oldham, PhD. These scanners use a broad, parallel beam which is projected through bi-

telecentric lenses to reduce stray and scattered light using methods developed by Thomas and Oldham (2010)²⁷⁹. The scanners use a red LED light source with an optical band pass-filter to narrow light emissions to the 632 ± 10 nm wavelength spectrum corresponding to the peak absorption wavelength of LMG making it ideal for PRESAGE® dosimeters.

The Duke Midsized Optical-CT Scanner for IROC-Houston (DMOS-IROC) model was used for all of the volumetric dosimetry in this study. The system was commissioned in 2012 and has since been used for remote auditing and in-house research^{12,143,242,280}. The main components of the system are fixed to a breadboard and include an LED light source, optical diffuser, narrow bandpass filter, telecentric collimator and lens, refractive index matching fluid tank and rotating stage (aquarium), aperture stop, and CCD camera. These components are illustrated in Figure 3.4.

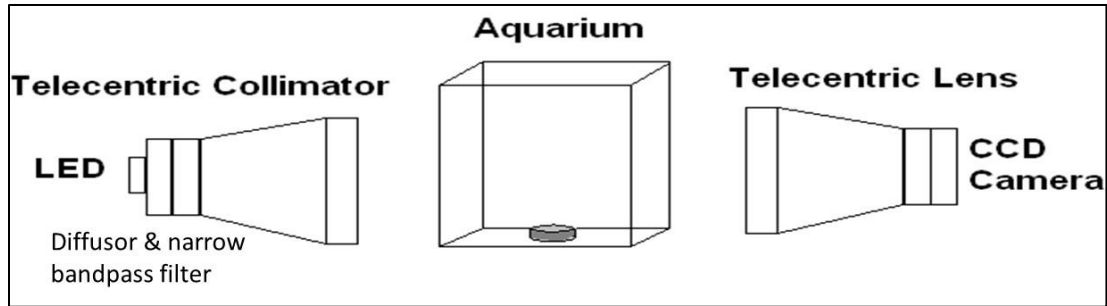


Figure 3.4: Diagram (top) and matching photograph (bottom) of the DMOS-IROC.

3.2.3.2.2 Acquisition of optical-CT data

Image acquisition and 3D reconstruction was completed using MATLAB® (Mathworks, Natick, MA) software developed by the Duke 3D Dosimetry and Optical Bio-Imaging Laboratory. The reconstructions were analyzed using A Computational Environment for Radiotherapy Research (CERR). This MATLAB-based program was designed for 3D gamma comparisons using treatment plans generated from a commissioned TPS²⁸¹. The mechanisms of the dosimeter readout and image reconstruction were discussed in detail by Thomas and Oldham (2010)²⁷⁹.

3.2.3.2.3 Acquisition of spectrophotometry data

The cuvette measurements in this study were performed using a GENESYS™ 10S UV-VIS spectrophotometer (Thermo Fisher Scientific, Waltham, MA, USA). This system is capable of measuring absorption over a wide spectrum of visible light wavelengths (400-700 nm). As mentioned previously, the optimal wavelength for dose response in PRESAGE® using LMG is 633 nm^{215,276}. Therefore spectrophotometer measurements for the purposes of measuring dose response in this study were performed using this single wavelength.

In addition, the optical density measurement of cuvettes from the spectrophotometer is highly susceptible reflective and refractive artifacts as a result of dosimeter placement or any surface damage to the cuvette. Cuvette measurements were made in triplicate to ensure these were minimized. Any found to have these problems were not used for dose measurements.

3.3 Results and discussion

Dosimeter fabrication ultimately became an iterative process of eliminating dosimeter artifacts including surface damage, undissolved particulates, and curing procedures. Dosimeters were fabricated in both cuvettes and cylindrical forms that responded to absorbed dose by a visual color change (shown in Figure 3.5 and Figure 3.6).

A qualitative analysis of the fabrication process as well as a quantitative analysis of the credentialing procedures are discussed in this section.



Figure 3.5: Photograph of PRESAGE® cuvettes irradiated to varying doses to demonstrate the associated visual color change.

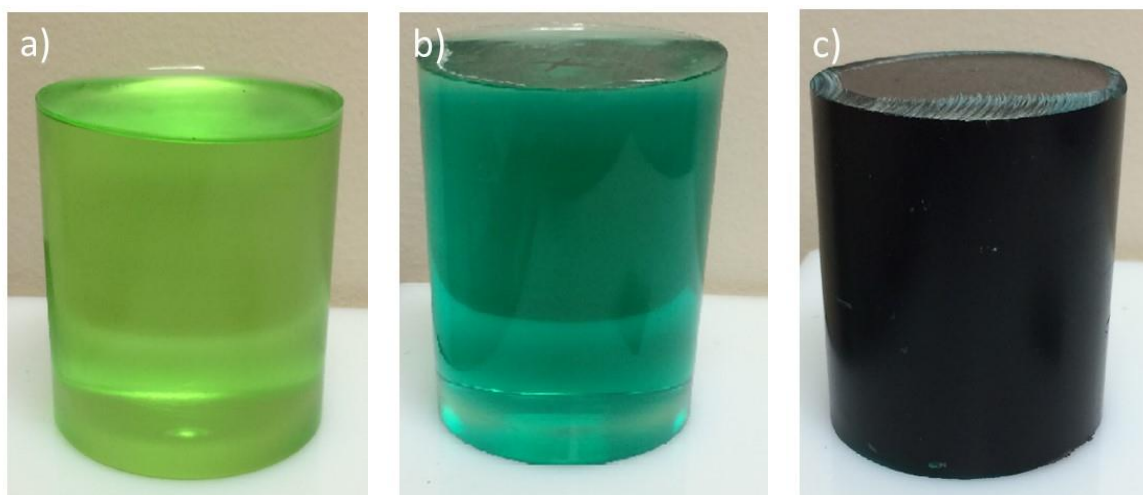


Figure 3.6: Photographs of PRESAGE® dosimeters demonstrating the visible color change as a result of LMG oxidation in a large volume. Dosimeter (a) was unirradiated, dosimeter (b) was irradiated to 4 Gy, and dosimeter (c) was irradiated to over 50 Gy.

3.3.1 Surface artifacts

Surface damage was a common result of mechanical damage during demolding (shown in Figure 3.7). The materials used for molding were a primary variable in this damage. Glassware was readily available but surface defects created bonding sites for the resin. This was partially alleviated by silicone based mold release solutions but these often created surface imperfections including opacities. Also the structural integrity of most glassware is susceptible to damage from the mechanical forces when demolding the polyurethane. Acrylic glass, such as polymethyl methacrylate (PMMA) offered much higher tensile strength and very little surface binding which allowed for easy demolding with very few surface imperfections. Finally, by storing dosimeters in extreme cold environments ($< -19^{\circ}\text{C}$), the cold dosimeters could be more easily removed by rapidly heating the molds in a water bath. This was found to remove the need for blunt force in demolding dosimeters and ultimately reduced surface artifacts.

3.3.2 Schlieren bands

Previous studies have shown that inhomogeneities within the dosimeter result in optical artifacts, known as Schlieren bands. Avoiding these artifacts requires thorough mixing of the components^{221,241}. Schlieren bands are difficult to see with the naked eye. During optical-CT imaging, they manifest as swirling patterns (shown in Figure 3.7) which result in imaging artifacts. A method by Thomas et al. (2011) introduced scatter restrictors into the optical-CT system to attempt to reduce these artifacts, although only with limited success²⁸². This experiment found that thorough mixing and combining polyurethane components at the end of fabrication, as well as rigorous mixing of all

components immediately before pouring into each mold reduced the formation of Schlieren bands.

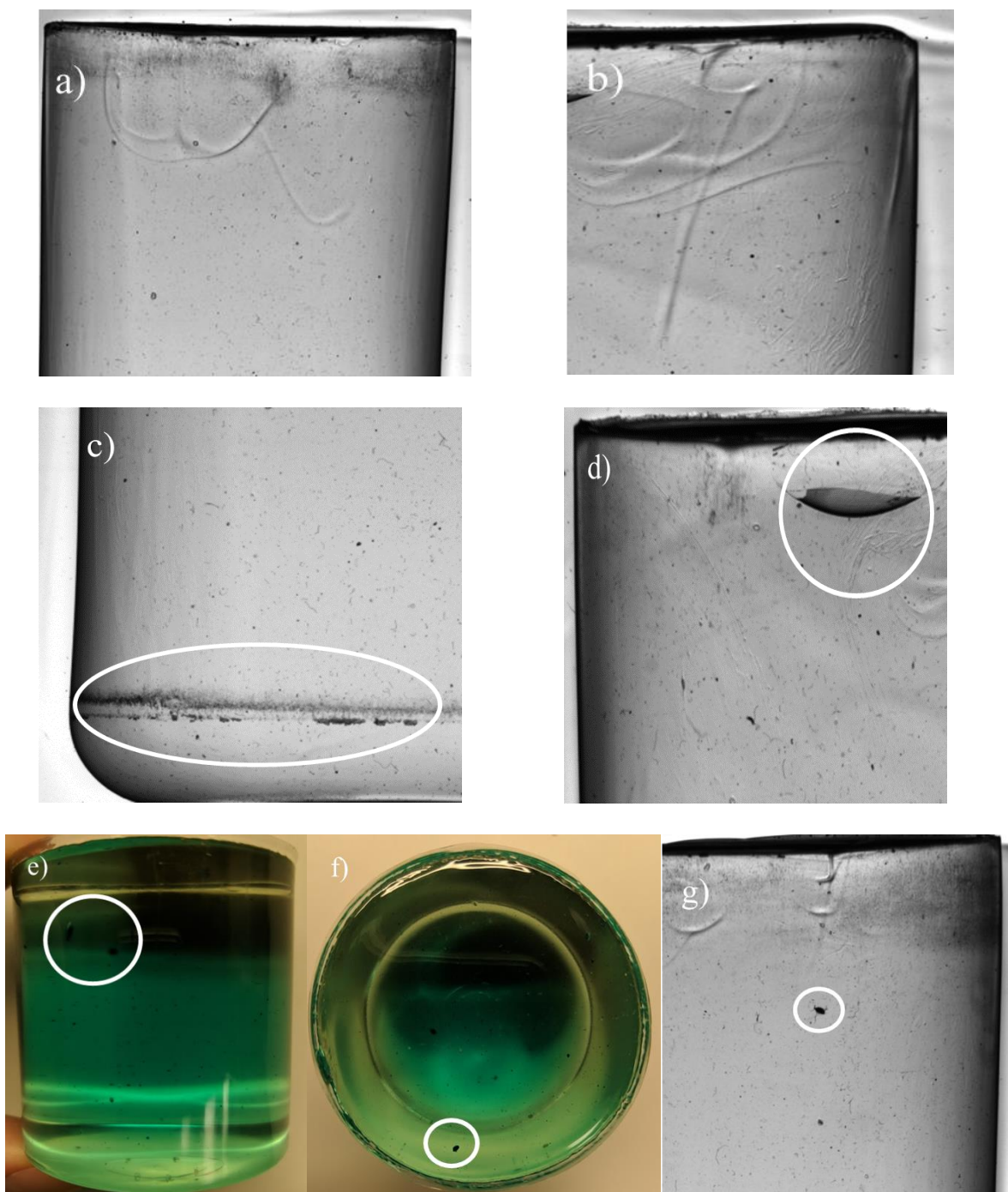


Figure 3.7: Images of many common fabrication artifacts. Schlieren bands (a and b), damage caused from dosimeter demolding (c and d), and undissolved particulates (e, f, and g).

3.3.3 Undissolved particulates

Undissolved particulates visible during optical scanning as well as through visual inspection created another obstacle, shown in Figure 3.7. Debris, such as dust, in the casting molds as well as generated from the air compressor and pressure tank would settle in the dosimeters during curing. This was generally reduced by thoroughly wiping down the pressure tank and casting molds before each use and keeping them sealed between fabrications. The compressed air inlets into the pressure tank were flushed prior to each use as well. Molds covered to reduce debris while curing in the pressure tank suffered from less efficient outgassing. Additionally, undissolved particulates are generally a byproduct of impurities of the dosimeter components that remain in the solution during fabrication. This was, in part, reduced by more vigorous mixing procedures to reduce clumping and promote dissolution of powders. With the addition of a glass fiber filter between fabrication steps 2 and 3 (see section 3.2.1.2), most of the undissolved particulates were further removed from the leuco dye/radical initiator combined solution. Filtration after combining with the polyurethane precursors was more difficult because of the added viscosity which greatly increased fabrication time. No particulates were found in Crystal Clear 206, so including filtration for these components was unnecessary.

3.3.4 Density uniformity

Three axial cross sections of a cylindrical dosimeter imaged by x-ray CT were used to investigate the uniformity of the electron density across the dosimeter volume (shown in Figure 3.8) which can be used to ensure homogenous curing of the polyurethane matrix as well as dispersion of high-Z components during fabrication. The PRESAGE® had an average CT value of 111.1 ± 2.91 making it nearly equivalent to soft

tissue. CT values were consistent between slices taken at different heights in the dosimeter demonstrating very little dependence along the central axis. An area profile analysis of the axial planes demonstrated some minor increase in variance in the central axial plane as shown in Table 3.5. This may demonstrate some minor spatial uniformity discrepancies that is limited by the curing process of the polyurethane.

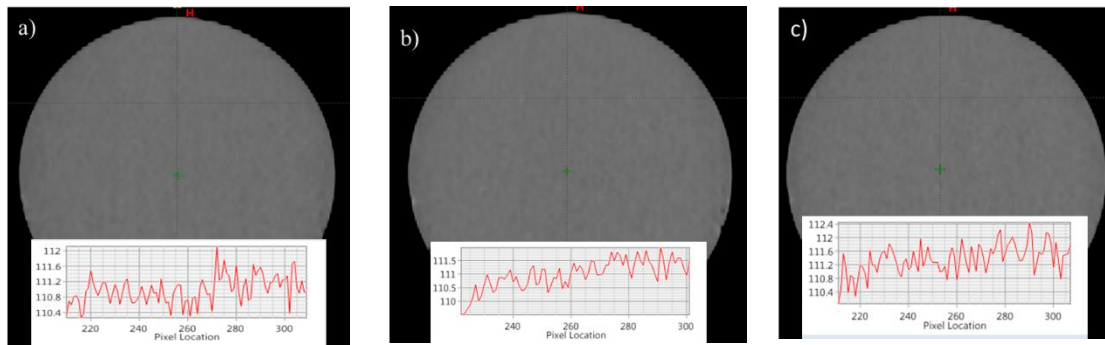


Figure 3.8: X-ray CT axial cross sections taken at the top (a), center (b), and bottom (c) of a cylindrical dosimeter with a line profile of CT number values along the central axis.

Table 3.5: Area profile analysis of the CT values in axial planes taken from a cylindrical PRESAGE® dosimeter.

Axial slice	Average CT#	SD	Min. CT#	Max. CT#
Top	111.0	2.91	99.0	123.0
Center	110.9	2.99	98.0	126.0
Bottom	111.4	2.91	100.0	125.0

3.3.5 Effects of pressurization during curing

Dosimeters manufactured and cured under different pressures demonstrated an observable change in the formation of air bubbles compared to dosimeters not cured under pressure (shown in Figure 3.9). Dosimeter shrinkage during curing as a function of the magnitude of pressurization is shown in Table 3.6. The laboratory was strictly climate controlled, although temperature and barometric pressure were recorded using a local barometer when measuring pour and cured volumes. The average shrinkage was $2.43\% \pm 0.59\%$ which is slightly higher than the $\sim 1\%$ recorded for generic polyurethane recorded in the literature²⁷⁸. There was no correlation found between shrinkage and temperature/pressure in the range observed in this investigation.

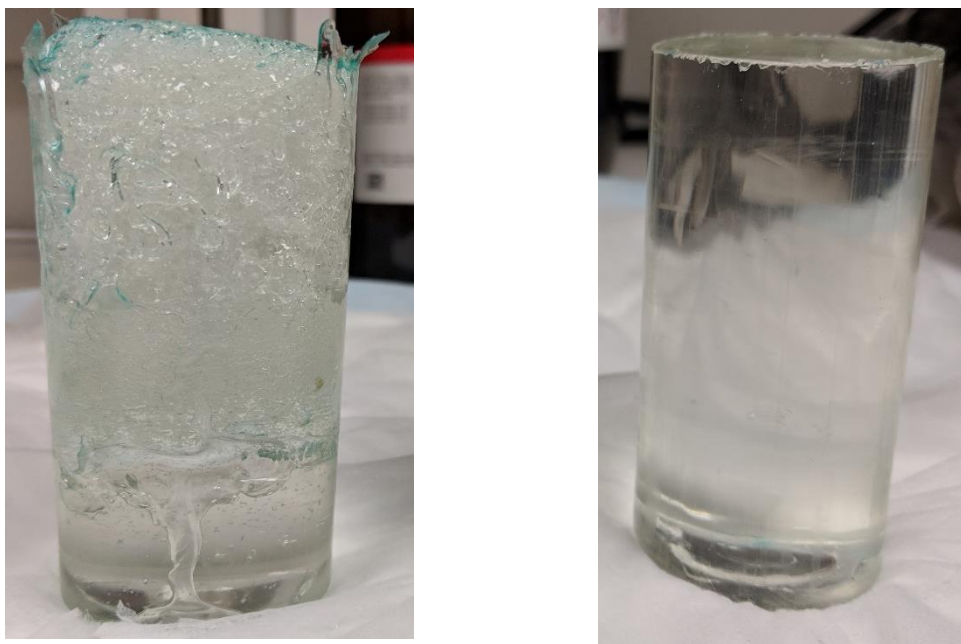


Figure 3.9: Polyurethane manufactured without pressurization (left) cures with trapped bubbles while the polyurethane pressurized to 60 psi (right) does not.

Table 3.6: Results of PRESAGE® shrinkage when cured under different pressures.

Temperatures at the time of pouring and when cured are included.

Pressure tank (psi):		40	50	60	70	80
Shrinkage (%)		2.87	3.28	1.58	2.36	3.05
Ambient temperature (°C)	@pour	20.0	20.6	21.1	20.6	21.1
	@cured	20.6	20.0	21.1	20.6	20.6
Barometric pressure (kPa)	@pour	103.25	102.81	102.84	102.74	102.40
	@cured	102.13	103.05	103.66	102.81	101.15

3.3.6 Dose response linearity and fabrication reproducibility

The measured change in optical density with respect to absorbed dose for each batch is shown in Figure 3.10. The cuvettes all showed a very linear dose response ($R^2 > 0.999$) up to 12 Gy with no signs of saturation. Intrabatch comparisons between Batches 1, 2 and 3 showed standard deviations between similarly irradiated dosimeters to be 7.76E-4, 10.22E-4, and 6.88E-4 (respectively). A comparison of cuvettes irradiated to a uniform dose, shown in Figure 3.11, was used to demonstrate reproducibility of dose response between batches. Dose linearity was similarly high ($R^2 > 0.999$), although the standard deviation increased slightly to 20.09E-4. This was primarily a result of variance between measured OD at high doses (<6 Gy) in which the discrepancies were more pronounced between formulations. Complete dose response data is available in the Appendix 1 (pg. 153).

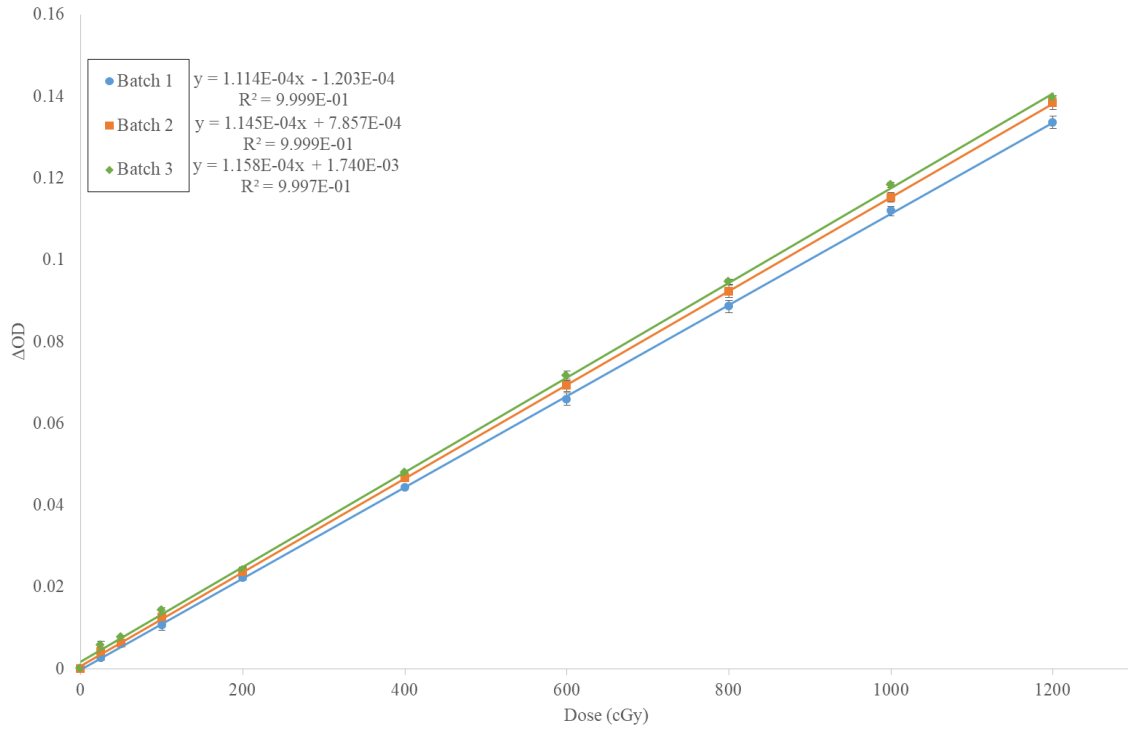


Figure 3.10: ΔOD as a function of absorbed dose as measured by PRESAGE® cuvettes from three fabrications of the same formulation with linear trends represented by solid lines. Error bars represent the standard deviation of the response of three cuvettes from each batch irradiated to each dose point.

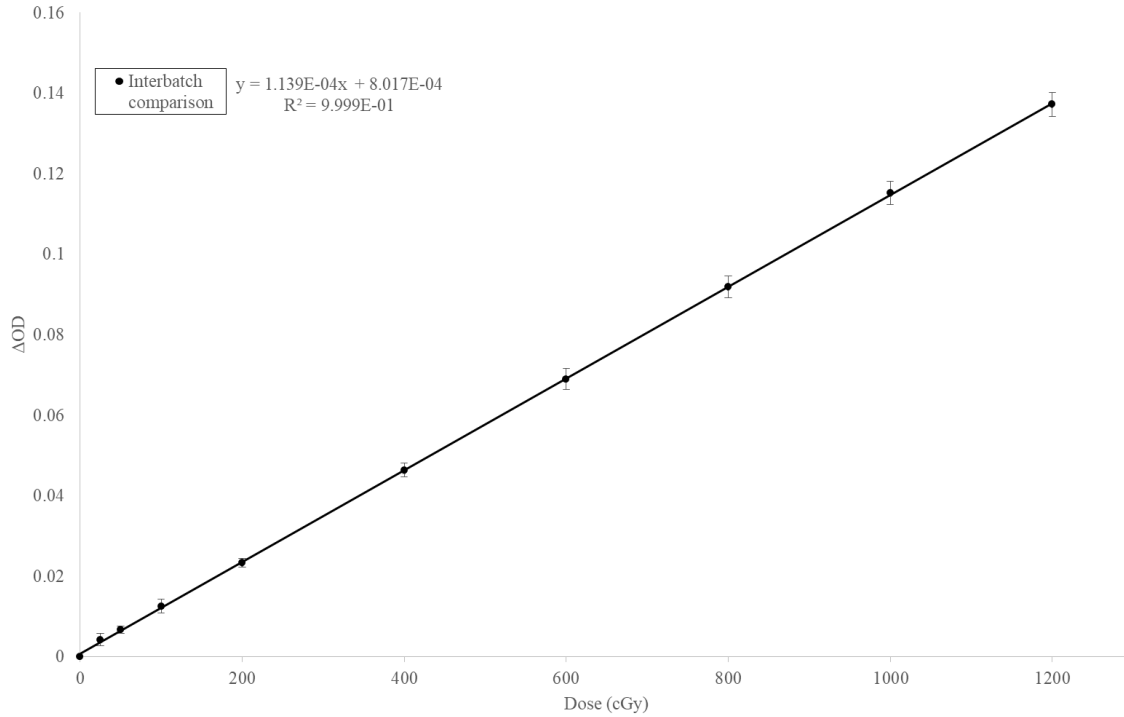


Figure 3.11: Average of all batches from Figure 3.10 and the linear trend represented by a solid line. Error bars represent the standard deviations of readings from all cuvettes at each dose point.

3.3.7 Temporal stability

Cuvettes from Batch 1 used in the linearity study were measured periodically over five days to measure the temporal stability of the dosimeters with respect to dose (shown in Figure 3.12). The findings show the greatest change in signal from irradiated cuvettes occurred between 1 and 4 hours after irradiation ($-2.38\% \pm 0.23\%$), followed by the change between 4 and 12 hours after irradiation ($-1.27\% \pm 0.14\%$). The signal stabilized between 24 and 72 hours after irradiation ($-0.24\% \pm 0.004\%$). After 5 days, the dose signal was reduced by $-3.95\% \pm 1.21\%$. This demonstrates that some dose signal is lost over time. On the other hand, the signal intensity of the unirradiated cuvettes increased

by $2.2\% \pm 0.01\%$ over the 5 day window which implies some natural darkening of the dosimeter occurs over time, which may be intrinsic to the dosimeter.

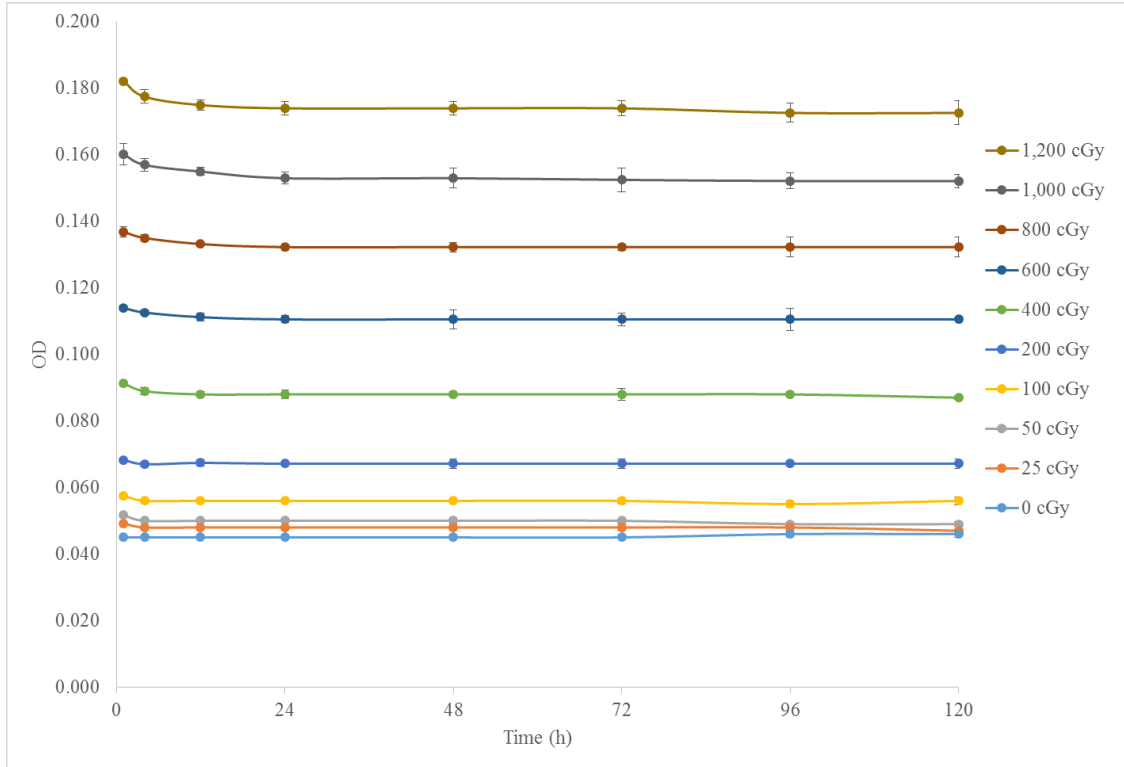


Figure 3.12: Change in dose response for PRESAGE® cuvettes irradiated to varying dose points over five days. Error bars represent the standard deviation between three cuvettes measured at each dose point. Lines were added between measurement points to aid the eye.

3.3.8 Volumetric analysis

A cylindrical dosimeter irradiated in the top down (AP) beam configuration, along with the image reconstructed dose, is shown in Figure 3.13. Isodose cross sections were

taken perpendicular to the central axis at the center of the dosimeter as well as 1 cm below the top and 1 cm above the bottom to investigate dose response uniformity, shown in Figure 3.14. Dose response in the PRESAGE® was normalized to the dose at the central axis in each plane. Line profiles taken through these cross sections compare the dose response of the PRESAGE® with TPS calculations. Good agreement was observed in all three planes with an average uniformity of $1.51\% \pm 0.63\%$ and a maximum disagreement of -4.57% . Agreement within each plane is shown in Table 3.7. The greatest discrepancies were observed in the top and bottom planes which implies that this is a result of fabrication rather than dose dependence. These results demonstrate that the dosimeters are fabricated with sufficient dispersion of dose-responding components.

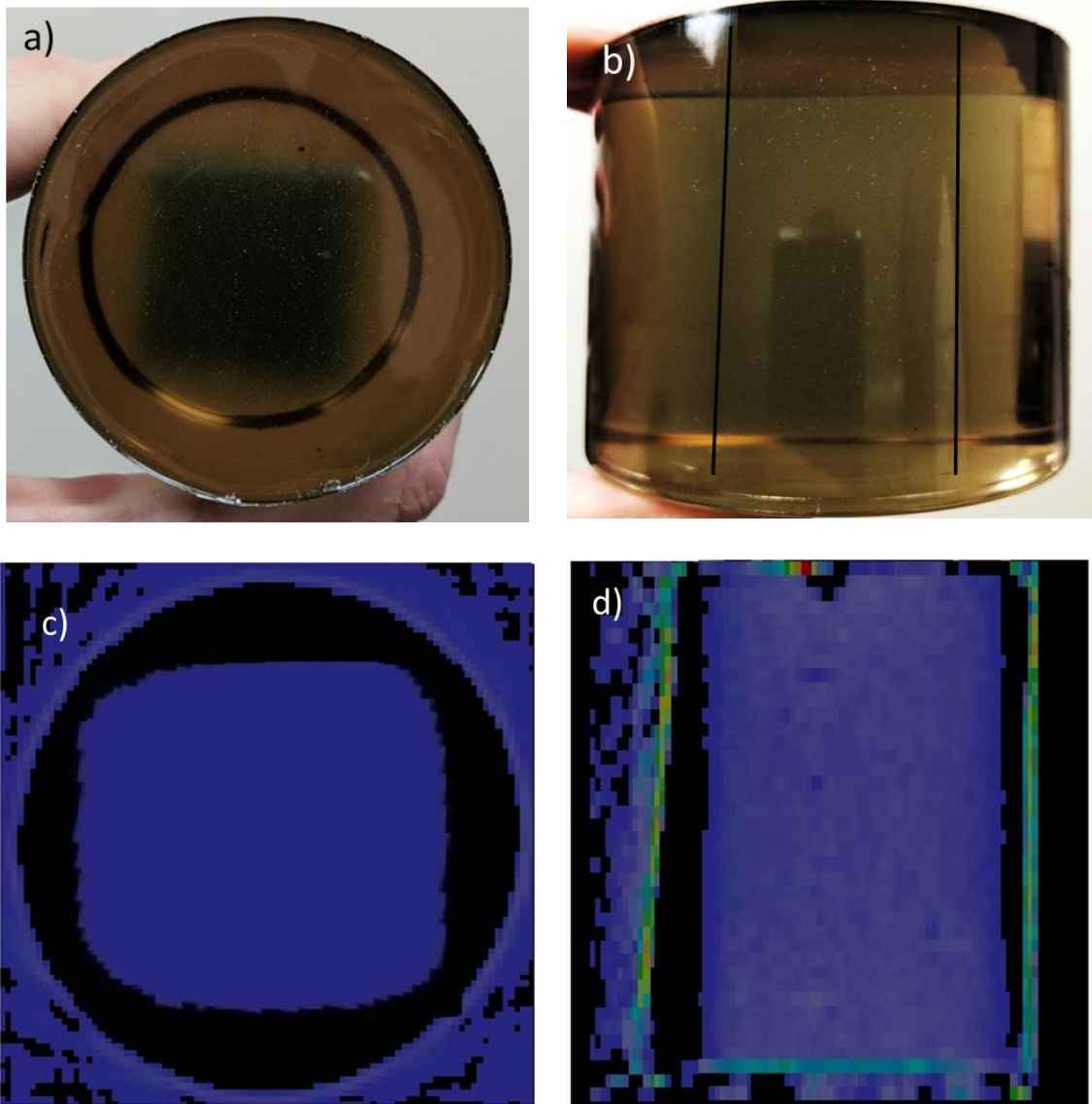


Figure 3.13: Cylindrical PRESAGE® irradiated from the top-down with a square field. The visual color change is shown in photographs of the top (a) and sides (b) of the dosimeter with lines drawn to give contrast. The dose image reconstruction in CERR is shown for the central transverse (c) and coronal (d) planes.

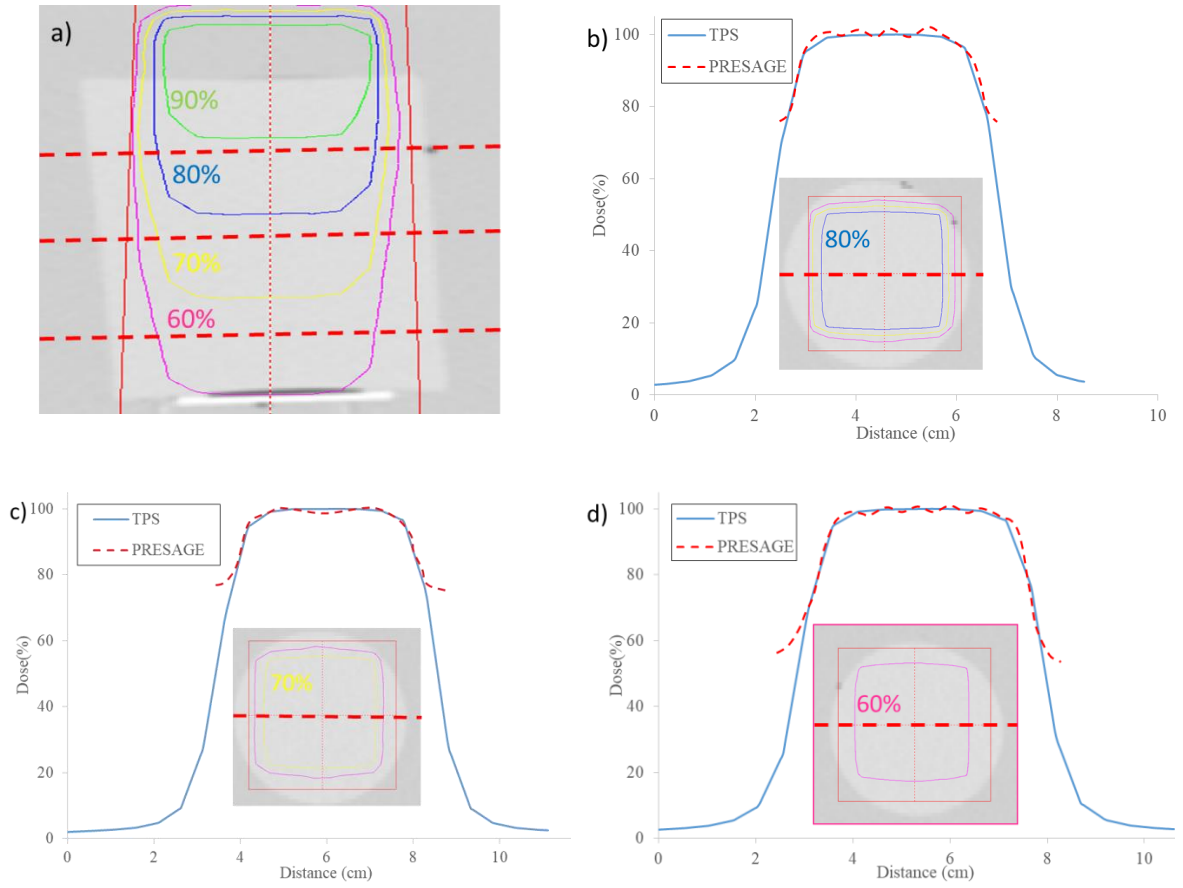


Figure 3.14: Isodose profiles of PRESAGE® top-down irradiation in a water phantom in the (a) sagittal plane with dashed lines representing axial cross section locations. Line profiles through these cross sections comparing the dose uniformity of PRESAGE® and TPS calculations are shown in (b) (c) and (d).

Table 3.7: Dose uniformity measured by line profiles through three central axis cross sections.

Coronal slice	Prescribed dose (cGy)	Uniformity (%)	SD	Highest discrepancy point (%)
Top	220.5	1.98	0.91	-4.57
Center	200	0.79	0.12	1.98
Bottom	179.6	1.77	0.86	-3.82

3.4 Conclusions

In this chapter, a PRESAGE® manufacturing protocol was adapted from the literature that was used for the production of dosimeters for the remainder of this study as well as for multiple future applications within this laboratory. Extensive reproductions demonstrated that fabrication in-house is possible using a diligent manufacturing protocol to reduce or eliminate many sources of imaging artifacts. These dosimeters have demonstrated physical and radiological properties similar to PRESAGE® in the literature. Dose linearity was demonstrated with no saturation observed and dosimeters responded uniformly throughout their volume. Temporal stability of the dose signal showed the greatest volatility within the first 24 hours followed by a period of stability. This stable period was used for future readouts unless otherwise stated. Characterization of PRESAGE® components on dose signal is further investigated in the next chapter.

Chapter 4: Evaluation of PRESAGE® active components and development of a low-quenching formulation

4.1 Rationale

The limitations of PRESAGE® dosimeters for proton therapy applications as a result of signal quenching are pervasive throughout 3D chemical dosimeters. As a result, most investigations into PRESAGE® application for proton therapy have been feasibility studies. A formulation of PRESAGE® seeking to eliminate quenching through an alteration of the chemical formulation has been shown to only be partially successful^{15,272}. This prototype formulation was released by Heuris Inc. and, as mentioned previously, is generally referred to as “proton PRESAGE®.”

The goal of this aim was to evaluate the effects of the active components in PRESAGE® formulations on specific dosimetric properties, including: dose sensitivity, temporal stability, and signal quenching at high LET. From these results, further optimization of the formulation sought the limits for minimizing signal quenching chemically. Finally, a single formulation was isolated to be used for future proton studies.

4.2 Evaluation of active components

The signaling components of PRESAGE® include the radical initiator and dose responders (described previously in Section 3.2.1.1), but previous studies have shown that the catalyst agent, used to improve polyurethane structural stability, can affect dosimetric properties^{216,221,225}. Therefore, these three components were evaluated to determine any contributions to changes of the dosimetric properties of PRESAGE®.

4.2.1 Materials and methods

4.2.1.1 Dosimeter compositions

PRESAGE® batches were made with different concentrations of material compositions using the methods described previously. The concentrations of LMG, radical initiator, and catalyst were altered individually for each batch. Measurements using the proton PRESAGE® formulation (see Table 3.4) were included. Additionally, two radical initiator halocarbon substitutes were compared: bromoform and chloroform. All batches were manufactured to the same total mass. To account for variations in the mass of the active component, the quantity of polyurethane resin was adjusted as needed for each formulation. All batch formulations are shown in Table 4.1.

The batches were cast into spectrophotometer cuvettes which were divided between photon and proton irradiation sets. Two cylindrical molds with dimensions 6.5 x 8.5 cm³ (diameter x height) were cast from the proton PRESAGE® formulation and used for a quenching comparison with cuvettes. All dosimeters were manufactured separately but irradiated within the same time frame (3-5 days) after manufacturing. Dosimeters were stored under similar conditions described previously including refrigeration (< 3°) and a dark environment.

Table 4.1: Composition (percent by weight) of the active components used in each PRESAGE® batch.

Batch	LMG (%)	Radical Initiator Type	%	DBTDL (%)	Initial OD
1	0.5	CHBr ₃	1.0	0.05	0.044
2	0.5	CHBr ₃	3.0	0.05	0.045
3	0.5	CHCl ₃	1.0	0.05	0.040
4	0.5	CHCl ₃	3.0	0.05	0.041
5	1.0	CHCl ₃	3.0	0.05	0.042
6	2.0	CHCl ₃	3.0	0.05	0.046
7	0.5	CHCl ₃	3.0	0.00	0.040
8	0.5	CHCl ₃	3.0	0.10	0.071
9	0.5	CHCl ₃	3.0	1.00	0.388

4.2.1.2 Dose sensitivity and temporal stability

Changes to the concentrations of active components have previously been shown to alter the change in optical density per unit of dose (OD cGy⁻¹), or dose sensitivity, for chemical dosimeters including PRESAGE®. Reduced sensitivity can limit the dose resolution for low-dose level measurements while heightened sensitivity may lead to regional dose saturation effectively reducing dose response linearity. Similarly, changes to these components have been shown to alter temporal stability and lead to signal fading that may limit potential applications for the dosimeter such as remote auditing. Therefore, it was important to investigate these properties and ensure that the formulations used going forward would be appropriate for such applications. These parameters were measured for each batch using the methods described below.

4.2.1.2.1 Photon irradiations and readout

Irradiations were performed similarly to the irradiations of cuvettes described in Section 3.2 using an Elekta Versa HDTM linac delivering 6 MV photons. Ten cuvettes from each batch were irradiated in a Solid Water® phantom to total doses ranging from 0 to 20 Gy. These irradiations were repeated for additional productions of each formulation. A photograph of the setup is shown in Figure 3.3. Readout for the dose response study was performed using the spectrophotometer (described in section 3.2.3.2.3) with prescans taken approximately 1 hour before irradiations and postscans taken 24 hours post-irradiation. For the temporal studies, cuvettes which were irradiated to 4 Gy from each formulation were readout at additional time points up to five days post-irradiation.

4.2.1.3 Proton signal quenching

The dosimeter batches were also irradiated using protons to investigate the relationship of the magnitude of dose quenching with the concentration of active components. The proton PRESAGE® formulation (batch 0 here), previously released by Heuris Pharma, LLC, also demonstrated such formulation dependence and was also used in the research into formulaic variations with other chemical dosimeters in high-LET fields^{217,272}. Three preliminary investigations into dose quenching were made using the PRESAGE® formulations in Table 4.1: (1) a correlation in quenching magnitude between cuvettes and large volume dosimeters, (2) signal quenching as a function of total dose, and (3) an investigation of the relationship between quenching magnitude and the concentration of each active component.

4.2.1.3.1 Proton study (1): Quenching comparison between cuvettes and large volumes

Cuvette studies are ideal when dosimetric response studies require large numbers of independent irradiations, although previous work has shown that cuvettes may respond differently compared to large volume dosimeters²⁴⁰. An investigation comparing the quenching magnitudes of a large volume dosimeter and a series of cuvettes was made for this study. Two cylindrical dosimeters made using the proton PRESAGE® formulation (batch 0) were irradiated independently at two depths in a water phantom to fully measure the beam profile including the dose plateau, the SOBP, and the distal falloff. Cuvettes from the same batch were then irradiated using the same beam configuration and to similar depths in Solid Water® with the cuvette centers placed at the center of the beam. Dose measurements were taken at 1 cm intervals.

PRESAGE® measurements were compared with relative ionization chamber measurements to determine dose quenching. To account for the difference in measured units (change in optical density and charge, respectively), a calibration coefficient for the PRESAGE® dose signal relative to ionization chamber measurements was determined. To reduce the contribution of quenching, this calibration was taken at a depth in the plateau region nearest to the dose entrance where LET was relatively low:

$$\varepsilon_{IC}^P = \frac{M_{IC}(d_{low-LET})}{M_P(d_{low-LET})} \quad \text{Eq. 4.1}$$

where ε_{IC}^P is the PRESAGE® calibration factor, M_P is the PRESAGE® signal measured at a depth of low-LET ($d_{low-LET}$), and the ionization chamber measurements (M_{IC}) taken at the same depth. This calibration coefficient can then be applied to PRESAGE®

measurements to determine relative dose at a reference depth (d). When compared to normalized ionization chamber measurements (M_{IC}^{norm}), the percent of dose quenching ($Q\%$) can be calculated at each depth using:

$$Q\%(d) = M_{IC}^{norm}(d) - \varepsilon_{IC}^P * M_P(d) \quad \text{Eq. 4.2}$$

4.2.1.3.2 Proton study (2): Dose-quenching function

Quenching as a function of dose was investigated using cuvettes from the proton PRESAGE® formulation. Cuvettes were irradiated by protons at a depth along the beam dose profile that undergoes dose quenching. The cuvettes were irradiated to different doses and the dose signal, dose linearity, and quenching magnitude were compared to low-LET photon measurements from section 3.3 for equivalent absolute doses.

4.2.1.3.3 Proton study (3): Interbatch quenching comparison

To measure and compare dose quenching between formulations, cuvettes from each formulation were irradiated in a Solid Water® phantom (shown in Figure 4.1). Dosimeters were positioned in a polystyrene slab and placed at depths along the beam profile: one in the proximal region and three along the SOBP. The ratio of the dose responses in the plateau region to the dose response at each of the depths in the SOBP was then calculated. This ratio is known as the peak-to-plateau ratio (PPR) and changes to this value represent changes to the quenching magnitude for each formulation without the necessity of normalization to an ionization chamber and can be calculated using:

$$PPR(d) = \frac{M_P(d)}{M_P(d_{low-LET})} \quad \text{Eq. 4.3}$$



Figure 4.1: Solid Water® configuration used for irradiation of cuvettes with the F2 proton beamline. The polystyrene slab used to hold cuvettes is shown in the loading position (left) and in an irradiation position (right).

4.2.1.3.4 Proton irradiations and readout

Irradiations were performed using PSPT on the fixed beam (F2) proton beamline at the PTC-H. All studies used a 225 MeV beam energy (range of 26.9 cm in water) with a small snout configuration and using range modulation to deliver a 10 cm SOBP. For studies (1) and (3), a total dose of 200 cGy was delivered to each dosimeter. For study (2), cuvettes were irradiated at a depth of 25.5 cm to doses ranging from 25-1200 cGy. An SOBP was used rather than a pristine Bragg peak to ensure a uniform dose was delivered across the whole volume of each cuvette. An aperture was used to shape the field to 10 x 10 cm². No range compensator was applied. All dosimeters were acclimated to room temperature for approximately 4 hours prior to irradiation and special care was taken to ensure they had no exposure to UV or fluorescent light prior to or during irradiation.

Similarly to the photon studies above, the dose signals were measured approximately 1 hour prior to irradiation and 24 hours post irradiation. For the cylindrical dosimeters, the dose profiles were taken along the central axis of the dosimeters and combined to generate a single, comprehensive profile covering the depths measured by cuvette irradiations.

4.2.1.3.5 Zebra dosimetry system

The Zebra (IBA Dosimetry, Schwarzenbruck, Germany), shown in Figure 4.2, is a commercial MLIC consisting of 180 parallel-plate ionization chambers which allows for depth dose profiles along the central axis of the beamline to be measured in a single irradiation. Each chamber of the Zebra has a diameter of 2.5 cm and separation of 2 mm between chambers. The beam resolution can be increased to 1 mm with the use of an attenuating plate (which was applied for all procedures of this study). The manufacturer's recommended maximum dose range is 33 cm WET allowing it to characterize all beam energies used clinically at the PTC-H. Investigations of the system report dose accuracy, relative to water tank ionization chamber measurements, to be within 1.5% within the SOBP region, beam range within 1 mm, and reproducibility within 1%¹⁰³.

Measured data is recorded by an attached computer and interpolated by the manufacture's OmniPro-InclineTM software.



Figure 4.2: Zebra dosimetry system setup for depth dose profile measurements on the fixed beamline (F2) at the PTC-H.

4.2.2 Results and discussion

Characterization of the active components of PRESAGE® mixtures was done by segregation of the batches into subsets with only a single varying component. As such, interbatch comparisons are shown in Table 4.2 (LMG), Table 4.3 (radical initiator), and Table 4.4 (catalyzing agent) in addition to the initial OD measured for each batch (shown in Figure 4.3). Initial OD is caused by ambient activation of the leuco dye during the manufacturing and curing process. These results show that variations between radical initiator concentrations have a minimal effect on initial OD (~1%) although changing the radical initiator type from CHCl_3 to CHBr_3 did increase this value by 11% for equivalent concentrations (% w/w). LMG concentration was also found to affect initial OD (10.3% OD per LMG (% w/w)). Changes to the concentration of DBTDL resulted in the largest variation in OD over the full range of data points ($\geq 600\%$ OD per DBTDL (% w/w)). This was a nonlinear relationship as the changes in dose signal were 2.5% and 73.2% when increasing DBTDL concentrations from 0 to 0.05% and 0.05% to 0.1%, respectively. Increasing DBTDL concentration to 1% resulted in substantial activation of

the leuco dye in the dosimeter that effected many dosimetric characteristics of the cuvettes as is discussed in the next few sections. The early activation of the leuco dye at DBTDL concentrations greater than 0.05% is likely a result of the excess heat generated by the exothermic reaction of the catalyst and polyurethane resins.

The photon irradiation results of the proton PRESAGE® formulation (batch 0) from the study in section 3.3 are included for comparison. Proton irradiation measurements of this formulation were novel for this chapter.

Table 4.2: PRESAGE® batches used for comparing the concentration of LMG on dosimetric properties. Compositions are shown as percent by weight for each active component.

Batch	LMG (%)	Radical Initiator Type	%	DBTDL (%)	Initial OD
4	0.5	CHCl ₃	3.0	0.05	0.041
5	1.0	CHCl ₃	3.0	0.05	0.042
6	2.0	CHCl ₃	3.0	0.05	0.046

Table 4.3 PRESAGE® batches used for comparing the type and concentration of the radical initiator on dosimetric properties. Compositions are shown as percent by weight for each active component.

Batch	LMG (%)	Radical Initiator Type	%	DBTDL (%)	Initial OD
1	0.5	CHBr ₃	1.0	0.05	0.044
2	0.5	CHBr ₃	3.0	0.05	0.045
3	0.5	CHCl ₃	1.0	0.05	0.040
4	0.5	CHCl ₃	3.0	0.05	0.041

Table 4.4: PRESAGE® batches used for comparing the concentration of the polyurethane catalyzing agent DBTDL on dosimetric properties. Compositions are shown as percent by weight for each active component.

Batch	LMG (%)	Radical Initiator Type	%	DBTDL (%)	Initial OD
7	0.5	CHCl ₃	3.0	0.00	0.040
4	0.5	CHCl ₃	3.0	0.05	0.041
8	0.5	CHCl ₃	3.0	0.10	0.071
9	0.5	CHCl ₃	3.0	1.00	0.388

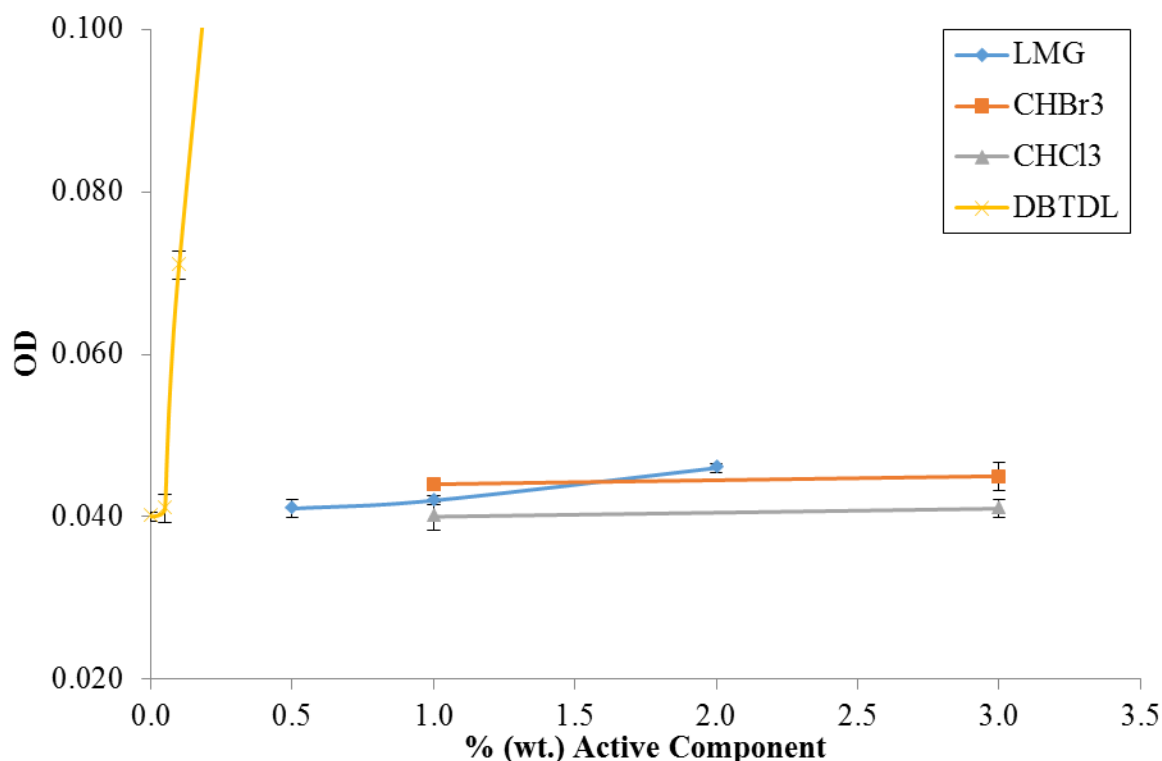


Figure 4.3: Initial OD for each batch of PRESAGE® represented as a function of changes to specific active components. The data point for 1% DBTDL ($\Delta OD \approx 0.4$) is not shown on this scale. Error bars represent the standard deviation among three batches for each formulation.

4.2.2.1 Dose response sensitivity

The change in OD as a function of low-LET dose was measured for each formulation. The complete results are available in Appendix 2 (pg. 154). All formulations, except batch 9, showed a linear dose response with different slopes. Interbatch comparisons of formulations with variable LMG concentration (shown in Figure 4.4) found dose sensitivity, referred to as slope in the figure, increased by approximately $142.1\% \pm 8.3\%$ ($10^{-5} \Delta OD \text{ cGy}^{-1} \text{ LMG}(\% \text{ w/w})^{-1}$). Comparisons between

radical initiator (shown in Figure 4.5) found that substituting chloroform in place of bromoform resulted in reduced dose response for equivalent concentrations (% w/w).

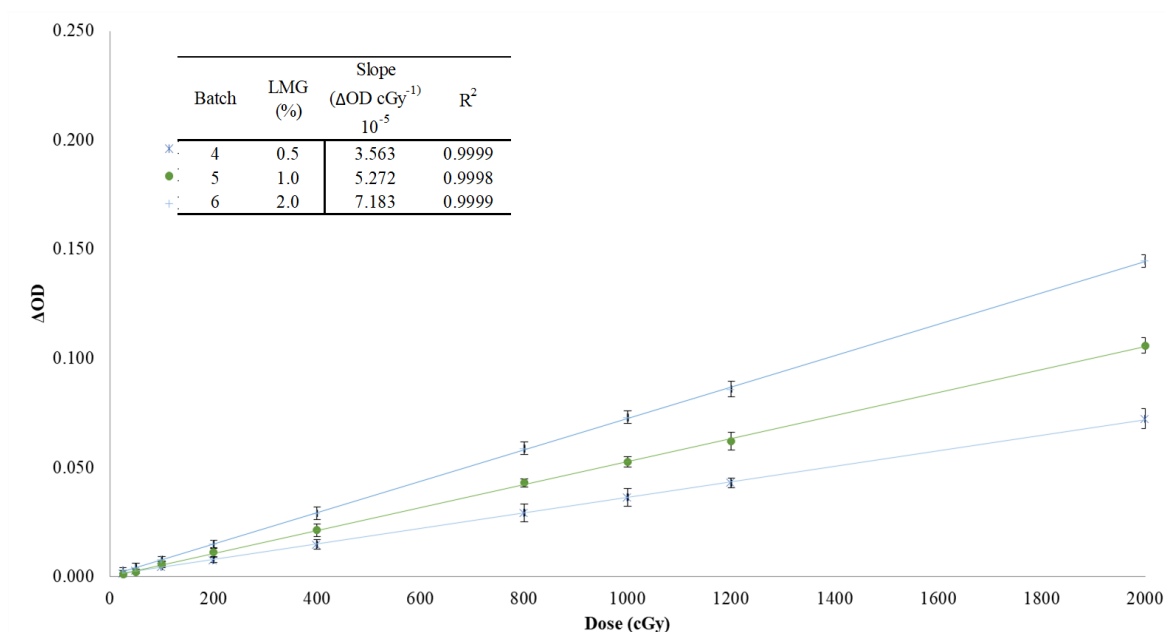


Figure 4.4: ΔOD as a function of absorbed dose as measured by PRESAGE® batches with variable LMG concentrations. The linear trends are represented by solid lines and error bars represent the standard deviations of readings from all cuvettes at each dose point.

The relationship between radical initiator concentration and dose sensitivity was less than what was found for LMG. The dose sensitivity increased by approximately $110.7\% \pm 3.2\%$ ($10^{-5} \Delta OD \text{ cGy}^{-1} \text{ CHBr}_3(\% \text{ w/w})^{-1}$) and $96.8\% \pm 2.1\%$ ($10^{-5} \Delta OD \text{ cGy}^{-1} \text{ CHCl}_3(\% \text{ w/w})^{-1}$) for bromoform and chloroform formulations, respectively.

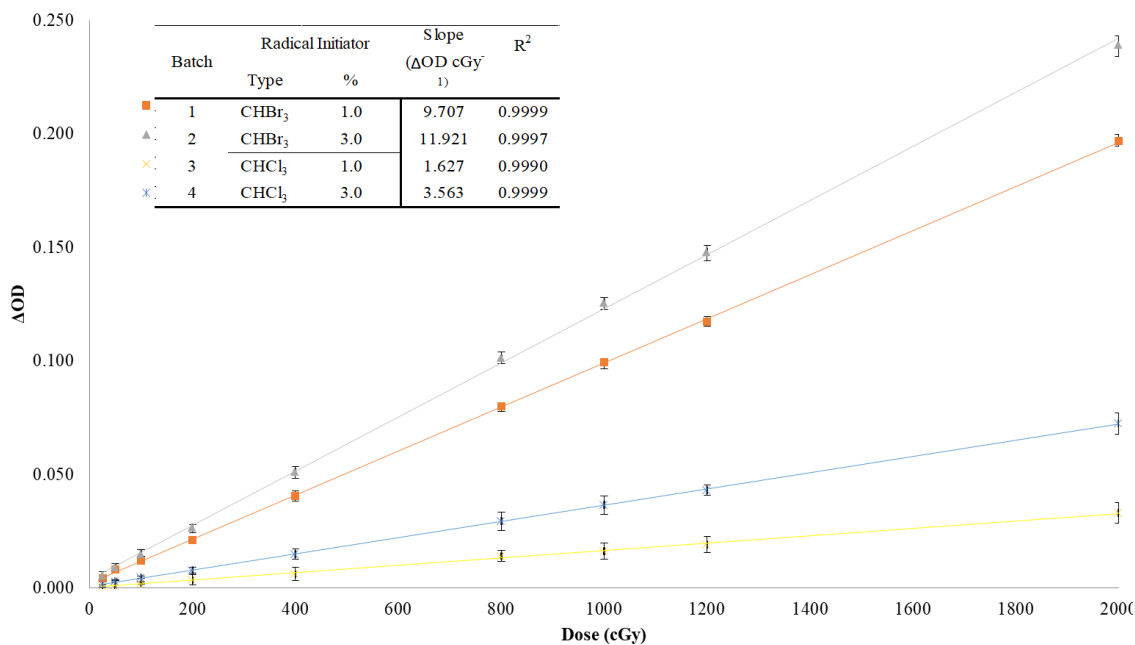


Figure 4.5: ΔOD as a function of absorbed dose measured by PRESAGE® batches with variable radical initiator type and concentration. The linear trends are represented by solid lines and error bars represent the standard deviations of readings from all cuvettes at each dose point.

The results of changes to the concentration of the catalyst agent, DBTDL, are shown in Figure 4.6. Dose sensitivity was found to be very susceptible to changes in these concentrations, with inconsistent trends. A comparison between dosimeters with 0% and 0.05% concentrations of DBTDL measured a change in dose sensitivity of $207.2\% \pm 12.3\%$ ($10^{-5} \Delta OD \text{ cGy}^{-1} \text{ DBTDL}(\% \text{ w/w})^{-1}$), but further increasing the concentration of catalyst to 0.1% resulted in reduced dose sensitivity to $-211.7\% \pm 27.5\%$ ($10^{-5} \Delta OD \text{ cGy}^{-1} \text{ DBTDL}(\% \text{ w/w})^{-1}$). While these values signify very high sensitivity to catalyst concentration, the absolute difference in dose response at with 2000 cGy was less than 4%. These results show that large increases in catalyst

concentrations beyond 0.05% would result in a dosimeter with reduced dose response. This is demonstrated by the results of batch 9 in which the dosimeter showed no change in OD with dose.

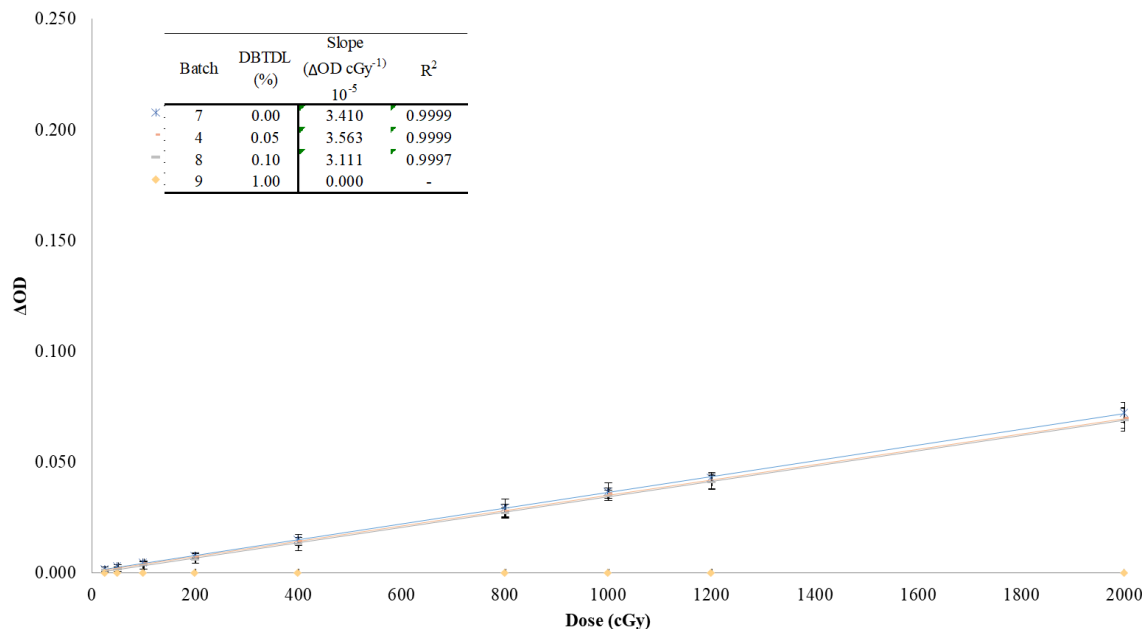


Figure 4.6: ΔOD as a function of absorbed dose as measured by PRESAGE® batches with variable DBTDL concentration. Batch 9 is covered by the x-axis. The linear trends are represented by solid lines and error bars represent the standard deviations of readings from all cuvettes at each dose point.

4.2.2.2 Temporal stability

The results of cuvettes from each formulation monitored over a five day period are shown in Table 4.5 and plotted in Figure 4.7. Similar to the results of the proton PRESAGE® measured in [Chapter 3] (and included here as batch 0), the findings show

the greatest change in signal occurring between 1 and 4 hours for all formulations. Formulations 5 and 6, which had increased LMG concentration, were found to have the highest reduction during this time period with -7.5% and -4.1% , respectively. Similarly, signal reduction was minimized between 24 and 48 hours with changes less than 1% for all formulations except 5 and 6 which were 1.9% and 2.0%, respectively. These results demonstrated that although dose signal stability was a function of leuco dye concentration, practical readout procedures including a 24 hour hold should be continued for all formulations.

Table 4.5: Changes to OD following irradiation for each formulation.

Batch	Time (hrs)			
	1 to 4	4 to 12	12 to 24	24 to 120
0	-2.4%	-1.3%	0.0%	-1.1%
1	-2.5%	-1.3%	-0.1%	0.0%
2	-2.3%	-1.2%	-0.1%	-0.5%
3	-2.2%	-2.3%	0.0%	-0.9%
4	-1.6%	-1.9%	0.0%	-0.9%
5	-4.1%	-1.3%	-0.1%	-0.7%
6	-7.5%	-4.2%	-2.0%	-1.4%
7	-1.2%	-0.9%	-1.9%	-2.0%
8	-3.8%	-2.0%	-0.2%	-0.7%
9	0.3%	0.5%	-0.8%	0.5%

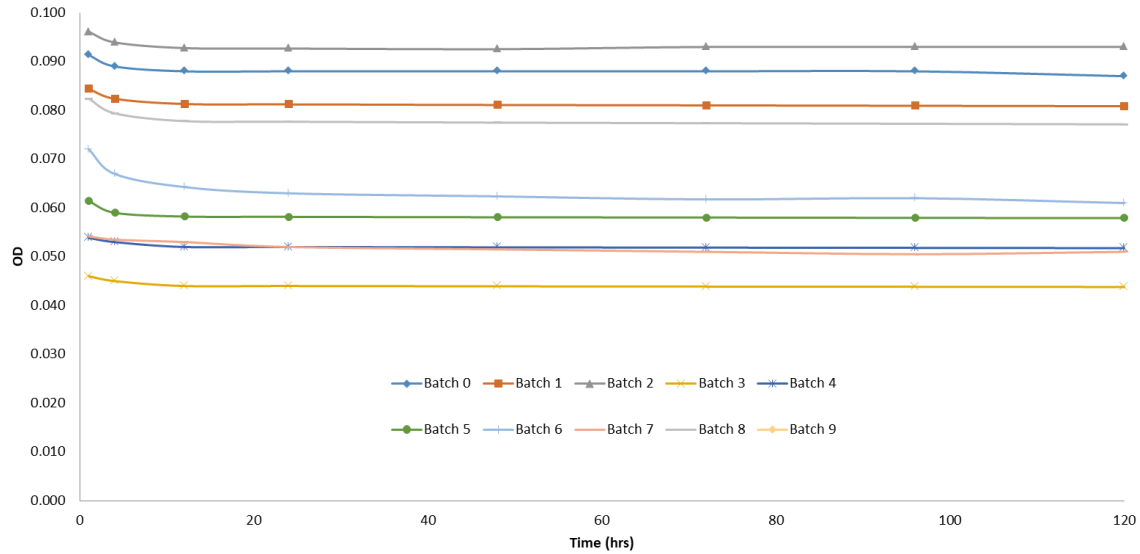


Figure 4.7: Change in dose signal over time for PRESAGE® cuvettes containing each formulation irradiated to 400 cGy. Lines between time points added to aid the eye.

4.2.2.3 Proton quenching studies

4.2.2.3.1 Proton study (1): Quenching comparison between cuvettes and large volumes

Relative dose as a function of depth measured for a 225-MeV proton beam using the Zebra dosimetry system as well as in the large volumes and cuvettes of the proton PRESAGE® formulation are shown in Figure 4.8. Both the cuvette and volumetric dosimeters were normalized to the dose reading at the most proximal depth (10 cm). The volumetric PRESAGE® dosimeters each captured an 8 cm length of the beam dose profile with 2 cm overlap. Together, a more comprehensive dose profile was constructed.

The principal finding of this study was that the cuvette system was able to accurately model the quenching observed in the volumetric PRESAGE® dosimeters. Quenching in the large volume dosimeter was similar to that reported from other studies

using a similar formulation^{15,265,272}. Maximum quenching was measured at 26.5% at a depth of 1 cm proximal to the distal falloff. Agreement between both PRESAGE® dosimetry systems is included in the plot below. The relative dose measured by the PRESAGE® agreed with MLIC measurements to within 98% for dose depths in the proximal 3 cm of the SOBP. The quenching magnitude in both systems increased to greater than 5% at the center of the SOBP (at a depth of 23 cm). Towards the distal falloff region (at a depth of 27 cm), the relative dose discrepancy between the cuvette and volumetric dosimeters increased to 71.7%. This can, in part, be attributed to volume averaging effects over the width of the cuvettes and signifies a region of the beam profile not suitable for cuvette dosimetry. The maximum depth found in which the two PRESAGE® systems showed agreement within 5% was 26 cm.

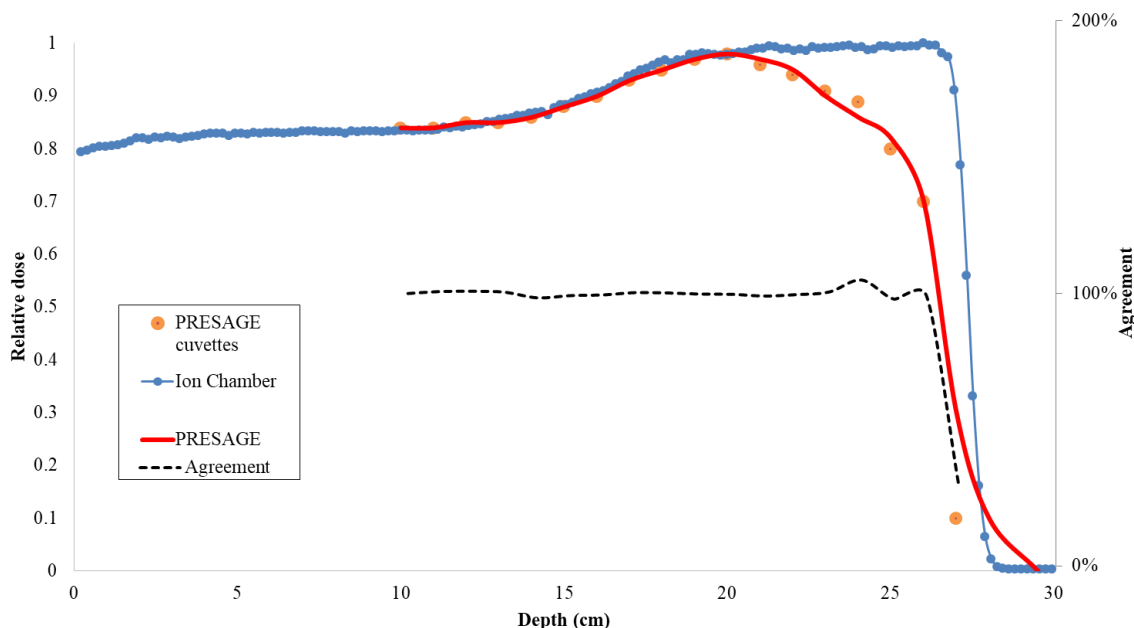


Figure 4.8: Relative depth dose comparison in a 225-MeV proton beam with 10 cm SOBP as measured by Multi-layer Ion Chamber (blue), large volume proton PRESAGE® (red), and cuvettes of proton PRESAGE® (orange points). The agreement between large volume and cuvette measurements is shown (black line).

4.2.2.3.2 Proton study (2): Dose-quenching function

The corresponding values of dose response for the proton PRESAGE® formulation cuvettes when irradiated with both low-LET photons and high-LET protons are shown in Figure 4.9. The low dose measurements (25 cGy) measured quenching at 50% which was well above all other dose points. Average quenching excluding the 25 cGy dose point was $22.7\% \pm 4.0\%$. The lower relative signal change at the 25 cGy point likely resulted in rounding errors within the readout equipment, possibly contributing to the apparently much larger quenching. Dose response linearity was observed across all dose points excluding the 25 cGy dose point with $R^2=0.999$. The result of this study

showed that although quenching as a function of dose was negligible for a single formulation, low dose measurements are susceptible to error.

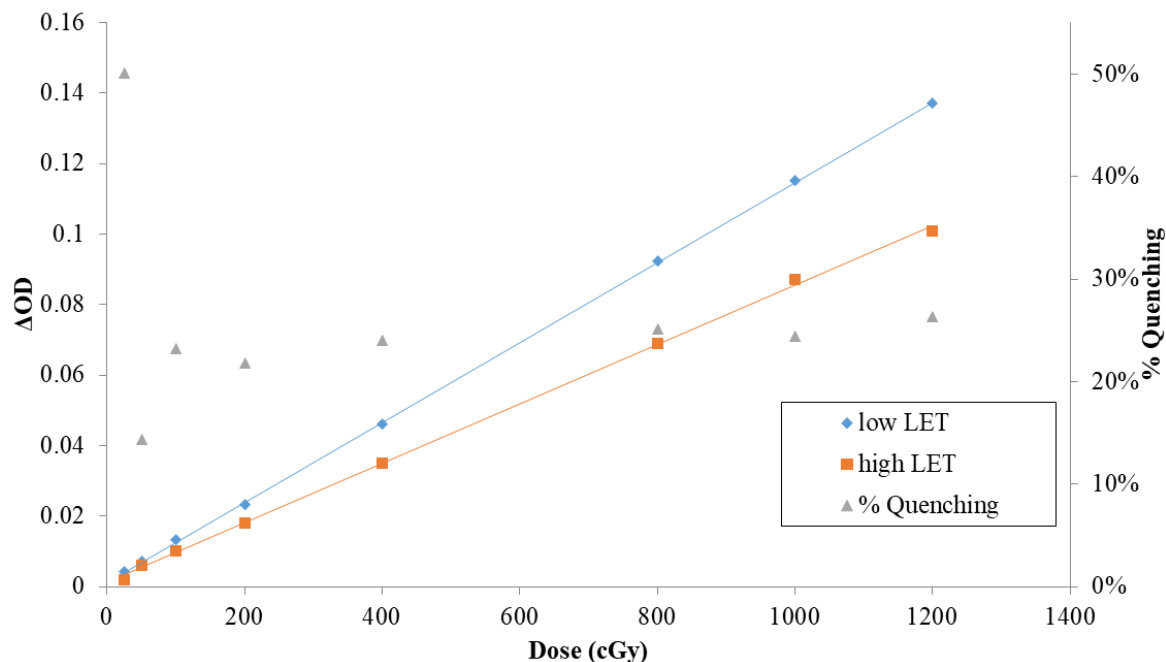


Figure 4.9: Dose responses for proton PRESAGE® when irradiated with photons and protons and calculated quenching. The linear trends are represented by solid lines.

4.2.2.3.3 Proton study (3): Interbatch quenching comparison

Based on the previous results, formulation quenching comparisons were made using cuvettes irradiated at three points along the SOBP. A low quenching (LQ) point was taken at a point approximately 2.5 cm into the SOBP (beam depth of 19.5 cm) which previously showed 98% relative dose agreement with ionization chamber measurements. A mid quenching (MQ) point was taken at approximately 5.5 cm into the SOBP (beam depth of 22.5 cm), and a high quenching (HQ) point was taken 8.5 cm into the SOBP

(beam depth of 25.5 cm). Relative dose response for each batch was normalized to measurements taken in the plateau region (at 10.5 cm depth). The complete results are available in Appendix 3 (pg. 155).

A peak-to-plateau ratio was calculated for cuvettes irradiated to each quenching point and quantified as a function of each active component (shown in Figure 4.10). A change in this ratio was found as a result of changes to LMG and radical initiator for all dose points with the largest change observed at the HQ depth. Increasing LMG concentration from 0.5% to 1.0% resulted in an increase in the peak-to-plateau ratio by $7.2\pm0.69\%$, while further increasing this concentration to 2.0% reduced the ratio by $11.5\pm1.36\%$. Similarly, changes to the concentration of radical initiator increased this ratio by $22.5\pm1.23\%$ and $13.3\pm1.02\%$ for bromoform and chloroform, respectively. These results indicated that leuco dye and radical initiator concentrations contributed to the magnitude of dose quenching in PRESAGE®. The limited number of formulations was sufficient to show the relationship was non-linear.

In contrast, the concentration of polyurethane catalyst did not show any influence on quenching. No change in the peak-to-plateau ratio was observed beyond the standard deviation as a result of DBTDL concentration.

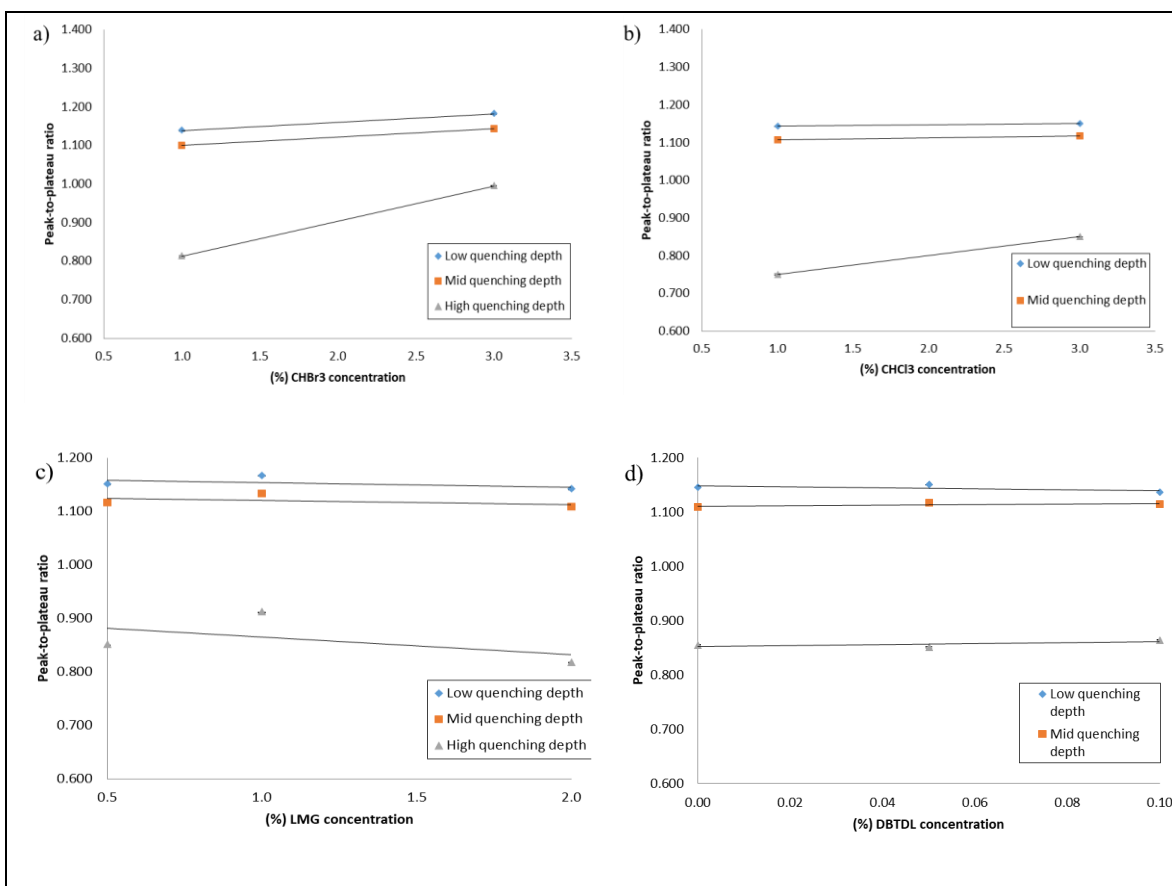


Figure 4.10: The peak-to-plateau ratios for several depths at which low, medium, and high quenching was observed. Ratios are a function of formulation active components: (a) CHBr₃, (b) CHCl₃, (c) LMG, and (d) DBTDL.

4.3 Reduced quenching formula optimization

The results of the previous studies found individual changes to LMG and radical initiator concentrations resulted in changes to the quenching magnitude. The next stage of this investigation was an iterative optimization of the PRESAGE® formulation to find the limits of quenching reduction through chemical manipulation. This formulation was then characterized for future proton dosimetry applications.

4.3.1 Materials and methods

PRESAGE® dosimeters were manufactured using the same procedure as section 4.2.1. Proton irradiations followed the Solid Water® phantom setup outlined in section 4.2.1.2.1. Four cuvettes were irradiated along the beam profile: one in the dose plateau and three along the SOBP. Three sets of cuvette measurements were made from each formulation batch. The cuvettes were used as relative dose measurements which were normalized to the dose point taken in the plateau region. Quenching was quantified relative to MLIC measurements for each dose point.

Initial formulation optimization used fixed increments of LMG and different concentrations of radical initiator. The radical initiator concentration was adjusted until a local quenching minimum was measured for each fixed concentration of LMG. Concentrations of each component were limited by the structural stability of polyurethane which, according to the manufacturer, should not fall below 70% (w/w) before curing problems arise. Multiple batches were produced for each irradiation and changes to the quenching magnitude of each formulation factored into the iterative analysis. This method was used for formulations using bromoform as well as chloroform radical initiators.

Finally, the radiological and physical properties of the reduced quenching dosimeters were characterized. A series of studies was used to determine a single, optimal formulation for further studies based on temporal and temperature stability, dose response linearity, and CT-RLSP relationship. Temporal and temperature stability were measured concurrently for irradiated and unirradiated dosimeters to measure the change in optical density. Measurements of unirradiated dosimeters were made following

depressurization after manufacture while signal fading was measured following irradiation of dosimeters to 2 Gy using low-LET photons and dosimeters were stored in both cold ($\leq 3^{\circ}\text{C}$) and warm ($\sim 21^{\circ}\text{C}$) temperatures. Dosimetric linearity was measured similarly to the methods described in Section 3.2.3 in which cuvettes were irradiated from 0.25-12 Gy using both low-LET photons and in the high-LET region Bragg peak region of a proton beam. The CT-RLSP relationship was used to determine whether a formulation would match the CT calibration curve used in proton treatment planning systems and was measured using a method described by Moyers et al. (2010)²⁸³. This method computed the RLSP of a dosimetric material by measuring the relative change in the depth of the distal 80% dose point with and without the dosimeters in the beamline and normalizing this change by the thickness of the dosimeters.

4.3.2 Results and discussion

Initial optimization studies found large variations in quenching and dose response as a result of varying concentrations of the LMG and radical initiator components. The radical initiator type affected the dosimetric properties sufficiently that optimization paths using each type were performed independently. A total of 108 formulations were investigated.



Figure 4.11: Photographs of two sample sets of cuvettes created for formulation optimization illustrating the visual dose response difference between formulations made using chloroform (left) and bromoform (right).

4.3.2.1 Quenching reduction formula optimization

All formulations showed varying magnitudes of quenching to dose points across the SOBP with the highest quenching observed at the distal-most point. Quenching was calculated relative to ionization chamber measurements using Eq. 4.2. Interbatch quenching comparisons were made at the distal-most point and are shown in Figure 4.12. The results of all measurements are shown in Appendix 4 (Bromoform-based) and Appendix 5 (Chloroform-based).

Quenching was found to be a function of both the LMG and radical initiator components across the full spectrum of concentrations, although the changes in quenching were non-linear with equivalent changes to LMG and radical initiator concentrations. Low dose-sensitivity (less than $0.01 \Delta\text{OD cm}^{-1} \text{ Gy}^{-1}$) formulations were generally found from concentrations of $\text{LMG} \leq 1\%$ and using a chloroform radical initiator. This contributed to much larger dose response variances as shown in the

figures. Dose sensitivity was found to be a function of both active components, although very high concentrations of radical initiator ultimately resulted in reduced dose signal. This was a function of LMG concentration as well as radical initiator type, but was generally observed when the ratio of RI:LMG (% w/w) surpassed 6:1 for chloroform and 12:1 for bromoform. This difference can, in part, be attributed to bromoform having nearly double the mass density of chloroform and therefore making the dose sensitivity a uniform function of radical initiator volume.

The magnitude of quenching ranged from as high as $72.33\% \pm 14.66\%$ and $76.26\% \pm 7.85\%$ to as low as $3.18\% \pm 1.76\%$ and $2.88\% \pm 3.52\%$ for chloroform and bromoform dosimeters respectively. The highest quenching magnitudes were observed at low and high concentrations of radical initiator for each LMG concentration resulting in a parabolic quenching response curve across the RI concentration spectrum with the highest quenching occurring at high RI concentrations. Quenching as a function of LMG concentration followed a similar trend, although the highest quenching was found in batches with lower concentrations of LMG. The lowest measured quenching for each LMG concentration is shown in Figure 4.13.

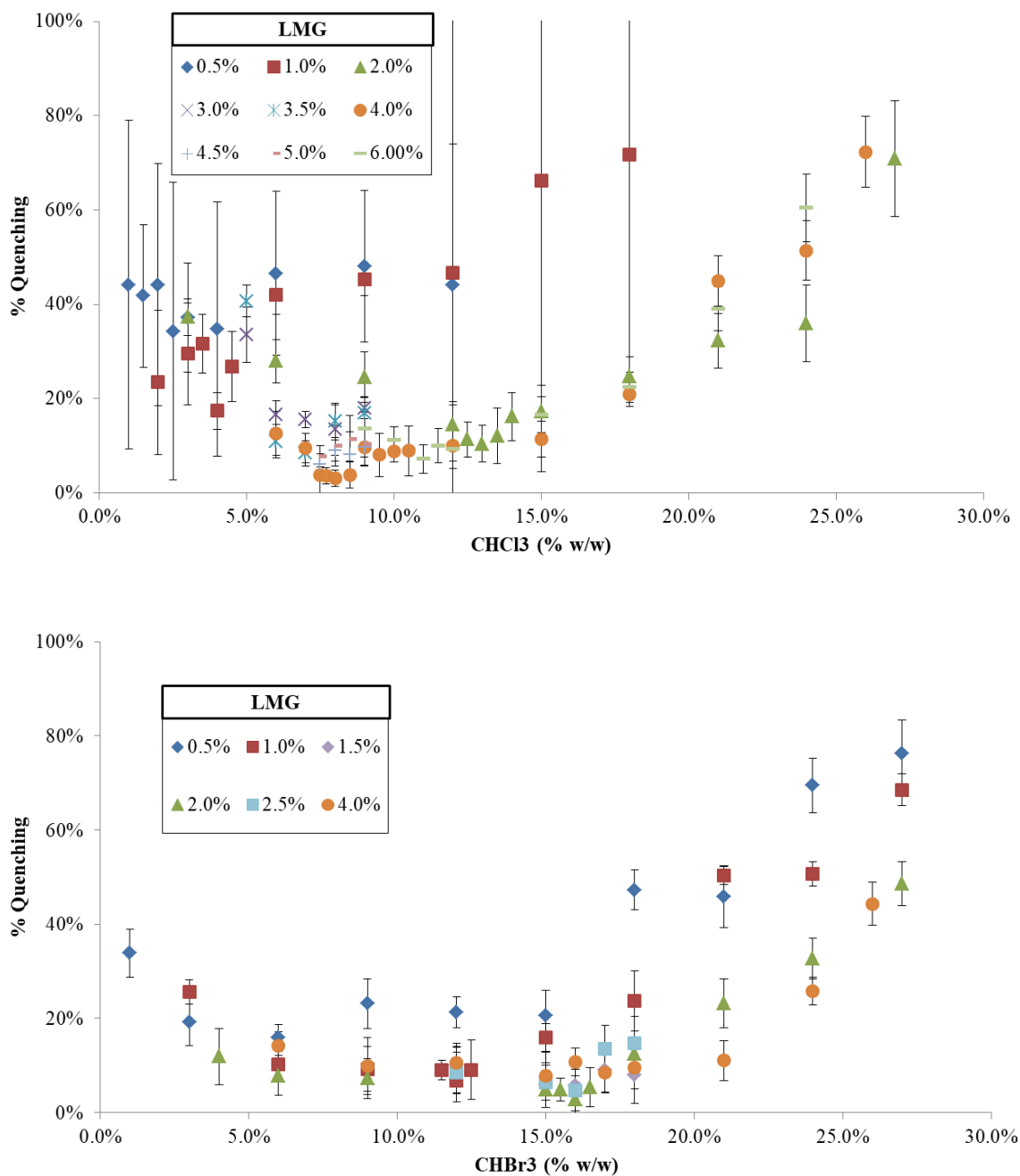


Figure 4.12: The percent of signal quenching measured at the distal-most point in the SOBP for each formulation using chloroform (top) and bromoform (bottom) as the radical initiator. Error bars represent the standard deviation between three intrabatch cuvette comparisons.

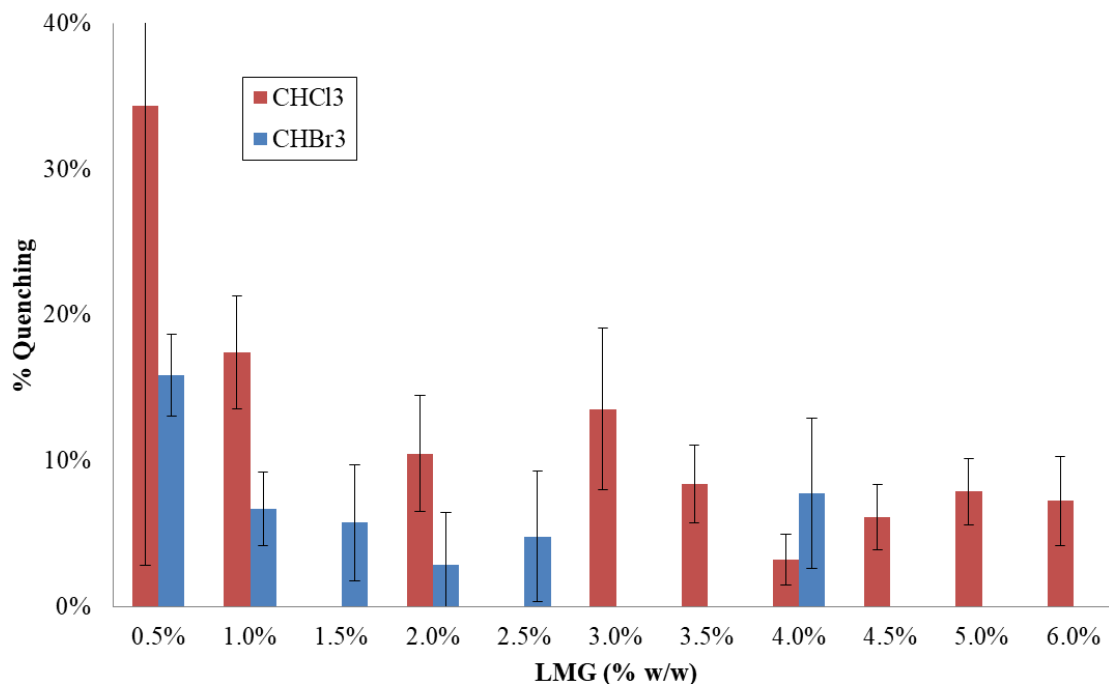


Figure 4.13: Minimum percent of signal quenching for PRESAGE® formulations across all concentrations of radical initiator and for each concentration of LMG. Error bars represent the standard deviation among three intrabatch cuvette comparisons.

Previous studies (see section 2.9) have hypothesized that the quenching found in PRESAGE® and other chemical dosimeters is likely a result of either saturation or free radical recombination. From the results of this study, formulations using low concentrations of either active component were found to show increased signal quenching. This can likely be attributed to saturation of these components in the high-LET region surrounding slow proton tracks. The effect was reduced by increasing the concentration of these components. Similarly, high concentrations of radical initiator relative to LMG resulting in reduced dose sensitivity and increased signal quenching can be attributed to free radical recombination.

4.3.2.2 Low-quenching formulation characterization

Formulations with the lowest measured quenching from each radical initiator type were found from the results of the previous section and were given the names LQCl (low-quenching chloroform-based) and LQBr (low-quenching bromoform-based). The compositions are shown in Table 4.6.

Table 4.6: Chemical composition of low-quenching PRESAGE® formulations. Percentages are listed by weight.

	LQCl	LQBr
Poly-A	46.32%	43.16%
Poly-B	41.68%	38.84%
RI	8.00%	16.00%
LMG	4.00%	2.00%
DBTDL	<< 1%	

4.3.2.2.1 Temporal and temperature studies

Temporal studies over a range of 1 hour to 9 days were made for dosimeters stored under cold ($\leq 3^{\circ}\text{C}$) and warm ($\sim 21^{\circ}\text{C}$) conditions for irradiated and unirradiated dosimeters. The results of the unirradiated dosimeters (shown in Figure 4.14) show an increase in OD over time for all dosimeters. LQCl dosimeters stored in cold conditions had less change ($1.48 \pm 0.58 \times 10^{-4} \Delta\text{OD day}^{-1}$) than LQBr dosimeters ($5.33 \pm 0.58 \times 10^{-4} \Delta\text{OD day}^{-1}$) over the full 9 days. Dosimeters stored under warm conditions were found to have increased OD change relative to their cold stored counterparts ($5.93 \pm 0.58 \times 10^{-4} \Delta\text{OD day}^{-1}$ and $13.33 \pm 1.00 \times 10^{-4} \Delta\text{OD day}^{-1}$, respectively). LQCl dosimeters showed very little change beyond 4 days whereas LQBr dosimeters continued to show change. The results of the irradiated dosimeters (shown in Figure 4.15) were normalized to

measurements at 24 hours. Similar to the unirradiated dosimeters, those stored under cold conditions were observed to undergo less change compared to dosimeters stored in warm conditions. Within the first 24 hours, LQCl dosimeters in cold storage saw signal fading of $12.0\% \pm 2.39\%$ while LQBr dosimeters decreased by $18.4\% \pm 3.09\%$. Dosimeters stored under warm conditions increased by $24.9\% \pm 4.02\%$ and $34.6\% \pm 5.65\%$ for both types, respectively. When stored in the cold, both dosimeter types reached a point of signal stability from 12 to 36 hours where dose signal changed by less than 5%, although this region of stability was not observed for dosimeters stored in warm conditions. These results demonstrate that both dosimeter types could be applied to long term and remote auditing studies, although care must be taken to ensure refrigeration prior to, and following, irradiations.

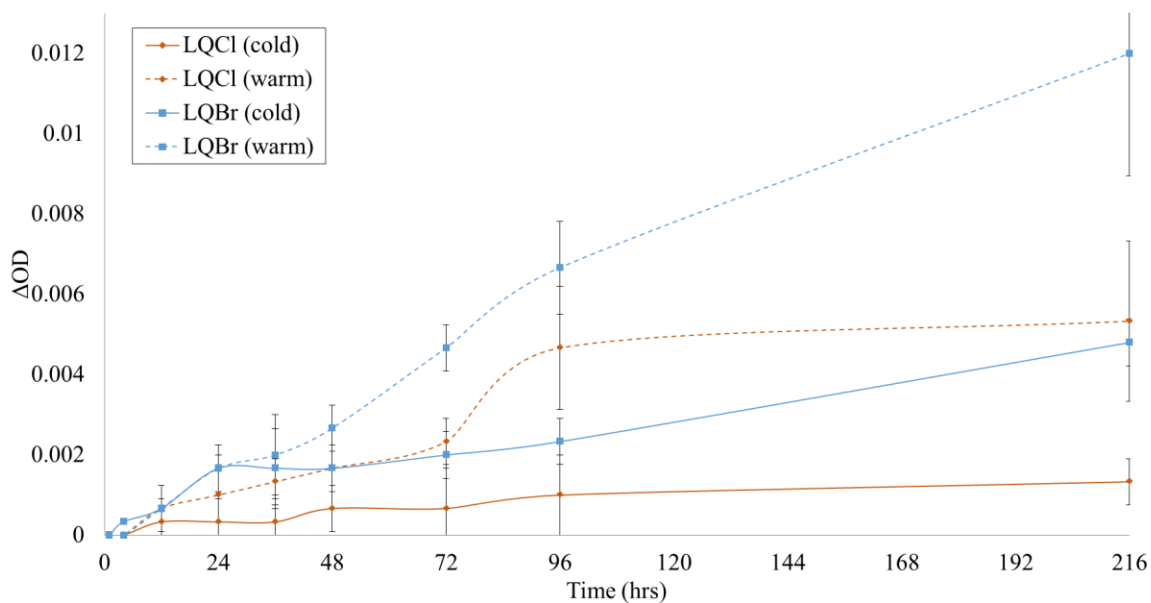


Figure 4.14: Comparison of the ΔOD of unirradiated, low-quenching chloroform and bromoform formulations of PRESAGE® when stored in cold ($\leq 3^{\circ}\text{C}$) and warm ($\sim 21^{\circ}\text{C}$) conditions. Error bars represent the standard deviation among intrabatch cuvette comparisons and connecting lines added to aid the eye.

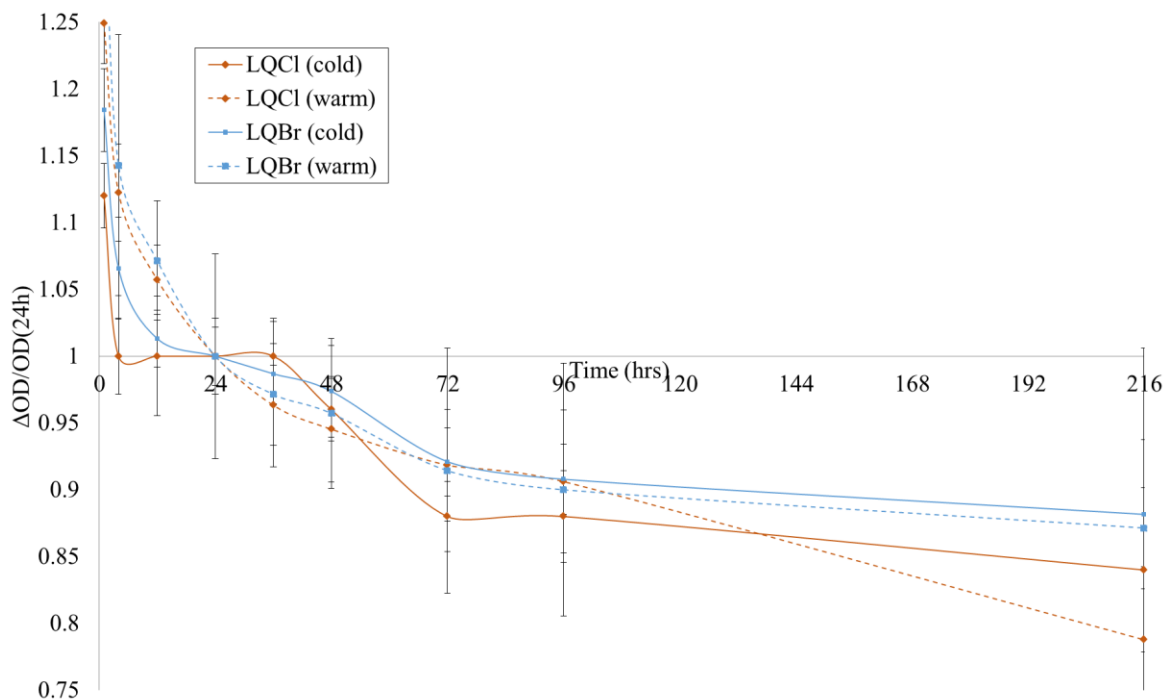


Figure 4.15: Temporal stability comparison between low-quenching chloroform and bromoform formulations of PRESAGE® when stored in cold ($\leq 3^{\circ}\text{C}$) and warm (room temperature) conditions after being irradiated to 200 cGy. Dose signal was normalized to readings taken at 24 hours. Error bars represent the standard deviation among intrabatch cuvette comparisons and connecting lines added to aid the eye.

4.3.2.2.2 Dose response linearity

Dosimeters from each low-quenching formulation were irradiated to varying doses using both low-LET photons and high-LET protons with the results plotted in Figure 4.16. Dose quenching was measured as the difference in signal responses between the cuvettes irradiated by each beam type for each dose level. The LQCl formulation showed dose linearity above 0.25 Gy, but lower sensitivity of the dosimeters resulted in dose signal averaging occurring in the readout equipment at low dose (≤ 0.25 Gy) points.

This was observed with both photon and proton irradiations. Average quenching for dose points above 0.25 Gy was $4.23\% \pm 1.63\%$. The LQBr formulation demonstrated greater linearity at lower doses, but the dosimeter dose response began to plateau above 10 Gy. This was observed in both photon and proton irradiations and was likely caused by dose saturation due to higher dose response sensitivity. Average quenching for dose points up to 8 Gy was $4.44\% \pm 1.20\%$. From these results, the LQCl formulation would be more applicable for higher dose measurements and may require a minimum dose threshold for relative dose response comparisons while the LQBr formulation would be more applicable for low dose studies and would require a linearity calibration correction applied when used for high studies.

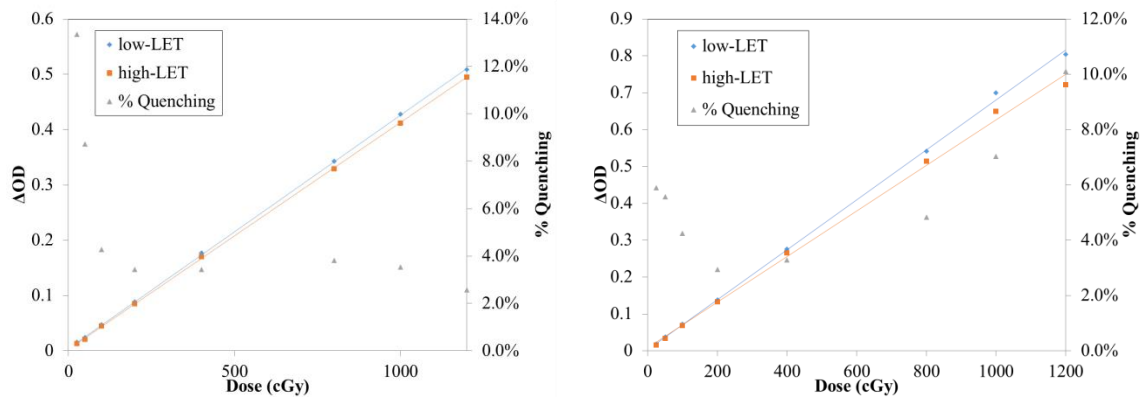


Figure 4.16: Dose responses for LQCl (left) and LQBr (right) PRESAGE® when irradiated by low-LET photons and high-LET protons and calculated quenching. Linear trends shown by solid lines.

4.3.2.2.3 CT-RLSP relationship

The methodology described by Moyers et al. (2010)²⁸³ was used to compute the RLSP of each dosimeter formulation which was measured using the Zebra dosimetry system and the results are shown in Figure 4.17. The measured RLSPs for the LQCl and LQBr formulations were 1.086 ± 0.003 and 1.130 ± 0.002 , respectively. The CT numbers for the dosimeters were 160 ± 1.2 and 1272 ± 4.5 for LQCl and LQBr, respectively. The calibration curve used by Eclipse TPS (Varian Medical Systems, Palo Alto, CA, USA), and made available by Grant et al. (2014)¹²⁶, is also shown in the figure below. The LQCl formulation matched the assigned RLSP by the TPS within $0.66\% \pm 0.31\%$ while the LQBr formulation matched within $36.21\% \pm 0.807\%$. As a result, the LQCl formulation could be used directly with the assigned TPS stopping power values while the LQBr formulation would generally require a manual correction to this value.

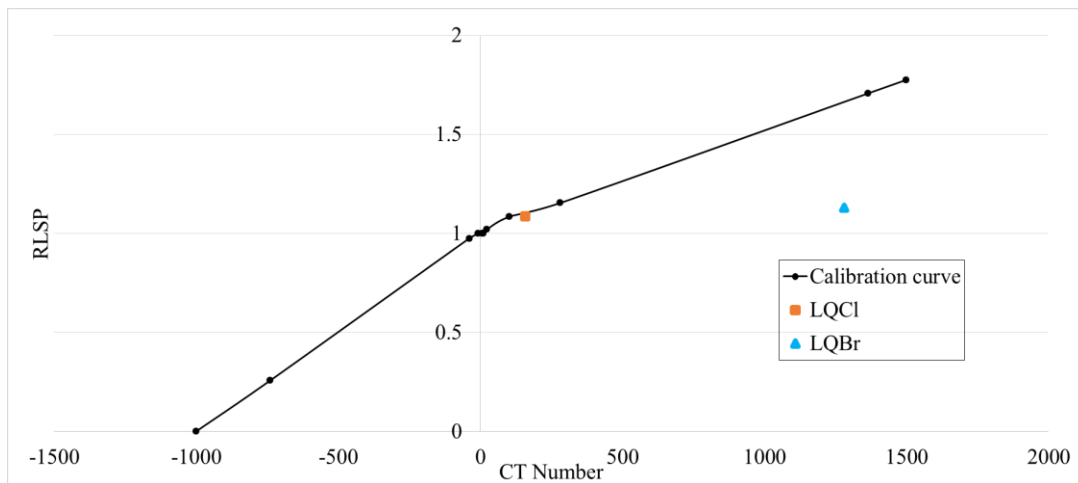


Figure 4.17: RLSP values of the LQCl and LQBr PRESAGE® formulations plotted alongside the calibration curve used in the Eclipse® TPS.

4.4 Conclusions

The chemical composition of PRESAGE® was shown to affect the dosimetric properties of the dosimeters, although to varying magnitudes. Dose sensitivity and dose response linearity were both found to be a function of LMG and radical initiator concentrations, whereas concentrations of the catalyzing agent DBDTL were found to limit the dose range when concentrations were increased.

Investigations into dose quenching in a large volume PRESAGE® irradiated by a high-LET proton beam were shown to be reproducible in cuvette studies. This allowed further studies to measure interbatch quenching as a function of LMG and radical initiator concentration across a large range of formulaic compositions. From the results of this study, formulations using low concentrations of either active component were found to show increased signal quenching. Similarly, high concentrations of radical initiator relative to LMG resulted in reduced dose sensitivity and increased signal quenching. These investigations showed that quenching is locally minimized with specific dose sensitivities and ratios of LMG and RI as well as dose sensitivity. Through formulaic alteration, quenching can be reduced to as low as ~3%.

Dosimeters with the lowest quenching were compared across specific parameters useful for clinical, research, and remote dosimetry. Because of discrepancies in dose linearity, temporal stability, and CT-RLSP relationships, the LQBr formulation was found to be less practical for the needs of this study, and therefore the LQCl formulation was used going forward.

Chapter 5: Development of a semi-empirical correction model for dose quenching

5.1 Rationale

Quenching in PRESAGE® has been shown to have some high-LET dependence which can be reduced through formulaic manipulation. As demonstrated in the previous chapter, low-quenching formulations were not able to completely eliminate under-response and as a result the measured dose distributions still disagree with ionization chamber and treatment planning predicted dose values. The observation of signal quenching in a proton beam is not unique to PRESAGE®^{257,284} or even 3D dosimetry^{108,264}, and the solution to quenching reduction has been through the use of an appropriate calibration correction. The implementation of a semi-empirical correction model for PRESAGE® in which experimentally measured dose responses have been correlated with calculated LET has been discussed^{15,243,269,285,286} but has yet to be comprehensively studied. The calculation of LET using Monte Carlo has been implemented in previous studies and demonstrated to have a high degree of accuracy in complex volumes^{76,287–289}.

The goal of this aim was to develop and apply a quenching correction factor to PRESAGE® as a way to reduce dose inaccuracies caused by quenching. This correction factor, being a function of LET, can be calculated for any beam. To study this, the quenching coefficient was measured and correlated with LET values calculated using Monte Carlo methods. An LET based quenching correction method would then be applicable to any additional irradiation configurations as long as the LET in the volume could be modeled and the dosimeters maintain a consistent dose response. After calculating the function, it was verified using several additional beam configurations.

The accuracy of the quenching-corrected dose distribution was used to verify the central hypothesis of this study testing agreement with ionization chamber measurements to within 3% and to calculated dose predictions using 5%/5mm 3D gamma criteria.

5.2 Materials and methods

5.2.1 Experimental measurements of depth-dose curves

The LQCI PRESAGE® formulation, described in section 4.3, was used for this study. To improve dose resolution, especially in volumes with high dose gradients such as in the Bragg peak, volumetric dosimeters were used rather than cuvettes here. These dosimeters were cylindrically cast with dimensions $8 \times 6.5 \text{ cm}^3$ (height \times diameter). Manufacturing and handling procedures were as described in section 3.2.1. All irradiations were made on the G1 PSPT beamline at the PTC-H using incident beam energies of 140 and 180 MeV. A field size of $4 \times 4 \text{ cm}^2$ was used to accommodate dosimeter dimensions.

The quenching correction factor was calibrated based on measurements of an unmodulated 140 MeV proton irradiation delivering 4 Gy to the Bragg peak. Additional dosimeters were then irradiated to measure the accuracy of this correction factor under differing irradiation variables. The first (Dosimeter A) was a reproducibility study in which a dosimeter was irradiated to the same conditions as that used for the quenching factor calibration. The second (Dosimeter B) irradiation followed the same setup but with a prescribed dose of 1 Gy to the Bragg peak. A third (Dosimeter C) was irradiated to 4 Gy with an incident proton energy of 180 MeV, and the final dosimeter (Dosimeter D) irradiated using a modulated 140 MeV beam to deliver a 4 cm SOBP.

All dosimeters were irradiated in a water phantom (as shown in Figure 5.1) to depths allowing the Bragg peaks to be captured with at least 2 cm of distal falloff. The dosimeters were irradiated at a gantry angle of 0° incident to the top surface of the water tank. This both reduced uncertainties from irradiations through the side walls and allowed depth in the phantom to be changed by adding or removing water from the tank.

Relative ionization chamber measurements were taken using the Zebra dosimetry system with the gantry rotated to 270° for each beam configuration.

5.2.2 Monte Carlo LET modeling

To calculate LET in a PRESAGE® volume, a Monte Carlo simulation of the passive scattering proton beamline at the PTC-H was adapted. This simulation uses the Monte Carlo N-Particle Transport code (MCNP) version 6.1 which simulates particle interactions in a rendered geometry²⁹⁰. This simulation adapted a model of the scattering and snout components of the G1 gantry unit based on commissioning blueprints used in previous studies at this institution. The model had been previously dosimetrically validated with experimental measurements and found agreement with treatment planning system predictions^{263,288,291}. Additionally, LET calculations from this model agreed with analytical calculations to within $\pm 5\%$ and has been cross validated with a GEANT4 model^{76,263}.

Calculating LET through Monte Carlo tools has led to a large number of different methods. The general definition of LET was discussed previously (see section 2.3.3), but MCNP simplifies the mechanisms of particle transport used to calculate energy deposition in a volume into discrete voxels. Energy lost as particles transverse a volume

are tallied and normalized. Two methods of normalization exist: dose averaged (known as LET_d) and fluence averaging (known as LET_ϕ). The calculation of LET_ϕ is generally considered the simpler of the two and can be determined by the energy deposition of a particle in a single voxel (E) and averaging over the contributions of all ionizing particles:

$$LET_\phi = \frac{\sum_{i=1}^n E_i}{n} \quad \text{Eq. 5.1}$$

where i is the individual tracked particle and n is the total fluence within the specified voxel. Both methods are described in more detail elsewhere^{76,292} and the average LET has been demonstrated to yield differing values²⁹³. For simplicity, LET_ϕ was chosen for the purposes of this experiment.

Beam modeling for each beam configuration was individually generated and all secondary particles were tracked. For each field, 10^7 particle histories were simulated to achieve a statistical uncertainty less than 1%. The tracking process partitioned the phantom and PRESAGE® into voxels and particle fluence and energy deposition were tallied throughout the simulated PRESAGE®. No tallies were taken within the surrounding phantom material although particle interactions were performed. It is important to note that voxel tallying results in volume averaging across the voxel length, but due to the existing dose averaging in the DMOS dose reconstructions, matching voxel lengths of 1 mm were adequate for these studies. The tallies for fluence and energy deposition were used to generate an LET value within each voxel using Eq. 5.1.

The irradiation setup was comprised of an LQCl PRESAGE® dosimeter affixed to a solid base inside of a water tank (shown in Figure 5.1). The dimensions of the PRESAGE® were determined from the mold used for all dosimeters manufactured in this study. The chemical composition for the PRESAGE® (shown in Table 4.6) was constituted as a homogenous material index while the base, sides, and water of the phantom were constructed independently. The phantom was oriented for top-down irradiation (with the gantry at 0°) and the dosimeter located along the central axis of the beam. The height of the water was adjusted to ensure the SOBP was fully captured within the dosimeter. The MCNP material and geometry decks for one such setup are shown in Appendix 6 (pg. 171).

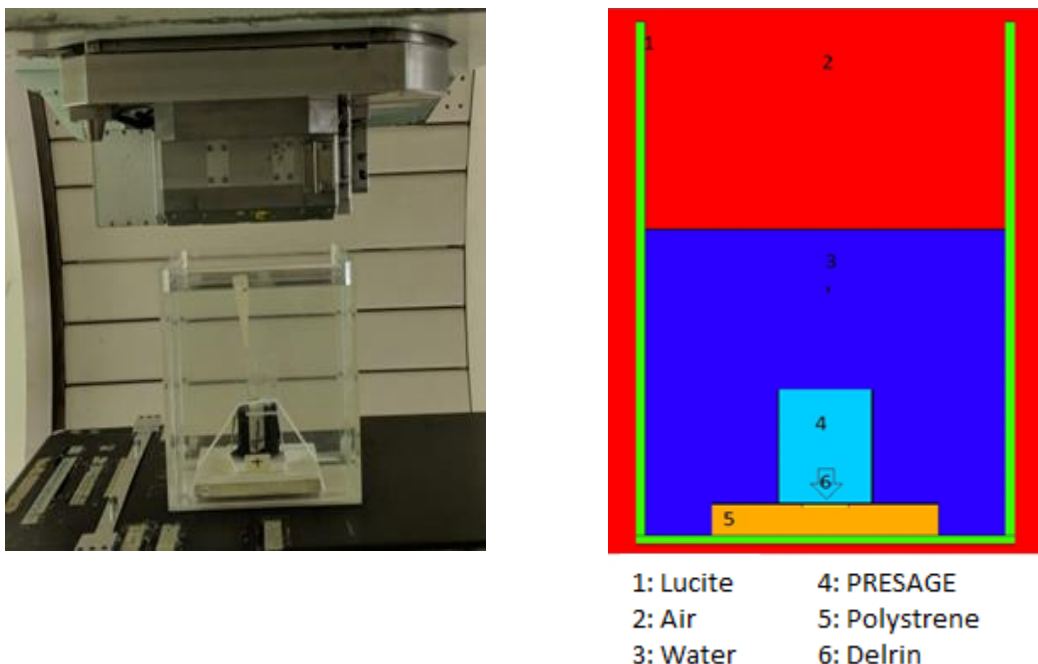


Figure 5.1: A photograph of the irradiation setup used for the experimental measurements (left). Monte Carlo LET modeling (right) was generated by a cross-sectional plane based on the MCNP input deck using the visual editor Vised®. Material are labeled.

5.2.3 Quenching correction factor

Quenching in PRESAGE® as measured relative to ionization chamber measurements was described previously in section 4.2 which quantified relative quenching between PRESAGE® and ionization chamber measurements at each depth, d , along a dose profile. This described the method to determine the percent of dose quenching ($Q\%$), at each depth between ionization chamber measurements and PRESAGE® dose response along the central dose profile of a proton beam with a specific incident energy (E):

$$Q\%(d, E) = M_{IC}^{norm}(d, E) - \varepsilon_{IC}^P(E) * M_P(d, E) \quad \text{Eq. 5.2}$$

where M_{IC}^{norm} is the normalized ionization chamber measurements, M_P is the PRESAGE® dose signal, and ε_{IC}^P is the calibration factor of PRESAGE® dose signal. This formulation was relevant to compare the magnitude of quenching observed between PRESAGE® formulations. To develop a calibration factor based on measured dose quenching, the PRESAGE® correlation coefficient (r_P) along the dose profile must be used and can be defined as the coefficient of these terms:

$$r_P(d, E) = \frac{\varepsilon_{IC}^P(E) * M_P(d, E)}{M_{IC}^{norm}(d, E)} \quad \text{Eq. 5.3}$$

This correlation demonstrates the efficiency of the PRESAGE® dosimeter to accurately measure dose signal along the dose profile. The quenching correction factor (QCF) as a function of depth is then the reciprocal of Eq. 5.3, and when multiplied with the measured PRESAGE® signal, a modified signal accounting for quenching is determined. The QCF can be calculated as:

$$QCF(d, E) = \frac{1}{r_P(d, E)} \quad \text{Eq. 5.4}$$

The QCF as a function of depth and incident energy makes the application of any one solution to another irradiation configuration impractical. In this study, the empirical correlation of QCF as a function of LET was made by fitting the calculated QCF from

Eq. 5.4 with LET_ϕ . The QCF-LET relationship was obtained and QCF as a function of LET (henceforth referred to as $QCF(LET_\phi)$) was derived allowing the application of the function to other irradiation configurations with LET_ϕ similarly modeled using Monte Carlo.

5.2.3.1 Application of QCF to additional dose distributions

A $QCF(LET_\phi)$ equation was applied to measured dose distributions of follow-up PRESAGE® irradiations described in section 5.2.1. For all unmodulated beam configurations, the dose response in PRESAGE® was measured along the central axis of the dosimeter. Dose signal was then renormalized to a point in the proximal region measured by the dosimeter for each beam configuration. Similarly, for each irradiation setup, Monte Carlo calculated LET_ϕ values were determined for each voxel within the dosimeter's volume. Voxel positions along the central axis were converted to depth, and from these values the quenching correction was calculated as such:

$$CM_P(LET_\phi) = M_P * QCF(LET_\phi) \quad \text{Eq. 5.5}$$

where CM_P is the quenching corrected PRESAGE® dose signal. A quenching corrected depth-dose curve was generated and compared to relative ionization chamber measurements. The dose difference along this profile was used to determine accuracy of the CM_P in regions of the pristine Bragg peaks.

LET modeling in an SOBP can be a more difficult task, although a preliminary study of this was necessary to demonstrate applications for more complex fields. The formulation of the SOBP, being an amalgamation of the dose distributions from many

modulated pristine Bragg peaks, can be modeled individually for each peak. This method is time intensive and impractical for routine applications. Rather, the simpler method using voxel averaged LET_{ϕ} values for the cumulative field contributions forming the SOBP was used for this study. The $QCF(LET_{\phi})$ was applied to the dose response of the dosimeter irradiated with a 4 cm SOBP for each voxel in the dose map. Additionally, Eclipse® beam modeling of this field was generated and compared using a 5%/5mm gamma analysis.

5.3 Results and Discussion

5.3.1 The QCF as a function of LET

The depth-dose curve through the central axis of the LQCI PRESAGE® dosimeter is shown in Figure 5.2. This irradiation configuration followed the quenching calibration parameters described previously and measured the dose distribution of an unmodulated 140 MeV proton beam. The dosimeter was placed at a depth in the water phantom to capture the Bragg peak as well as the distal falloff and some portion of the dose plateau. As previously discussed, the dose signal was normalized to a low-LET dose point in the plateau, approximately 0.5 cm deep in the dosimeter to reduce optical-CT surface artifacts. Ionization chamber measurements for the same beam configuration were taken and are also shown in the figure. Quenching was calculated along the dose profile using Eq. 4.2. The average quenching observed for all points proximal to the Bragg peak was $1.92\% \pm 2.37\%$. Similar to the results shown in section 4.3, quenching increased greatly in the distal falloff region (at the depths of distal-90% and beyond) with an average of $51.45\% \pm 74.58\%$. The large variance resulted from large dose discrepancies below distal-25%. These discrepancies were a result of high dose

quenching as well as low dose signal artifacts. To reduce susceptibility of the QCF calculation to these discrepancies, quenching in this region was not included in the data subset, and as a result the quenching in the region between the distal-90% and distal-25% became $37.76\% \pm 17.42\%$.

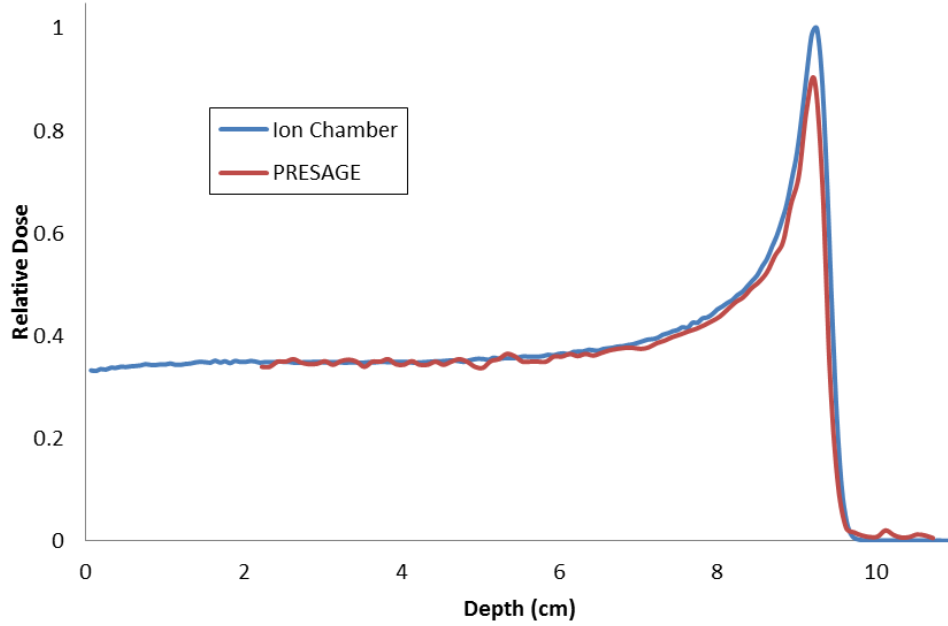


Figure 5.2: Relative depth-dose curves as measured by the LQCl PRESAGE® and ionization chamber measurements for an unmodulated 140 MeV proton beam. PRESAGE® dose was normalized to a point approximately 0.5 cm deep in the dosimeter.

Using Eq. 5.4, the QCF(d) was calculated from PRESAGE® and ionization chamber measurements. The LET_ϕ for the same dose depths was calculated using Eq. 5.1 based on the Monte Carlo modeling of irradiation configuration. Both the calculations are compared in Figure 5.3 as a function of beam depth. The QCF(d) and LET_ϕ for each depth were compared and the relationship is shown in Figure 5.4. From this relationship,

$QCF(LET_\phi)$ was derived. A third order polynomial fit of the data was found to produce an $R^2 > 0.985$ showing good agreement across the LET_ϕ spectrum. The resulting formula for QCF as a function of LET_ϕ was therefore derived to be:

$$QCF(LET_\phi) = (1.215 \times 10^{-3}) * LET_\phi^3 - (1.318 \times 10^{-2}) * LET_\phi^2 + (5.330 \times 10^{-2}) * LET_\phi + 0.975 \quad \text{Eq. 5.6}$$

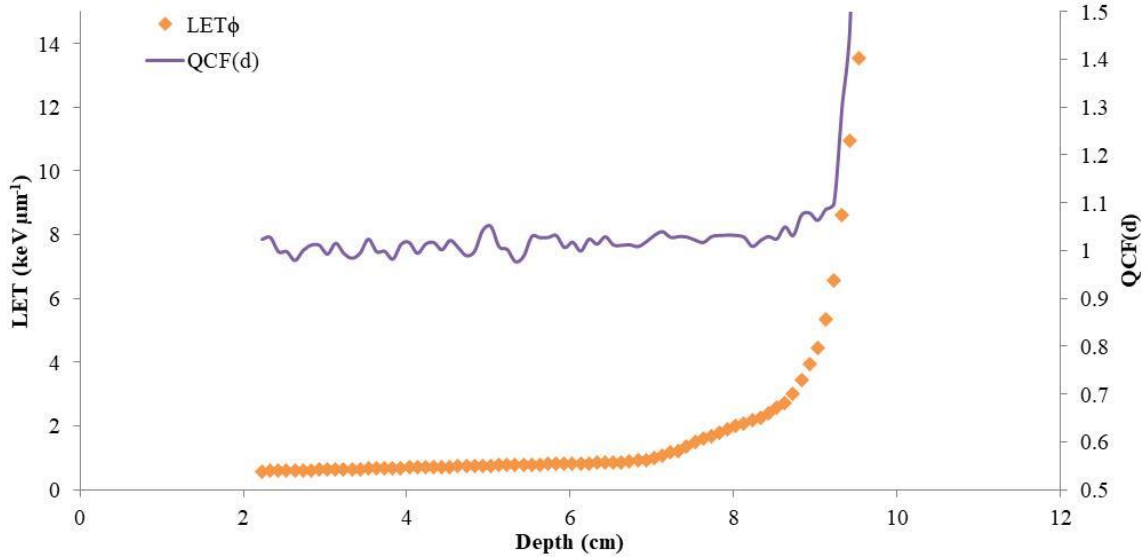


Figure 5.3: $QCF(d)$ calculated from PRESAGE® and ionization chamber measurements along the beam central axis of the beam for an unmodulated 140 MeV PSPT proton irradiation along with LET_ϕ calculated using Monte Carlo.

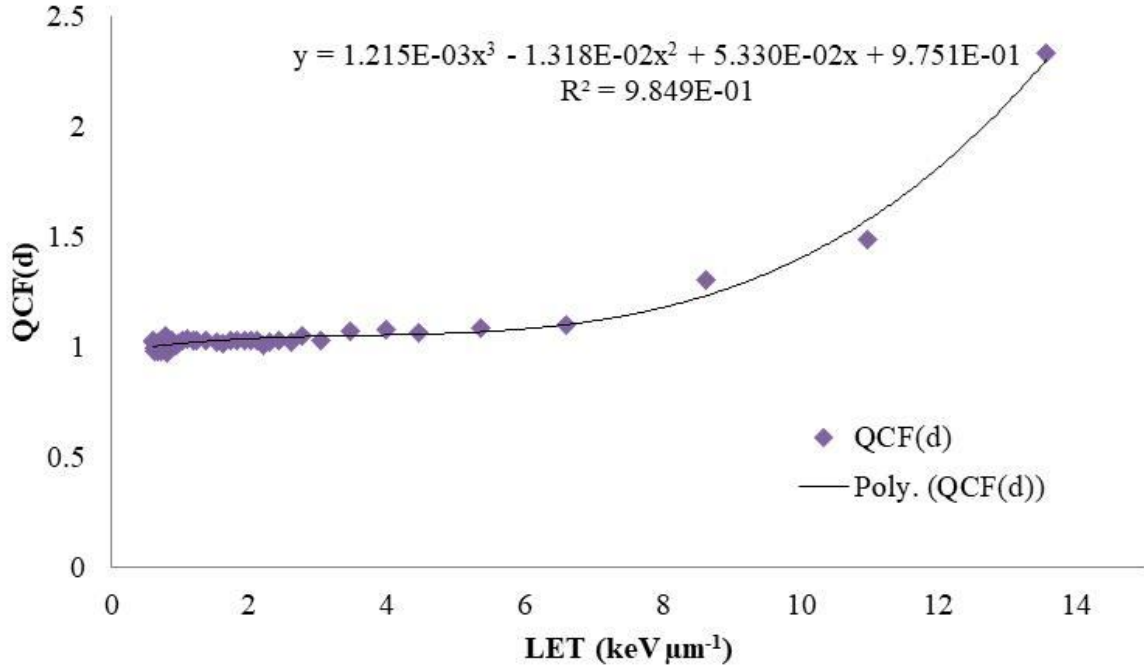


Figure 5.4: The measured QCF as a function of LET for all dose depths as measured in the LQCl PRESAGE® dosimeter irradiated with unmodulated 140 MeV PSPT protons. A third order polynomial line has been fitted to the points.

5.3.2 Application of the QCF

5.3.2.1 Calibration dosimeter

The $QCF(LET_\phi)$ empirical formula given in Eq. 5.6 acts as a scalar (as shown in Eq. 5.5) for dose signal quenching corrections to a PRESAGE® dose distribution with known LET_ϕ . This correction was first applied to the calibration irradiation previously described in order to demonstrate the accuracy of the correction factor. For each dose point along the beam profile, the scalar was calculated from the LET_ϕ depth profile shown in Figure 5.2. The resulting quenching-corrected depth-dose curve is shown in Figure 5.5. This showed reduced quenching at nearly all dose points in the Bragg peak as

well as proximal and distal regions. The uncorrected quenching was measured to be 9.82% at maximum dose in Bragg peak, but with the quenching correction applied, this was reduced to 0.17%. Similarly, average quenching in the distal falloff region was reduced from $37.76\% \pm 17.42\%$ to $1.52\% \pm 5.49\%$ for the uncorrected and quenching corrected dose curves, respectively. Perhaps the greatest area of improvement was observed in the region proximal and adjacent (<1 cm) to the Bragg peak where the average dose quenching changed from $5.24\% \pm 2.74\%$ to $0.2\% \pm 1.92\%$. After the application of the quenching correction certain dose points were found to have negative quenching with the greatest over-response being 3.39% relative to ionization chamber measurements. In the low-LET plateau region of the dose curve, the $QCF(LET_\phi)$ multiplier was less than 1.01 (or $\sim 1\%$ change) for all depths which resulted in very little adjustment to the relative dose at these depths. Part (c) of Figure 5.5 illustrates the improved relative agreement between the PRESAGE® and ionization chamber measurements especially towards the end of the particles range.

The robustness of the $QCF(LET_\phi)$ empirical formula was tested on a series of follow-up irradiations with altered beam configurations.

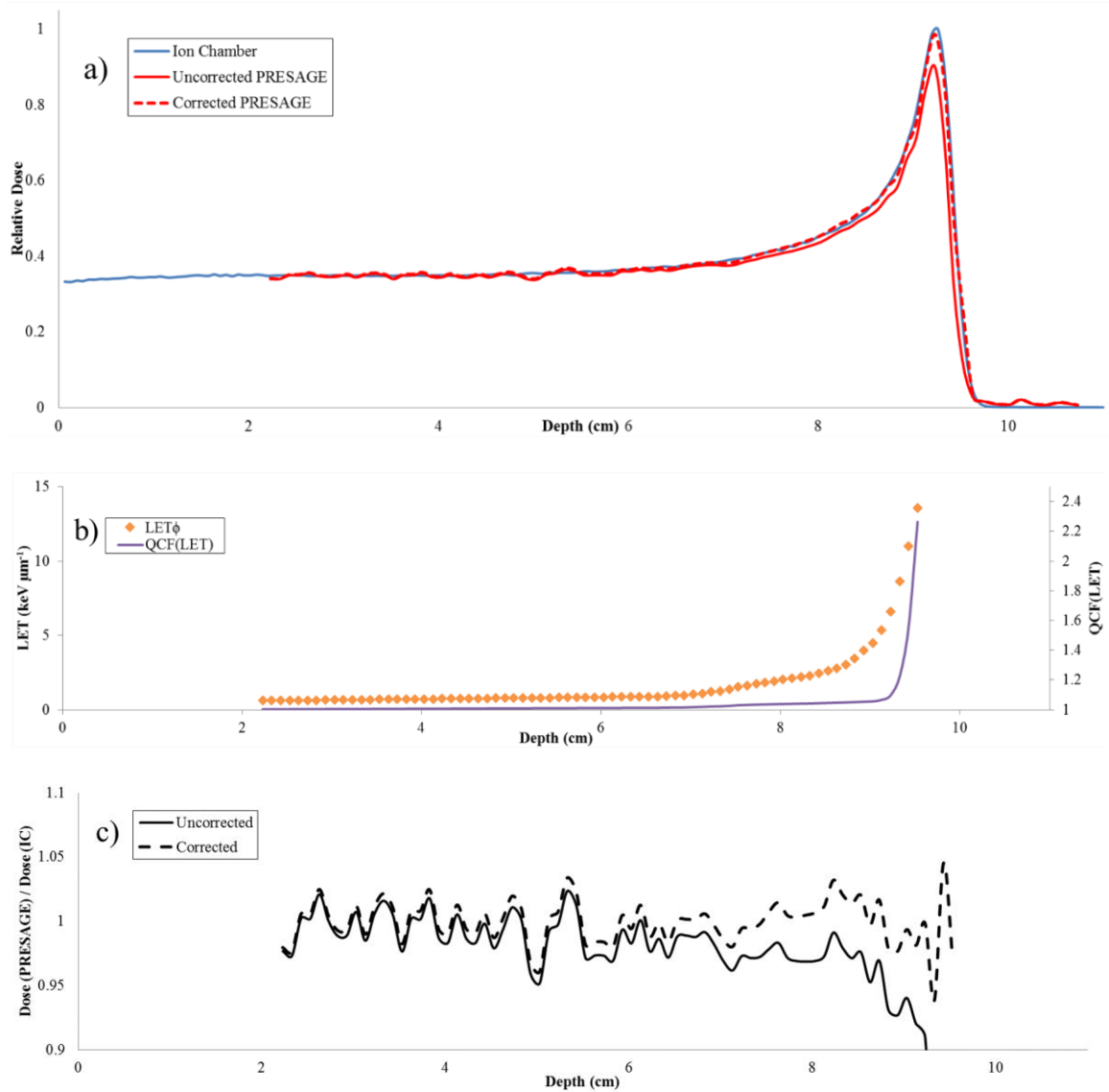


Figure 5.5: Results of the calibration dosimeter used in the calculation of $QCF(LET_\phi)$ and its application to correct dose quenching for an unmodulated 140 MeV proton irradiation. Plot (a) compares the depth-dose curves of the uncorrected and quenching-corrected PRESAGE® with ionization chamber readings. The Monte Carlo calculated LET_ϕ and $QCF(LET_\phi)$ are shown in plot (b), and the agreement of PRESAGE® to ionization chamber is shown in plot (c).

5.3.2.2 Dosimeter A - Reproducibility

The reproducibility of the quenching correction was measured by irradiation of another PRESAGE® dosimeter (Dosimeter A) to similar conditions as the calibration dosimeter. These results are shown in Figure 5.6. Similar to the calibration irradiation, the application of the quenching correction resulted in improved dose signal agreement to ionization chamber measurements at nearly all comparison points although agreement was generally lower than what was observed in the calibration study. The uncorrected dose quenching at the Bragg peak was measured to be 10.92% which was reduced to 2.37% with the application of the correction factor. Similar to the previous dosimeter, the greatest discrepancy for Dosimeter A was observed in the distal falloff region. The application of the quenching correction resulted in an average measured PRESAGE® dose signal $31.7\% \pm 46.1\%$ greater than that by the ionization chamber. This demonstrated some limitations in the accuracy of this correction method in this region of the dose distribution. Similar quenching in the proximal regions was observed in this dosimeter as that in the previous calibration study.

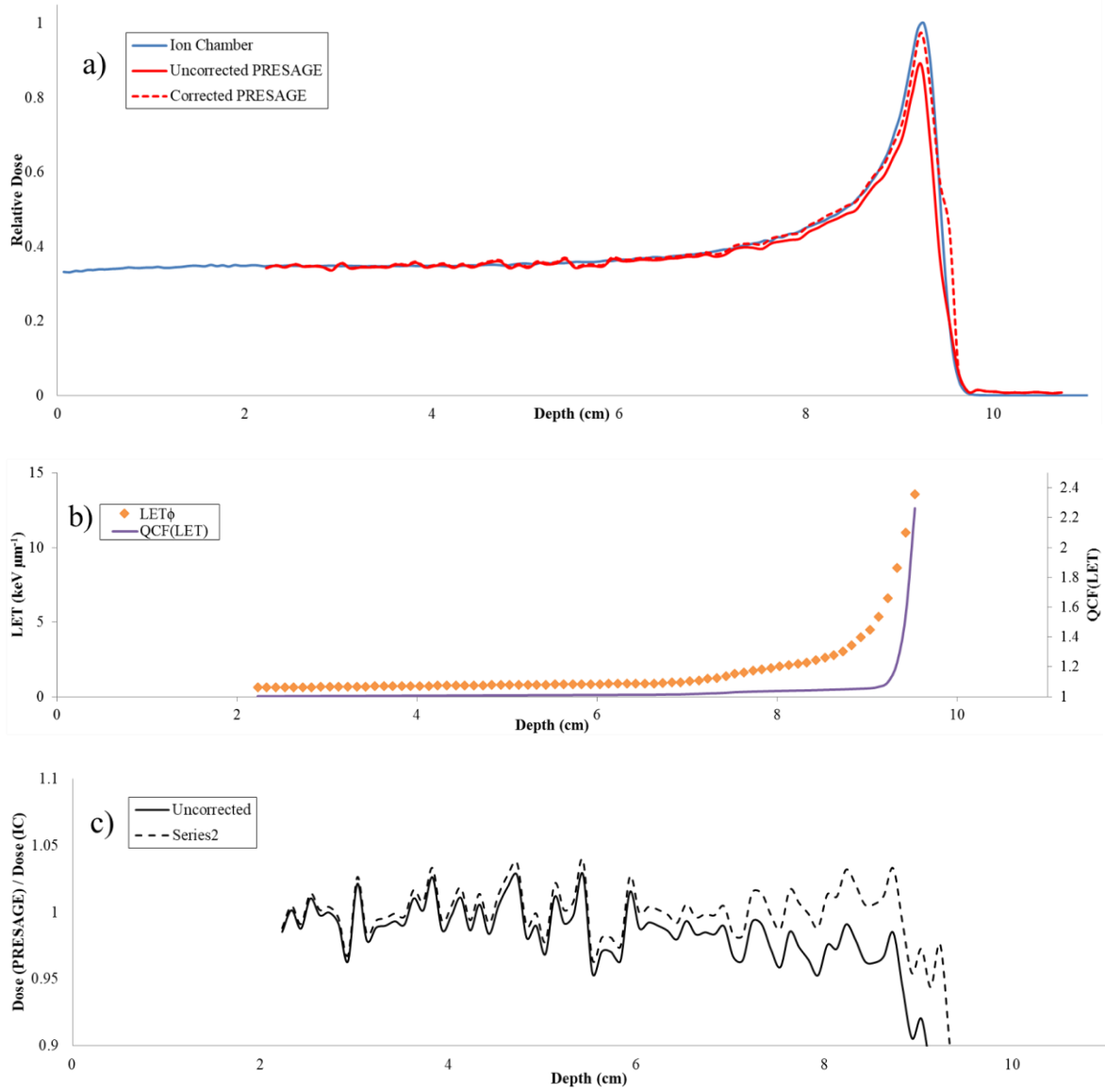


Figure 5.6: Results of the quenching correction in Dosimeter A demonstrating reproducibility of the application of the $QCF(LET\phi)$ function. Plot (a) compares the depth-dose curves of the uncorrected and quenching-corrected PRESAGE® with ionization chamber readings. The Monte Carlo calculated $LET\phi$ and $QCF(LET\phi)$ are shown in plot (b), and the agreement of PRESAGE® to ionization chamber is shown in plot (c).

5.3.2.3 Dosimeter B – Low dose

The application of the $QCF(LET_\phi)$ function to Dosimeter B demonstrated the accuracy of this quenching correction method on a dosimeter that was irradiated to a lower dose than that of the calibration dosimeter. The dose response linearity for this PRESAGE® formulation was discussed previously (see 4.3) and demonstrated lower dose sensitivity of the dosimeter which led to low signal artifacts around 0.25 Gy. The results of this study are shown in Figure 5.7. Low dose signal artifacts in the plateau region lead to higher signal variance in the plateau region making normalization of the dosimeter at a low-LET point susceptible to error. Rather, normalization was based on a dose signal average over 2 cm of the plateau calculated to be $0.349\% \pm 0.012\%$. Due to the low LET in the plateau region, the application of the quenching correction did not appreciably increase the standard deviation here. Uncorrected dose quenching measured in the Bragg peak was 7.20% and with the application of the $QCF(LET_\phi)$ function was measured to be -2.92%. The larger uncertainty in the normalization for this reconstruction was approximately equivalent with this over dose. In the distal falloff region, the quenching corrected dose response was similarly measured to be greater than ionization chamber measurements by $44.1\% \pm 36.7\%$. This study demonstrated limitations of this dosimeter to lower prescribed doses. Uncertainties resulting from low dose signals in the region used for dose signal normalization were magnified with the application of the $QCF(LET_\phi)$ function suggesting that alternative methods maybe required for future low dose studies.

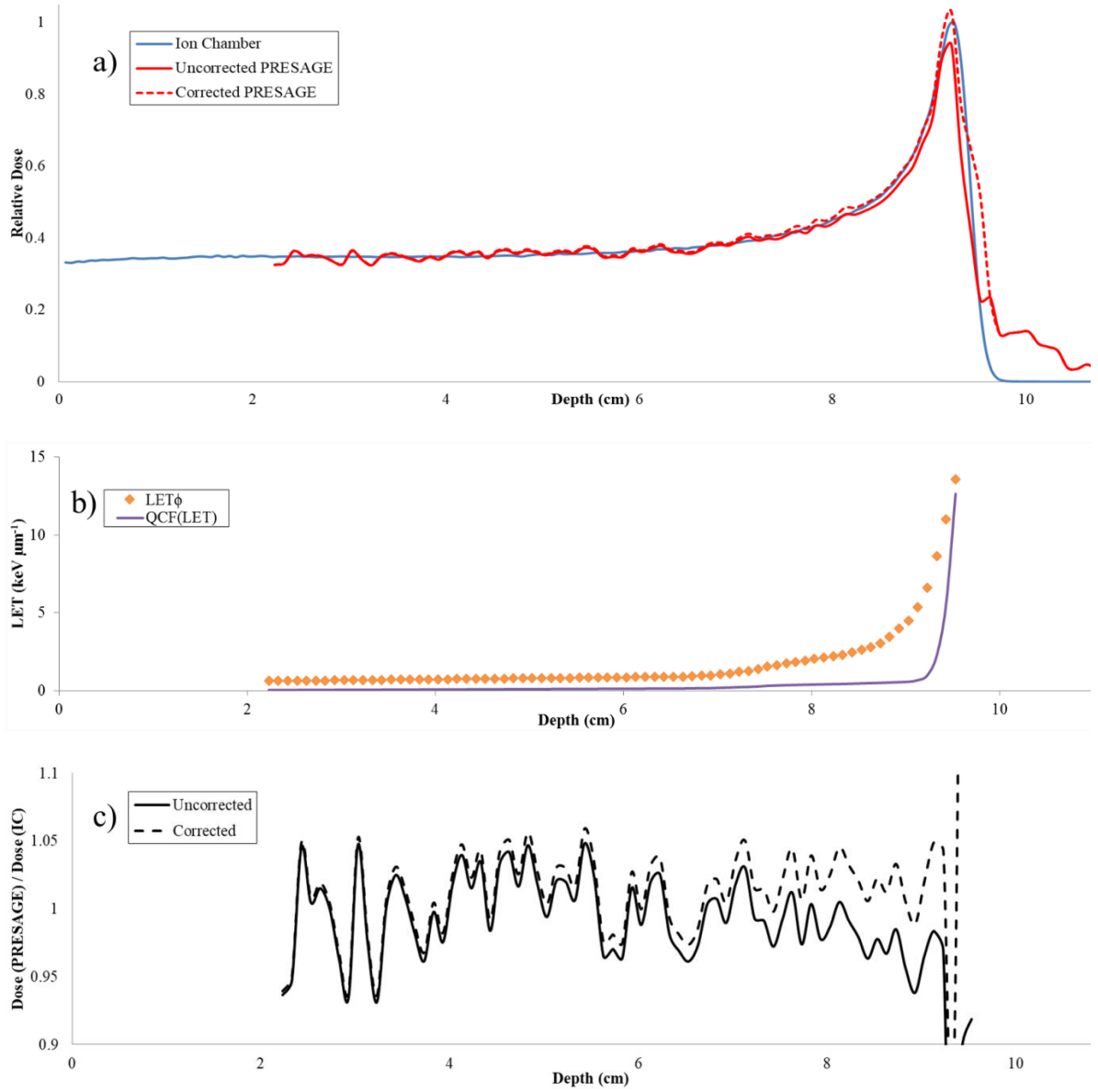


Figure 5.7: Results of the quenching correction in Dosimeter B demonstrating the application of the $\text{QCF}(\text{LET}_\phi)$ function in a low dose irradiation. Plot (a) compares the depth-dose curves of the uncorrected and quenching-corrected PRESAGE® with ionization chamber readings. The Monte Carlo calculated LET_ϕ and $\text{QCF}(\text{LET}_\phi)$ are shown in plot (b), and the agreement of PRESAGE® to ionization chamber is shown in plot (c).

5.3.2.4 Dosimeter C – Energy dependence

The final unmodulated beam irradiation investigated the accuracy of the QCF(LET_φ) function when applied to a dosimeter irradiated to a different incident energy than that used in the calibration study. The QCF(LET_φ) function generated by the calibration dosimeter using 140 MeV protons was applied to Dosimeter C irradiated with 180 MeV. The change in calculated LET_φ along the central axis was minimal in the plateau region relative to the Monte Carlo simulation of the 140 MeV beam. At the Bragg peak of LET_φ was calculated to be 0.12 (keV μm⁻¹), or 1.82%, lower. The most substantial variation in LET_φ was observed around the distal-25% depth in which the LET_φ was calculated to be 3.1 (keV μm⁻¹), or 23.17%, lower. These values agreed well with those of Monte Carlo modeling studies for similar energies^{263,286,292}.

The results of the measured dose and the application of the QCF(LET_φ) function are shown in Figure 5.8. In the plateau region, dose signal increased by approximately 0.5% with the application of the quenching correction. Relative dose agreement with ionization chamber measurements in this region averaged 98.6%±0.87% and 99.1%±0.91% for uncorrected and quenching corrected PRESAGE®, respectively. With the application of the QCF(LET_φ) function, quenching in the Bragg peak was reduced from 9.97% to 2.77% showing a similar trend to the results of Dosimeter B. Similar to previous studies, the greatest dose discrepancies were found in the distal regions where quenching was reduced from 33.19%±29.16% to 21.48%±26.22%. These results demonstrated that a quenching correction function generated from one beam energy can be applied to other energies and achieve good dose agreement with expected values.

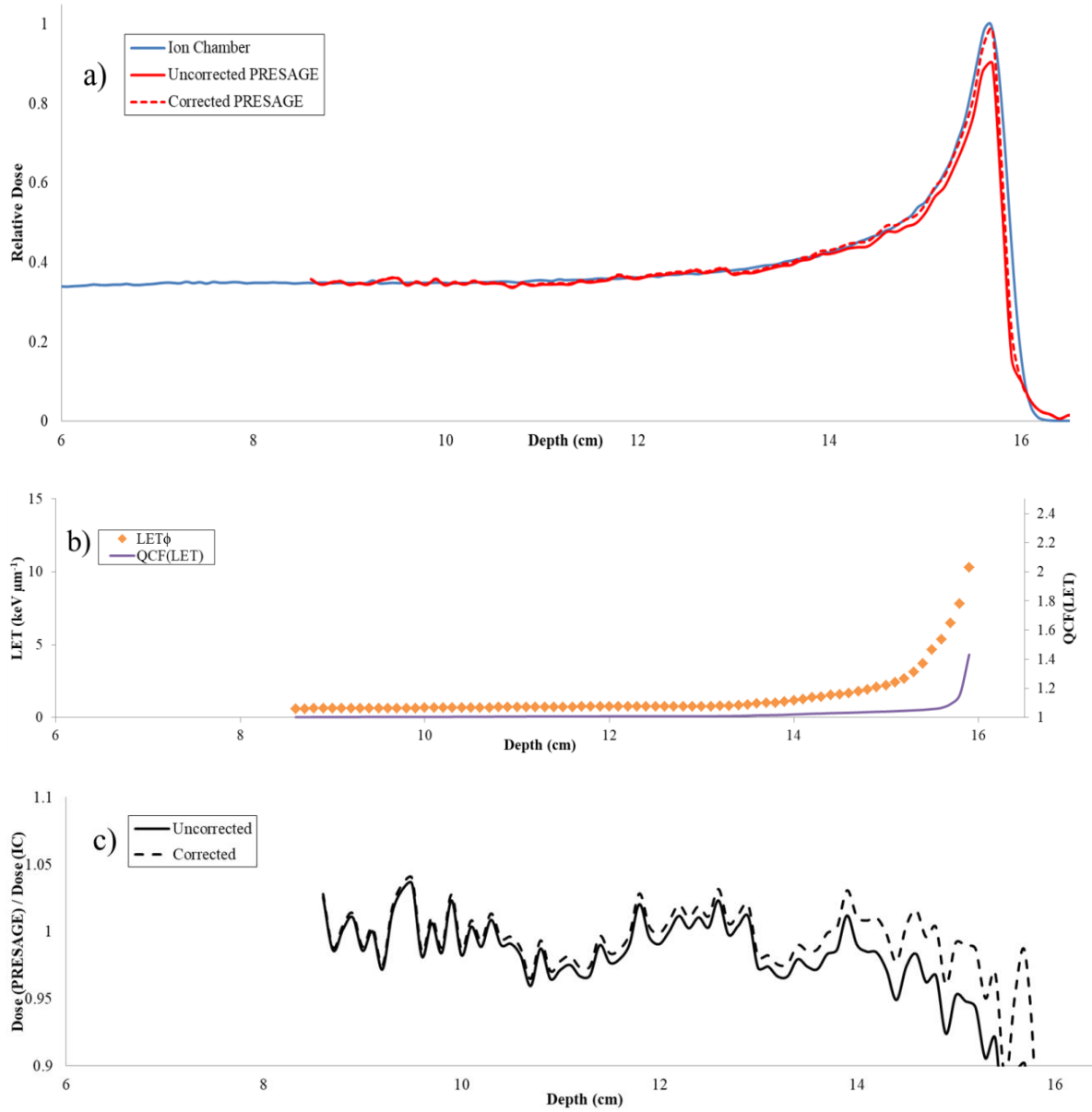


Figure 5.8: Results of the quenching correction in Dosimeter C demonstrating the application of the $\text{QCF}(\text{LET}_\phi)$ function when applied to a 180 MeV irradiation. Plot (a) compares the depth-dose curves of the uncorrected and quenching-corrected PRESAGE® with ionization chamber readings. The Monte Carlo calculated LET_ϕ and $\text{QCF}(\text{LET}_\phi)$ are shown in plot (b), and the agreement of PRESAGE® to ionization chamber is shown in plot (c).

5.3.2.5 Dosimeter D – Modulated beam

The final application of the $QCF(LET_\phi)$ function investigated the accuracy of the tool when applied to a modulated beam and was compared to both ionization chamber measurements and Eclipse® TPS dose predictions. To accommodate the length of a 4 cm SOBP (reduced to 3.68 cm in LQCI PRESAGE®) within Dosimeter D, very little of the plateau region was captured within the sensitive volume and as a result dose normalization was taken in the proximal region (approximately 3 cm deep in the dosimeter).

For comparison with ionization chamber measurements, a dose depth curve was taken along the central axis of the dosimeter and the results are shown in Figure 5.9. The integral dose forming the proximal side of the SOBP showed a general overresponse as a result of the application of the $QCF(LET_\phi)$ function as illustrated by part (a) of the figure. Without the quenching correction, the measured dose for 2.71 cm (or 71%) of the SOBP region agreed with ionization chamber measurements to within 3%. With quenching correction a total of 3.23 cm (or 87%) of the SOBP agreed to within this margin. Dose disagreement with ionization chamber measurements beyond this region increased with depth as shown in part (c) of the figure. This averaged $7.57\% \pm 8.80\%$ in the remaining SOBP length. The maximum quenching found in the SOBP was measured at the distal most point to be 42.1% uncorrected which was reduced to 29.3% corrected. In the distal falloff region, quenching correction function resulted in reduced quenching from $54.45\% \pm 7.88\%$ to $47.38\% \pm 8.78\%$.

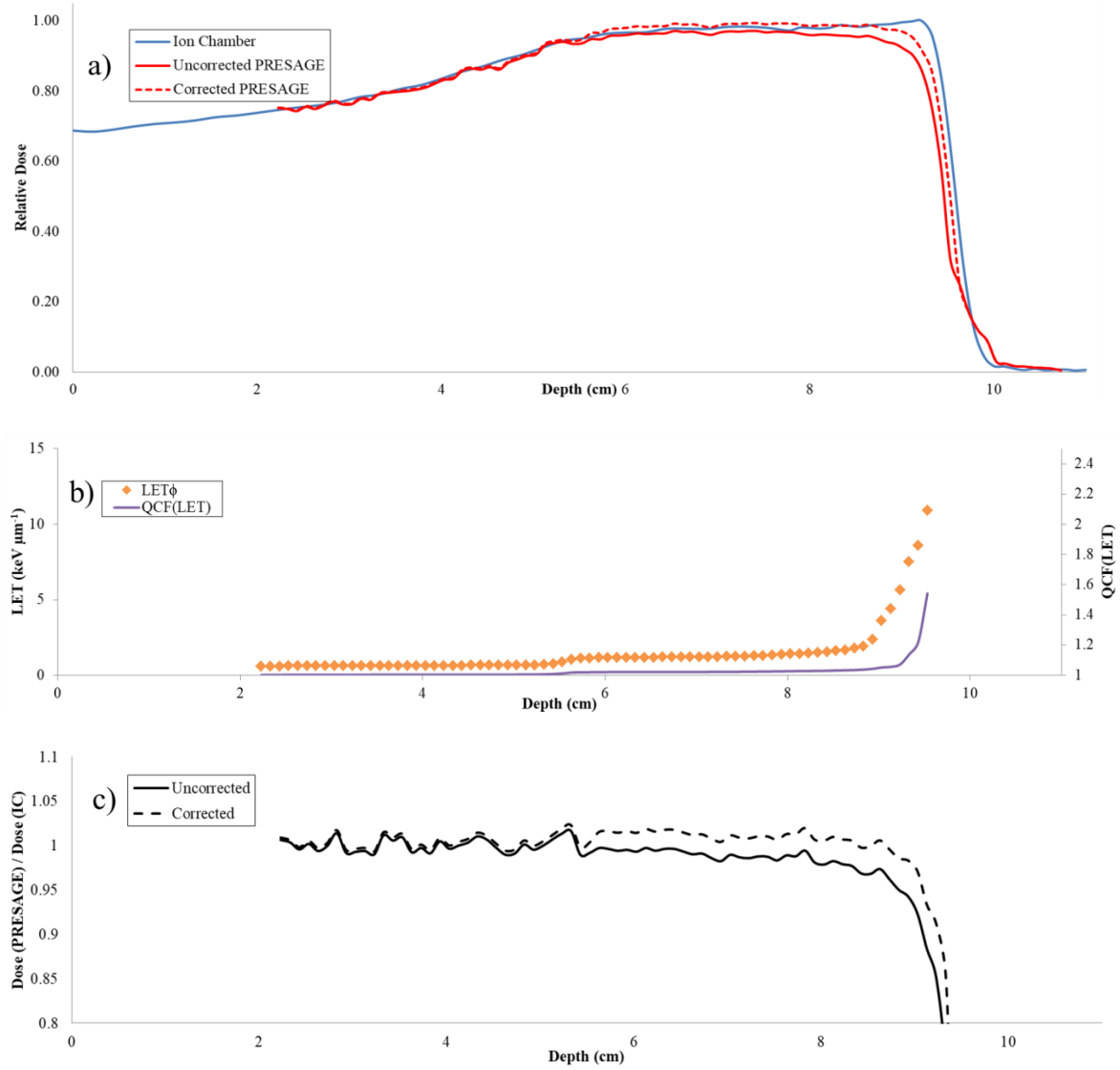


Figure 5.9: Results of the quenching correction in Dosimeter D demonstrating the application of the $QCF(LET_\phi)$ function when applied to a 140 MeV proton beam with a 4 cm SOBP. Plot (a) compares the depth-dose curves of the uncorrected and quenching-corrected PRESAGE® with ionization chamber readings. The Monte Carlo calculated LET_ϕ and $QCF(LET_\phi)$ are shown in plot (b), and the agreement of PRESAGE® to ionization chamber is shown in plot (c).

The $QCF(LET_\phi)$ function was applied to the full dose reconstruction of the modulated SOBP irradiation for Dosimeter D by element-wise multiplication of the dose array with the quenching scalar for each voxel using MATLAB®. 3D gamma analysis calculations were made in the CERR® software environment by comparing the corrected and uncorrected doses in Dosimeter D with an Eclipse® dose prediction. Gamma criteria of 5%/5mm with a 10% minimum dose threshold were used and the gamma maps are shown in Figure 5.10. The uncorrected PRESAGE® dose resulted in a pass rate of 79.1% with failing voxels primarily occurring in the final 1 cm of the SOBP as well as the entirety of the distal falloff region. These increased to 92.7% for the quenching corrected dose. Failing voxels in these measurements were reduced in the SOBP region although still occurring in the majority of the distal falloff region. These trends were similar to those observed in the depth-dose curve investigation done previously.

These passing rates are low relative to many other studies that have used PRESAGE® in photon irradiation studies, usually with more complex dose distributions, and usually yielding passing rates greater than 99% using stricter gamma criteria^{12,141,143,236,242,252,253}. As a result of the quenching factor, no previous PRESAGE® applications for a modulated proton beam have shown higher gamma passing rates using similar criteria. The application of the quenching correction function on the PRESAGE® in this study showed demonstrable improvement to the dose agreement and, for simple fields, showed passing rates greater than 90%.

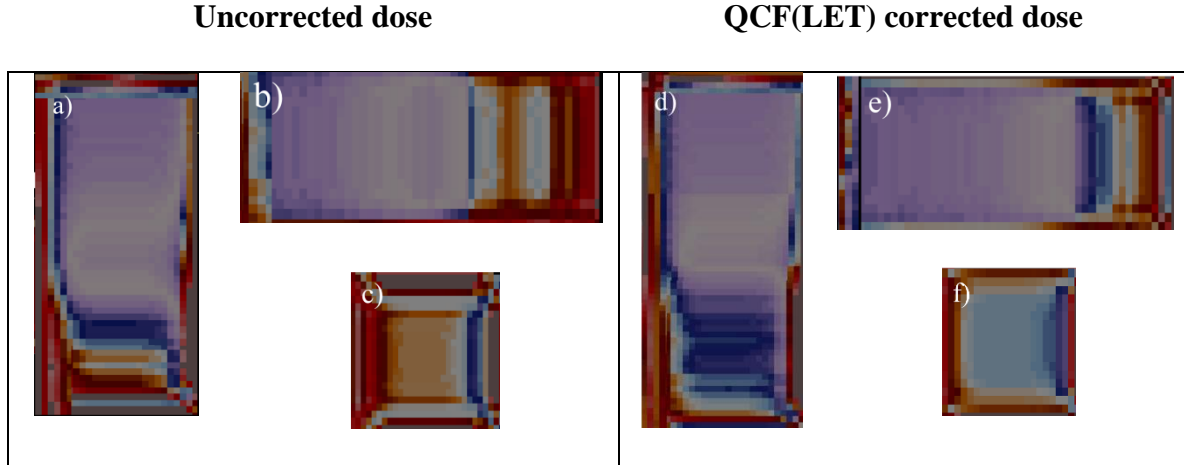


Figure 5.10: Representations of the gamma passing maps for the dose response of an LQCl PRESAGE® and an Eclipse® TPS prediction for a 4 cm SOBP, 140 MeV PSPT proton beam. Cross-sectional planes along the central axis of the transverse (a and d) and sagittal (b and e) planes. The coronal plane was taken at a depth approximately 1 cm proximal to the distal-90%.

5.4 Conclusions

In this chapter, the dose quenching in LQCl PRESAGE® was correlated with Monte Carlo calculated LET to generate a quenching correction factor that sought to further reduce the signal quenching in the high-LET portion of a proton beam. From the results of this study, a polynomial quenching correction function using LET predictions was produced and tested against several field setups. For unmodulated beams, the quenching correction resulted in noteworthy improvement to dose accuracy in the proximal and Bragg peak regions. In most cases, dose errors in the distal falloff regions were reduced for all irradiations but only the calibration dosimeter was able to achieve agreement to within 5%. Low-dose irradiations resulted in error propagation through the dose signal normalization process and would likely require additional steps to use this

formulation for such in the future or would require the use of the LQBr formulation which demonstrated higher dose sensitivity.

These results are very promising for future applications of both this formulation of PRESAGE® as well as other dosimeters that suffer from dose quenching. The preliminary applications of this correction method for modulated fields was tested and found similarly promising results against both ionization chamber measurements and TPS predictions.

The quenching correction function derived in this study sought to investigate the relationship between quenching and LET, but the results of the study have shown that a comprehensive quenching correction function may require additional variables such as total dose, incident energy, and beam fractionation. Additionally, LET itself is a complicated beam characteristic that can be defined and expressed in a number of ways and alternative LET calculation methods would likely result in a slightly different quenching correction especially in the distal falloff region.

Chapter 6: Conclusions and future works

6.1 Discussion and conclusions

PRESAGE® has previously shown promising results when incorporated as a 3D dosimetry tool for conventional and highly modulated photon therapies, but its adoption and use with protons has been hindered primarily by the observed dose signal quenching effect in the high-LET portion of the Bragg peak. The purpose of this study was to investigate the mechanisms causing this signal quenching in PRESAGE® and to evaluate potential methods of correction.

The first aim of this study was the development of a PRESAGE® manufacturing protocol and a characterization of the radiological and dosimetric properties of locally manufactured dosimeters. This procedure was important for subsequent portions of this study as well as for future works within this laboratory. Dosimeter fabrication became an iterative process of eliminating dosimeter artifacts including surface damage, undissolved particulates, and Schlieren bands. Additionally, the effects of pressurization and ambient temperature during the curing process found average shrinking of $2.43\% \pm 0.59\%$ and determined sufficient pressurization to eliminate the formation of air bubbles. The uniformity of density across the volume had a relative standard deviation less than 3% with the greatest discrepancies observed within a few millimeters of the dosimeter edges which further encouraged the exclusion of data from these regions.

This aim also demonstrated the dosimetric properties of in-house manufactured dosimeters. Dose linearity comparisons between intrabatch and interbatch productions of the same formulation showed dosimeters responded linearly ($R^2 > 0.999$) to at least 12 Gy with the greatest discrepancies observed beyond 6 Gy showing good agreement between batch formulations in a wide dose range and between separate batches. This also demonstrated the reproducibility of dosimeters manufactured in-house. Next, dose response in cylindrical dosimeters showed dose signal agreements of $1.51\% \pm 0.63\%$ through cross sections of uniform dose demonstrating dose response uniformity across the dosimeter's volume. Finally, temporal stability tests found optimal dose readout windows after irradiation. Long term stability (5 days) of the dose signal was consistent up to 12 Gy (which is relevant for remote dosimetry applications of these dosimeters).

The second stage of this study was the investigation of the formulaic composition on dosimetric properties of PRESAGE®. Dose response sensitivity and temporal stability were both affected by concentrations of LMG, radical initiator, and the polyurethane catalyzing agent (DBTDL). Formulations with high concentrations of CHBr_3 as the radical initiator component showed improved low dose sensitivity but higher initial ODs made the production of useable large volume dosimeters difficult.

The relationship between dose quenching and formulaic composition was next investigated. An interbatch dose comparison between dosimeter formulations, when irradiated in an SOBP, was compared to ionization chamber measurements to correlate quenching magnitude with the concentrations of specific chemical components. Changes in concentrations of LMG and radical initiator resulted in non-linear changes to the magnitude of quenching demonstrated that quenching was, in part, controlled by the

relative concentration of both of these components. In contrast, the concentration of the polyurethane catalyst did not show any influence on quenching.

The next stage was an iterative optimization of the PRESAGE® formulation to find the limits of quenching reduction through chemical manipulation. Concentrations of each active component were adjusted to find a local quenching minimum. This investigation also produced comprehensive results of the effects of formulation on radiological and physical properties, dose sensitivity, and dose saturation useful for future studies. The quenching magnitude in this experimental setup was found to range from as high as $72.33\% \pm 14.66\%$ and $76.26\% \pm 7.85\%$ to as low as $3.18\% \pm 1.76\%$ and $2.88\% \pm 3.52\%$ for chloroform and bromoform dosimeters respectively. Two promising formulations were localized for further study and referred to as LQCl (low-quenching chloroform-based) and LQBr (low-quenching bromoform-based) and a series of studies tested their durability and radiological properties. The LQBr dosimeter showed superior low-dose sensitivity but the LQCl dosimeter had better linearity at high doses, long term signal stability, and more ideal radiological properties, and as a result the LQCl dosimeter was found to be preferable for general use and was used going forward for this study.

To account for remaining dose quenching, a correction method was developed and applied based on Monte Carlo modeling of the LET. MCNP simulations of proton irradiations in the dosimeters provided LET distributions for beam configurations. A correlation coefficient was developed to compare measured dose quenching to predicted LET, and based on the results of a reference dosimeter, a semi-empirical quenching correction factor (QCF) was developed. The robustness of this model was investigated through its application to additional dose distributions using beam configurations of

different dose, incident energy, and modulation to the reference dosimeter. Dose discrepancies in the Bragg peak and proximal regions were reduced from approximately 10% to below 3% for all irradiations. These improvements were less apparent, but generally improved, in the distal regions. Finally, the feasibility of the QCF application applied to a dose distribution volume was tested using 3D gamma analysis for a single field, SOBP irradiation with pass rates increasing from 79.1% to 92.7% with the application of the QCF. For this study, the calculation and application of the QCF function was a manual process and therefore relatively simple fields were used as a preliminary investigation. In all, these results suggested that a quenching correction function generated from one reference beam could be applied to different beam configurations and achieve greatly improved dose accuracies.

The central hypothesis of this investigation stated that the mechanisms causing signal quenching in PRESAGE® when irradiated by a proton beam can be evaluated and corrected for resulting in a system that yields relative dose measurements agreeing with ionization chamber measurements to $\pm 3\%$ in the Bragg peak and calculated doses to 5%/5mm. In-house manufacturing and formulaic optimization methods covered in the first two specific aims improved the native dose accuracy of the dosimeters but were unable to confirm the hypothesis. The third specific aim applied the semi-empirical QCF to the measured dose distributions yielding relative dose measurements agreeing with both ionization chamber measurements and calculated doses to within the gamma criteria of the central hypothesis. QCF corrected dose accuracy still suffered in the region of distal falloff as a result of steep dose gradients and LET values much higher than those in the Bragg peak. These regions covered very little volume in the tested field

configurations allowing them to pass gamma analysis but could pose more of a problem for overlapping fields and would require further investigation before the dosimeters application as a clinical dosimetry tool. The results of the methods of quenching reduction laid out in this work have demonstrated that PRESAGE® can be corrected for in part, and based on the results of the relatively simple fields investigated, this confirms the dose accuracy requirements of the hypothesis.

6.2 Future works

The demands for 3D dosimetry across all modalities have been discussed and progress continues to be made using PRESAGE® as well as other systems. The works presented in this investigation demonstrate several potential courses of direction for future works based on the findings presented. Foremost are continued investigations into improvements and applications for proton dosimetry. This investigation has demonstrated that dose quenching is, in part, a function of dosimeter composition. Further investigations may give a better understanding of the chemical mechanisms resulting in dose quenching and seek to eliminate it. An ideal dosimeter would give a linear dose response across any LET spectrum without the need for post-irradiation signal corrections.

The current need for a semi-empirical quenching correction function requires that the next steps to clinical applications are improving the accuracy and ease of use for these systems. The correction functions must be tested with more complex dose distributions and more extreme variations of beam configurations including beam energy, dose, dose rate, and fractionation as well as with more complex phantom systems. The calculation of the correction functions and their applications to 3D measured dose volumes must also

be streamlined and automated and made more user friendly before they can be introduced for general use. Additionally, the popularity of spot scanning proton therapy continues to grow, so the investigations of this quenching correction system must be applied to that modality to further ensure its usefulness in the future.

The application of PRESAGE® as a robust, remote auditing tool has been one of its greatest appeals to researchers. Beyond protons, the works of this study open the doors to applications of formulation fine-tuning for specific applications. These may include controlled dose sensitivity for low-dose or SRS treatment QA, dosimeters with long-term temporal stability or reusability, and even dosimeters molded to anthropomorphically mimic anatomical sites.

Appendix

1. ΔOD measurements used for dose linearity and fabrication reproducibility from dosimeters manufactured for Chapter 3:

AOD													
Batch 1							Batch 2						
Dosimeter		A	B	C	Avg.	SD	A		B	C	Avg.	SD	Avg/cGy
Dose	MU												
0	0	0	0	0	0	0	0	0	0	0	0	0	
25	35.511	0.003	0.003	0.002	0.003	5.774E-04	1.067E-04	0.005	0.004	0.004	0.004	5.774E-04	1.733E-04
50	71.023	0.006	0.006	0.006	0.006	1.062E-18	1.200E-04	0.006	0.006	0.007	0.006	5.774E-04	1.267E-04
100	142.045	0.011	0.01	0.011	0.011	5.774E-04	1.067E-04	0.012	0.014	0.012	0.013	1.155E-03	1.267E-04
200	284.091	0.023	0.022	0.022	0.022	5.774E-04	1.117E-04	0.024	0.024	0.023	0.024	5.774E-04	1.183E-04
400	568.182	0.043	0.045	0.045	0.044	1.155E-03	1.108E-04	0.047	0.046	0.047	0.047	5.774E-04	1.167E-04
600	852.273	0.065	0.066	0.067	0.066	1.000E-03	1.100E-04	0.068	0.069	0.071	0.069	1.528E-03	1.156E-04
800	1136.364	0.089	0.088	0.089	0.089	5.774E-04	1.108E-04	0.092	0.091	0.094	0.092	1.528E-03	1.154E-04
1000	1420.455	0.111	0.113	0.112	0.112	1.000E-03	1.120E-04	0.116	0.114	0.116	0.115	1.155E-03	1.153E-04
1200	1704.545	0.132	0.135	0.134	0.134	1.528E-03	1.114E-04	0.138	0.137	0.14	0.138	1.528E-03	1.153E-04
AOD													
Batch 3							Interbatch						
Dosimeter		A	B	C	Avg.	SD	Avg/cGy	Avg	SD	Avg/cGy			
Dose	MU												
0	0	0	0	0	0	0		0	0	0			
25	35.511	0.007	0.01		0.005	0.006	1.155E-03	2.267E-04	0.004	1.481E-03	1.689E-04		
50	71.023	0.008	0.01		0.007	0.008	5.774E-04	1.533E-04	0.007	8.660E-04	1.333E-04		
100	142.045	0.014	0.01		0.015	0.014	5.774E-04	1.433E-04	0.013	1.740E-03	1.256E-04		
200	284.091	0.024	0.02		0.025	0.024	1.000E-03	1.200E-04	0.023	1.000E-03	1.167E-04		
400	568.182	0.048	0.05		0.048	8.498E-18	1.200E-04	0.046	1.732E-03	1.158E-04			
600	852.273	0.073	0.07		0.071	1.155E-03	1.194E-04	0.069	2.693E-03	1.150E-04			
800	1136.364	0.095	0.09		0.095	5.774E-04	1.183E-04	0.092	2.759E-03	1.149E-04			
1000	1420.455	0.118	0.12		0.118	5.774E-04	1.183E-04	0.115	2.863E-03	1.152E-04			
1200	1704.545	0.14	0.14		0.139	5.774E-04	1.164E-04	0.137	2.949E-03	1.144E-04			

2. Δ OD measurements used for interbatch dose sensitivity in Chapter 4:

Batch	Dose (cGy)	25	50	100	200	400	800	1000	1200	2000
	Initial OD	Δ OD								
0	0.045	0.005	0.007	0.015	0.025	0.048	0.095	0.118	0.139	0.234
1	0.044	0.004	0.008	0.012	0.021	0.040	0.080	0.099	0.117	0.197
2	0.045	0.005	0.009	0.015	0.027	0.051	0.101	0.126	0.148	0.239
3	0.040	0.001	0.001	0.002	0.003	0.006	0.014	0.016	0.019	0.033
4	0.041	0.002	0.003	0.005	0.008	0.015	0.029	0.037	0.043	0.072
5	0.042	0.001	0.002	0.006	0.011	0.021	0.043	0.053	0.062	0.106
6	0.046	0.003	0.004	0.008	0.015	0.029	0.059	0.073	0.086	0.145
7	0.040	0.001	0.002	0.004	0.007	0.014	0.028	0.035	0.041	0.069
8	0.071	0.001	0.002	0.004	0.006	0.013	0.026	0.032	0.038	0.062
9	0.388	0.000	0.000	0.000	0.000	0.000	0.000	0.000	0.000	0.000

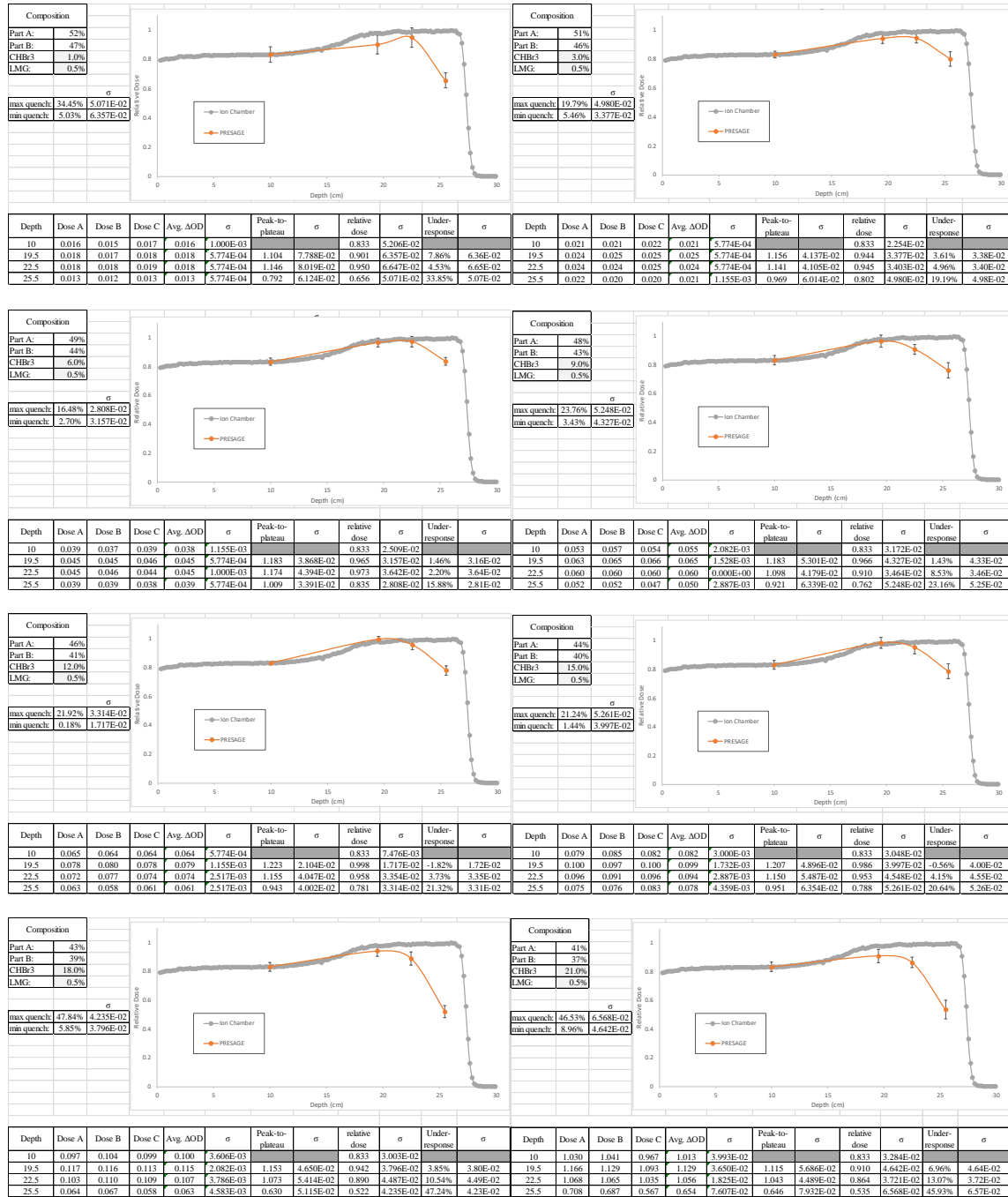
StDev										
Batch	Dose (cGy)	25	50	100	200	400	800	1000	1200	2000
	Initial OD	Δ OD								
0	5.774E-04	5.774E-04	5.774E-04	1.732E-03	1.155E-03	2.309E-03	1.732E-03	1.732E-03	2.309E-03	2.887E-03
1	5.774E-04	1.732E-03	1.155E-03	1.732E-03	1.732E-03	2.309E-03	2.309E-03	2.887E-03	1.732E-03	2.309E-03
2	1.732E-03	1.732E-03	1.732E-03	1.155E-03	2.309E-03	2.887E-03	2.309E-03	2.887E-03	4.041E-03	5.196E-03
3	1.732E-03	5.774E-04	2.309E-03	5.774E-04	2.309E-03	2.887E-03	2.309E-03	3.464E-03	3.464E-03	4.619E-03
4	1.155E-03	1.155E-03	5.774E-04	5.774E-04	1.155E-03	2.309E-03	4.041E-03	4.041E-03	2.309E-03	4.619E-03
5	5.774E-04	5.774E-04	5.774E-04	1.155E-03	1.732E-03	2.887E-03	1.732E-03	2.309E-03	4.041E-03	3.464E-03
6	5.774E-04	1.155E-03	1.732E-03	1.155E-03	1.732E-03	2.887E-03	2.887E-03	2.887E-03	3.464E-03	2.887E-03
7	5.774E-04	1.155E-03	5.774E-04	5.774E-04	1.155E-03	1.732E-03	2.887E-03	2.309E-03	3.464E-03	4.619E-03
8	1.732E-03	5.774E-04	1.155E-03	1.732E-03	1.732E-03	2.887E-03	2.309E-03	2.309E-03	2.887E-03	5.196E-03
9	5.774E-03	0.000E+00	0.000E+00	0.000E+00	0.000E+00	0.000E+00	0.000E+00	0.000E+00	0.000E+00	0.000E+00

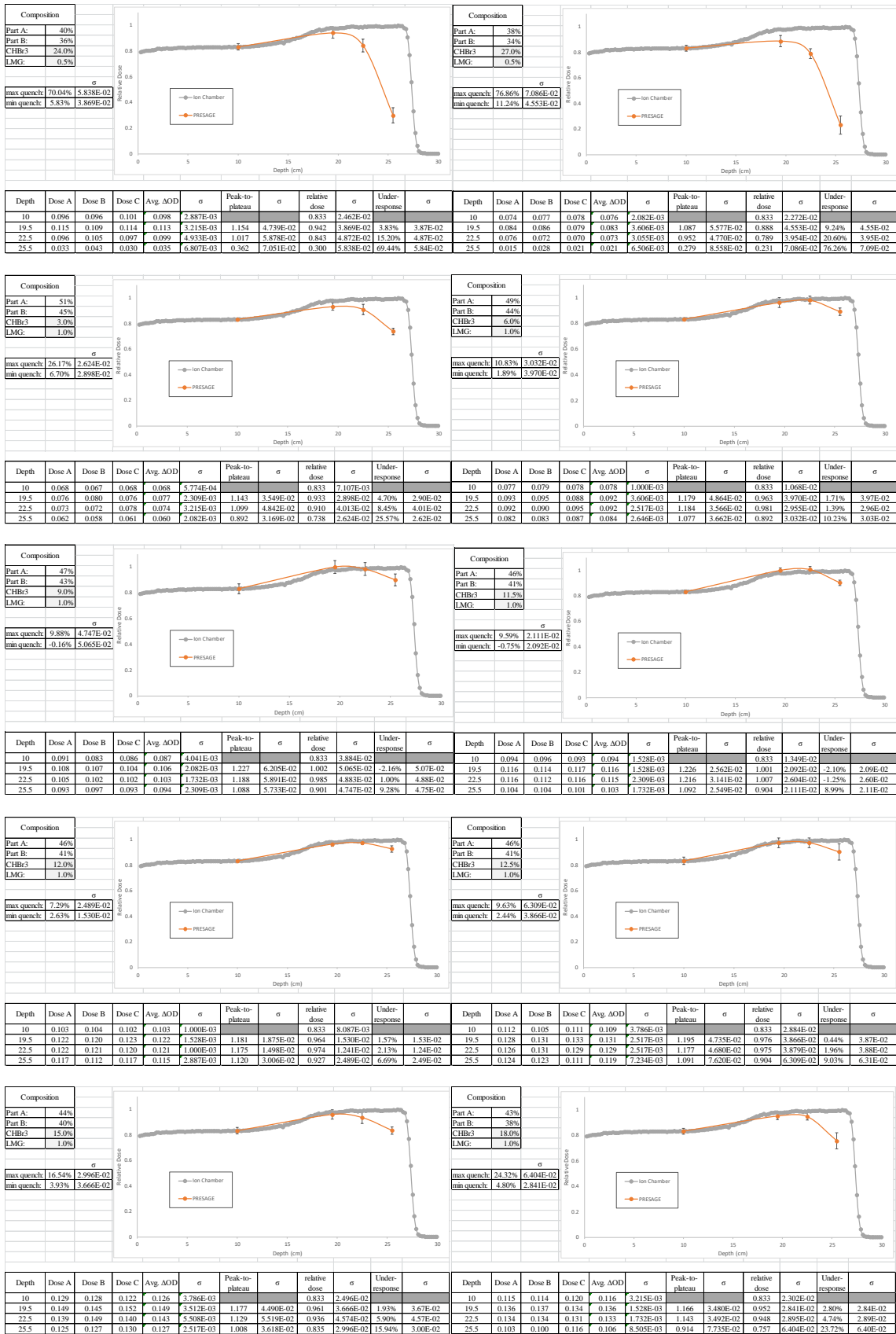
3. Interbatch quenching comparison in Chapter 4:

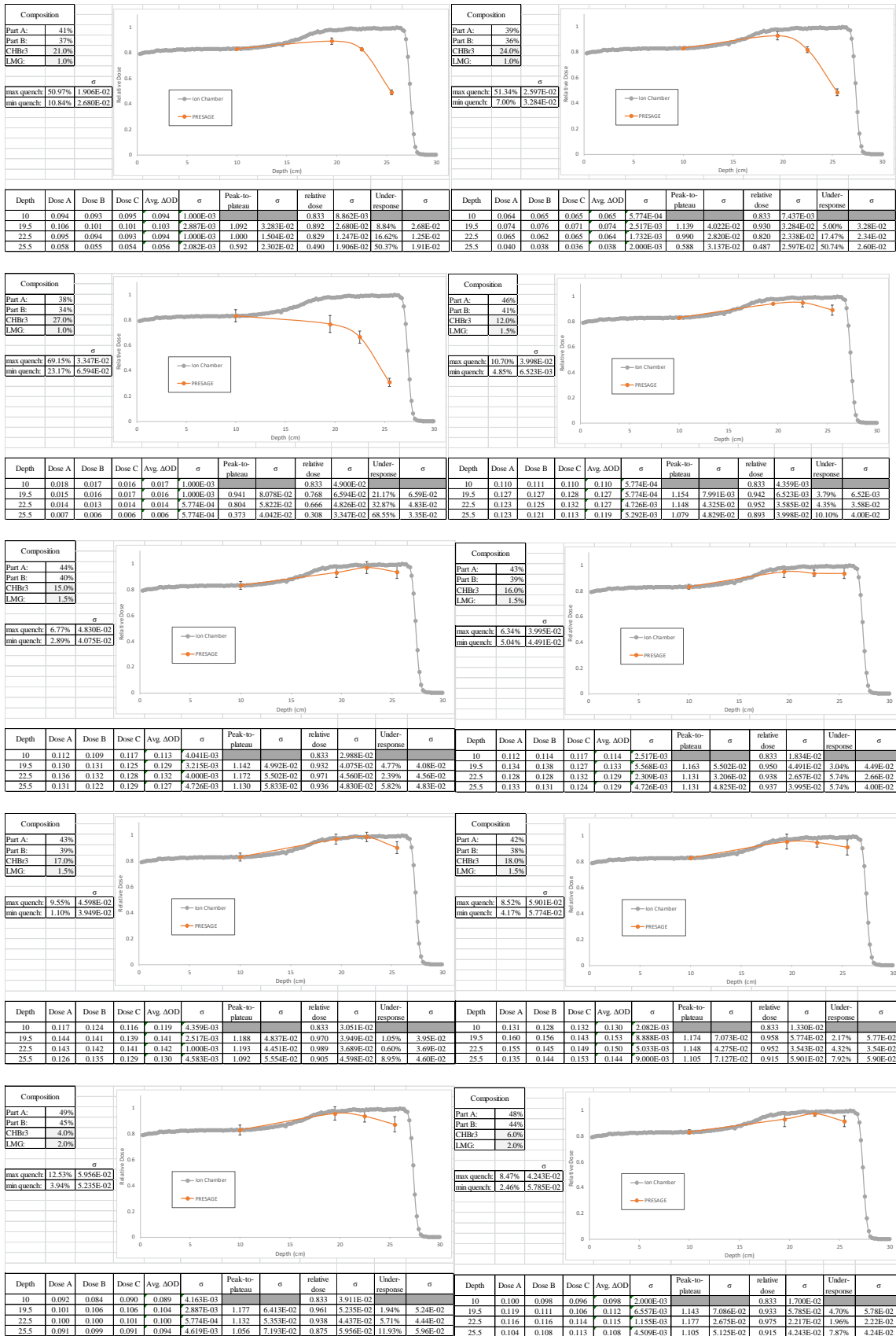
Depth	Batch 0					
	ΔOD	σ	Peak-to-Plateau	σ	Under-response	σ
10	0.019	1.160E-03				
19.5	0.022	1.155E-03	1.179	9.818E-04	0.018	1.158E-03
22.5	0.022	1.155E-03	1.142	1.011E-03	0.049	1.158E-03
25.5	0.018	1.000E-03	0.947	1.137E-03	0.211	1.080E-03
Depth	Batch 1					
	ΔOD	σ	Peak-to-Plateau	σ	Under-response	σ
10	0.016	1.700E-03				
19.5	0.018	5.774E-04	1.138	1.001E-03	0.052	1.139E-03
22.5	0.018	5.774E-04	1.100	5.249E-04	0.084	1.139E-03
25.5	0.013	5.774E-04	0.813	7.106E-04	0.323	1.139E-03
Depth	Batch 2					
	ΔOD	σ	Peak-to-Plateau	σ	Under-response	σ
10	0.021	0.000577				
19.5	0.025	5.774E-04	1.181	4.889E-04	0.016	5.774E-04
22.5	0.024	5.774E-04	1.143	5.052E-04	0.048	5.774E-04
25.5	0.021	1.155E-03	0.995	8.703E-04	0.171	8.662E-04
Depth	Batch 3					
	ΔOD	σ	Peak-to-Plateau	σ	Under-response	σ
10	0.003	1.000E-03				
19.5	0.003	1.000E-03	1.143	8.750E-04	0.048	1.000E-03
22.5	0.003	1.000E-03	1.107	9.032E-04	0.078	1.000E-03
25.5	0.002	1.000E-03	0.821	1.217E-03	0.316	1.000E-03
Depth	Batch 4					
	ΔOD	σ	Peak-to-Plateau	σ	Under-response	σ
10	0.006	1.000E-03				
19.5	0.007	1.000E-03	1.150	8.696E-04	0.042	1.000E-03
22.5	0.007	1.155E-03	1.117	9.649E-04	0.070	1.078E-03
25.5	0.005	1.155E-03	0.850	1.359E-03	0.292	1.078E-03

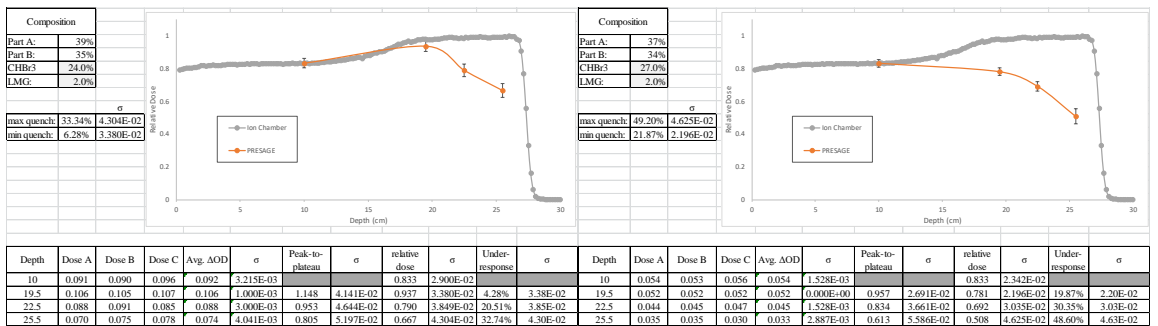
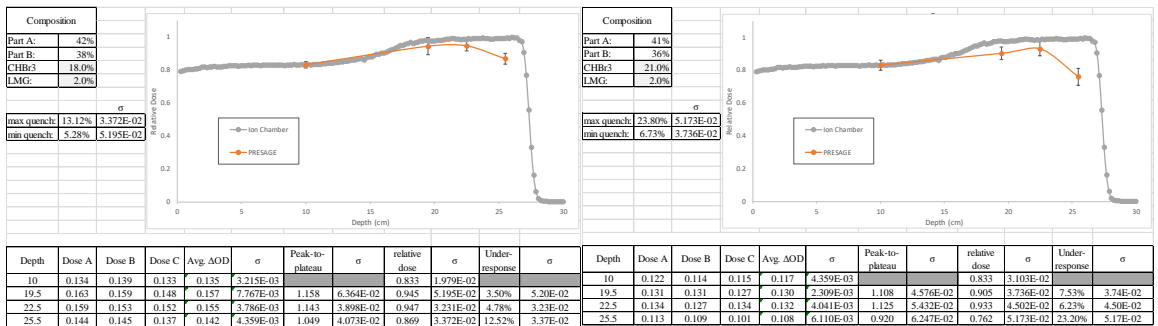
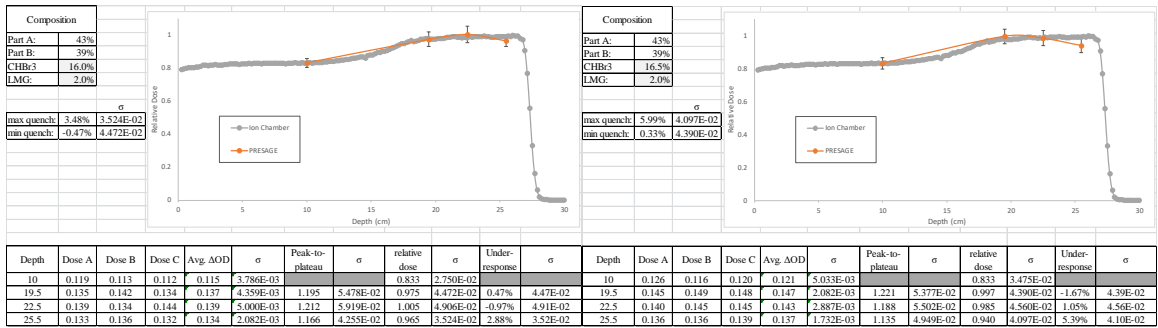
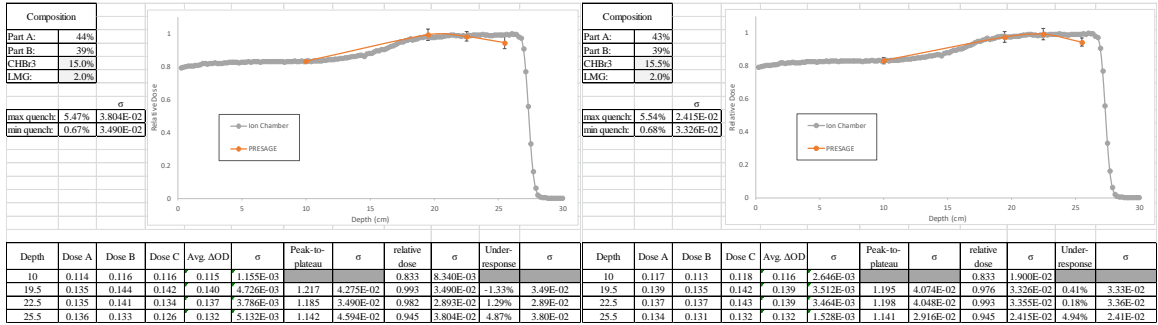
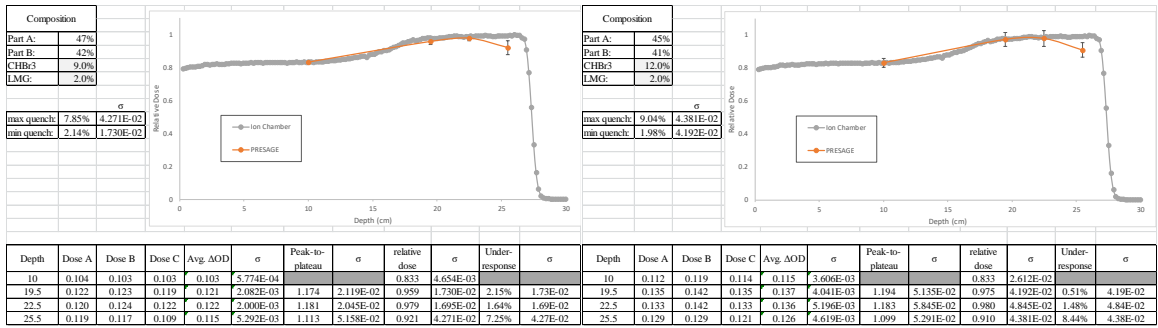
Depth	Batch 5					
	ΔOD	σ	Peak-to-Plateau	σ	Under-response	σ
10	0.009	5.774E-04				
19.5	0.011	1.155E-03	1.167	7.424E-04	0.028	8.662E-04
22.5	0.010	5.774E-04	1.133	7.643E-04	0.056	5.774E-04
25.5	0.008	1.155E-03	0.911	9.507E-04	0.241	8.662E-04
Depth	Batch 6					
	ΔOD	σ	Peak-to-Plateau	σ	Under-response	σ
10	0.012	1.000E-03				
19.5	0.014	5.774E-04	1.142	6.908E-04	0.049	7.887E-04
22.5	0.013	5.774E-04	1.108	5.209E-04	0.077	7.887E-04
25.5	0.010	5.770E-04	0.817	7.067E-04	0.320	7.885E-04
Depth	Batch 7					
	ΔOD	σ	Peak-to-Plateau	σ	Under-response	σ
10	0.006	5.774E-04				
19.5	0.006	1.000E-03	1.145	6.885E-04	0.046	7.887E-04
22.5	0.006	5.774E-04	1.109	7.111E-04	0.076	5.774E-04
25.5	0.005	5.770E-04	0.855	6.754E-04	0.288	5.772E-04
Depth	Batch 8					
	ΔOD	σ	Peak-to-Plateau	σ	Under-response	σ
10	0.004	1.155E-03				
19.5	0.005	0.000E+00	1.136	5.082E-04	0.053	5.775E-04
22.5	0.005	0.000E+00	1.114	0.000E+00	0.072	5.775E-04
25.5	0.004	1.155E-03	0.864	6.687E-04	0.281	1.155E-03
Depth	Batch 9					
	ΔOD	σ	Peak-to-Plateau	σ	Under-response	σ
10	0.000	0.000E+00				
19.5	0.000	0.000E+00	-	-	-	-
22.5	0.000	0.000E+00	-	-	-	-
25.5	0.000	0.000E+00	-	-	-	-

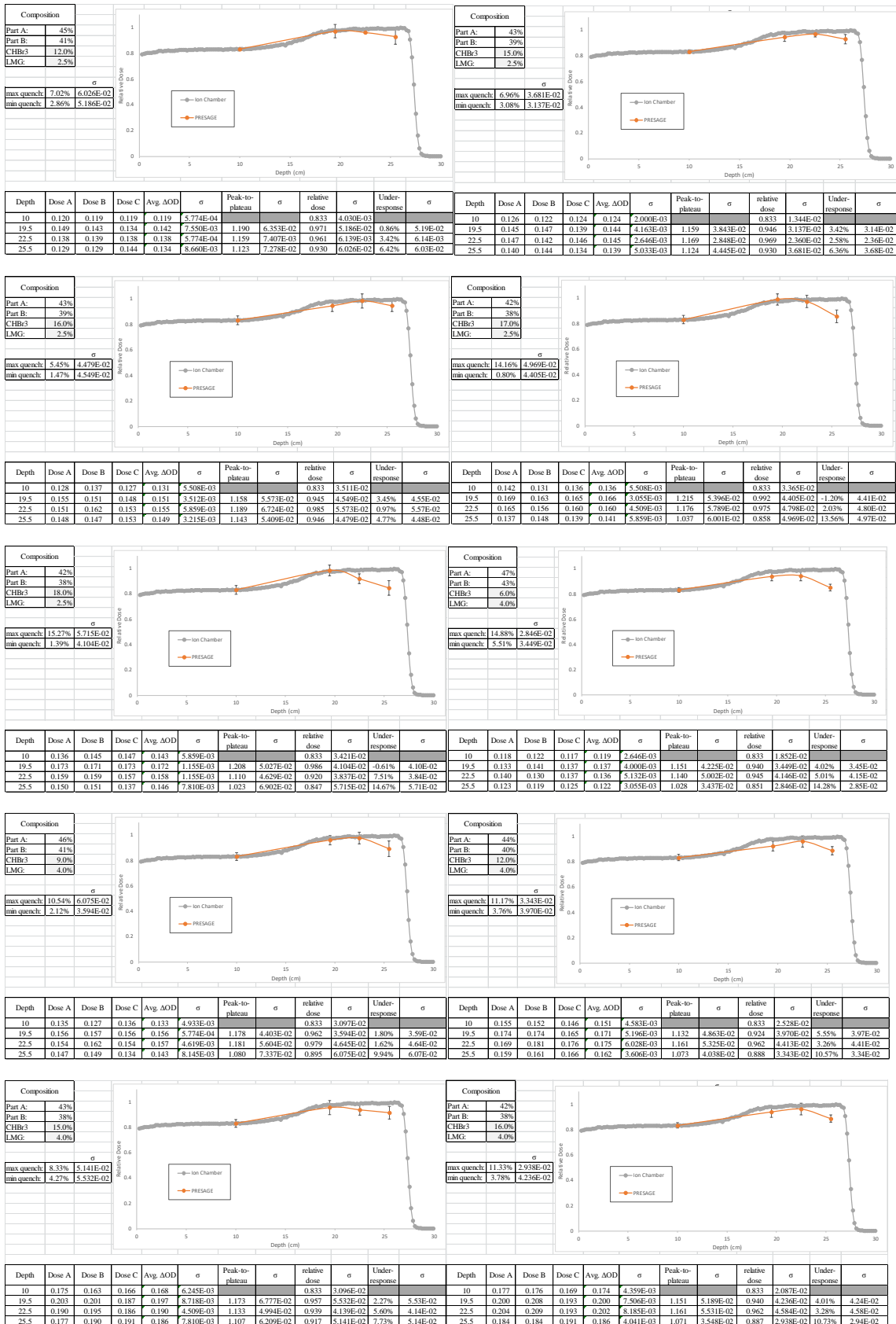
4. Formulation quenching measurements (Bromoform based dosimeters)











Composition

Part A: 46%
Part B: 41%
CHBr3 9.0%
LMG: 4.0%

σ

max quench: 10.54%
min quench: 2.12%

Composition

Part A: 44%
Part B: 40%
CHBr3 12.0%
LMG: 4.0%

σ

max quench: 11.17%
min quench: 3.76%

Composition

Part A: 43%
Part B: 38%
CHBr3 15.0%
LMG: 4.0%

σ

max quench: 8.33%
min quench: 4.27%

Composition

Part A: 42%
Part B: 38%
CHBr3 16.0%
LMG: 4.0%

σ

max quench: 11.33%
min quench: 3.78%

Composition

Part A: 42%
Part B: 38%
CHBr3 16.0%
LMG: 4.0%

σ

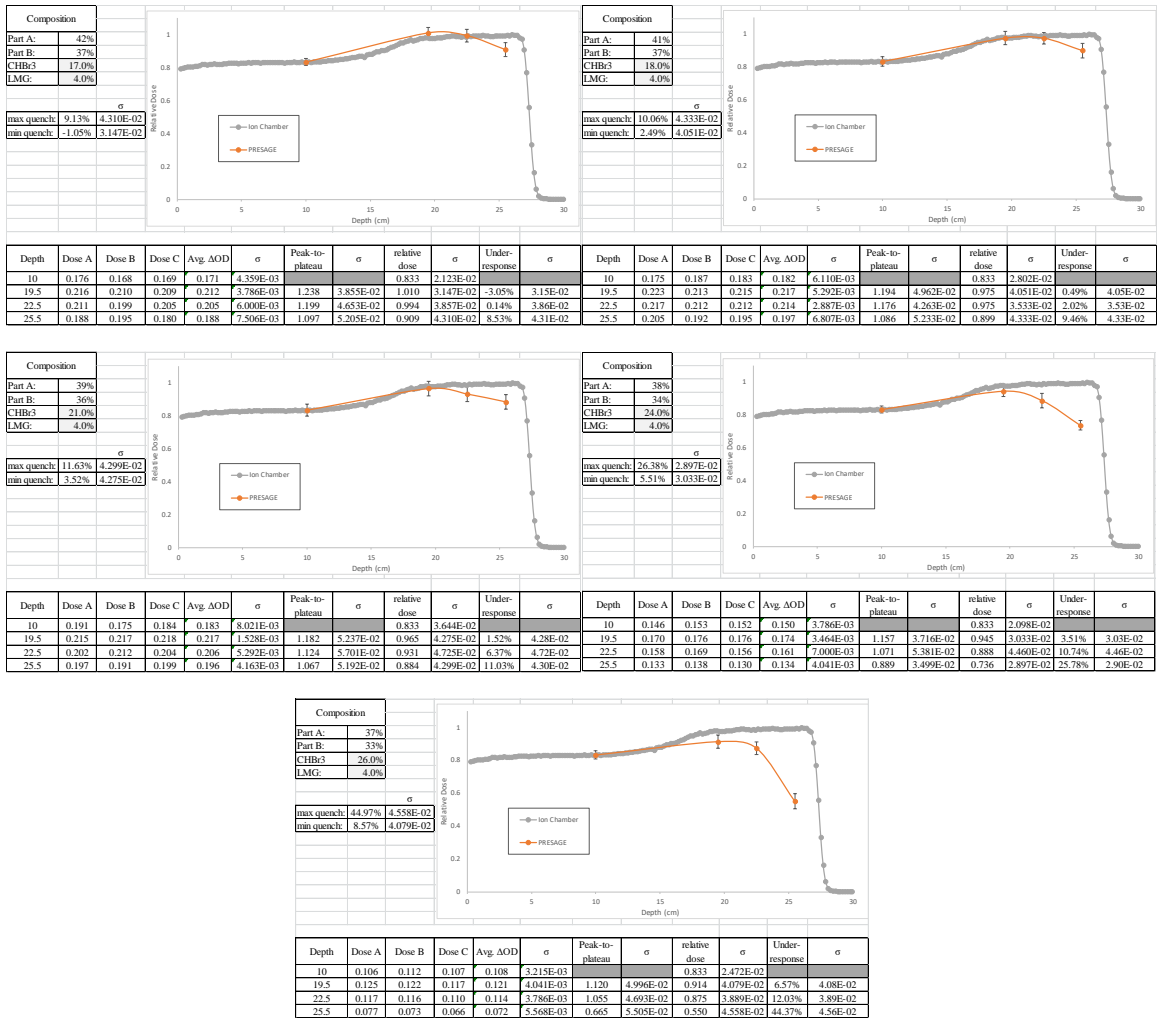
max quench: 11.33%
min quench: 3.78%

Composition

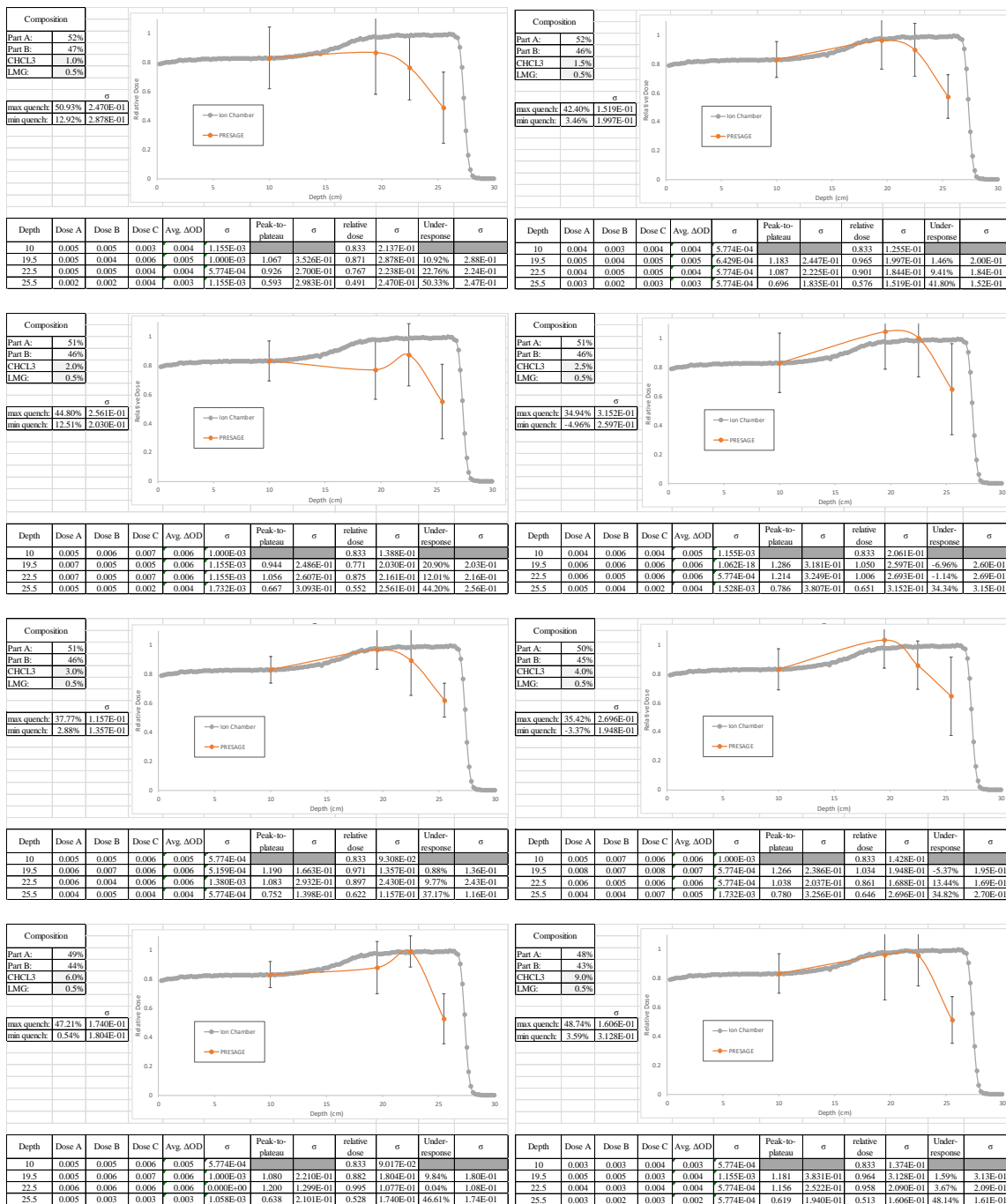
Part A: 42%
Part B: 38%
CHBr3 16.0%
LMG: 4.0%

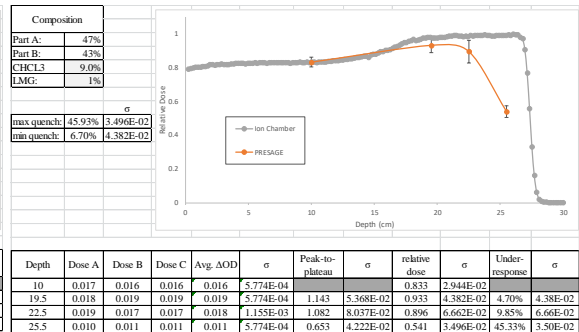
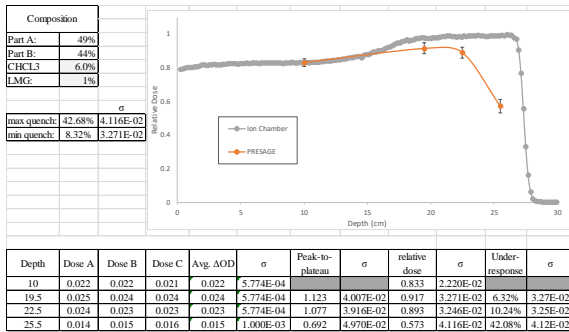
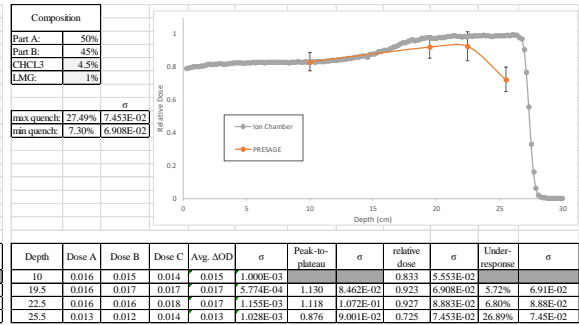
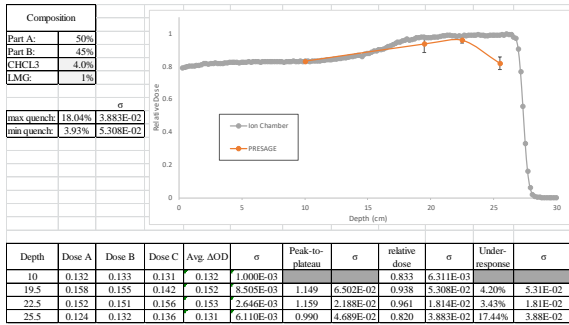
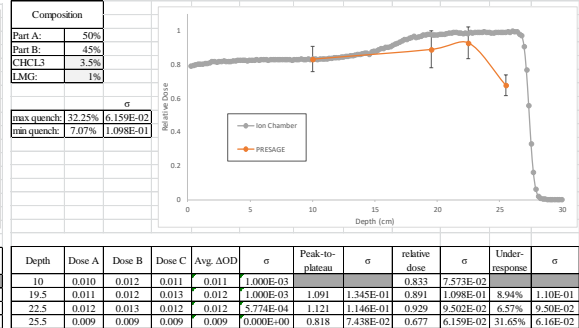
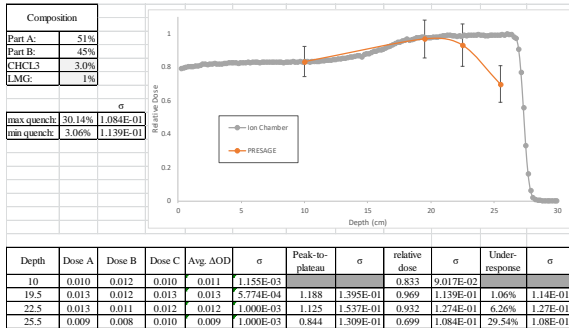
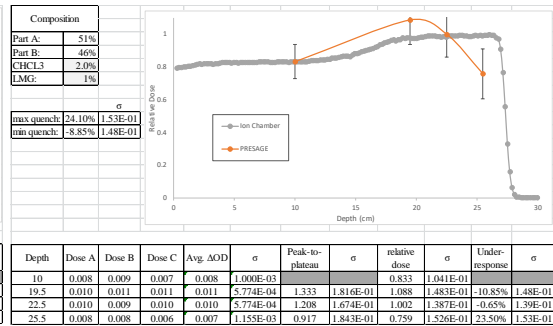
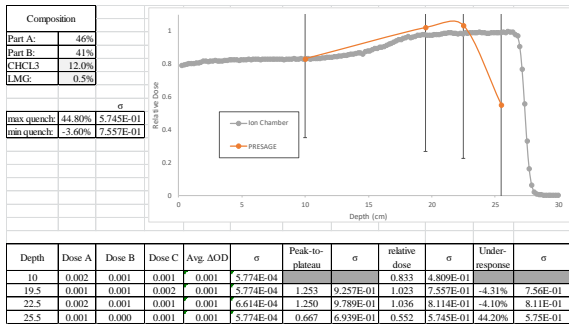
σ

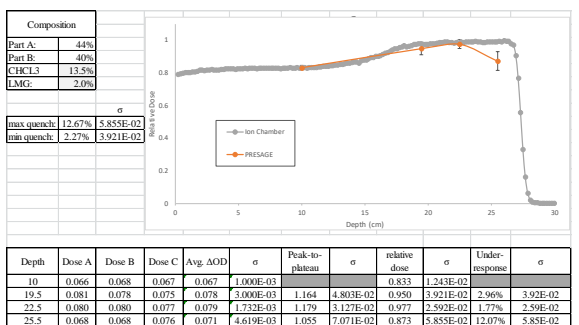
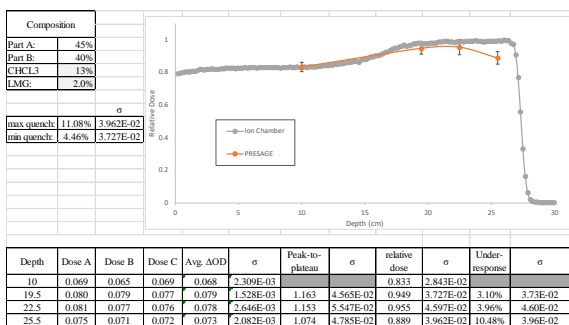
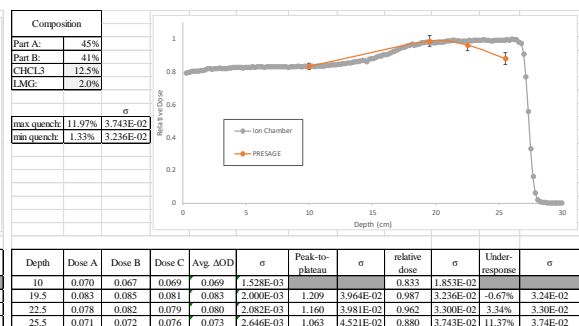
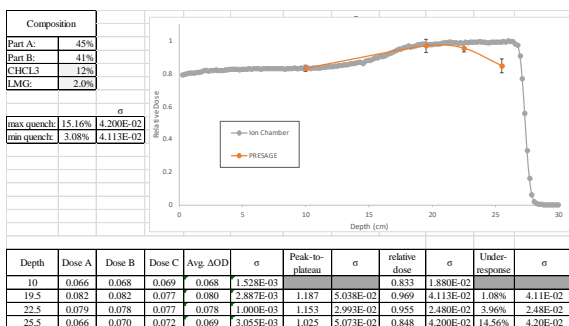
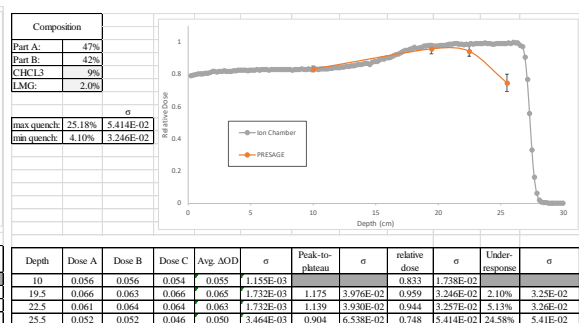
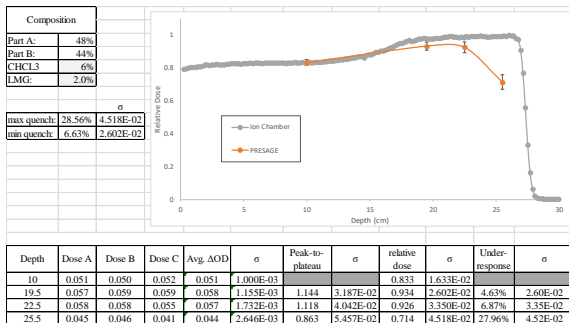
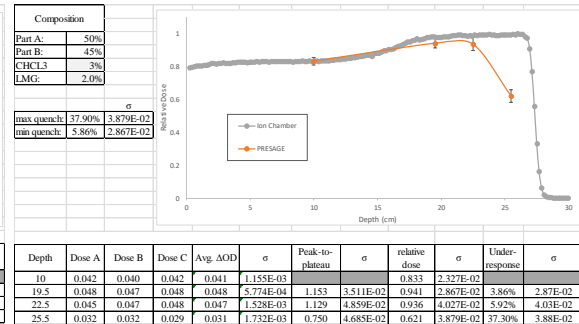
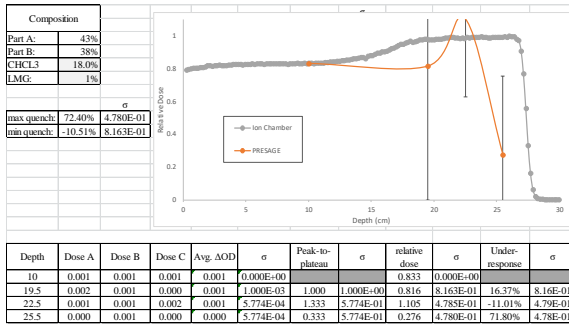
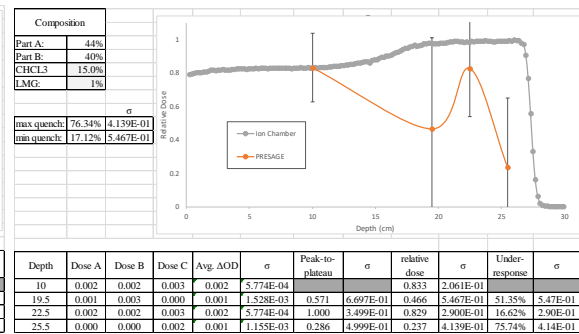
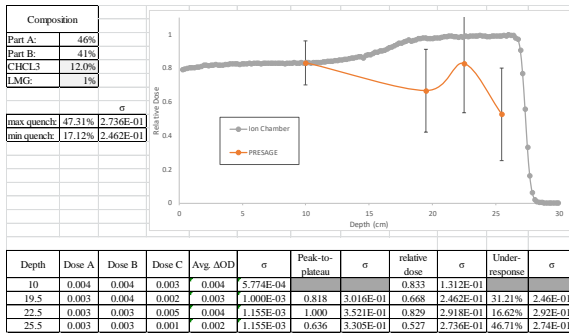
max quench: 11.33%
min quench: 3.78%

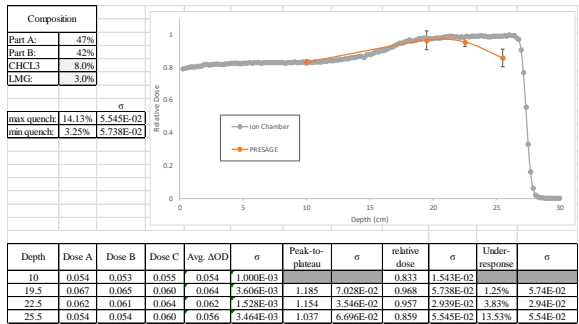
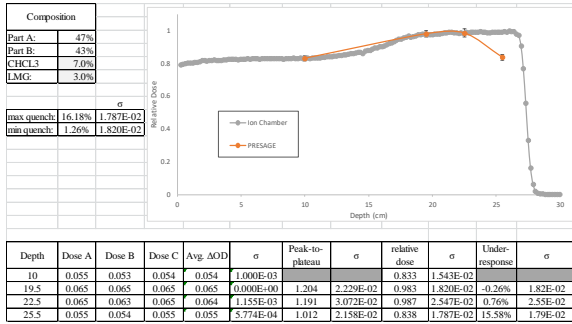
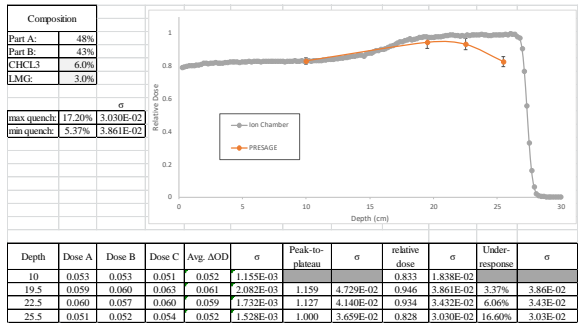
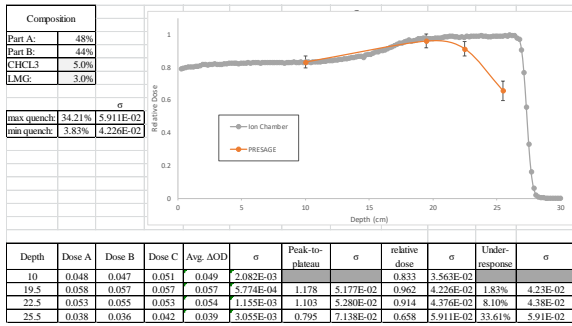
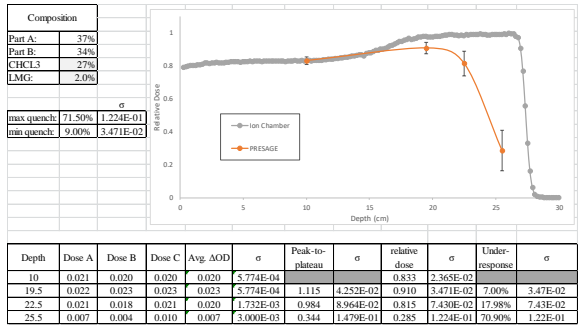
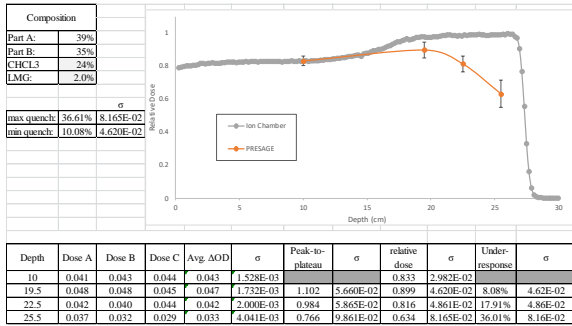
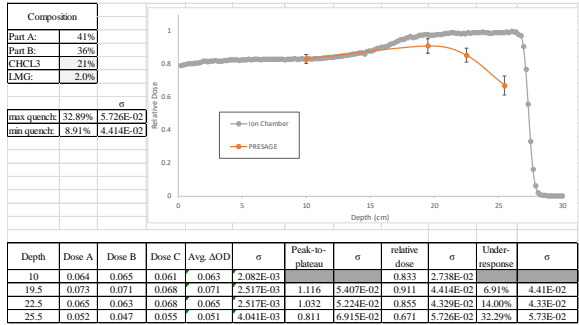
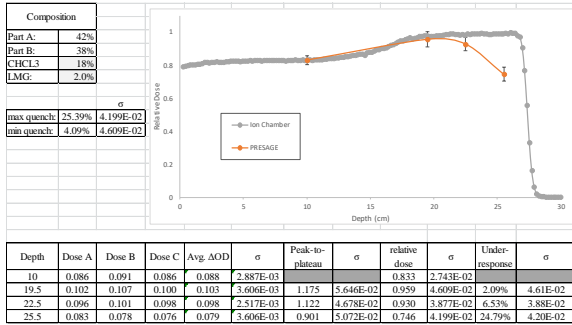
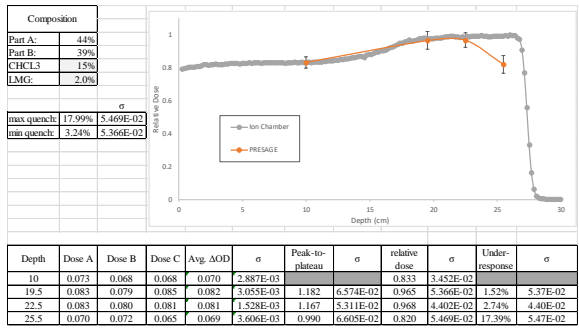
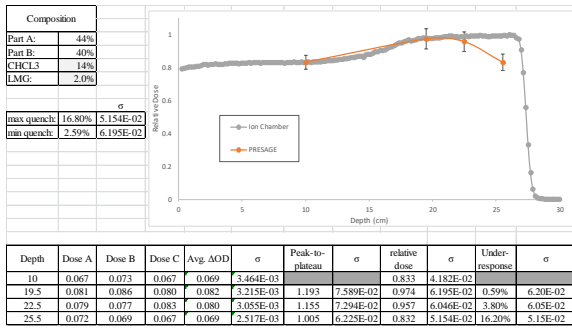


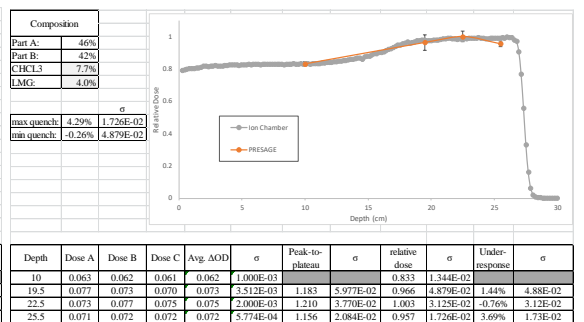
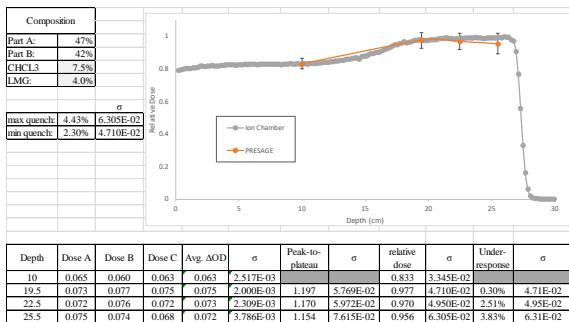
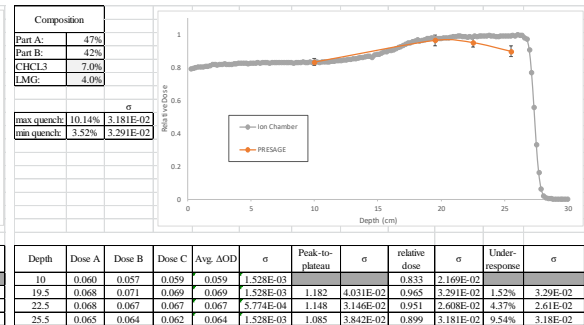
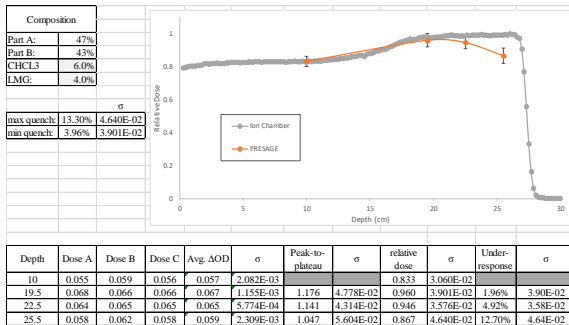
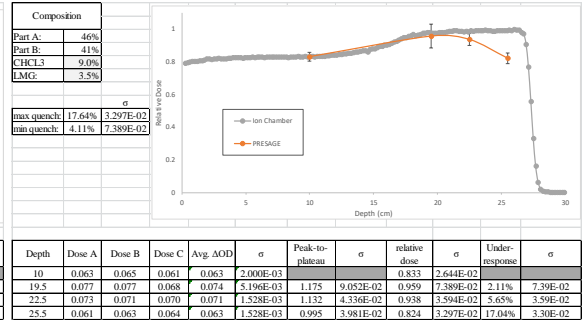
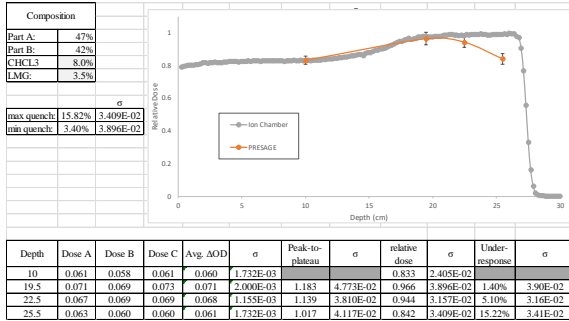
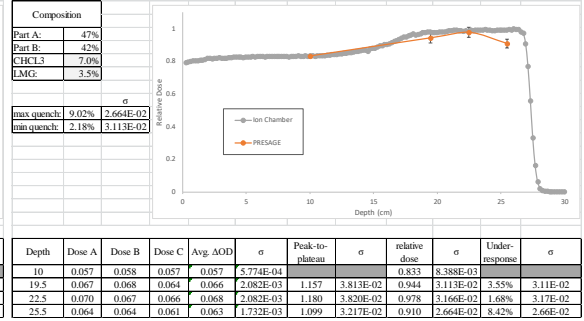
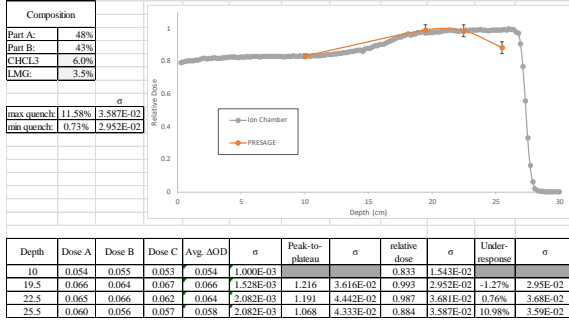
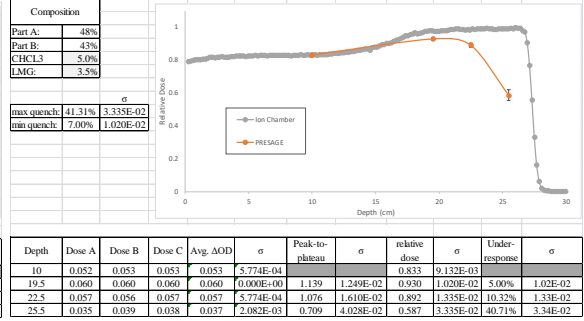
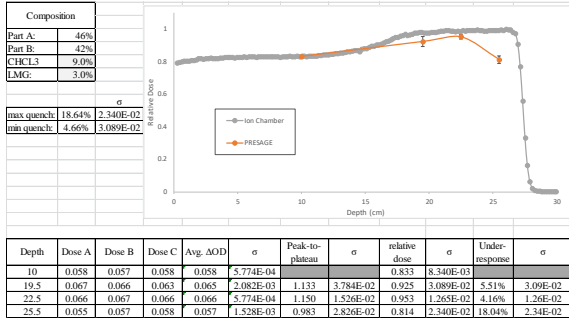
5. Formulation quenching measurements (Chloroform based dosimeters)

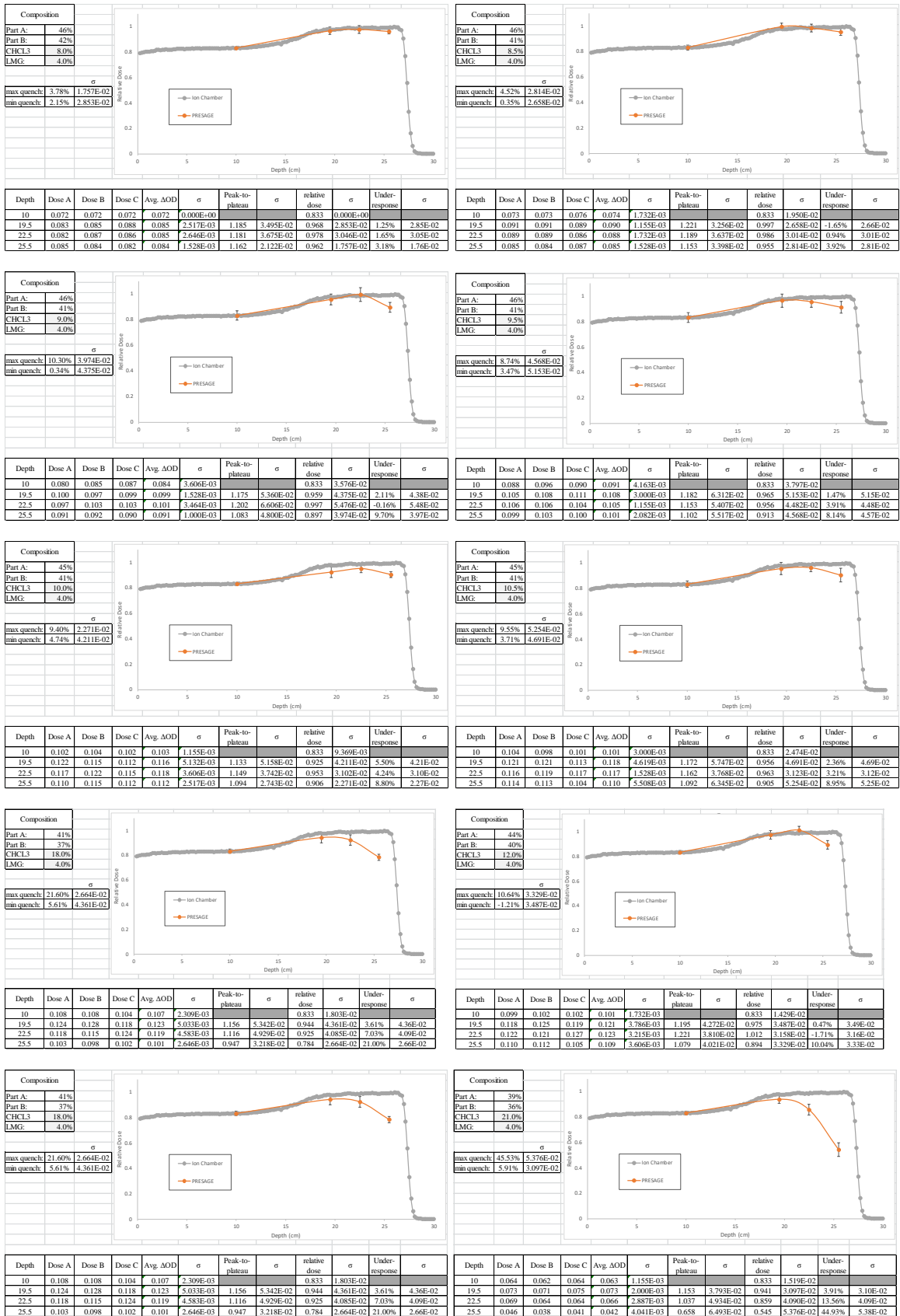


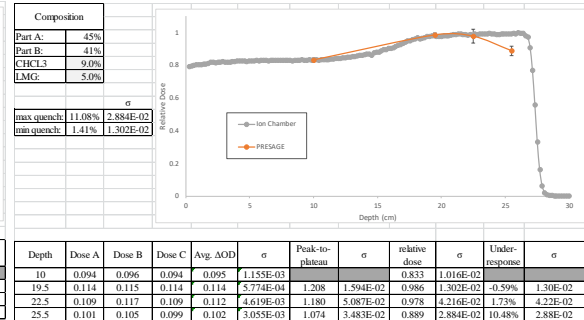
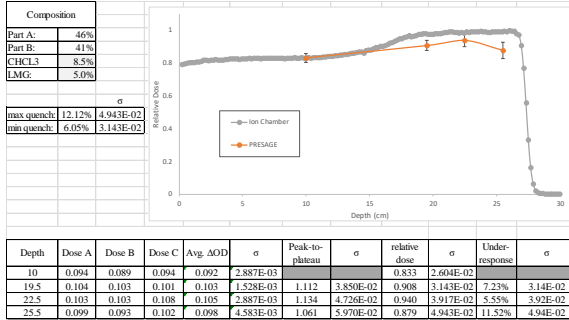
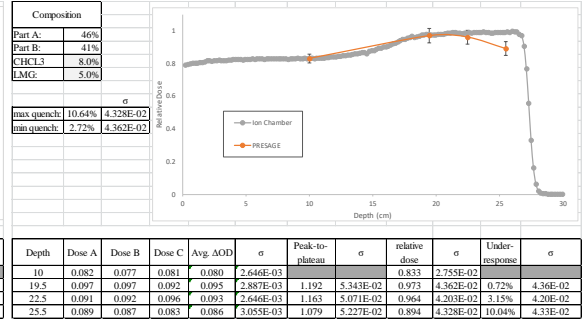
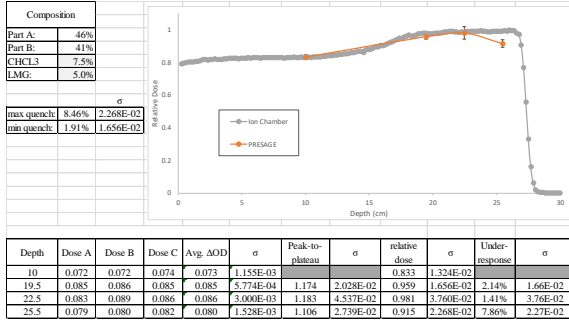
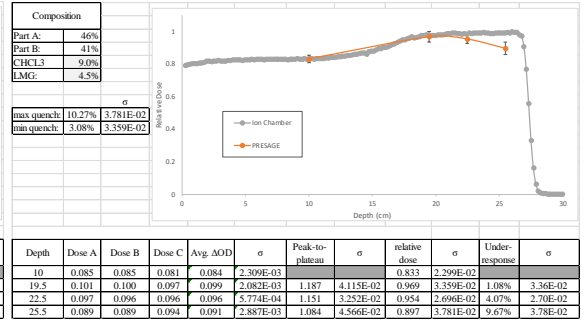
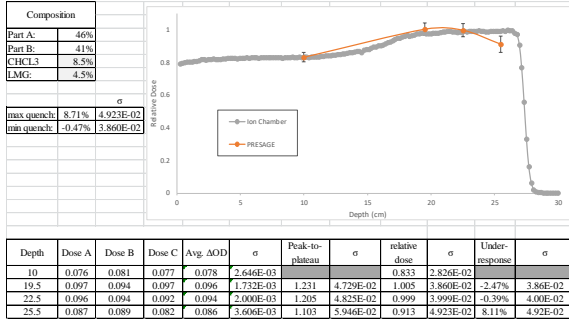
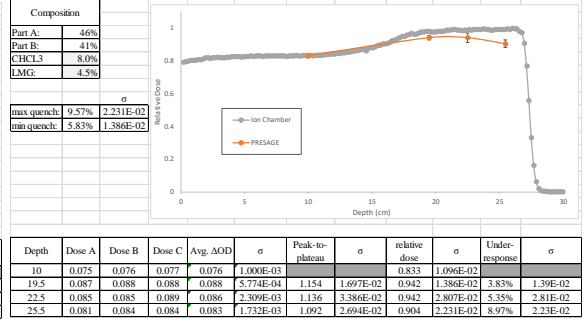
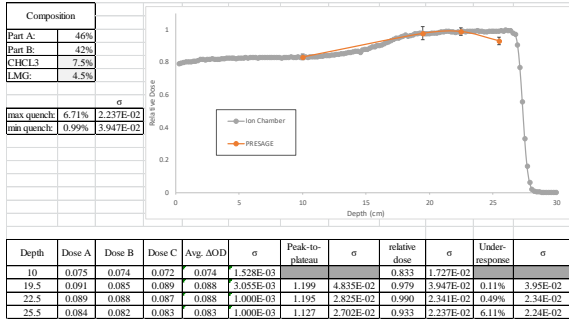
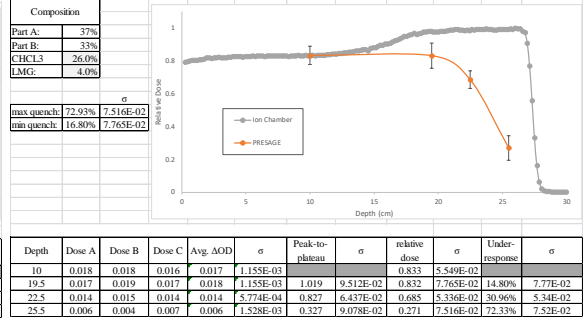
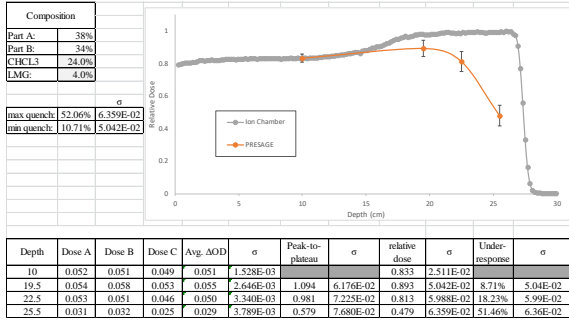


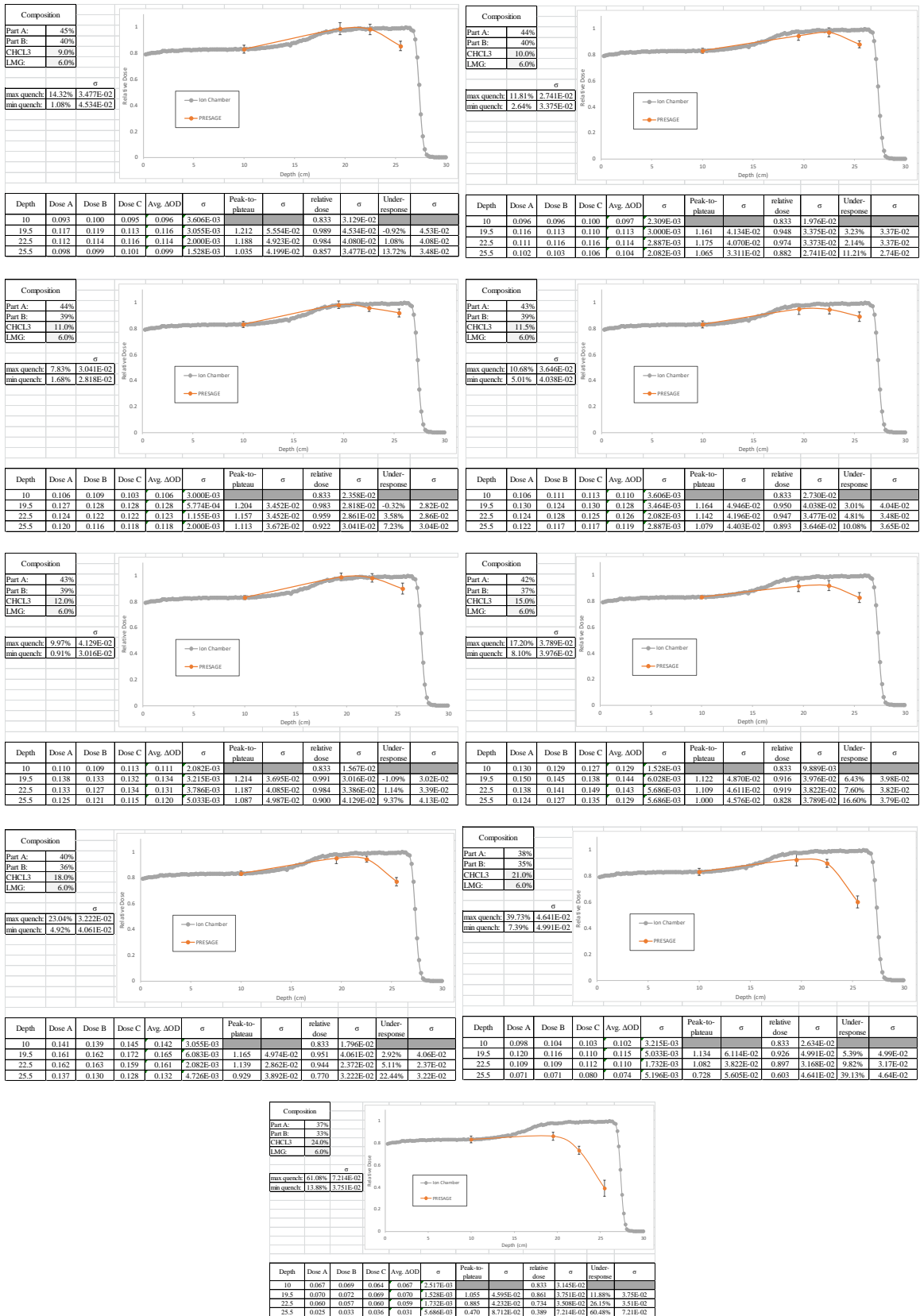












6. MCNP6.1 material and geometric cards.

PRESAGE in water tank irradiation

c Cell Cards

```
c ccccccccccccccccccccccccccccccccccccccccccccccccccccccccccccc80
401 502 -1.109 -542 -541 521          imp:p,n,e,h=1 $PRESAGE
402 504 -1.41 -521 532 -533 534 -535 536  imp:p,n,e,h=1 $PRESAGE base
403 505 -1.04 -521 510 -537 538 -539 540 #402 imp:p,n,e,h=1 $Foam base
404 501 -1.00 -512 -502 504 -506 508 510 #401
      #402 #403          imp:p,n,e,h=1 $Water
405 503 -1.18 -501 502 -511 510 -505 507  imp:p,n,e,h=1 $Wall1
406 503 -1.18 -504 503 -511 510 -505 507  imp:p,n,e,h=1 $Wall2
407 503 -1.18 -505 506 -511 510 -501 503  imp:p,n,e,h=1 $Wall3
408 503 -1.18 -508 507 -511 510 -501 503  imp:p,n,e,h=1 $Wall4
409 503 -1.18 -510 509 -501 503 -505 507  imp:p,n,e,h=1 $Wall5
498 506 -1.23E-3 -550 #401 #402 #403 #404 #405 #406
      #407 #408 #409          imp:p,n,e,h=1 $Surrounding air
499 0      550          imp:p,n,e,h=0 $Universe
c ccccccccccccccccccccccccccccccccccccccccccccccccccccccccccccc80
```

c Surface Cards

```
c ccccccccccccccccccccccccccccccccccccccccccccccccccccccccccccc80
c
```

c Planar Surfaces (Water tank)

```
501 px 12.5          $Depth (parallel to Y) walls
502 px 11.9
503 px -12.5
504 px -11.9
c
505 py 15          $Width (parallel to X) walls
506 py 14.6
507 py -15
508 py -14.6
c
```

509 pz 0 \$Height (parallel to Z) walls

510 pz 0.6

511 pz 33.3

c

c Planar Surfaces (materials)

512 pz 20 \$Water height (minus 0.6cm)

521 pz 2.6 \$Top of polystyrene

532 pz 2.38 \$Base dimensions

533 px 1.5

534 px -1.5

535 py 1.5

536 py -1.5

537 px 7.5 \$Foam dimensions

538 px -7.5

539 py 7.5

540 py -7.5

541 pz 9.9 \$top of PRESAGE

c

c Cylindrical Surfaces

542 cz 3.1 \$PRESAGE cylinder

c

c Spherical Surfaces

550 so 100 \$Air

c

c ccc80

c Data Cards

c ccc80

c

c Material Definitions

m501 1000 0.667 8000 0.333 \$Water

m502 1000 -0.08661505 6000 -0.5988283 8000 -0.18749065

17000 -0.071272 50000 -0.000094 \$PRESAGE

m503 1000 -0.080538 6000 -0.599848 8000 -0.319614 \$Lucite

References

1. Klein EE, Hanley J, Bayouth J, Yin F-F, Simon W, Dresser S, Serago C, Aguirre F, Ma L, Arjomandy B, Liu C, Sandin C, Holmes T. Task Group 142 report: Quality assurance of medical accelerators. *Med Phys*. 2009;36(9):4197. doi:10.1118/1.3190392
2. Molloy JA, Chan G, Markovic A, McNeeley S, Pfeiffer D, Salter B, Tome WA. Quality assurance of U.S.-guided external beam radiotherapy for prostate cancer: Report of AAPM Task Group 154. *Med Phys*. 2011;38(2):857-871. doi:10.1118/1.3531674
3. Ibbott GS, Molineu A, Followill DS. Independent evaluations of IMRT through the use of an anthropomorphic phantom. *Technol Cancer Res Treat*. 2006;5(5):481-487. doi:d=3025&c=4214&p=15273&do=detail [pii]
4. Ibbott GS, Haworth A, Followill DS. Quality Assurance for Clinical Trials. *Front Oncol*. 2013;3:311. doi:10.3389/fonc.2013.00311
5. Das IJ, Cheng C-W, Chopra KL, Mitra RK, Srivastava SP, Glatstein E. Intensity-Modulated Radiation Therapy Dose Prescription, Recording, and Delivery: Patterns of Variability Among Institutions and Treatment Planning Systems. *JNCI J Natl Cancer Inst*. 2008;100(5):300-307. doi:10.1093/jnci/djn020
6. Taylor PA, Kry SF, Alvarez P, Keith T, Lujano C, Hernandez N, Followill DS. Results From the Imaging and Radiation Oncology Core Houston's Anthropomorphic Phantoms Used for Proton Therapy Clinical Trial Credentialing. *Int J Radiat Oncol Biol Phys*. 2016;95(1):242-248.

doi:10.1016/j.ijrobp.2016.01.061

7. Fong PM, Keil DC, Does MD, Gore JC. Polymer gels for magnetic resonance imaging of radiation dose distributions at normal room atmosphere. *Phys Med Biol.* 2001;46(12):3105-3113. doi:10.1088/0031-9155/46/12/303
8. Deene Y De, Hurley C, Venning A, Vergote K, Mather M, Healy BJ, Baldock C. A basic study of some normoxic polymer gel dosimeters. *Phys Med Biol.* 2002;47(19):3441-3463. doi:10.1088/0031-9155/47/19/301
9. Schreiner LJ. Review of Fricke gel dosimeters. *J Phys Conf Ser.* 2004;3:9-21. doi:10.1088/1742-6596/3/1/003
10. Sakhalkar H, Sterling D, Adamovics J, Ibbott G, Oldham M. Investigation of the feasibility of relative 3D dosimetry in the Radiologic Physics Center Head and Neck IMRT phantom using Presage/optical-CT. *Med Phys.* 2009;36(7):3371-3377. doi:10.1118/1.3148534
11. Oldham M, Sakhalkar H, Guo P, Adamovics J. An investigation of the accuracy of an IMRT dose distribution using two- and three-dimensional dosimetry techniques. *Med Phys.* 2008;35(5):2072-2080. doi:10.1118/1.2899995
12. Juang T, Grant R, Adamovics J, Ibbott G, Oldham M. On the feasibility of comprehensive high-resolution 3D remote dosimetry. *Med Phys.* 2014;41(7):071706. doi:10.1118/1.4884018
13. PTCOG - Facilities in Planning Stage. <https://www.ptcog.ch/index.php/facilities-in-planning-stage>. Accessed October 6, 2017.

14. Wu C, Xu Y, Qian X, Adamovics J, Cascio E, Lu H. Dosimetric assessment of the PRESAGE dosimeter for a proton pencil beam. *J Phys Conf Ser.* 2012;444:5-8. doi:10.1088/1742-6596/444/1/012055
15. Zhao L, Das IJ, Zhao Q, Thomas A, Adamovics J, Oldman M. Determination of the depth dose distribution of proton beam using PRESAGE TM dosimeter. *J Phys Conf Ser.* 2010;250(1):012035. doi:10.1088/1742-6596/250/1/012035
16. Zhao L, Newton J, Oldham M, Das IJ, Cheng C-W, Adamovics J. Feasibility of using PRESAGE® for relative 3D dosimetry of small proton fields. *Phys Med Biol.* 2012;57(22):N431-N443. doi:10.1088/0031-9155/57/22/N431
17. RÖNTGEN WC. On a new kind of rays. *Science (80-).* 1896;3(59):227-231. <http://science.sciencemag.org/content/3/59/227.abstract>.
18. Pusey A. Roentgen-Rays in the treatment of skin diseases and for the removal of hair. *J Cutan Genitourin Dis.* 1900;18:302-315. doi:10.1001/archderm.1983.01650260070022
19. Belot J. *Radiotherapy in Skin Disease*. Rebman; 1905.
20. Grubbé EH. Priority in the Therapeutic Use of X-rays. *Radiology.* 1933;21(2):156-162. doi:10.1148/21.2.156
21. del Regato J. *Radiological Physicists*. Amer Inst of Physics; 1985.
22. Curie Sklodowska M. Radium and Radioactivity. *Century Mag.* 1904:461-466.
23. Curie E. Marie and Pierre Curie and the discovery of radium. *Br J Radiol.*

1950;23(271):409-412. doi:10.1259/0007-1285-23-271-409

24. Metzenbaum M. Radium: Its value in the treatment of lupus, rodent ulcer, and epithelioma. *Int Clin A Q J Illus Clin Lect.* 1905;4(14):21-31.
25. Mackee GM. *X-Rays and Radium in the Treatment of Diseases of the Skin.* Lea & Febiger; 1921.
26. Bright C. A British radium discovery. *J Ind Eng Chem.* 1910;2:558.
27. Thames HD. Early fractionation methods and the origins of the NSD concept. *Acta Oncol (Madr).* 1988;27(2):89-103. doi:10.3109/02841868809090329
28. Siegel RL, Miller KD, Jemal A. Cancer statistics, 2016. *CA Cancer J Clin.* 2016;66(1):7-30. doi:10.3322/caac.21332
29. Valdivieso M, Kujawa AM, Jones T, Baker LH. Cancer survivors in the United States: A review of the literature and a call to action. *Int J Med Sci.* 2012;9(2):163-173. doi:10.7150/ijms.3827
30. Taylor BN, Thompson A. *The International System of Units.*; 2008. doi:10.1007/BF01449764
31. Berry R, Oliver R. Effect of Post-irradiation Incubation Conditions on Recovery between Fractionated Doses of X-rays. *Nature.* 1964;201:94. <http://dx.doi.org/10.1038/201094b0>.
32. Elkind MM, Sutton H. X-ray damage and recovery in mammalian cells in culture. *Nature.* 1959;184(4695):1293-1295. doi:10.1038/1841293a0

33. Ramroth J, Cutter DJ, Darby SC, Higgins GS, McGale P, Partridge M, Taylor CW. Dose and Fractionation in Radiation Therapy of Curative Intent for Non-Small Cell Lung Cancer: Meta-Analysis of Randomized Trials. *Int J Radiat Oncol Biol Phys.* 2016;96(4):736-747. doi:10.1016/j.ijrobp.2016.07.022
34. Fletcher GH. Regaud lecture perspectives on the history of radiotherapy. *Radiother Oncol.* 1988;12(4):253-271. doi:10.1016/0167-8140(88)90015-1
35. *Radiotherapy Dose Fractionation.* 2nd ed.; 2016. https://www.rcr.ac.uk/system/files/publication/field_publication_files/bfco163_dose_fractionation_2nd_ed_march2017.pdf. Accessed January 6, 2018.
36. Bushberg JT, Seibert JA, Leidholdt EM, Boone JM. *The Essential Physics of Medical Imaging.* 3rd ed.; 2012.
37. Lawrence EO, Livingston MS. The production of high speed light ions without the use of high voltages. *Phys Rev.* 1932;40(1):19-35. doi:10.1103/PhysRev.40.19
38. Wilson RR. Radiological Use of Fast Protons. *Radiology.* 1946;47(5):487-491. doi:10.1148/47.5.487
39. Tobias CA, Lawrence JH, Born JL, McCombs RK, Roberts JE, Anger HO, Low-Beer BVA, Huggins CB. Pituitary Irradiation with High-Energy Proton Beams A Preliminary Report. *Cancer Res.* 1958;18(2):121-134.
40. Wilson R. *A Brief History of the Harvard University Cyclotrons.* Harvard University Department of Physics; 2004.
41. Seltzer S, Berger M. Energy Loss Straggling of Protons and Mesons: Tabulation of

the Vavilov Distribution. *Stud Penetration Charg Part Matter; Nucl Sci Ser.* 1964;39:187.

42. Brown A, Suit H. The centenary of the discovery of the Bragg peak. *Radiother Oncol.* 2004;73(3):265-268. doi:10.1016/j.radonc.2004.09.008
43. Niemierko A, Urie M, Goitein M. Optimization of 3D radiation therapy with both physical and biological end points and constraints. *Int J Radiat Oncol.* 1992;23(1):99-108. doi:10.1016/0360-3016(92)90548-V
44. Lomax AJ, Bortfeld T, Goitein G, Debus J, Dykstra C, Tercier PA, Coucke PA, Mirimanoff RO. A treatment planning inter-comparison of proton and intensity modulated photon radiotherapy. *Radiother Oncol.* 1999;51(3):257-271. doi:10.1016/S0167-8140(99)00036-5
45. Weber DC, Wang H, Cozzi L, Dipasquale G, Khan HG, Ratib O, Rouzaud M, Veas H, Zaidi H, Miralbell R. RapidArc, intensity modulated photon and proton techniques for recurrent prostate cancer in previously irradiated patients: A treatment planning comparison study. *Radiat Oncol.* 2009;4:34. doi:10.1186/1748-717X-4-34
46. Steneker M, Lomax A, Schneider U. Intensity modulated photon and proton therapy for the treatment of head and neck tumors. *Radiother Oncol.* 2006;80(2):263-267. doi:10.1016/j.radonc.2006.07.025
47. Chera BS, Vargas C, Morris CG, Louis D, Flampouri S, Yeung D, Duvvuri S, Li Z, Mendenhall NP. Dosimetric Study of Pelvic Proton Radiotherapy for High-Risk

Prostate Cancer. *Int J Radiat Oncol Biol Phys.* 2009;75(4):994-1002.
doi:10.1016/j.ijrobp.2009.01.044

48. Widesott L, Pierelli A, Fiorino C, Lomax AJ, Amichetti M, Cozzarini C, Soukup M, Schneider R, Hug E, Di Muzio N, Calandrino R, Schwarz M. Helical tomotherapy vs. Intensity-modulated proton therapy for whole pelvis irradiation in high-risk prostate cancer patients: Dosimetric, normal tissue complication probability, and generalized equivalent uniform dose analysis. *Int J Radiat Oncol Biol Phys.* 2011;80(5):1589-1600. doi:10.1016/j.ijrobp.2010.10.005
49. Simone CB, Ly D, Dan TD, Ondos J, Ning H, Belard A, O'Connell J, Miller RW, Simone NL. Comparison of intensity-modulated radiotherapy, adaptive radiotherapy, proton radiotherapy, and adaptive proton radiotherapy for treatment of locally advanced head and neck cancer. *Radiother Oncol J Eur Soc Ther Radiol Oncol.* 2011;101(3):376-382. doi:10.1016/j.radonc.2011.05.028
50. Remick J, Schonewolf C, Gabriel P, Kralik JC, Levin WP, Kucharczuk JC, Pechet TT, Rengan R, Simone II CB, Berman AT. First Clinical Report of Proton Beam Therapy Versus Intensity Modulated Radiation Therapy for Postoperative Radiation Therapy for Non-Small Cell Lung Cancer. *Int J Radiat Oncol • Biol • Phys.* 2018;93(3):E422-E423. doi:10.1016/j.ijrobp.2015.07.1624
51. Reiazi R, Norozi A, Etedadialiabadi M. A Literature Survey on Cost-Effectiveness of Proton Beam Therapy in the Management of Breast Cancer Patients. 2015;8(6). doi:10.17795/ijcp-4373
52. Lievens Y, Pijls-Johannesma M. Health Economic Controversy and Cost-

Effectiveness of Proton Therapy. *YSRAO*. 2013;23:134-141.
doi:10.1016/j.semradonc.2012.11.005

53. Peeters A, Grutters JPC, Pijls-Johannesma M, Reimoser S, De Ruyscher D, Severens JL, Joore MA, Lambin P. How costly is particle therapy? Cost analysis of external beam radiotherapy with carbon-ions, protons and photons. *Radiother Oncol*. 2010;95:45-53. doi:10.1016/j.radonc.2009.12.002
54. Isacsona U, Hagbergayc H, Johanssond K-A, Monteliusb A, Jungb B. Potential advantages of protons over conventional radiation beams for paraspinal tumours. *Radiother Oncol*. 1997;45:63-70.
55. Zhang X, Li Y, Pan X, Xiaoqiang L, Mohan R, Komaki R, Cox JD, Chang JY. Intensity-modulated proton therapy reduces the dose to normal tissue compared with intensity-modulated radiation therapy or passive scattering proton therapy and enables individualized radical radiotherapy for extensive stage IIIB non-small-cell lung cancer. *Radiat Oncol Biol*. 77:357-366. doi:10.1016/j.ijrobp.2009.04.028
56. Cozzi L, Fogliata A, Lomax A, Bolsi A. A treatment planning comparison of 3D conformal therapy, intensity modulated photon therapy and proton therapy for treatment of advanced head and neck tumours. *Radiother Oncol*. 2001;61(3):287-297.
57. Park J, Park Y, Lee SU, Kim T, Choi Y-K, Kim J-Y. Differential dosimetric benefit of proton beam therapy over intensity modulated radiotherapy for a variety of targets in patients with intracranial germ cell tumors. 2012. doi:10.1186/s13014-015-0441-5

58. Frank S. Proton Therapy Eliminates Unnecessary Radiation Exposure and is Medically Necessary. *Am J Manag Care*. 2016;(August).
59. Chuong MD, Mehta MP, Langen K, Regine WF. Counterpoints: Is Proton Beam Therapy Better Than Standard Radiation Therapy? *Clin Adv Hematol Oncol*. 2014;12(12).
60. Shioyama Y, Tokuuye K, Okumura T, Kagei K, Sugahara S, Ohara K, Akine Y, Ishikawa S, Satoh H, Sekizawa K. Clinical evaluation of proton radiotherapy for non-small-cell lung cancer. *Int J Radiat Oncol Biol Phys*. 2003;56(1):7-13. doi:10.1016/S0360-3016(02)04416-4
61. Mendenhall N, Wong W, Bryant C, Vora SA, Henderson RH, Keole SR, Hoppe BS, Vargas CE, Nichols RC, Daniels TB, Mendenhall WM, Morris CG, Schild SE. Comparison of clinical outcomes with IMRT and proton therapy for prostate cancer. *J Clin Oncol*. 2017;35(15_suppl):e16555-e16555. doi:10.1200/JCO.2017.35.15_suppl.e16555
62. Fischer-Valuck BW, Mazur TR, Gay HA, Olsen LA, Altman MB, Michalski JM. A Treatment Planning Comparison of Proton Therapy and Intensity Modulated Radiation Therapy (IMRT) for Prostate Cancer Using the Normal Tissue Complication Probability (NTCP). *Int J Radiat Oncol • Biol • Phys*. 2018;96(2):E274. doi:10.1016/j.ijrobp.2016.06.1312
63. Ladra MM, Szymonifka JD, Mahajan A, Friedmann AM, Yong Yeap B, Goebel CP, MacDonald SM, Grosshans DR, Rodriguez-Galindo C, Marcus KJ, Tarbell NJ, Yock TI, Szymonifka J, Goebel C, Yock Massa- TI, Grosshans D. Preliminary

Results of a Phase II Trial of Proton Radiotherapy for Pediatric Rhabdomyosarcoma. *J Clin Oncol.* 2014;32:3762-3770. doi:10.1200/JCO.2014.56.1548

64. Gunther JR, Sato M, Chintagumpala M, Ketonen L, Jones JY, Allen PK, Paulino AC, Fatih Okcu M, Su JM, Weinberg J, Boehling NS, Khatua S, Adesina A, Dauser R, Whitehead WE, Mahajan A. Imaging Changes in Pediatric Intracranial Ependymoma Patients Treated With Proton Beam Radiation Therapy Compared to Intensity Modulated Radiation Therapy. *Radiat Oncol Biol.* 2015;93(1):54-63. doi:10.1016/j.ijrobp.2015.05.018
65. Merchant TE, Sherwood SH, Mulhern RK, Rose SR, Thompson SJ, Sanford RA, And □, Kun LE. CNS germinoma: disease control and long-term functional outcome for 12 children treated with craniospinal irradiation. *Int J Radiat Oncol Biol Phys.* 2000;46(5):1171-1176.
66. Mabbott DJ, Monsalves E, Spiegler BJ, Bartels U, Janzen L, Guger S, Laperriere N, Andrews N, Bouffet E. Longitudinal evaluation of neurocognitive function after treatment for central nervous system germ cell tumors in childhood. *Cancer.* 2011;117(23):5402-5411. doi:10.1002/cncr.26127
67. Bragg WH, Kleeman R. XXXIX. On the α particles of radium, and their loss of range in passing through various atoms and molecules. *London, Edinburgh, Dublin Philos Mag J Sci.* 1905;10(57):318-340. doi:10.1080/14786440509463378
68. Newhauser WD, Zhang R. The physics of proton therapy. *Phys Med Biol.* 2015;60(8):R155-R209. doi:10.1088/0031-9155/60/8/R155

69. Bethe H. Zur Theorie des Durchgangs schneller Korpuskularstrahlen durch Materie. *Ann Phys.* 1930;397(3):325-400. doi:10.1002/andp.19303970303
70. Janni JF. Energy loss, range, path length, time-of-flight, straggling, multiple scattering, and nuclear interaction probability: In two parts. Part 1. For 63 compounds Part 2. For elements $1 < Z < 92$. *At Data Nucl Data Tables.* 1982;27(2):147-339. doi:[https://doi.org/10.1016/0092-640X\(82\)90004-3](https://doi.org/10.1016/0092-640X(82)90004-3)
71. Paganetti H. Range uncertainties in proton therapy and the role of Monte Carlo simulations. *Phys Med Biol.* 2012;57(11):R99-117. doi:10.1088/0031-9155/57/11/R99
72. Deasy J. ICRU Report 49, Stopping Powers and Ranges for Protons and Alpha Particles. *J ICRU.* 1994;21(5):709-710. doi:10.1118/1.597176
73. Ziegler JF, Ziegler MDD, Biersack JPP. SRIM – The Stopping and Range of Ions in Matter (2010). *Nucl Instruments Methods Phys Res Sect B Beam Interact with Mater Atoms.* 2010;268(11-12):1818-1823. doi:10.1016/J.NIMB.2010.02.091
74. Berger M. ESTAR, PSTAR, AND ASTAR: Computer Programs for Calculating. National Institute of Standards and Technology (NIST), Physics Laboratory. <https://physics.nist.gov/PhysRefData/Star/Text/PSTAR.html>. Published 2005. Accessed October 6, 2017.
75. Seltzer SM, Bartlett DT, Burns DT, Dietze G, Menzel HG, Paretzke HG, Wambersie A. Fundamental quantities and units for ionizing radiation. *J ICRU.* 2011;11(1):1-41. doi:10.1093/jicru/ndr011

76. Guan F, Peeler C, Bronk L, Geng C, Taleei R, Randeniya S, Ge S, Mirkovic D, Grosshans D, Mohan R, Titt U. Analysis of the track-and dose-averaged LET and LET spectra in proton therapy using the geant4 Monte Carlo code. doi:10.1118/1.4932217
77. Hawkins RB. A microdosimetric-kinetic theory of the dependence of the RBE for cell death on LET. *Med Phys*. 1998;25(7):1157-1170. doi:10.1118/1.598307
78. Bauer J, Sommerer F, Mairani A, Unholtz D, Farook R, Handrack J, Frey K, Marcelos T, Tessonnier T, Ecker S, Ackermann B, Ellerbrock M, Debus J, Parodi K. Integration and evaluation of automated Monte Carlo simulations in the clinical practice of scanned proton and carbon ion beam therapy. *Phys Med Biol*. 2014;59.
79. Moliere G. Theorie der Streuung schneller geladener Teilchen II Mehrfach-und Vielfachstreuung. *Zeitschrift fur Naturforsch - Sect A J Phys Sci*. 1948;3(2):78-97. doi:10.1515/zna-1948-0203
80. Bethe HA. Molière's Theory of Multiple Scattering. *Phys Rev*. 1953;89(6):1256-1266. doi:10.1103/PhysRev.89.1256
81. Fano U. Inelastic Collisions and the Molière Theory of Multiple Scattering. *Phys Rev*. 1954;93(1):117-120. doi:10.1103/PhysRev.93.117
82. Highland VL. Some practical remarks on multiple scattering. *Nucl Instruments Methods*. 1975;129(2):497-499. doi:https://doi.org/10.1016/0029-554X(75)90743-0
83. Gottschalk B. On the scattering power of radiotherapy protons. *Med Phys*.

2009;37(1):352-367. doi:10.1118/1.3264177

84. Paganetti H, Bortfeld T. *Proton Beam Radiotherapy - The State of the Art.*; 2005. doi:10.1118/1.1999671
85. Van Goethem MJ, Van Der Meer R, Reist HW, Schippers JM. Geant4 simulations of proton beam transport through a carbon or beryllium degrader and following a beam line. *Phys Med Biol.* 2009;54:5831-5846. doi:10.1088/0031-9155/54/19/011
86. Moyers MF, Lesyna DA. Exposure from residual radiation after synchrotron shutdown. *Radiat Meas.* 2009;44(2):176-181. doi:10.1016/j.radmeas.2009.01.009
87. DeLuca PM, Wambersie A, Whitmore G. Prescribing, recording, and reporting proton-beam therapy. *J ICRU.* 2007;7(2):1-210. doi:10.1093/jicru/ndm021
88. Smith A, Gillin M, Bues M, Zhu XR, Suzuki K, Mohan R, Woo S, Lee A, Komaki R, Cox J, Hiramoto K, Akiyama H, Ishida T, Sasaki T, Matsuda K. The M. D. Anderson proton therapy system. *Med Phys.* 2009;36(9Part1):4068-4083. doi:10.1118/1.3187229
89. Chu WT, Ludewigt BA, Renner TR. Instrumentation for treatment of cancer using proton and light-ion beams. *Rev Sci Instrum.* 1993;64(8):2055-2122. doi:10.1063/1.1143946
90. Koehler AM, Schneider RJ, Sisterson JM. Flattening of proton dose distributions for large-field radiotherapy. *Med Phys.* 1977;4(4):297-301. doi:10.1118/1.594317
91. Grusell E, Montelius A, Brahme A, Rikner G, Russell K. A general solution to charged particle beam flattening using an optimized dual-scattering-foil technique,

- with application to proton therapy beams. *Phys Med Phys Med Biol.* 1994;39.
92. Weber U, Becher W, Kraft G. Depth scanning for a conformal ion beam treatment of deep seated tumours. *Phys Med Biol.* 2000;45(00):3627-3641.
 93. Kawachi K, Kanai T, Matsuzawa H, Inada T. Three dimensional spot beam scanning method for proton conformation radiation therapy. *Acta Radiol Suppl.* 1983;364:81-88.
 94. Gillin MT, Sahoo N, Bues M, Ciangaru G, Sawakuchi G, Poenisch F, Arjomandy B, Martin C, Titt U, Suzuki K, Smith AR, Zhu XR. Commissioning of the discrete spot scanning proton beam delivery system at the University of Texas M.D. Anderson Cancer Center, Proton Therapy Center, Houston. *Med Phys.* 2009;37(1):154-163. doi:10.1118/1.3259742
 95. DeLuca PM, Wambersie A, Whitmore G. ICRU Report 78: Prescribing, Recording and Reporting Proton-Beam Therapy. In: *Journal of the ICRU.* Vol 7. ; 2008:1-210. doi:10.1093/jicru/ndm042
 96. Arjomandy B, Sahoo N, Zhu XR, Zullo JR, Wu RY, Zhu M, Ding X, Martin C, Ciangaru G, Gillin MT. An overview of the comprehensive proton therapy machine quality assurance procedures implemented at The University of Texas M. D. Anderson Cancer Center Proton Therapy Center–Houston. *Med Phys.* 2009;36(6):2269-2282. doi:10.1118/1.3120288
 97. Hiramoto K, Umezawa M, Saito K, Tootake S, Nishiuchi H, Hara S, Tanaka M, Matsuda K, Sakurabata H, Moriyama K. The synchrotron and its related

- technology for ion beam therapy. *Nucl Instruments Methods Phys Res Sect B Beam Interact with Mater Atoms*. 2007;261(1):786-790. doi:10.1016/j.nimb.2007.04.287
98. Ash D, Bates T. Report on the Clinical Effects of Inadvertent Radiation Underdosage in 1045 Patients. *Clin Oncol*. 1994;6:214-225.
 99. Determination of Absorbed Dose in a Patient Irradiated by Beams of X or Gamma Rays in Radiotherapy Procedures. *J ICRU*. 1976;Report 24.
 100. Andreo P, Huq MS, Kanai T, Laitano F, Smyth V, Zealand N, Vynckier S, Burns DT, Hohlfield K. Absorbed Dose Determination in External Beam Radiotherapy. *Iaea Trs-398*. 2000;2004(April):181. doi:10.1097/00004032-200111000-00017
 101. Task Group 20: Protocol for heavy charged-particle therapy beam dosimetry. *AAPM Am Assoc Phys Med*. 1986.
 102. Verhey L, Blattman H, DeLuca P, Miller D. ICRU Report 59: Clinical proton dosimetry, Part I: beam production, beam delivery and measurement of absorbed dose. *J ICRU*. 1998;59(15):1-67.
 103. Dhanesar S, Sahoo N, Kerr M, Taylor MB, Summers P, Zhu XR, Poenisch F, Gillin M. Quality assurance of proton beams using a multilayer ionization chamber system. *Med Phys*. 2013;40(9):092102. doi:10.1118/1.4817481
 104. Aguirre JF, Tailor RC, Ibbott G, Stovall M, Hanson WF. Thermoluminescence dosimetry as a tool for the remote verification of output for radiotherapy beams: 25 years of experience. *Int At Energy Agency*. 2003.
 105. Pai S, Das IJ, Dempsey JF, Lam KL, LoSasso TJ, Olch AJ, Palta JR, Reinstein LE,

- Ritt D, Wilcox EE. TG-69: Radiographic film for megavoltage beam dosimetry. *Med Phys*. 2007;34(6):2228-2258. doi:10.1118/1.2736779
106. Kim J, Yoon M, Kim S, Shin D, Lee SB, Lim YK, Kim DW, Park SY. Three-dimensional radiochromic film dosimetry of proton clinical beams using a gafchromic EBT2 film array. *Radiat Prot Dosimetry*. 2012;151(2):272-277. doi:10.1093/rpd/ncs010
 107. Arjomandy B, Tailor R, Anand A, Sahoo N, Gillin M, Prado K, Vicic M. Energy dependence and dose response of Gafchromic EBT2 film over a wide range of photon, electron, and proton beam energies. *Med Phys*. 2010;37(5):1942-1947. doi:10.1118/1.3373523
 108. Daniel Kirby, Stuart Green, Hugo Palmans, Richard Hugtenburg, Cecile Wojnecki, David Parker, Kirby D, Green S, Palmans H, Hugtenburg R, Wojnecki C, Parker D. LET dependence of GafChromic films and an ion chamber in low-energy proton dosimetry. *Phys Med Biol* Daniel Kirby *et al* *Phys Med Biol*. 2010;55(2):417-433. doi:10.1088/0031-9155/55/2/006
 109. Yeo IJ, Teran A, Ghebremedhin A, Johnson M, Patyal B. Radiographic film dosimetry of proton beams for depth-dose constancy check and beam profile measurement. *J Appl Clin Med Phys*. 2015;16(3):318-328. doi:10.1120/jacmp.v16i3.5402
 110. Mumot M, Mytsin G V, Molokanov AG, Malicki J. The comparison of doses measured by radiochromic films and semiconductor detector in a 175 MeV proton beam. *Phys Medica*. 2008;25:105-110. doi:10.1016/j.ejmp.2008.06.001

111. Spielberger B, Scholz M, Kr mer M, Kraft G, Krämer M, Kraft G. Calculation of the x-ray film response to heavy charged particle irradiation. 2002;47. doi:10.1088/0031-9155/47/22/313
112. Spielberger B, Scholz M, Krämer M, Kraft G. Experimental investigations of the response of films to heavy-ion irradiation. *Phys Med Biol B Spielberger al Phys Med Biol Phys Med Biol*. 2001;46(46):2889-2897.
113. Spielberger B, Krämer M, Kraft G. Three-dimensional dose verification with x-ray films in conformal carbon ion therapy. *Phys Med Biol Phys Med Biol*. 2003;48:497-505.
114. Arjomandy B, Sahoo N, Ding X, Gillin M. Use of a two-dimensional ionization chamber array for proton therapy beam quality assurance. *Med Phys*. 2008;35(9):3889-3894. doi:10.1118/1.2963990
115. Nichiporov D, Solberg K, Hsi W, Wolanski M, Mascia A, Farr J, Schreuder A. Multichannel detectors for profile measurements in clinical proton fields. *Med Phys*. 2007;34(7):2683-2690. doi:10.1118/1.2746513
116. Oozeer R, Mazal A, Rosenwald JC, Belshi R, Nauraye C, Ferrand R, Biensan S. A model for the lateral penumbra in water of a 200-MeV proton beam devoted to clinical applications. *Med Phys*. 1997;24(10):1599-1604. doi:10.1118/1.597967
117. Liengsawangwong P, Sahoo N, Ding X, Lii M, Gillin MT, Zhu XR. Dosimetric Characteristics of a Two-Dimensional Diode Array Detector Irradiated with Passively Scattered Proton Beams. *Cancers (Basel)*. 2015;7:1425-1435.

118. Erik Grusell, Joakim Medin. General characteristics of the use of silicon diode detectors for clinical dosimetry in proton beams. *Phys Med Biol Erik Grusell al Phys Med Biol Phys Med Biol*. 2000;45(45):2573-2582.
119. Newhauser WD, Myers KD, Rosenthal SJ, Smith AR. Proton beam dosimetry for radiosurgery: implementation of the ICRU Report 59 at the Harvard Cyclotron Laboratory. *Phys Med Biol*. 2002;47(8):1369-1389. doi:10.1088/0031-9155/47/8/310
120. Pacilio M, Angelis C De, Onori S, Azario L, Fidanzio A, Miceli R, Piermattei A, Kacperek A. Characteristics of silicon and diamond detectors in a 60 MeV proton beam. *Phys Med Biol*. 2002;47(8):N107-N112. doi:10.1088/0031-9155/47/8/403
121. Mumot M, Mytsin G V., Molokanov AG, Malicki J. The comparison of doses measured by radiochromic films and semiconductor detector in a 175 MeV proton beam. *Phys Medica*. 2009;25(3):105-110. doi:10.1016/J.EJMP.2008.06.001
122. Son J, Baek T, Lee B, Shin D, Park SY, Park J, Lim YK, Lee SB, Kim J, Yoon M. A comparison of the quality assurance of four dosimetric tools for intensity modulated radiation therapy. *Radiol Oncol*. 2015;49(3):307-313. doi:10.1515/raon-2015-0021
123. Lomax AJ. Intensity modulated proton therapy and its sensitivity to treatment uncertainties 2: the potential effects of inter-fraction and inter-field motions. *Phys Med Biol*. 2008;53(4):1043-1056. doi:10.1088/0031-9155/53/4/015

124. Engelsman M, Schwarz M, Dong L. Physics Controversies in Proton Therapy. *Semin Radiat Oncol.* 2013;23(2):88-96. doi:10.1016/J.SEMRADONC.2012.11.003
125. Yang M, Zhu XR, Park PC, Titt U, Mohan R, Virshup G, Clayton JE, Dong L. Comprehensive analysis of proton range uncertainties related to patient stopping-power-ratio estimation using the stoichiometric calibration. *Phys Med Biol.* 2012;57(13):4095-4115. doi:10.1088/0031-9155/57/13/4095
126. Grant RL, Summers PA, Neihart JL, Blatnica AP, Sahoo N, Gillin MT, Followill DS, Ibbott GS. Relative stopping power measurements to aid in the design of anthropomorphic phantoms for proton radiotherapy. *J Appl Clin Med Phys.* 2014;15(2):4523.
127. Giraud P, Elles S, Helfre S, De Rycke Y, Servois V, Carette M-F, Alzieu C, Bondiau P-Y, Dubray B, Touboul E, Housset M, Rosenwald J-C, Cosset J-M. Conformal radiotherapy for lung cancer: different delineation of the gross tumor volume (GTV) by radiologists and radiation oncologists. *Radiother Oncol.* 2002;62(1):27-36. doi:10.1016/S0167-8140(01)00444-3
128. Moyers MF, Miller DW, Bush DA, Slater JD. Methodologies and tools for proton beam design for lung tumors. *Int J Radiat Oncol.* 2001;49(5):1429-1438. doi:10.1016/S0360-3016(00)01555-8
129. van Herk M. Errors and margins in radiotherapy. *Semin Radiat Oncol.* 2004;14(1):52-64. doi:10.1053/J.SEMRADONC.2003.10.003

130. Nath R, Biggs PJ, Bova FJ, Ling CC, Purdy JA, Van de Geijn J, Weinhaus MS. AAPM code of practice for radiotherapy accelerators: Report of AAPM Radiation Therapy Task Group No. 45. *Med Phys.* 1994;21(7):1093-1121. doi:10.1118/1.597398
131. Bissonnette JP, Balter PA, Dong L, Langen KM, Lovelock DM, Miften M, Moseley DJ, Pouliot J, Sonke JJ, Yoo S. Quality assurance for image-guided radiation therapy utilizing CT-based technologies: A report of the AAPM TG-179. *Med Phys.* 2012;39(4):1946-1963. doi:10.1118/1.3690466
132. Coutrakon G, Bauman M, Lesyna D, Miller D, Nusbaum J, Slater J, Johanning J, Miranda J, DeLuca PM, Siebers J, Ludewigt B. A prototype beam delivery system for the proton medical accelerator at Loma Linda. *Med Phys.* 1991;18(6):1093-1099. doi:10.1118/1.596617
133. Pedroni E, Bacher R, Blattmann H, Böhringer T, Coray A, Lomax A, Lin S, Munkel G, Scheib S, Schneider U, Tourovsky A. The 200-MeV proton therapy project at the Paul Scherrer Institute: Conceptual design and practical realization. *Med Phys.* 1995;22(1):37-53. doi:10.1118/1.597522
134. Landberg T, Chavaudra J, Dobbs J, Hanks G, Johansson K, Möller T, Purdy J. ICRU Report 50: Prescribing, recording and reporting photon beam therapy. *J ICRU.* 1993;26(1). doi:10.2307/3578862
135. Ipe N. Shielding Design and Radiation Safety of Charged Particle Therapy Facilities. *PTCOG.* 2009;1.

136. Kooy HM, Rosenthal SJ, Engelsman M, Mazal A, Slopsema RL, Paganetti H, Flanz JB. The prediction of output factors for spread-out proton Bragg peak fields in clinical practice. *Phys Med Biol*. 2005;50(24):5847-5856. doi:10.1088/0031-9155/50/24/006
137. Sahoo N, Zhu XR, Arjomandy B, Ciangaru G, Lii M, Amos R, Wu R, Gillin MT. A procedure for calculation of monitor units for passively scattered proton radiotherapy beams. *Med Phys*. 2008;35(11):5088-5097. doi:10.1118/1.2992055
138. Hogstrom KR, Mills MD, Eyer JA, Palta JR, Mellenberg DE, Meoz RT, Fields RS. Dosimetric evaluation of a pencil-beam algorithm for electrons employing a two-dimensional heterogeneity correction. *Int J Radiat Oncol*. 1984;10(4):561-569. doi:10.1016/0360-3016(84)90036-1
139. Harms WB, Low DA, Wong JW, Purdy JA. A software tool for the quantitative evaluation of 3D dose calculation algorithms. *Med Phys*. 1998;25(10):1830-1836. doi:10.1118/1.598363
140. Low DA, Harms WB, Mutic S, Purdy JA. A technique for the quantitative evaluation of dose distributions. *Med Phys*. 1998;25(5):656-661. doi:10.1118/1.598248
141. Oldham M, Thomas A, O'Daniel J, Juang T, Ibbott G, Adamovics J, Kirkpatrick JP. A Quality Assurance Method that Utilizes 3D Dosimetry and Facilitates Clinical Interpretation. *Int J Radiat Oncol*. 2012;84(2):540-546. doi:10.1016/J.IJROBP.2011.12.015

142. Pulliam KB, Huang JY, Howell RM, Followill D, Bosca R, O'Daniel J, Kry SF. Comparison of 2D and 3D gamma analyses. *Med Phys*. 2014;41(2):021710. doi:10.1118/1.4860195
143. Lafratta R, Ibbott G, Adamovics J, Followill D. Comparison of 2D and 3D Gamma calculations for an IMRT QA phantom. *J Phys Conf Ser*. 2015;573(1):012055. doi:10.1088/1742-6596/573/1/012055
144. Xing A, Arumugam S, Deshpande S, George A, Vial P, Holloway L, Goozee G. Evaluation of 3D Gamma index calculation implemented in two commercial dosimetry systems. *J Phys Conf Ser*. 2015;573(1):012054. doi:10.1088/1742-6596/573/1/012054
145. Molineu A, Hernandez N, Nguyen T, Ibbott G, Followill D. Credentialing results from IMRT irradiations of an anthropomorphic head and neck phantom. *Med Phys*. 2013;40(2):022101. doi:10.1118/1.4773309
146. Kry SF, Alvarez P, Molineu A, Amador C, Galvin J, Followill DS. Algorithms Used in Heterogeneous Dose Calculations Show Systematic Differences as Measured With the Radiological Physics Center's Anthropomorphic Thorax Phantom Used for RTOG Credentialing. *Int J Radiat Oncol*. 2013;85(1):e95-e100. doi:10.1016/J.IJROBP.2012.08.039
147. Bush DA, Slater JD, Garberoglio C, Do S, Lum S, Slater JM. Partial Breast Irradiation Delivered With Proton Beam: Results of a Phase II Trial. *Clin Breast Cancer*. 2011;11(4):241-245. doi:10.1016/J.CLBC.2011.03.023

148. Mendenhall NP, Li Z, Hoppe BS, Marcus RB, Mendenhall WM, Nichols RC, Morris CG, Williams CR, Costa J, Henderson R. Early Outcomes From Three Prospective Trials of Image-Guided Proton Therapy for Prostate Cancer. *Int J Radiat Oncol*. 2012;82(1):213-221. doi:10.1016/J.IJROBP.2010.09.024

149. Chang JY, Komaki R, Lu C, Wen HY, Allen PK, Tsao A, Gillin M, Mohan R, Cox JD. Phase 2 study of high-dose proton therapy with concurrent chemotherapy for unresectable stage III nonsmall cell lung cancer. *Cancer*. 2011;117(20):4707-4713. doi:10.1002/cncr.26080

150. Summers P, Ibbott G, Moyers M, Grant R, Followill D. TH-C-144-11: Radiological Physics Center (RPC) Approval of Proton Centers for NCI-Sponsored Clinical Trials. *Med Phys*. 2013;40(6Part33):548-548. doi:10.1118/1.4815805

151. Taylor P. TU-G-BRB-03: IROC Houston's Proton Beam Validation for Clinical Trials. *Med Phys*. 2015;42(6):3629. doi:10.1118/1.4925748

152. Guidelines for the Use of Proton Radiation Therapy in NCI- Sponsored Cooperative Group Clinical Trials. IROC-H. [http://rpc.mdanderson.org/rpc.mdanderson.org/RPC/nci guidelines/ATC_Proton_Guidelines_May2010.pdf](http://rpc.mdanderson.org/rpc.mdanderson.org/RPC/nci_guidelines/ATC_Proton_Guidelines_May2010.pdf). Published 2012. Accessed January 7, 2018.

153. Bäck A. Quasi 3D dosimetry (EPID, conventional 2D/3D detector matrices). *J Phys Conf Ser*. 2015;573(1):012012. doi:10.1088/1742-6596/573/1/012012

154. Cirio R, Garelli E, Schulte R, Amerio S, Boriani A, Bourhaleb F, Coutrakon G, Donetti M, Giordanengo S, Koss P, Madon E, Marchetto F, Nastasi U, Peroni C, Santuari D, Sardo A, Scielzo G, Stasi M, Trevisiol E. Two-dimensional and quasi-three-dimensional dosimetry of hadron and photon beams with the Magic Cube and the Pixel Ionization Chamber. *Phys Med Biol*. 2004;49(16):3713-3724.
155. Bedford JL, Lee YK, Wai P, South CP, Warrington AP. Evaluation of the Delta⁴ phantom for IMRT and VMAT verification. *Phys Med Biol*. 2009;54(9):N167-N176. doi:10.1088/0031-9155/54/9/N04
156. Fricke H, Morse S. The chemical action of Roentgen rays on dilute ferrosulphate solutions as a measure of dose. *Am J Roentgenol Radium Ther Nucl Med*. 1927;18:430-432.
157. Alexander P, Charlesby A, Ross M. The Degradation of Solid Polymethylmethacrylate by Ionizing Radiation. *Proc R Soc A Math Phys Eng Sci*. 1954;223(1154):392-404. doi:10.1098/rspa.1954.0123
158. Day M, Stein G. Chemical Effects of Ionizing Radiation in some Gels. *Nature*. 1950;166(4212):146-147. doi:10.1038/166146a0
159. Keall P, Baldock C. A theoretical study of the radiological properties and water equivalence of Fricke and polymer gels used for radiation dosimetry. *Australas Phys Eng Sci Med*. 1999;22(3):85-91.
160. Baldock C, De Deene Y, Doran S, Ibbott G, Jirasek A, Lepage M, McAuley KB, Oldham M, Schreiner LJ. Polymer gel dosimetry. *Phys Med Biol*. 2010;55(5):R1-

63. doi:10.1088/0031-9155/55/5/R01

161. Gore JC, Kang YS, Schulz RJ. Measurement of radiation dose distributions by nuclear magnetic resonance (NMR) imaging. *Phys Med Biol*. 1984;29(10):1189-1197.
162. Gore JC, Ranade M, Maryański MJ, Schulz RJ. Radiation dose distributions in three dimensions from tomographic optical density scanning of polymer gels: I. Development of an optical scanner. *Phys Med Biol*. 1996;41(12):2695-2704.
163. Ceckler TL, Wolff SD, Yip V, Simon SA, Balaban RS. Dynamic and chemical factors affecting water proton relaxation by macromolecules. *J Magn Reson*. 1992;98(3):637-645. doi:10.1016/0022-2364(92)90018-3
164. Buxton G V., Greenstock CL, Helman WP, Ross AB. Critical Review of rate constants for reactions of hydrated electrons, hydrogen atoms and hydroxyl radicals in Aqueous Solution. *J Phys Chem Ref Data*. 1988;17(2):513-886. doi:10.1063/1.555805
165. Panajkar MS, Guha SN, Gopinathan C. Reactions of Hydrated Electron with N,N'-Methylenebisacrylamide in Aqueous Solution: A Pulse Radiolysis Study. *J Macromol Sci Part A*. 1995;32(1):143-156. doi:10.1080/10601329508011070
166. Baldock C, Burford RP, Billingham N, Wagner GS, Patval S, Badawi RD, Keevil SF. Experimental procedure for the manufacture and calibration of polyacrylamide gel (PAG) for magnetic resonance imaging (MRI) radiation dosimetry. *Phys Med Biol*. 1998;43(3):695-702.

167. Lepage M, Jayasakera PM, B\$aumuml\$ck S \$Aring\$ J, Baldock C. Dose resolution optimization of polymer gel dosimeters using different monomers. *Phys Med Biol.* 2001;46(10):310. doi:10.1088/0031-9155/46/10/310
168. Baselga J, Pi rola IF, Hern ndez-fuentes I, Llorente MA. Stress-strain behavior of polyacrylamide networks. *Makromol Chemie Macromol Symp.* 1988;20-21(1):369-382. doi:10.1002/masy.19880200139
169. Jirasek AI, Duzenli C. Effects of crosslinker fraction in polymer gel dosimeters using FT Raman spectroscopy. *Phys Med Biol.* 2001;46(7):1949-1961. doi:10.1088/0031-9155/46/7/315
170. De Deene Y, De Wagter C, Van Duyse B, Derycke S, De Neve W, Achten E. Three-dimensional dosimetry using polymer gel and magnetic resonance imaging applied to the verification of conformal radiation therapy in head-and-neck cancer. *Radiother Oncol.* 1998;48(3):283-291. doi:10.1016/S0167-8140(98)00087-5
171. Senden RJ, Jean P De, McAuley KB, Schreiner LJ. Polymer gel dosimeters with reduced toxicity: a preliminary investigation of the NMR and optical dose–response using different monomers. *Phys Med Biol.* 2006;51(14):3301-3314. doi:10.1088/0031-9155/51/14/001
172. Yvonne Roed, Lawrence Pinsky GI. The assessment of polymer gel for 3D dosimetry in magnetic resonance-image guided radiotherapy. In: *6th MR in RT.* ; 2018.
173. De Deene Y, Hanselaer P, De Wagter C, Achten E, De Neve W. An investigation

- of the chemical stability of a monomer/polymer gel dosimeter. *Phys Med Biol.* 2000;45(4):859-878.
174. Deene Y De, Pittomvils G, Visalatchi S. The influence of cooling rate on the accuracy of normoxic polymer gel dosimeters. *Phys Med Biol.* 2007;52(10):2719-2728. doi:10.1088/0031-9155/52/10/006
 175. Maryanski M, Gore J, Schulz R. Three-dimensional detection, dosimetry and imaging of an energy field by formation of a polymer in a gel. *Magn Reson Imaging.* 1997;15(8).
 176. Maryanski MJ, Gore JC, Kennan RP, Schulz RJ. NMR relaxation enhancement in gels polymerized and cross-linked by ionizing radiation: a new approach to 3D dosimetry by MRI. *Magn Reson Imaging.* 1993;11(2):253-258. <http://www.ncbi.nlm.nih.gov/pubmed/8455435>. Accessed January 7, 2018.
 177. Maryanski MJ, Ibbott GS, Eastman P, Schulz RJ, Gore JC. Radiation therapy dosimetry using magnetic resonance imaging of polymer gels. *Med Phys.* 1996;23(5):699-705. doi:10.1118/1.597717
 178. Roed Y, Ding Y, Wen Z, Wang J, Pinsky L, Ibbott G. The potential of polymer gel dosimeters for 3D MR-IGRT quality assurance. *J Phys Conf Ser.* 2017;847(1):012059. doi:10.1088/1742-6596/847/1/012059
 179. Deene Y De. Fundamentals of MRI measurements for gel dosimetry. *J Phys Conf Ser.* 2004;3(1):87-114. doi:10.1088/1742-6596/3/1/009
 180. Oldham M, Siewerdsen JH, Shetty A, Jaffray DA. High resolution gel-dosimetry

- by optical-CT and MR scanning. *Med Phys.* 2001;28(7):1436-1445.
doi:10.1118/1.1380430
181. Hilts M, Audet C, Duzenli C, Jirasek A. Polymer gel dosimetry using x-ray computed tomography: a feasibility study. *Phys Med Biol.* 2000;45(9):2559-2571.
 182. Hilts M. X-ray computed tomography imaging of polymer gel dosimeters. *J Phys Conf Ser.* 2006;56(1):95-107. doi:10.1088/1742-6596/56/1/009
 183. Olsson LE, Fransson A, Ericsson A, Mattsson S. MR imaging of absorbed dose distributions for radiotherapy using ferrous sulphate gels. *Phys Med Biol.* 1990;35(12):1623-1631.
 184. Harris PJ, Piercy A, Baldock C. A method for determining the diffusion coefficient in Fe(II/III) radiation dosimetry gels using finite elements. *Phys Med Biol.* 1996;41(9):1745-1753. doi:10.1088/0031-9155/41/9/013
 185. Kron T, Jonas D, Pope JM. Fast T1 imaging of dual gel samples for diffusion measurements in NMR dosimetry gels. *Magn Reson Imaging.* 1997;15(2):211-221. doi:10.1016/S0730-725X(96)00352-9
 186. Baldock C, Harris PJ, Piercy AR, Healy B. Experimental determination of the diffusion coefficient in two-dimensions in ferrous sulphate gels using the finite element method. *Australas Phys Eng Sci Med.* 2001;24(1):19-30.
 187. Schulz RJ, DeGuzman AF, Nguyen DB, Gore JC. Dose-response curves for Fricke-infused agarose gels as obtained by nuclear magnetic resonance. *Phys Med Biol.* 1990;35(12):1611-1622.

188. Olsson LE, Westrin BA, Fransson A, Nordell B. Diffusion of ferric ions in agarose dosimeter gels. *Phys Med Biol.* 1992;37(12):2243-2252. doi:10.1088/0031-9155/37/12/006
189. Hazle JD, Hefner L, Nyerick CE, Wilson L, Boyer AL. Dose-response characteristics of a ferrous-sulphate-doped gelatin system for determining radiation absorbed dose distributions by magnetic resonance imaging (Fe MRI). *Phys Med Biol.* 1991;36(8):1117-1125. doi:10.1088/0031-9155/36/8/007
190. Rae WID, Willemse CA, Lötter MG, Engelbrecht JS, Swarts JC. Chelator effect on ion diffusion in ferrous-sulfate-doped gelatin gel dosimeters as analyzed by MRI. *Med Phys.* 1996;23(1):15-23. doi:10.1118/1.597787
191. Tseng YJ, Huang S-C, Chu WC. A least-squares error minimization approach in the determination of ferric ion diffusion coefficient of Fricke-infused dosimeter gels. *Med Phys.* 2005;32(4):1017-1023. doi:10.1118/1.1879452
192. Duzenli C, Sloboda R, Robinson D. A spin-spin relaxation rate investigation of the gelatin ferrous sulphate NMR dosimeter. *Phys Med Biol.* 1994;39(10):1577-1592.
193. Lee HJ, Alqathami M, Kadbi M, Wang J, Blencowe A, Ibbott GS. Feasibility of Using 3-Dimensional (3D) Radiochromic Dosimeters for Real-Time 2-Dimensional and 3D Dose Distribution Measurements in Magnetic Resonance–Guided Radiation Therapy. *Int J Radiat Oncol.* 2016;96(2):E631. doi:10.1016/j.ijrobp.2016.06.2208
194. Scharf K. Spectrophotometric measurement of ferric ion concentration in the

- ferrous sulphate (Fricke) dosimeter. *Phys Med Biol.* 1971;16(1):006.
doi:10.1088/0031-9155/16/1/006
195. Oldham M. Radiochromic 3D Detectors. *J Phys Conf Ser.* 2015;573(1):012006.
doi:10.1088/1742-6596/573/1/012006
 196. Appleby A, Leghrouz A. Imaging of radiation dose by visible color development in ferrous-agarose-xylene orange gels. *Med Phys.* 1991;18(2):309-312.
doi:10.1118/1.596676
 197. Gupta BL, Narayan GR. $G(\text{Fe}^{3+})$ values in the FBX dosimeter. *Phys Med Biol.* 1985;30(4):337-340. doi:10.1088/0031-9155/30/4/007
 198. Gupta BL, Gomathy KR. Consistency of ferrous sulphate-benzoic acid-xylene orange dosimeter. *Int J Appl Radiat Isot.* 1974;25(11-12):509-513.
doi:10.1016/0020-708X(74)90077-5
 199. Kelly RG, Jordan KJ, Battista JJ. Optical CT reconstruction of 3D dose distributions using the ferrous-benzoic-xylene (FBX) gel dosimeter. *Med Phys.* 1998;25(9):1741-1750. doi:10.1118/1.598356
 200. Bero MA, Gilboy WB, Glover PM, El-masri HM. Tissue-equivalent gel for non-invasive spatial radiation dose measurements. *Nucl Instruments Methods Phys Res Sect B Beam Interact with Mater Atoms.* 2000;166-167:820-825.
doi:10.1016/S0168-583X(99)00873-3
 201. Jordan K, Avvakumov N. Radiochromic leuco dye micelle hydrogels: I. Initial investigation. *Phys Med Biol.* 2009;54(22):6773-6789. doi:10.1088/0031-

202. Babic S, Battista J, Jordan K. Radiochromic leuco dye micelle hydrogels: II. Low diffusion rate leuco crystal violet gel. *Phys Med Biol.* 2009;54(22):6791-6808. doi:10.1088/0031-9155/54/22/003
203. Vandecasteele J, Ghysel S, Baete SH, De Deene Y. Radio-physical properties of micelle leucodye 3D integrating gel dosimeters. *Phys Med Biol.* 2011;56(3):627-651. doi:10.1088/0031-9155/56/3/007
204. Vandecasteele J, De Deene Y. Evaluation of radiochromic gel dosimetry and polymer gel dosimetry in a clinical dose verification. *Phys Med Biol.* 2013;58(18):6241-6262. doi:10.1088/0031-9155/58/18/6241
205. Jordan K, Sekimoto M. Non-diffusing radiochromic micelle gel. *J Phys Conf Ser.* 2010;250(1):012031. doi:10.1088/1742-6596/250/1/012031
206. Kirov AS, Piao JZ, Mathur NK, Miller TR, Devic S, Trichter S, Zaider M, Soares CG, LoSasso T. The three-dimensional scintillation dosimetry method: test for a ¹⁰⁶Ru eye plaque applicator. *Phys Med Biol.* 2005;50(13):3063-3081. doi:10.1088/0031-9155/50/13/007
207. Pönisch F, Archambault L, Briere TM, Sahoo N, Mohan R, Beddar S, Gillin MT. Liquid scintillator for 2D dosimetry for high-energy photon beams. *Med Phys.* 2009;36(5):1478-1485. doi:10.1118/1.3106390
208. Suchaworska N, Liu PZY, Ralston A, Naseri P, Abolfathi P, Lee J, Warrenner K, McKenzie DR. Scintillators for 3D and 4D dosimetry: current status and future

- potential for clinical translation. *J Phys Conf Ser.* 2013;444(1):012075.
doi:10.1088/1742-6596/444/1/012075
209. Goulet M, Rilling M, Gingras L, Beddar S, Beaulieu L, Archambault L. Novel, full 3D scintillation dosimetry using a static plenoptic camera. *Med Phys.* 2014;41(8):082101. doi:10.1118/1.4884036
210. Karger CP, Jäkel O, Hartmann GH, Heeg P. A system for three-dimensional dosimetric verification of treatment plans in intensity-modulated radiotherapy with heavy ions. *Med Phys.* 1999;26(10):2125-2132. doi:10.1118/1.598728
211. Hui C, Robertson D, Alsanea F, Beddar S. Fast range measurement of spot scanning proton beams using a volumetric liquid scintillator detector. *Biomed Phys Eng express.* 2015;1(2). doi:10.1088/2057-1976/1/2/025204
212. Archambault L, Poenisch F, Sahoo N, Robertson D, Lee A, Gillin MT, Mohan R, Beddar S. Verification of proton range, position, and intensity in IMPT with a 3D liquid scintillator detector system. *Med Phys.* 2012;39(3):1239-1246. doi:10.1118/1.3681948
213. Beaulieu L, Beddar S. Review of plastic and liquid scintillation dosimetry for photon, electron, and proton therapy. *Phys Med Biol.* 2016;61(20):R305-R343. doi:10.1088/0031-9155/61/20/R305
214. Beddar S. Real-time volumetric scintillation dosimetry. *J Phys Conf Ser.* 2015;573(1):012005. doi:10.1088/1742-6596/573/1/012005
215. Adamovics J, Maryanski M. New 3D radiochromic solid polymer dosimeter from

- leuco dyes and a transparent polymeric matrix. *Med Phys*. 2003;30:1349.
216. Høye EM, Skyt PS, Balling P, Muren LP, Taasti VT, Swakoń J, Mierzwińska G, Rydygier M, Bassler N, Petersen JBB. Chemically tuned linear energy transfer dependent quenching in a deformable, radiochromic 3D dosimeter. *Phys Med Biol*. 2017;62(4):N73-N89. doi:10.1088/1361-6560/aa512a
 217. Høye EM, Balling P, Yates ES, Muren LP, Petersen JBB, Skyt PS. Eliminating the dose-rate effect in a radiochromic silicone-based 3D dosimeter. *Phys Med Biol*. 2015;60(14):5557-5570. doi:10.1088/0031-9155/60/14/5557
 218. Kaplan LP, Høye EM, Balling P, Muren LP, Petersen JBB, Poulsen PR, Yates ES, Skyt PS. Determining the mechanical properties of a radiochromic silicone-based 3D dosimeter. *Phys Med Biol*. 2017;62(14):5612-5622. doi:10.1088/1361-6560/aa70cd
 219. De Deene Y, Skyt PS, Hil R, Booth JT. FlexyDos3D: a deformable anthropomorphic 3D radiation dosimeter: radiation properties. *Phys Med Biol*. 2015;60(4):1543-1563. doi:10.1088/0031-9155/60/4/1543
 220. Schreiner LJ. True 3D chemical dosimetry (gels, plastics): Development and clinical role. *J Phys Conf Ser*. 2015;573(1):012003. doi:10.1088/1742-6596/573/1/012003
 221. Alqathami M, Blencowe A, Qiao G, Butler D, Geso M. Optimization of the sensitivity and stability of the PRESAGETM dosimeter using trihalomethane radical initiators. *Radiat Phys Chem*. 2012;81(7):867-873.

doi:10.1016/J.RADPHYSICHEM.2012.03.022

222. Juang T, Newton J, Niebanck M, Benning R, Adamovics J, Oldham M. Customising PRESAGE® for diverse applications. *J Phys Conf Ser.* 2013;444:012029. doi:10.1088/1742-6596/444/1/012029
223. Juang T, Das S, Adamovics J, Benning R, Oldham M. On the need for comprehensive validation of deformable image registration, investigated with a novel 3-dimensional deformable dosimeter. *Int J Radiat Oncol Biol Phys.* 2013;87(2):414-421. doi:10.1016/j.ijrobp.2013.05.045
224. Mostaar A, Hashemi B, Zahmatkesh MH, Aghamiri SMR, Mahdavi SR. Development and characterization of a novel PRESAGE formulation for radiotherapy applications. *Appl Radiat Isot.* 2011;69(10):1540-1545. doi:10.1016/J.APRADISO.2011.06.014
225. Gorjiara T, Hill R, Kuncic Z, Adamovics J, Bosi S, Kim J-H, Baldock C. Investigation of radiological properties and water equivalency of PRESAGE® dosimeters. *Med Phys.* 2011;38(4):2265-2274. doi:10.1118/1.3561509
226. Adamovics J, Maryanski MJ. A new approach to radiochromic three-dimensional dosimetry-polyurethane. *J Phys Conf Ser.* 2004;3(1):172-175. doi:10.1088/1742-6596/3/1/020
227. Alqathami M, Blencowe A, Ibbott G. Experimental determination of the influence of oxygen on the PRESAGE® dosimeter. *Phys Med Biol.* 2016;61(2):813-824. doi:10.1088/0031-9155/61/2/813

228. Guo P, Adamovics J, Oldham M. Quality assurance in 3D dosimetry by optical-CT. *J Phys Conf Ser.* 2006;56(1):191-194. doi:10.1088/1742-6596/56/1/025
229. Guo PY, Adamovics JA, Oldham M. Characterization of a new radiochromic three-dimensional dosimeter. *Med Phys.* 2006;33(5):1338-1345. doi:10.1118/1.2192888
230. Guo P, Adamovics J, Oldham M. A practical three-dimensional dosimetry system for radiation therapy. *Med Phys.* 2006;33(10):3962-3972. doi:10.1118/1.2349686
231. Sakhalkar HS, Adamovics J, Ibbott G, Oldham M. A comprehensive evaluation of the PRESAGE/optical-CT 3D dosimetry system. *Med Phys.* 2008;36(1):71-82. doi:10.1118/1.3005609
232. Vidovic AK, Juang T, Meltsner S, Adamovics J, Chino J, Steffey B, Craciunescu O, Oldham M. An investigation of a PRESAGE® in vivo dosimeter for brachytherapy. *Phys Med Biol.* 2014;59(14):3893-3905. doi:10.1088/0031-9155/59/14/3893
233. Huang O. Evaluation of PRESAGE® dosimeters for brachytherapy sources and the 3D dosimetry and characterization of the new AgX100 125I seed model. *UT GSBS Diss Theses (Open Access).* August 2013. http://digitalcommons.library.tmc.edu/utgsbs_dissertations/393. Accessed January 7, 2018.
234. Irwin JS. Characterization of the New Xofigo Axxent Electronic Brachytherapy Source Using PRESAGE(TM). *UT GSBS Diss Theses (Open Access).* August

2014. http://digitalcommons.library.tmc.edu/utgsbs_dissertations/503. Accessed January 7, 2018.
235. Choi GW. Measurement of the Electron Return Effect Using PRESAGE Dosimeter. *UT GSBS Diss Theses (Open Access)*. August 2016. http://digitalcommons.library.tmc.edu/utgsbs_dissertations/690. Accessed January 5, 2018.
236. Mein S, Rankine L, Adamovics J, Li H, Oldham M. Development of a 3D remote dosimetry protocol compatible with MRgIMRT: *Med Phys*. 2017;44(11):6018-6028. doi:10.1002/mp.12565
237. Ibbott GS, Thwaites DI. Audits for advanced treatment dosimetry. *J Phys Conf Ser*. 2015;573(1):012002. doi:10.1088/1742-6596/573/1/012002
238. Yates ES, Balling P, Petersen JBB, Christensen MN, Skyt PS, Bassler N, Kaiser F-J, Muren LP. Characterization of the optical properties and stability of PresageTM following irradiation with photons and carbon ions. *Acta Oncol (Madr)*. 2011;50(6):829-834. doi:10.3109/0284186X.2011.565368
239. Lafratta R. QUALITY ASSURANCE OF ADVANCED TREATMENT MODALITIES USING PRESAGE® DOSIMETERS. 2015.
240. Jackson J, Juang T, Adamovics J, Oldham M. An investigation of PRESAGE® 3D dosimetry for IMRT and VMAT radiation therapy treatment verification. *Phys Med Biol*. 2015;60(6):2217-2230. doi:10.1088/0031-9155/60/6/2217
241. Thomas A, Newton J, Adamovics J, Oldham M. Commissioning and

- benchmarking a 3D dosimetry system for clinical use. *Med Phys.* 2011;38(8):4846-4857. doi:10.1118/1.3611042
242. Klawikowski SJ, Yang JN, Adamovics J, Ibbott GS. PRESAGE 3D dosimetry accurately measures Gamma Knife output factors. *Phys Med Biol.* 2014;59(23):N211-N220. doi:10.1088/0031-9155/59/23/N211
 243. Wang Z, Thomas A, Newton J, Ibbott G, Deasy J, Oldham M. Dose Verification of Stereotactic Radiosurgery Treatment for Trigeminal Neuralgia with Presage 3D Dosimetry System. *J Phys Conf Ser.* 2010;250(1). doi:10.1088/1742-6596/250/1/012058
 244. Klawikowski S, Adamovics J, Alqathami M, Benning R, Ibbott G. SU-E-T-511: Do Presage 3D Dosimeters Show Dose Fractionation Sensitivity? *Med Phys.* 2014;41(6Part19):344-344. doi:10.1118/1.4888844
 245. Pelliccia D, Poole CM, Livingstone J, Stevenson AW, Smyth LML, Rogers PAW, Häusermann D, Crosbie JC, IUCr. Image guidance protocol for synchrotron microbeam radiation therapy. *J Synchrotron Radiat.* 2016;23(2):566-573. doi:10.1107/S1600577515022894
 246. Gagliardi FM, Cornelius I, Blencowe A, Franich RD, Geso M. High resolution 3D imaging of synchrotron generated microbeams. *Med Phys.* 2015;42(12):6973-6986. doi:10.1118/1.4935410
 247. Annabell N, Yagi N, Umetani K, Wong C, Geso M. Evaluating the peak-to-valley dose ratio of synchrotron microbeams using PRESAGE fluorescence. *J*

Synchrotron Radiat. 2012;19(Pt 3):332-339. doi:10.1107/S0909049512005237

248. Grant RL, Crowder ML, Ibbott GS, Simon J, Frank RK, Rogers J, Loy HM, Adamovics J, Newton J, Oldham M, Stearns S, Wendt RE. Three-Dimensional Dosimetry of a Beta-Emitting Radionuclide Using PRESAGE Dosimeters. *J Phys Conf Ser.* 2010;250(1). doi:10.1088/1742-6596/250/1/012095
249. Wai P, Adamovics J, Krstajic N, Ismail A, Nisbet A, Doran S. Dosimetry of the microSelectron-HDR Ir-192 source using PRESAGETM and optical CT. *Appl Radiat Isot.* 2009;67(3):419-422. doi:10.1016/J.APRADISO.2008.06.038
250. Adamson J, Yang Y, Rankine L, Newton J, Adamovics J, Craciunescu O, Oldham M. Towards comprehensive characterization of Cs-137 Seeds using PRESAGE[®] dosimetry with optical tomography. *J Phys Conf Ser.* 2013;444(1):012100. doi:10.1088/1742-6596/444/1/012100
251. Thomas A, O'Daniel J, Adamovics J, Ibbott G, Oldham M. Comprehensive quality assurance for base of skull IMRT. *J Phys Conf Ser.* 2013;444(1):012050. doi:10.1088/1742-6596/444/1/012050
252. Grant R, Ibbott G, Yang J, Adamovics J, Followill D. Investigation of 3D dosimetry for an anthropomorphic spine phantom. *J Phys Conf Ser.* 2013;444(1):012020. doi:10.1088/1742-6596/444/1/012020
253. Bache ST, Juang T, Belley MD, Koontz BF, Adamovics J, Yoshizumi TT, Kirsch DG, Oldham M. Investigating the accuracy of microstereotactic-body-radiotherapy utilizing anatomically accurate 3D printed rodent-morphic dosimeters. *Med Phys.*

2015;42(2):846-855. doi:10.1118/1.4905489

254. Abolfath R, Peeler CR, Newpower M, Bronk L, Grosshans D, Mohan R. A model for relative biological effectiveness of therapeutic proton beams based on a global fit of cell survival data. *Sci Rep*. 2017;7(1):8340. doi:10.1038/s41598-017-08622-6
255. Karger CP, Jäkel O, Palmans H, Kanai T. Dosimetry for ion beam radiotherapy. *Phys Med Biol*. 2010;55(21):R193-R234. doi:10.1088/0031-9155/55/21/R01
256. Jirasek A, Duzenli C. Relative effectiveness of polyacrylamide gel dosimeters applied to proton beams: Fourier transform Raman observations and track structure calculations. *Med Phys*. 2002;29(4):569-577. doi:10.1118/1.1460873
257. Gustavsson H, Bäck SAJ, Medin J, Grusell E, Olsson LE. Linear energy transfer dependence of a normoxic polymer gel dosimeter investigated using proton beam absorbed dose measurements. *Phys Med Biol*. 2004;49(17):3847-3855.
258. Vatnitsky SM. Radiochromic film dosimetry for clinical proton beams. *Appl Radiat Isot*. 1997;48(5):643-651. doi:10.1016/S0969-8043(97)00342-4
259. Bäck SA, Medin J, Magnusson P, Olsson P, Grusell E, Olsson LE. Ferrous sulphate gel dosimetry and MRI for proton beam dose measurements. *Phys Med Biol*. 1999;44(8):1983-1996.
260. Heufelder J, Stiefel S, Pfaender M, Lüdemann L, Grebe G, Heese J. Use of BANG® polymer gel for dose measurements in a 68 MeV proton beam. *Med Phys*. 2003;30(6):1235-1240. doi:10.1118/1.1575557
261. Schmid AI, Laistler E, Sieg J, Dymerska B, Wieland M, Naumann J, Jaekel O,

- Berg A. Monomer consumption in MAGIC-type polymer gels in the Bragg-peak of proton beams observed by volume selective ^1H MR-spectroscopy (MRS): proof of principle for high resolution MRS-methodology with a sensitive rf-detector. *J Phys Conf Ser.* 2013;444(1):012096. doi:10.1088/1742-6596/444/1/012096
262. Park M, Kim G, Ji Y, Kim K, Park S, Jung H. SU-E-T-753: Three-Dimensional Dose Distributions of Incident Proton Particle in the Polymer Gel Dosimeter and the Radiochromic Gel Dosimeter: A Simulation Study with MCNP Code. *Med Phys.* 2015;42(6Part24):3510-3510. doi:10.1118/1.4925117
263. Robertson D, Mirkovic D, Sahoo N, Beddar S. Quenching correction for volumetric scintillation dosimetry of proton beams. *Phys Med Biol.* 2013;58(2):261-273. doi:10.1088/0031-9155/58/2/261
264. Nadrowitz R, Coray A, Boehringer T, Dunst J, Rades D. A liquid fluorescence dosimeter for proton dosimetry. *Phys Med Biol.* 2012;57(5):1325-1333. doi:10.1088/0031-9155/57/5/1325
265. Al-Nowais S, Doran S, Kacperek A, Krstajic N, Adamovics J, Bradley D. A preliminary analysis of LET effects in the dosimetry of proton beams using PRESAGETM and optical CT. *Appl Radiat Isot.* 2009;67(3):415-418. doi:10.1016/J.APRADISO.2008.06.032
266. Nowais S Al, Kacperek A, Brunt JNH, Adamovics J, Nisbet A, Doran SJ. An investigation of the response of the radiochromic dosimeter PRESAGE to irradiation by 62 MeV protons. *J Phys Conf Ser.* 2010;250(1):012034. doi:10.1088/1742-6596/250/1/012034

267. Gorjiara T, Kuncic Z, Doran S, Adamovics J, Baldock C. Water and tissue equivalence of a new PRESAGE® formulation for 3D proton beam dosimetry: A Monte Carlo study. *Med Phys*. 2012;39(11):7071-7079. doi:10.1118/1.4757922
268. Grant R, Ibbott G, Zhu X, Adamovics J, Oldham M, Followill D. Investigation of Proton Beam Dose Distributions with 3D Dosimetry. *Int J Radiat Oncol*. 2011;81(2):S885-S886. doi:10.1016/j.ijrobp.2011.06.1584
269. Doran S, Gorjiara T, Kacperek A, Adamovics J, Kuncic Z, Baldock C. Issues involved in the quantitative 3D imaging of proton doses using optical CT and chemical dosimeters. *Phys Med Biol*. 2015;60(2):709-726. doi:10.1088/0031-9155/60/2/709
270. Krstaji N, Wai P, Adamovics J, Doran S. Spectrophotometry of PRESAGE polyurethane dosimeters. *J Phys Conf Ser*. 2004;3(1):244-247. doi:10.1088/1742-6596/3/1/038
271. Andrews HL, Murphy RE, LeBrun EJ. Gel Dosimeter for Depth-Dose Measurements. *Rev Sci Instrum*. 1957;28(5):329-332. doi:10.1063/1.1715877
272. Gorjiara T, Kacperek A, Kuncic Z, Baldock C, Doran S. Preliminary characterization of PRESAGE for 3D dosimetry of 62 MeV proton beam. *J Phys Conf Ser*. 2013;444(1):012058. doi:10.1088/1742-6596/444/1/012058
273. Adamovics J, Jordan K, Dietrich J. PRESAGE - Development and optimization studies of a 3D radiochromic plastic dosimeter—Part 1. *J Phys Conf Ser*. 2006;56(1):172-175. doi:10.1088/1742-6596/56/1/020

274. Niebanck M, Juang T, Newton J, Adamovics J, Wang Z, Oldham M. Investigating the reproducibility of a complex multifocal radiosurgery treatment. *J Phys Conf Ser.* 2013;444(1):012072. doi:10.1088/1742-6596/444/1/012072
275. Blanksby SJ, Ellison GB. Bond dissociation energies of organic molecules. *Acc Chem Res.* 2003;36(4):255-263. doi:10.1021/ar020230d
276. Adamovics J, Maryanski MJ. Characterisation of PRESAGETM: A new 3-D radiochromic solid polymer dosimeter for ionising radiation. *Radiat Prot Dosimetry.* 2006;120(1-4):107-112. doi:10.1093/rpd/nci555
277. Jenkins AD, Kennedy JF. *Macromolecular Chemistry*. Vol 1. The Royal Society of Chemistry; 1980. doi:10.1039/9781847556554
278. Clemitson IR. *Castable Polyurethane Elastomers*. Vol 53.; 2008. doi:10.1201/9781420065770.fmatt
279. Thomas A, Oldham M. Fast, large field-of-view, telecentric optical-CT scanning system for 3D radiochromic dosimetry. *J Phys Conf Ser.* 2010;250(1):1-5. doi:10.1088/1742-6596/250/1/012007
280. Iqbal K, Gifford KA, Ibbott G, Grant RL, Buzdar S. Comparison of an anthropomorphic PRESAGE[®] dosimeter and radiochromic film with a commercial radiation treatment planning system for breast IMRT: a feasibility study. *J Appl Clin Med Phys.* 2014;15(1):4531. <http://www.ncbi.nlm.nih.gov/pubmed/24423854>. Accessed January 7, 2018.
281. Deasy JO, Blanco AI, Clark VH. CERR: A computational environment for

- radiotherapy research. *Med Phys*. 2003;30(5):979-985. doi:10.1118/1.1568978
282. Thomas A, Pierquet M, Jordan K, Oldham M. A method to correct for spectral artifacts in optical-CT dosimetry. *Phys Med Biol*. 2011;56(11):3403-3416. doi:10.1088/0031-9155/56/11/014
 283. Moyers MF, Sardesai M, Sun S, Miller DW. Ion Stopping Powers and CT Numbers. *Med Dosim*. 2010;35(3):179-194. doi:10.1016/j.meddos.2009.05.004
 284. Zeidan OA, Sriprisan SI, Lopatiuk-Tirpak O, Kupelian PA, Meeks SL, Hsi WC, Li Z, Palta JR, Maryanski MJ. Dosimetric evaluation of a novel polymer gel dosimeter for proton therapy. *Med Phys*. 2010;37(5):2145-2152. doi:10.1118/1.3388869
 285. Sakhalkar H, Sterling D, Adamovics J, Ibbott G, Oldham M. Investigating the Feasibility of 3D Dosimetry in the RPC IMRT H&N Phantom. *J Phys Conf Ser*. 2009;164(2009):12058. doi:10.1088/1742-6596/164/1/012058
 286. Wang LLW, Perles LA, Archambault L, Sahoo N, Mirkovic D, Beddar S. Determination of the quenching correction factors for plastic scintillation detectors in therapeutic high-energy proton beams. *Phys Med Biol*. 2012;57(23):7767-7781. doi:10.1088/0031-9155/57/23/7767
 287. Granville DA, Sawakuchi GO. Comparison of linear energy transfer scoring techniques in Monte Carlo simulations of proton beams. *Phys Med Biol*. 2015;60(14):N283-N291. doi:10.1088/0031-9155/60/14/N283
 288. Sawakuchi GO, Sahoo N, Gasparian PBR, Rodriguez MG, Archambault L, Titt U,

- Yukihara EG. Determination of average LET of therapeutic proton beams using Al₂O₃:C optically stimulated luminescence (OSL) detectors. *Phys Med Biol*. 2010;55(17):4963-4976. doi:10.1088/0031-9155/55/17/006
289. Grassberger C, Paganetti H. Elevated LET components in clinical proton beams. *Phys Med Biol*. 2011;56(20):6677-6691. doi:10.1088/0031-9155/56/20/011
290. Goorley T, James M, Booth T, Brown F, Bull J, Cox LJ, Durkee J, Elson J, Fensin M, Forster RA, Hendricks J, Hughes HG, Johns R, Kiedrowski B, Martz R, Mashnik S, McKinney G, Pelowitz D, Prael R. Initial MCNP6 Release Overview. *Nucl Technol*. 2012. doi:10.13182/NT11-135
291. Titt U, Zheng Y, Vassiliev ON, Newhauser WD. Monte Carlo investigation of collimator scatter of proton-therapy beams produced using the passive scattering method. *Phys Med Biol*. 2008;53(2):487-504. doi:10.1088/0031-9155/53/2/014
292. Chang W, Koba Y, Katayose T, Yasui K, Omachi C, Hariu M, Saitoh H. Correction of stopping power and LET quenching for radiophotoluminescent glass dosimetry in therapeutic proton beam. *Phys Med Biol*. 2017;62(23):8869. doi:10.1088/1361-6560/aa9155
293. ICRU Report 16: Linear Energy Transfer. *J ICRU*. 1970. doi:10.1093/jicru/os9.1.Report16

Vita

Mitchell Scott Carroll was born in Tallahassee, Florida on May 14, 1985, the daughter of Rick and Mary Carroll. He entered Furman University in Greenville, South Carolina in 2003 and received his Bachelor of Sciences with a major in Physics in 2007. For the next three years he studied Nuclear Engineering at Texas A&M University. In 2010 he entered The University of Texas MD Anderson Cancer Center UTHealth Graduate School of Biomedical Sciences.

Permanent mailing address:

520 Short St.

Tallahassee, FL 32308

Permanent email address:

mitchellscarroll@yahoo.com